



**HAL**  
open science

# A chemical route to design plasmonic-semiconductor nanomaterials heterojunction for photocatalysis applications

Issraa Shahine

► **To cite this version:**

Issraa Shahine. A chemical route to design plasmonic-semiconductor nanomaterials heterojunction for photocatalysis applications. Theoretical and/or physical chemistry. Université de Lorraine, 2019. English. NNT : 2019LORR0105 . tel-02397817

**HAL Id: tel-02397817**

**<https://hal.univ-lorraine.fr/tel-02397817>**

Submitted on 6 Dec 2019

**HAL** is a multi-disciplinary open access archive for the deposit and dissemination of scientific research documents, whether they are published or not. The documents may come from teaching and research institutions in France or abroad, or from public or private research centers.

L'archive ouverte pluridisciplinaire **HAL**, est destinée au dépôt et à la diffusion de documents scientifiques de niveau recherche, publiés ou non, émanant des établissements d'enseignement et de recherche français ou étrangers, des laboratoires publics ou privés.



## AVERTISSEMENT

Ce document est le fruit d'un long travail approuvé par le jury de soutenance et mis à disposition de l'ensemble de la communauté universitaire élargie.

Il est soumis à la propriété intellectuelle de l'auteur. Ceci implique une obligation de citation et de référencement lors de l'utilisation de ce document.

D'autre part, toute contrefaçon, plagiat, reproduction illicite encourt une poursuite pénale.

Contact : [ddoc-theses-contact@univ-lorraine.fr](mailto:ddoc-theses-contact@univ-lorraine.fr)

## LIENS

Code de la Propriété Intellectuelle. articles L 122. 4

Code de la Propriété Intellectuelle. articles L 335.2- L 335.10

[http://www.cfcopies.com/V2/leg/leg\\_droi.php](http://www.cfcopies.com/V2/leg/leg_droi.php)

<http://www.culture.gouv.fr/culture/infos-pratiques/droits/protection.htm>



**UNIVERSITÉ  
DE LORRAINE**



Laboratoire de Chimie et Physique  
Approche Multi-échelles des Milieux Complexes

ECOLE DOCTORALE C2MP : Chimie - Mécanique - Matériaux- Physique

## **THESE**

Pour obtenir le grade de

**Docteur**

De

**L'UNIVERSITE DE LORRAINE**

Spécialité : Chimie-physique

Présentée et soutenue publiquement par

**Issraa SHAHINE**

Le 26 Avril 2019

---

### **A chemical route to design plasmonic-semiconductor nanomaterials heterojunction for photocatalysis applications**

---

#### **Jury**

<b>Pr. Nadine Millot</b>	Université de Bourgogne	Rapporteur
<b>Pr. Grégory Barbillon</b>	EPF - Ecole d'ingénieurs	Rapporteur
<b>Dr. El-Eulmi Bendeif</b>	Université de Lorraine	Examinateur
<b>Pr. Stéphane Roux</b>	Université de Franche-Comté	Examinateur
<b>Dr. Yann Battie</b>	Université de Lorraine	Invité

Directeur de thèse  
**Pr. Jean-Jacques Gaumet**

Co-Directeur de thèse  
**Dr. Suzanna Akil**



## **Acknowledgement**

The success and final outcome of this thesis required a lot guidance and assistance from many people. And I am extremely privileged to have got this all along the completion of my thesis. All that I have done is only due to such supervision and assistance, and I would not forget to thank them.

Firstly, I would like to express my sincere gratitude to my supervisor Dr. Suzanna Akil for the continuous support of my Ph.D study and related research, for her patience, motivation, and immense knowledge. Her guidance helped me in all the time of research and writing of this thesis. I could not have imagined having a better advisor and mentor for my Ph.D study. She has been a tremendous mentor for me, thanks for allowing me to grow as a research scientist. Her kind support and friendly relationship have been priceless.

Besides, I would also like to thank my thesis director Prof. Jean Jacques Gaumet for his encouragement, and giving support and guidance.

I respect and thank my thesis committee: Pr. Nadine Millot, Pr. Grégory Barbillon, Pr. Stéphane Roux, Dr. El-Eulmi Bendeif, and Dr. Yann Battie, for their insightful comments and encouragement, and also for the solid questions which incited me to widen my research from various perspectives.

My sincere thanks also goes to Prof. Olivier Pages, and Prof. Aotmane En-Naciri, who provided me an opportunity to join their team as intern, and who gave access to the laboratory and research facilities. Without their precious support, it would not be possible to conduct this research.

I also thank Dr. Safi Jradi for the stimulating discussions. I am gratefully indebted to his great efforts and valuable comments on this thesis.

With a special mention to Prof. Nazir Fazel. It was fantastic to have the opportunity to meet just a kind and supportive person. Thanks for helping me enormously, especially with the last task of doing the final formatting and printing of this thesis. Thank you so much. I will always be your “petite fille”!

A very special thanks to the “Ecole Doctorale C2MP” for helping and providing the funding of the work at University of Lorraine. I owe my deep gratitude to the state of France which gave me the opportunity to complete my studies in France.

I would also like to say heartfelt thanks to my lab mates and friends for the fruitful discussions, and sleepless nights we were working together before deadlines, and for all the fun we have had in this journey. Precisely, I thank my friends Mohamed Ch. and his wife Fatima M., Yehia M., Hassan H., and Hassan O. for their support. In particular, I am grateful to my special friends Amal and Sahar for enlightening my way with every single moment they let me smile. Thanks for being aside!

Also, a special thanks to Hussein Ahmad and his family, who have been by my side throughout all this period.

I am thankful to and fortunate enough to get constant encouragement and guidance from my friend Hassan El Dor. Thanks for being aside to overcome numerous obstacles I faced.

I would like to thank my family for accepting nothing less than excellence from me, and for all of the sacrifices that they’ve made on my behalf: my parents and to my brothers Yaakoub and Rodwan, and sister Safaa for supporting me spiritually throughout my life in general. Thank you my father for steering me in the right direction whenever I needed. Thanks mom for your sincere prayers seeking success and were what sustained me thus far.

Last but not the least, to my lovely friend Rana, who has been by my side throughout this PhD, living every single minute of it, and without whom, I would not have had the courage to embark on this journey in the first place. Thanks for her advices and feedbacks on my research and for always being so supportive of my work. Words cannot express how grateful I am to her, she was always my support in the moments when there was no one to answer my queries. Thank you sister!

Overall, I thank God, who gave me life, grant me strength, and steadfast me on the straight path.

Issraa Shahine

## Abstract

Hybrid heterojunctions composed of semiconductors and metallic nanostructures have perceived as a sustainable technology, due to their perfect effectiveness in improving, renovating, and enriching the properties of the integrated components. The cooperative coupling results in the variation of the system's functional properties, by which the metal-generated surface plasmon resonance can enhance the charge separation, light absorption, as well as luminescence of the semiconductor. This phenomenon enables strong interactions with other photonic elements such as quantum emitters. These multifaceted functionalities arise from the synergic exciton-plasmon interaction between the linked units. Thereby, hybrid systems become suitable for various applications including: solar energy conversion, optoelectronic devices, light-emitting diodes (LED), photocatalysis, biomedical sensing, etc.

Au-ZnO nanostructures have received growing interest in these applications, where the deposition of gold nanoparticles (GNPs) promotes the system's response towards the visible region of the light spectrum through their surface plasmon resonance (SPR). Based on a specific size and purity of ZnO nanostructures, as well as the GNPs, and a definite inter-distance between the nanoparticles, the properties of the ZnO nanostructures are varied, especially the photoemission and photocatalytic ones.

In this context, we have focused on the construction of size-tunable ZnO nanocrystals (NCs), then incorporated into GNPs solutions using a simple chemical way. This work is divided into two parts: the first is to perform synthesis of pure ZnO NCs having excellent UV photoluminescence. This was achieved through a low-temperature aqueous synthesis, resulting in rough and amorphous structures. The synthesis was followed by a post-thermal treatment in order to crystallize the obtained particles. The synthesis was followed by structural and optical studies (SEM, TEM, XRD, photoluminescence). The photocatalytic activities of ZnO NCs were studied through tailoring their ability to degrade the methylene blue (MB) dye. In addition, the relationship between ZnO structures, luminescence, and photocatalytic properties was explored in details.

In the second step, the obtained ZnO NCs were added to gold nanoparticles of various sizes and volume fractions. The effective role of GNPs concerning their size, amount, and their capping molecule on the photoemission of the ZnO nanostructures was emphasized through

the charge and/or energy transfer between the constituents in the hybrid system. In the same way, the systems photocatalytic activities were examined after coupling ZnO to GNPs.

Further advancement in the integration of the ZnO NCs into PMMA polymer layers was featured in order to obtain large area template of homogenous ZnO properties. The PMMA-assembled ZnO nanoparticles could be promising substrates as catalysts for growing ZnO nanowires, metallic nanoparticles and hybrid nanomaterials.

## Résumé en français

L'ingénierie de nanomatériaux hybrides semi-conducteurs/plasmoniques représente une technologie durable en raison de l'efficacité parfaite du couplage pour améliorer, rénover et enrichir les propriétés des composants intégrés. Ce couplage a pour résultat la variation des propriétés fonctionnelles du système, grâce auquel les plasmons de surface générés par les métaux peuvent améliorer la séparation des charges, l'absorption de la lumière et la luminescence du semi-conducteur. Ce phénomène permet de fortes interactions avec d'autres éléments photoniques tels que les émetteurs quantiques. Ces fonctionnalités aux multiples facettes découlent de l'interaction synergique exciton-plasmon entre les unités liées. Ainsi, les nanomatériaux hybrides conviennent à diverses applications, notamment: conversion de l'énergie solaire, dispositifs optoélectroniques, diodes électroluminescentes (LED), photocatalyse, détection biomédicale, etc.

Les nanostructures Au-ZnO suscitent un intérêt croissant dans ces applications où le couplage de ZnO à de nanoparticules d'or (GNPs) favorise la réponse du système dans le domaine du visible grâce à leur résonance plasmon de surface (SPR). En fonction de la taille de deux nanomatériaux, de la distance qui les sépare et leurs rapports massiques dans un échantillon, les propriétés des particules hybrides peuvent varier.

Dans ce contexte, nous nous sommes concentrés sur la construction de nano-cristaux (NCs) de ZnO purs de dimensions contrôlables, puis incorporés dans des solutions de GNPs par une simple voie chimique.

Ce travail est divisé en deux parties: la première consiste à effectuer une synthèse de nanocristaux de ZnO (NCs) purs présentant d'excellentes propriétés de photoluminescence dans l'UV. Ceci a été réalisé par une synthèse à basse température, aboutissant à des structures rugueuses et amorphes. La synthèse a été suivie d'un traitement post-thermique afin de cristalliser les nanoparticules obtenues. Une étude structurale et optique poussée a été établie à la suite de la synthèse (SEM, TEM, DRX, photoluminescence). Les activités photocatalytiques des ZnO NCs ont été étudiées en mesurant leur capacité à dégrader le bleu de méthylène (MB). De plus, la relation entre les structures en ZnO, la luminescence et les propriétés photocatalytiques a été explorée en détail.

Dans la deuxième étape, les ZnO NCs obtenus ont été couplés ajoutés à des nanoparticules d'or de tailles et fractions volumiques variables. Le rôle effectif des GNPs concernant leur

morphologie, leur contenu et leur effet SPR sur la photoémission des nanostructures de ZnO est souligné par le transfert de charge et / ou d'énergie entre les constituants du système hybride. De plus, l'activité photocatalytique du système hybride a été examinée.

Comme débouché et perspective de ce travail de thèse, l'intégration des ZnO NC dans une couche nanoporeuse de polymère (PMMA) a été réalisée et caractérisée afin d'obtenir un substrat de large surface à base de ZnO. Les ZnO NCs assemblés dans du PMMA pourraient être des substrats prometteurs en tant que catalyseurs pour la croissance de nanofils de ZnO, de nanomatériaux métalliques et de matériaux hybrides.

## Publications

Shahine, I.; Beydoun, N.; Gaumet, J.J.; Bendeif, E.-E.; Rinnert, H.; Magri, P.; Naciri, A.E.; Miska, P.; Jradi, S.; Akil, S. Pure, Size Tunable ZnO Nanocrystals Assembled into Large Area PMMA Layer as Efficient Catalyst. *Catalysts* (2019), 9, 2, 162.

Shahine, I.; Beydoun, N.; Gaumet, J.J.; Jradi, S.; Akil, S. A universal strategy to design plasmon-exciton coupling: heterojunction-based high performance ZnO-Au photocatalysts, to be submitted to *Advanced functional materials*.

## Contributions at international conferences

- “Tunable Photoemission and Photocatalytic Activity of Au-ZnO Nanostructures ”  
Shahine I., Jradi S., Beydoun N. and Akil S. GDR Or-Nano, June 20-21, Bordeaux, France (2019). (Oral presentation)
- “Size controlled photoemission and photocatalytic activity of Au-ZnO nanostructures”  
**Shahine I.**, Jradi S., Beydoun N., El-Eulmi B., Gaumet J-J., En-Naciri A., Rinnert H. and Akil S. Materials Research Society (MRS) Fall Meeting & Exhibit, November 25-30, Boston, Massachusetts, USA (2018). (Poster)
- “ZnO-Au heterojunction enhanced the photoluminescence of ZnO nanocrystals”  
**Shahine I.**, J-J. Gaumet, A. En-Naciri, P. Miska, B. El-Eulmi, H. Rinnert, S. Jradi, S. Akil. The 9<sup>th</sup> International Conference on Metamaterials, Photonic Crystals and Plasmonics (META), 24-31 July 2018, Marseille, France (2018). (Oral presentation)
- “ZnO-Au heterojunction enhanced the photoluminescence of ZnO nanocrystals”  
**I. Shahine**, J-J. Gaumet, A. En-Naciri, P. Miska, B. El-Eulmi, H. Rinnert and S. Akil. European Materials Research Society (E-MRS) Spring Meeting, June 18-22, Strasbourg, France (2018). (Oral presentation)
- “ZnO-Au heterojunction enhanced the photoluminescence of ZnO nanocrystals”  
**I. Shahine**, J-J. Gaumet, A. En-Naciri, H. Rinnert, P. Magri, and S. Akil. Materials Research Society (MRS) Fall Meeting & Exhibit, 26Nov – 1Dec, Boston, USA (2017). (Poster)

# Table of contents

Acknowledgement .....	i
Abstract.....	iii
Résumé en français .....	v
Publications.....	vii
Contributions at international conferences .....	vii
Table of contents.....	1
List of figures.....	5
List of schemes .....	10
List of tables.....	11
List of abbreviations .....	12
List of symbols.....	13
List of chemicals .....	14
General Introduction .....	15
1. Chapter 1 State of Art .....	17
1.1 Introduction .....	17
1.2 Plasmonic-semiconductor hybrid nanomaterials .....	19
1.3 ZnO-Au: The studied plasmonic-semiconductor nanomaterial .....	25
1.3.1 ZnO nanostructures .....	25
1.3.2 Gold nanoparticles .....	28
1.4 New/Enhanced features brought by plasmonic-semiconductor heterojunction .....	29
1.5 Tunable optical properties (absorption and fluorescence) .....	29
1.5.1 Heterojunction modified absorption of both materials .....	29
1.5.2 Heterojunction modified SC's fluorescence .....	31
1.5.3 SERS enhancement.....	35
1.5.4 Stimulating charge transfer after photo-induced charge separation .....	37
1.6 Applications of plasmonic-semiconductor heterojunctions .....	40
1.6.1 Solar cells.....	40
1.6.2 Catalysis-based applications .....	42
1.7 Engineering of plasmonic-semiconductor nanomaterials .....	42
1.8 Conclusion.....	43
1.9 References .....	44

2. Chapter 2 Synthesis and characterization of pure ZnO nanostructures highly efficient for photocatalysis.....	62
2.1 Introduction .....	62
2.2 Experimental part .....	66
2.2.1 Synthesis process .....	66
2.2.1.1 Preparation of stock solutions (Zn and O sources).....	66
2.2.1.2 Preparation of ZnO QDs seeds .....	67
2.3 Results and discussion.....	68
2.3.1 Optimization of the synthesis reaction parameters .....	68
2.3.1.1 Effect of raw materials concentration.....	69
2.3.1.2 Role of synthesis time, temperature, and post-thermal treatment .....	71
2.3.1.3 Effects of synthesis time.....	71
2.3.1.4 Effects of synthesis temperature.....	72
2.3.2 Structural properties.....	75
2.3.2.1 TGA Analysis .....	75
2.3.2.2 XRD analysis.....	76
2.3.2.3 XPS analysis .....	80
2.3.2.4 SEM analysis .....	80
2.3.2.5 TEM analysis.....	81
2.3.3 Optical properties.....	83
2.3.3.1 Absorption measurements .....	83
2.3.3.2 Photoluminescence measurements .....	84
2.3.3.3 Photocatalytic activity .....	87
2.4 Conclusion.....	94
2.5 References .....	95
3. Chapter 3 ZnO-Au heterojunction enhanced the fluorescence and photocatalytic properties of ZnO NPs .....	104
3.1 Introduction .....	104
3.2 Experimental part .....	106
3.2.1 Reagents.....	106
3.2.2 Synthesis of gold nanoparticles (GNPs) .....	106
3.2.3 Coupling ZnO to GNPs.....	107
3.3 Results and discussion.....	108
3.3.1 Role of the semiconductor part (ZnO size) in the interaction with GNPs.....	108
3.3.2 Role of the plasmonic part (GNPs size or number, capping) in the interaction with ZnO nanocrystals .....	113

3.3.3	Photocatalytic performance of ZnO-GNPs.....	125
3.3.4	Other strategies of plasmon-exciton coupling .....	134
3.3.4.1	Real-time synthesis of GNPs over ZnO NPs: real-time interaction .....	134
3.3.4.2	Capping GNPs after reduction.....	135
3.3.4.3	Tailoring the heterojunction distance between ZnO and GNPs: Free capping hybrid nanoparticles .....	136
3.4	Conclusion.....	140
3.5	References .....	141
4.	Chapter 4 Conclusions and perspectives.....	149
4.1	Conclusions .....	149
4.2	Future work and perspectives.....	150
4.3	References .....	153
5.	Chapter 5 Supplementary information.....	154
5.1	Appendix-A.....	154
5.1.1	Effect of dilution in PL measurements .....	154
5.1.2	Reproducibility (Stability of dispersions).....	156
5.1.3	Raw materials ZnO coupled into different CTAB-capped GNPs.....	157
5.1.4	Raw materials ZnO coupled into different CTAB-capped GNPs.....	157
5.1.5	CTAB-capped ZnO NPs (no GNPs) .....	158
5.1.6	ZnO NPs embedded PMMA holes .....	159
5.1.7	Role of ZnO mass embedded in PMMA holes .....	160
5.1.8	Different stabilizers mediated the heterojunction distance .....	160
5.1.9	Large area monolayer of ZnO NPs .....	161
5.2	Appendix-B .....	161
5.2.1	Characterization techniques:.....	161
5.2.1.1	Photoluminescence (PL).....	162
5.2.1.2	UV-visible absorption spectroscopy.....	163
5.2.1.3	X-Ray diffraction (XRD).....	163
5.2.1.4	Transmission electron microscopy (TEM) .....	164
5.2.1.5	Scanning electron microscopy (SEM).....	164
5.2.1.6	Photocatalysis .....	165
5.2.1.7	Thermogravimetric analysis (TGA) .....	165
5.2.1.8	X-ray photoelectron spectroscopy (XPS).....	166
5.2.1.9	Atomic Force microscopy (AFM) .....	166
5.2.1.10	Optical microscopy.....	167

5.3 References .....167

## List of figures

Figure 1 (a-d) TEM images showing the stepwise direct heterogeneous deposition of linear nanoparticle heterotetramers: (a) Pt nanoparticles, (b) Pt-Fe <sub>3</sub> O <sub>4</sub> heterodimers, (c) Au-Pt-Fe <sub>3</sub> O <sub>4</sub> heterotrimers, and (d) Cu <sub>9</sub> S <sub>5</sub> -Au-Pt-Fe <sub>3</sub> O <sub>4</sub> heterotetramers. (e-h) TEM images and schematic representations showing a series of metal/semiconductor heterodimers (same synthetic conditions for all steps) aimed at understanding the site-selective deposition of Ag onto Pt-Fe <sub>3</sub> O <sub>4</sub> heterodimers: (e) Ag grown off Fe <sub>3</sub> O <sub>4</sub> nanoparticles, (f) Ag grown off Pt nanoparticles, (g) Ag grown indiscriminately off both Fe <sub>3</sub> O <sub>4</sub> and Pt nanoparticles when both are present as a physical mixture, and (h) Ag grown exclusively off the Pt domain when Pt and Fe <sub>3</sub> O <sub>4</sub> are directly attached as heterodimers. Adapted from ref. [9].	17
Figure 2 Calculated intensity of the electric field within the Co core in Co-Ag core-shell nanoparticles at resonance (continuous violet line) and maximum Faraday rotation of Co-Ag nanoparticles embedded in oil (n = 1.5018) (dashed blue line) as a function of the Co concentration. Calculations show an excellent agreement with the experimental measurements (red dots). The error bars represent the standard error calculated by taking multiple measurements. Adapted from ref. [11].	18
Figure 3 (A-C) TEM images of CdSe-Au hybrid nanoparticles obtained by changing QAu from 2, 4 to 6 μmol, respectively. The nanoparticles are seen as dimeric units, all with a similar size of ~3.4 nm for the CdSe component. (D) High-resolution TEM image and a schematic drawing of the CdSe-Au hybrid nanoparticles. Adapted from ref. [9].	19
Figure 4 Band structures of metal-semiconductor junctions for (a,b) an n-type semiconductor and (c,d) a p-type semiconductor in thermodynamic equilibrium. Adapted from ref. [79].	24
Figure 5 The signal light absorption spectrum of SQDs. The signal light absorption spectrum of SQDs for different distance d. The inset shows a complex system composed of a SQDs to a MNPs. A SQDs with radius r is placed in the vicinity of a MNPs with radius R. The center-to-center distance is d. Adapted from ref. [160].	30
Figure 6 UV-vis absorption spectra of pure CdS nanorods (blue curve), Au nanoparticles (red curve), and high Au-CdS heterostructures (10.8 wt %, yellow curve). The green- and purple-dotted lines indicate the excitation source of a 532 nm laser and a 405 nm laser, respectively. Adapted from ref. [162].	30
Figure 7 Absorption spectra of ZnO QDs (16.7 μM) in the absence and presence of Au NP (0.67 μM) of five different sizes. The inset shows the change in the surface plasmon band of Au NP upon interaction with the ZnO QDs. Adapted from ref. [163].	31
Figure 8 Photoluminescence spectra for the (a) ZnO/Ag and (b) ZnO/Au nanoparticles under excitation at 325 nm. (c) The ZnO UV-band intensity increases with increasing the metal nanoparticle concentration. Error bars represent the standard deviation for three separate measurements. Adapted from ref. [179].	32
Figure 9 a) SERS spectra from Au-coated ZnO nanorods of 150 nm in diameter, Au thin film (5 nm thick), and a bare Si substrate with R6G of 1 μM. b) Comparison of SERS spectra of Au-coated ZnO nanorods of diameter of 400 and 150 nm with R6G of 1 μM. Adapted from ref. [212].	36
Figure 10 Optical characteristics of assemblies with 54 Au NP and 1 CdSe NP. Inset: field enhancement factor due to a single Au NP. Upper part: geometry of the complex. Adapted from ref. [214].	37

Figure 11 Two charge separation mechanisms in these hybrid heterostructures. Mechanism A starts by excitation at the metal at 532 nm, thus forming hot electrons ( $e^-$ ) and holes ( $h^+$ ) in the metal. The hot electrons are then transferred to the semiconductor's conduction band. Mechanism B starts with excitation at the semiconductor at 405 nm, thus forming electron-hole pairs at the semiconductor. Photogenerated electrons are then trapped by the gold. Adapted from ref. [162].	40
Figure 12 J–V characteristics of the bare ZnO-nanorod and ZnO/Au-hybrid DSSCs, measured at 1 sun, AM 1.5 G illumination, (b) short-circuit photocurrent density of the bare ZnO-nanorod and ZnO/Au-hybrid DSSCs measured at different incident wavelengths and (c) optical absorptions of dye N719 in 0.1 mM KOH aqueous solution for bare ZnO-nanorod and ZnO/Au-hybrid photoelectrodes. The optical absorption was measured by removing the dye molecules from the respective photoelectrodes (size = 1 cm <sup>2</sup> ) by dipping them in a 0.1 mM KOH aqueous solution (2 mL) for 5 min. Adapted from ref. [80].	41
Figure 13 Energy-band diagram depicting the possible electron-transfer path in the ZnO/Au-hybrid DSSC, showing the Schottky barrier formed at the ZnO/Au interface. The dashed line in Au represents the position of the Fermi level of gold after electron injection from dye N719. Adapted from ref. [80].	41
Figure 14 Image of the solution A3 after post-thermal treatment solution of as-synthesized QDs showing the two separated gradations: the transparent supernatant phase and the bottom white precipitate.	68
Figure 15 Photoluminescence measurements of different samples of ZnO QDs solutions (A1, A2 and A3) after annealing at 150°C (a) the full PL spectrum showing break line at the missing data points over the region of the second order of the laser. (b) ZnO UV region of the PL spectrum, (c) zoom in the UV-region of the smoothed PL spectrum of the solution A1 (0.1 M raw materials).	69
Figure 16 UV zone of the photoluminescence spectra of ZnO nanostructures in solution (a) effect of the time of the reaction carried on at 80°C, (b) Effect of the reaction temperature on the ZnO UV-emission lasting for 20 minutes, (c) Effect of 150°C annealing on the ZnO synthesis reaction done at 80°C for 20 minutes, (d) Sum-up of the reaction temperature conditions to obtain UV-exciton emission.	71
Figure 17 TEM images on for the supernatant part of the solutions synthesized at (a) 80°C, (b) 150°C.	73
Figure 18 TGA measurements of the powders synthesized at 80°C representing the percentage of weight loss with its corresponding derivative.	75
Figure 19 XRD measurements of the powdered ZnO NPs synthesized at 80°C and annealed at different temperatures: (a) XRD patterns, (b) the variation of the (101) plane peak intensity and position with increasing the annealing temperatures, (c) the evolution of the crystallite size as a function of annealing temperature, (d) illustration of the variation of the cell volume and number of atoms per unit cell as a function of crystallite size.	78
Figure 20 (a) XPS measurements of the synthesized ZnO NCs before (black curve) and after annealing at 250°C (red curve), (b) O <sub>1s</sub> spectrum, (c) Zn <sub>2p</sub> spectrum.	80
Figure 21 SEM images of the synthesized ZnO NCs: (a) before annealing (n/a), annealed at (b-g) 80, 100, 150, 250, 500 and 800°C, respectively. The scale bar in images (a-c) is 5 μm, (d-f) 500 nm, and (g) 2 μm.	81
Figure 22 (a) Bright field TEM image of the as-prepared ZnO NCs before annealing. ZnO sample annealed at 80°C (b) TEM image (c) Diffraction of the crystal, (d-f) TEM images of	

the annealed samples 150,250, and 800°C respectively. The scale bar in images (a-b) is 5 nm and in (d-f) is 100 nm.....	82
Figure 23 (a) UV-Vis absorption spectroscopy of the as-prepared non-annealed (n/a) ZnO NPs and after annealing at different temperatures, (b) zoom in the UV region of the ZnO nanocrystals annealed at 80°C, and (c) magnification of the UV-Vis absorption spectra of the ZnO nanocrystals annealed at 800°C.....	83
Figure 24 Photoemission colors under 365 nm UV lamp light of ZnO NCs annealed at different temperatures. ....	85
Figure 25 Photoluminescence of ZnO NPs dispersed in water: (a) the full PL spectrum of all samples before and after annealing and showing break line at the missing data points over the region of the second order of the laser, (b) a zoom in the ZnO UV region of the PL spectrum showing the maximum position of the UV emission wavelength, (c) a zoom in the ZnO UV region of the PL spectrum of the non-annealed (n/a) ZnO and the annealed ZnO at 80 and 100°C. ....	85
Figure 26 Optical absorption spectra showing (a) the evolution of MB absorption in the absence of a catalyst under different irradiation times until 120 min, the inset shows the different irradiation times, (b-h) the degradation of MB using ZnO NPs at different irradiation times until 140 min: (b) non-annealed (n/a) ZnO NPs, the legend in (a) shows different irradiation times of the MB/ZnO solution and belongs to the other curves, (c-h) annealed ZnO NCs at 80, 100, 150, 250, 500, 800°C, respectively. ....	89
Figure 27 (a) 1 <sup>st</sup> order equation of the kinetic reaction of different sizes of ZnO NPs annealed at different temperatures plotted by $\ln(C_0/C)$ versus irradiation time and (b) comparative photodegradation rates of MB dye with different sizes of ZnO NPs annealed at various temperatures.....	92
Figure 28 UV-PL modification factor of the hybrids after the addition of G1 in a ratio $R_{G1/ZnO}=0.1$ to ZnO nanoparticles of different sizes. The different sized gray spheres represent ZnO NPs of specific size and the gold spheres capped with the green shell represent the gold nanoparticles capped by the CTAB respectively. Only one sphere from each hybrid system is represented for simplification. ZnO NPs of different sizes were obtained by annealing ZnO nanocrystals of small size at different temperatures ranging from 80 to 800°C.....	109
Figure 29 ZnO NPs annealed at 250°C (a) SEM-FEG image and (b) TEM image and (c) extinction (black) and average photoluminescence (red) of three PL spectrum measured separately (laser power is slightly different).....	114
Figure 30 SEM images of the fabricated gold nanoparticles after centrifugation and dispersion in water (a) G1, (b) G2, (c) G3, (d) G4. The scale in all images is 200 nm. ....	115
Figure 31 Extinction spectra of the CTAB-capped gold nanoparticles produced using 0.2 M of CTAB as a capping agent (a) G1 of $[HAuCl_4]= 5 \times 10^{-5} M$ , (b) G2 of $[HAuCl_4]= 8 \times 10^{-5} M$ , (c) G3 of $[HAuCl_4]= 10^{-3} M$ , (d) G4 of $[HAuCl_4]= 10^{-2} M$ (smoothed curve). ....	116
Figure 32 Extinction spectra of ZnO NPs solution before and after the addition of GNPs (a) G1 ( $R_{G1/ZnO}=2$ ), (b) G2 ( $R_{G2/ZnO}=2$ ), (c) G3 ( $R_{G3/ZnO}=2$ ), (g) G4 ( $R_{G4/ZnO}=0.1$ ), the inset in (d) is the zoom in UV region of the extinction spectrum of coupling G4 to ZnO NPs in a ratio $R_{G4/ZnO}=2$ .....	118
Figure 33 UV-zone of the PL spectra (right), and the UV-PL modification factor (left) of ZnO NPs solutions before and after the addition of (a,b) G1, (c,d) G2, (e,f) G3, and (g,h) G4. ...	120
Figure 34 UV-PL modification factor of ZnO NPs solutions before and after the addition of increased sizes GNPs G1, G2, G3, and G4 for all GNPs/ZnO ratios. ....	122

Figure 35 SEM image of the CTAB-capped GNPs loaded over ZnO NPs (annealed at 250°C). The inset shows a zoom in a specific region to clarify the contact between ZnO NPs and capped gold NPs. ....	125
Figure 36 Absorption of ZnO ( $T_{ann}=250^{\circ}\text{C}$ )-MB mixture with UV irradiation for different irradiation time intervals lasting for 140 min using (a) diluted solution of ZnO catalyst, and (b) concentrated solution of the same ZnO catalyst, (c) the variation of $\ln C_0/C$ of both catalysts concentrations with irradiation time lasting for 140 min, (d) % degradation of MB by different concentrations of ZnO catalyst.....	127
Figure 37 Absorption of G1-loaded ZnO ( $T_{ann}=250^{\circ}\text{C}$ )-MB mixture with UV irradiation for different irradiation time intervals lasting for 140 min at different GNPs/ZnO ratios (a) $R_{G1/ZnO}=0.1$ , (b) $R_{G1/ZnO}=0.5$ , (c) $R_{G1/ZnO}=2$ , (d) % degradation of MB using the three ratios G1/ZnO mixed with MB as a function of irradiation time. ....	128
Figure 38 Absorption of G2-loaded ZnO ( $T_{ann}=250^{\circ}\text{C}$ )-MB mixture with UV irradiation for different irradiation time intervals lasting for 140 min at different GNPs/ZnO ratios (a) $R_{G2/ZnO}=0.1$ , (b) $R_{G2/ZnO}=0.5$ , (c) $R_{G2/ZnO}=1$ , (d) $R_{G2/ZnO}=2$ , (e) % degradation of MB using the four ratios G2/ZnO mixed with MB as a function of irradiation time. ....	130
Figure 39 Absorption of G3-loaded ZnO ( $T_{ann}=250^{\circ}\text{C}$ )-MB mixture with UV irradiation for different irradiation time intervals lasting for 140 min at different GNPs/ZnO ratios (a) $R_{G3/ZnO}=0.1$ , (b) $R_{G3/ZnO}=0.5$ , (c) $R_{G3/ZnO}=1$ , (d) $R_{G3/ZnO}=2$ , (e) % degradation of MB using the four ratios G3/ZnO mixed with MB as a function of irradiation time. ....	131
Figure 40 Absorption of G4-loaded ZnO ( $T_{ann}=250^{\circ}\text{C}$ )-MB mixture with UV irradiation for different irradiation time intervals lasting for 140 min at different GNPs/ZnO ratios (a) $R_{G4/ZnO}=0.5$ , (b) $R_{G4/ZnO}=1$ , (c) $R_{G4/ZnO}=2$ , (d) % degradation of MB using the three ratios G4/ZnO mixed with MB as a function of irradiation time. ....	132
Figure 41 % degradation of MB using GNPs/ZnO catalyst in different sizes at (a) $R_{GNPS/ZnO}=0.1$ , (b) $R_{GNPS/ZnO}=0.5$ , (c) $R_{GNPS/ZnO}=1$ , (d) $R_{GNPS/ZnO}=2$ . ....	133
Figure 42 Different sizes of GNPs (S1, S2, S3 and S4) coupled into ZnO surfaces in real time, obtained by the reduction of the CTAB-capped gold precursor after being loaded into ZnO NPs (a) extinction spectrum, (b) UV region of the PL spectrum and (c) UV-PL modification factor. The different dimensions of the green shell capped-golden spheres represents the CTAB-capped GNPs of different sizes.....	134
Figure 43 CTAB-capped Au1 (modified Au1) coupled into ZnO at $R=0.1$ ; (a) Extinction spectra, the inset represents the extinction spectra of bare ZnO as well as the bare gold nanoparticles used ( $Au1=CTAB$ ), (b) UV zone of the PL spectrum, (c) evolution of the UV-PL modification factor (F) with respect to ZnO after the addition of Au1 with and without CTAB capping. ....	136
Figure 44 SEM image of the fabricated pure GNPs (Au1).....	137
Figure 45 (a) Extinction spectrum of the synthesized pure gold nanoparticles Au1 of initial gold precursor concentration $[HAuCl_4]=5 \times 10^{-5}$ M, hybrids after loading the ZnO NPs with different densities of pure GNPs (Au1) to have consecutive ratios of $R=0.1, 0.5, 1$ and $2$ ( $R=0$ represents the bare ZnO NPs without any addition of GNPs) (b) Extinction spectra, (c) UV-zone of the photoluminescence spectra and (d) UV-PL modification factor.....	138
Figure 46 SEM images of the Au1 loaded over ZnO NPs annealed at 250°C ( $R=0.5$ ). The inset shows a zoom in over a specific zone of the Au1 loaded over ZnO. ....	140

Figure 47 Room temperature average photoluminescence spectrum of ZnO NPs embedded PMMA nanolayer over Si substrate taken at four different positions. The inset corresponds to the PL measurements of the silicon (Si) substrate as a reference. ....	151
Figure 48 Optical Dark-field (a,b) and AFM (c) image of ZnO NPs-loaded PMMA nanolayer on Si substrate. (a) PMMA layer without ZnO and (b,c) PMMA nanoholes embedded with ZnO NPs, (d) AFM profile of (c). ....	152
Figure 49 The variation of UV-PL intensity height ( $\Delta I$ ) as a function of increasing dilution factors Df1, Df2, Df3 corresponding to addition of 0.1, 1 and 2 ml of D.I. water to the clear dispersion solution representing Df0 as a reference. The black squared line represents the variation of $\Delta I$ of the diluted solutions that were normally stirred, ....	155
Figure 50 (a) Typical PL spectrum of the repeated samples of ZnO NC annealed at 250°C then dispersed in water, (b) zoom in the UV region of different repeated samples of ZnO NC solutions. ....	156
Figure 51 Full range (UV-Vis) extinction spectrum of CTAB-capped gold nanoparticles (a) G1 of $[HAuCl_4] = 5 \times 10^{-5}$ M, (b) G2 of $[HAuCl_4] = 8 \times 10^{-5}$ M, (c) G3 of $[HAuCl_4] = 10^{-3}$ M, (d) G4 of $[HAuCl_4] = 10^{-2}$ M. The inset in each spectrum illustrates the CTAB (green lines)-capped GNPs (golden spheres). ....	157
Figure 52 UV-PL modification factor of the raw material synthesis ZnO NPs annealed at 150°C upon coupling with different ratios $R_{GNPs/raw ZnO} = 0.1, 0.5, 1$ and 2 into CTAB-capped gold nanoparticles ; (a) G1, (b) G2, (c) G3 and (d) G4. ....	158
Figure 53 ZnO NPs before and after the addition of 0.2 M CTAB solution (a) extinction spectrum and (b) UV zone of the photoluminescence spectrum. ....	159
Figure 54 (a) Room temperature average PL spectra of ZnO dispersion embedded in PMMA holes with MIBK solvent. The average spectra for samples spin-coated over different speeds are taken over 5 different positions, except for the samples of 10000rpm speed that illustrates the average PL of 4 positions, (b) zoom in the PL spectra of the speeds higher than 250 rpm. ....	159
Figure 55 Room temperature PL spectrum of ZnO NPs embedded in PMMA dissolved in MIBK solvent, spin-coated over ITO substrate at a spin-coating speed 250 rpm. ....	160
Figure 56 Different stabilizers as PVA, PVP, PEG, $K_3$ citrate (2 mg) dissolved in 2 ml water (a) Room temperature PL spectra, (b) UV-Vis absorption spectra. ....	161

## List of schemes

Scheme 1 (a) Schematic energy level structure of (left) molecular dyes, (center) quantum dots and (right) bulk semiconductor. The dotted arrow indicates the electronic transition responsible for the luminescence [37]. (b) Illustration of the increasing energy gap by decreasing the size of the QDs. Adapted from ref. [38].	21
Scheme 2 A schematic diagram showing the PL enhancement (a) and quenching (b) processes. Adapted from ref. [197].	33
Scheme 3 A schematic diagram for the coupling between bandgap and surface plasmon resonance, and carriers transfer between the defect level and the Pt Fermi level. It results in enhanced bandgap emission and suppressed defect emission. Adapted from ref. [199].	34
Scheme 4 The CT pathways in semiconductor–metal heterostructures (a) semiconductor-to-molecule-to-metal, (b) metal-to-semiconductor-to molecule, (c) metal-to-molecule-to-semiconductor. Adapted from ref. [213].	36
Scheme 5 Schematic presentation of the electron transfer processes in Au-semiconductor heterostructures. For Au-semiconductor heterostructure where (a) only Au is excited, (b) only semiconductor is excited, and (c) there are simultaneous excitations of both Au and semiconductor. The electron transfer path 1 refers for semiconductor excitation followed by electron transfer to Au, path 2 follows just the reverse process, and path 3 shows the coupling of exciton of the semiconductor and plasmon of Au. Here, $E_{sp}$ refers to the Au surface plasmon state and EF refers to the Au Fermi level. Adapted from ref. [219].	38
Scheme 6 Proposed mechanism of the photocatalysis of Au/ZnO nanostructures upon excitation of the visible light. Adapted from ref. [65].	38
Scheme 7 Proposed mechanism of the photocatalysis of Au/ZnO nanostructures under UV light irradiation. Adapted from ref. [65].	39
Scheme 8 Schematic Presentation of the Photocatalytic Degradation of Evans Blue at the ZnO–Au Hybrids Surfaces. Adapted from ref. [163].	42
Scheme 9 Schematic diagram of the synthesis of ZnO NCs.	68
Scheme 10 Schematic representation of the photocatalytic activity of the ZnO NPs by degradation of methylene blue (MB) dye. (The photoluminescence of ZnO NPs is also indicated). The TEM image corresponds to the synthesized ZnO NPs annealed at 250°C. The inset in the TEM image is the SEM image of the same sample.	87
Scheme 11 Schematic representation of the ZnO nanocrystals with annealing temperatures showing the size and number effect on the photocatalytic activity. The gray spheres represents the ZnO NCs.	93
Scheme 12 Schematic representation of the synthesis of the CTAB-capped gold nanoparticles of different sizes using $5 \times 10^{-5}$ M, $8 \times 10^{-5}$ M, $10^{-3}$ M and $10^{-2}$ M of gold precursor concentration for G1, G2, G3 and G4 respectively.	107
Scheme 13 The mechanism of the UV-PL enhancement of ZnO NPs by GNPs under UV-irradiation.	124
Scheme 14 Schematic representation of the charge transfer and the photocatalytic activity of CTAB-capped gold nanoparticles of different sizes loaded into ZnO NPs (DL: defect luminescence).	126
Scheme 15 Simplified mechanisms of semiconductor (electronic bands; left) and molecular based excitation/emission processes (discrete energy levels; right). Adapted from ref. [1].	162

---

## List of tables

Table 1 Reported emission colors from ZnO and deep level defect states responsible for this emission. ....	28
Table 2 List of some synthesis methods for crystalline ZnO nanostructures .....	62
Table 3 Percentage of ZnO composition in the raw synthesis product and the lattice parameters (a, b and c) of ZnO samples before and after annealing at different temperatures. ....	77
Table 4 Absorption peak position and the optical band gap energy of the ZnO samples without and with annealing at different temperatures.....	84
Table 5 Photocatalytic activity of ZnO samples representing the percentage of degradation of MB with the photodegradation rate and the relative regression coefficient. ....	90

## List of abbreviations

0D: Zero dimensional	PC: Photocatalysis
1D: One dimensional	PL: Photoluminescence
2D: Two dimensional	PR: Plasmon resonance
3D: Three dimensional	QDs: Quantum dots
CB: Conduction band	SC: Semiconductor
DL: Defect luminescence	SEM: Scanning electron microscopy
DLB: Defect level band	SERS: Surface enhancement Raman Spectroscopy
DOS: Density of states	SP: Surface plasmons
$E_{Fm}$ : Fermi level of metal	$T_{ann}$ : Annealing temperature
$E_{Fs}$ : Fermi level of semiconductor	TEM: Transmission electron microscopy
$E_g$ : Band gap energy	TGA: Thermal gravimetric analysis
ESCA: Electron spectroscopy for chemical analysis	TVTC: Thermal vapor transport and condensation
FWHM: Full-width at half-maximum	UHV: Ultra high vacuum
GNPs: Gold nanoparticles	UV: Ultraviolet
HNPs: Hybrid nanoparticles	VB: Valence band
I: Intensity	Vis: Visible
KE: Kinetic energy	XPS: X-ray photoelectron spectroscopy
LED: Light emitting diode	XRD: X-ray diffraction
LSPR: Localized surface plasmon resonance	
M: Metal	
MB: Methylene blue	
MNPs: Metallic nanoparticles	
NBE: Near band edge	
NCs: Nanocrystals	
NCQD: Nanocrystal quantum dot	
NIR: Near infrared	
NPs: Nanoparticles	
NR: Nanorods	
NW: Nanowires	
OSC: Oxide semiconductor	

## List of symbols

$^{\circ}\text{C}$ : Degree Celsius	$r$ : Photodegradation rate
$a$ : Nanocrystal radius	$R$ : Ratio
$a_0$ : Bohr radius	$R_{\text{Bohr}}$ : Bohr radius
$a_{\text{EB}}$ : Electron binding energy	$S$ : Surface
$C$ : Concentration	$T$ : Temperature
$C_0$ : Equilibrium concentration	$t$ : Time
$\epsilon$ : Dielectric constant	$T_{\text{syn}}$ : Synthesis temperature
$e^-$ : Electron	$t_{\text{syn}}$ : Synthesis time
$e$ : Electron charge	$V$ : Cell volume
$E_K$ : Kinetic energy	$V_{\text{O}}$ : Oxygen vacancy
$eV$ : Electron volt	$V_{\text{O}}^{\bullet}$ : Singly ionized oxygen vacancy
$eV_{\text{bi}}$ : Forward bias	$V_{\text{O}}^{\bullet\bullet}$ : Double charged oxygen vacancy
$e_{\Phi}$ : Work function	$V_{\text{Zn}}$ : Zinc vacancy
$F$ : Modification factor	$W$ : Depletion layer
$h$ : Planck's constant	$Zn_i$ : Zinc interstitials
$\hbar$ : Planck's constant $(h)/2\pi$	$Zn_{\text{O}}$ : Zinc antisites
$h^+$ : Hole	$\theta$ : Theta
$\text{HO}^{\bullet}$ : Hydroxyl radicals	$\lambda$ : Wavelength
$K$ : Adsorption coefficient	$\nu$ : Frequency
$K$ : Numerical factor referred to the crystallite-shape constant	$\varphi$ : Surface work function
$K_{\text{app}}$ : Apparent pseudo-first order rate constant	
$M$ (unit): Molar	
$m_e^*$ : Electron effective mass	
$m_h^*$ : Hole effective mass	
min: Minutes	
$n$ : Refractive index	
$\text{O}_2^{\bullet-}$ : Superoxide radical anion	
$\text{O}_i$ : Oxygen interstitial	
$\text{O}_{\text{Zn}}$ : Oxygen antisites	

## List of chemicals

Ag: Silver	SiO <sub>2</sub> : Silicon dioxide
Au: Gold	SnO <sub>2</sub> : Tin dioxide
BiSe: Bismuth selenide	SrTiO <sub>3</sub> : Strontium titanate
CdS: Cadmium sulfide	TiO <sub>2</sub> : Titanium dioxide
CdSe: Cadmium selenide	WO <sub>3</sub> : Tungsten oxide
Co: Cobalt	Zn(NO <sub>3</sub> ) <sub>2</sub> ·6H <sub>2</sub> O: Zinc nitrate hexahydrate
CTAB: Cetyl-trimethyl-ammouium bromide	Zn(OH) <sub>2</sub> : Zinc hydroxide
Cu: Copper	ZnNO <sub>3</sub> : Zinc nitrate
Fe: Iron	ZnO: Zinc oxide
Fe <sub>2</sub> O <sub>3</sub> : Ferrous oxide	ZnS: Zinc sulfide
GaN: Gallium nitride	α-Fe <sub>2</sub> O <sub>3</sub> : Haematite
GaSe: Gallium selenide	
H <sub>2</sub> O: Water	
HAuCl <sub>4</sub> : Tetrachloroauric acid	
InGaN: Indium gallium nitride	
ITO: Indium tin oxide	
K <sub>3</sub> citrate: Tripotassium citrate	
LiOH: Lithium hydroxide	
MB: Methylene blue	
NaOH: Sodium hydroxide	
Ni: Nickel	
O: Oxygen	
PbS: Lead sulfide	
PEG: Polyethylene glycol	
PMMA: Polymethyl methacrylate	
Pt: Platinium	
PVA: Polyvinyl alcohol	
PVP: Polyvinyl pyridine	
S: Sulfur	
Si: Silicon	

## General Introduction

The research in this PhD thesis is focused on the investigation of the plasmon-exciton interaction in particular in ZnO-Au hybrid nanomaterials in order to control both the fluorescence and the photocatalytic features of ZnO nanostructures.

Chapter 1 gives an overview of the plasmon-exciton interactions between metallic nanoparticles (MNPs) and luminescent semiconductors, focusing on the Au/ZnO materials, their different fabrication methods as well as their important properties and applications. We show here how considerable efforts have been made to enhance the photoluminescence (PL) of the hybrid systems, as well as the photocatalytic activities in order to use them as multifunctional materials in many scientific fields.

In chapter 2, we introduced a facile fabrication way of surfactant-free ZnO quantum dots based on the synthesis method. This method is favorable among other methods as it is fast, economical, and achieved without the addition of any ligand or organic linkers. Through this chapter, we studied the influence of the reaction parameters that lead to the formation of highly luminescent and well-crystalline ZnO nanostructures. The post-thermal treatment (annealing) was found to be crucial in order to obtain crystalline and highly luminescent ZnO. We have also examined the effect of different annealing temperatures of the obtained ZnO nanostructures, emphasizing on the possibility of controlling the luminescent properties and the photocatalytic activities of the formed nanostructures through this process. A critical annealing temperature was optimum to obtain efficient ZnO nanoparticles.

Chapter 3 presents the optical properties of the hybrid nanomaterials attained by a simple way, *via* coupling the synthesized ZnO NPs with gold nanoparticles (GNPs) of different plasmonic properties. The ZnO luminescence was controlled through tuning the GNPs properties (size, number), as well as the ZnO-GNPs inter-distance, which is attained by the capping molecular link. ZnO emission resulted in two important phenomena; enhancement as well as quenching. Both were obtained upon coupling ZnO NPs with GNPs under various experimental conditions through the charge and/or energy transfer between both constituents. Despite the progress in the hybrid interactions, it is still difficult to understand the exact mechanism of the exciton emission evolution induced by the surface plasmons (SP) of the GNPs because of the limited fundamental understanding of the exciton-plasmon interaction. In this chapter, we aimed to show how does a chemical route of control for the synthesis parameters of ZnO, GNPs, the hybrid NPs, and for the separating distance between the ZnO and GNPs can

be an efficient and universal way to get strong or weak coupling, or un-coupling between the exciton and the plasmons.

Finally, chapter 4 provides the major conclusions derived from the present work and a reflection on some future insights. Thus, we presented various suggestions as further experimental studies for exploiting the hybrid systems obtained in applications such as SERS and catalysis.

# 1. Chapter 1 State of Art

## 1.1 Introduction

The association of functional units, in order to design hybrid nanoparticles (HNPs), leads to advanced materials with multiple performances, retaining the beneficial features of the responsible compounds, or displaying special traits not seen in either components, thanks to their organization and their molecular engineering [1–5].

Different hybrid combinations including metal/metal, metal/semiconductor, metal/magnet, and magnet/semiconductor have been investigated [6–8]. Novel abilities could be realized at the nanoscale heterojunction resulting from the large specific surface area, and/or the quantum confinement effect. Figure 1 shows TEM images and schematic representations of a series of different hybrid nanostructures.

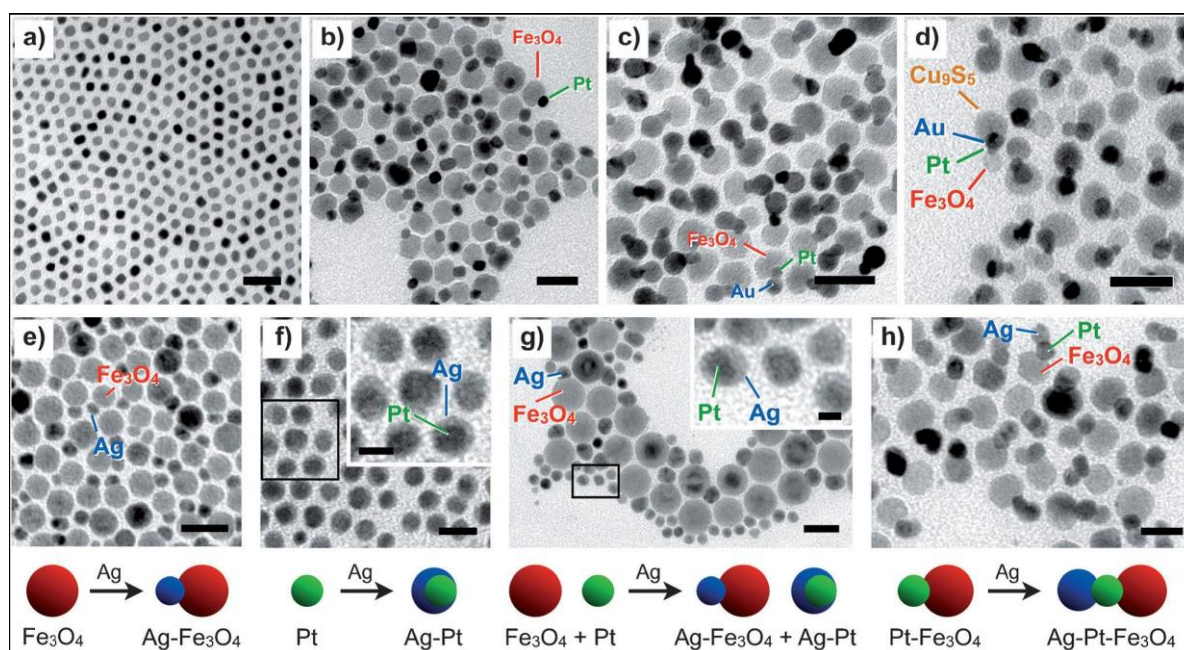


Figure 1 (a-d) TEM images showing the stepwise direct heterogeneous deposition of linear nanoparticle heterotetramers: (a) Pt nanoparticles, (b) Pt-Fe<sub>3</sub>O<sub>4</sub> heterodimers, (c) Au-Pt-Fe<sub>3</sub>O<sub>4</sub> heterotrimers, and (d) Cu<sub>9</sub>S<sub>5</sub>-Au-Pt-Fe<sub>3</sub>O<sub>4</sub> heterotetramers. (e-h) TEM images and schematic representations showing a series of metal/semiconductor heterodimers (same synthetic conditions for all steps) aimed at understanding the site-selective deposition of Ag onto Pt-Fe<sub>3</sub>O<sub>4</sub> heterodimers: (e) Ag grown off Fe<sub>3</sub>O<sub>4</sub> nanoparticles, (f) Ag grown off Pt nanoparticles, (g) Ag grown indiscriminately off both Fe<sub>3</sub>O<sub>4</sub> and Pt nanoparticles when both are present as a physical mixture, and (h) Ag grown exclusively off the Pt domain when Pt and Fe<sub>3</sub>O<sub>4</sub> are directly attached as heterodimers. Adapted from ref. [9].

Hybrid heterojunctions are simple, flexible, allow the precise control over the particle's size and shape, and facilitate the fabrication of wide spatial architectures (0, 1, 2, or 3 dimension

structures). Most of the resulting structures show improved optical, chemical, physical, and mechanical properties of the materials. For example, in Pt/Ni alloy nanoparticles, Park *et al.* showed that the catalytic behavior in the hybrid system is more efficient than that when Pt nanoparticles were alone [10]. Another example is the Co core/Ag shell hybrid system demonstrated by Wang *et al.* The localized surface plasmon resonance (LSPR) of the silver (Ag) shell enhances the magneto-optical Faraday rotation of the Co/Ag system as a result of enhancing the electromagnetic field [11]. This is shown in Figure 2.

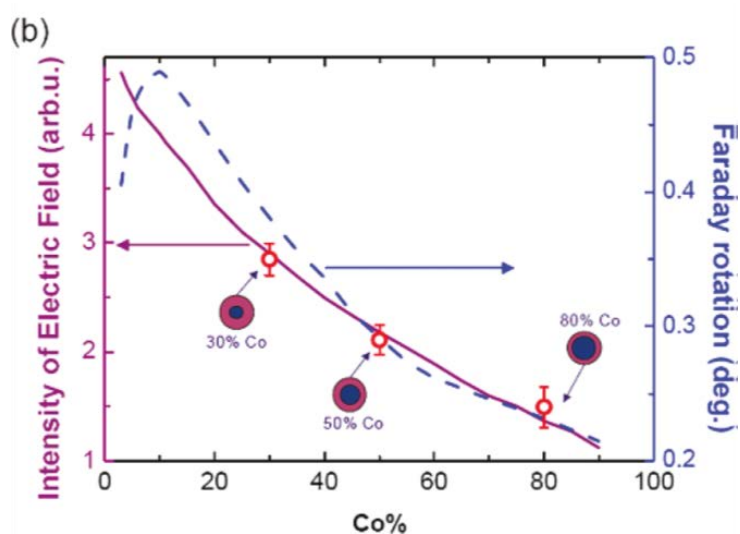


Figure 2 Calculated intensity of the electric field within the Co core in Co-Ag core-shell nanoparticles at resonance (continuous violet line) and maximum Faraday rotation of Co-Ag nanoparticles embedded in oil ( $n = 1.5018$ ) (dashed blue line) as a function of the Co concentration. Calculations show an excellent agreement with the experimental measurements (red dots). The error bars represent the standard error calculated by taking multiple measurements. Adapted from ref. [11].

In another reports concerning hybrid nanostructures, Homaei *et al.* showed in their studies that the immobilization of actinide by ionic exchange and hydrophobic interactions on gold nanorods could significantly enhance its storage, stability at extreme pH, in addition to thermal stability and resistance [12].

Adding up metals into semiconducting materials to form metal/semiconductor (M/SC) heterojunction has been considered as a special category of the hybrid systems due to the collective interactions computing the semi-conduction trait with the localized surface plasmon resonance, where these two characters turn out to be crucial in constructing functional hybrids used in different chemical, physical, and biological domains [13]. This type of arrangement will lead to sum of applications that cannot be addressed by each element alone. In accordance to theoretical studies, MNPs are polarized by the exciton through near-field coupling, where

the MNPs recouple to the exciton altering their own optical properties as well as that of the whole system. This coupling process is largely improved by the plasmonic fields at the junction interface [14–16]. Figure 3 shows TEM images for Au-CdSe nanosystems.

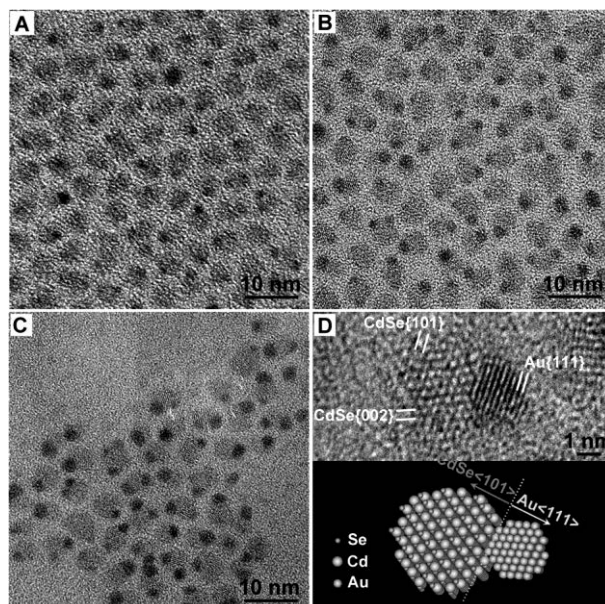


Figure 3 (A-C) TEM images of CdSe-Au hybrid nanoparticles obtained by changing QAu from 2, 4 to 6  $\mu\text{mol}$ , respectively. The nanoparticles are seen as dimeric units, all with a similar size of  $\sim 3.4$  nm for the CdSe component. (D) High-resolution TEM image and a schematic drawing of the CdSe-Au hybrid nanoparticles. Adapted from ref. [9].

## 1.2 Plasmonic-semiconductor hybrid nanomaterials

Because of their photostability and spectral tunability, hybrid nanomaterials consisting of semiconducting nanostructures with plasmon-based metallic nanoparticles have attracted much attention in recent years for their usage in light emitting displays, photovoltaics and photocatalysis [8,17,18].

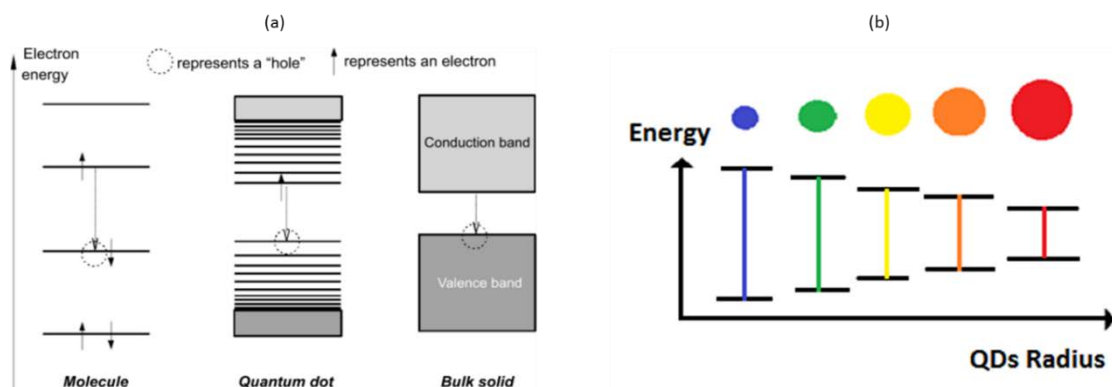
In general, semiconductors (SCs) are materials of electric conductivity ranging between that of a conductor and an insulator, which can be roughly classified into either elemental or compound systems. Alessandro Volta originally suggested the title ‘semiconductor’ in 1782 [19,20], whereas Michael Faraday gave the first experimental observation in 1833 [21].

SCs are capable of changing their properties to vary the construction and potentials of current electronic and optoelectronic devices containing solar cells, photodetectors, and light-emitting diodes (LED) [22,23]. Due to the presence of many atoms, the electronic energy levels in bulk semiconductors split into a lower electron-filled band called the valence band (VB),

and a higher electron-empty band called the conduction band (CB). These bands are separated by the bandgap that refers to the energy difference between the VB upper boundary and the bottom of the CB in the SC. When the electrons are stimulated by an external perturbation (e.g. absorption of light energy or heat), and if this energy is bigger than or equal the fundamental band gap energy of the semiconducting material, an electron ( $e^-$ ) of effective mass ( $m_e^*$ ) rises from the valence band to the conduction band leaving behind a positive hole ( $h^+$ ) of effective mass ( $m_h^*$ ).

Due to their charge, the  $e^-h^+$  pairs are referred to charge carriers named the excitons of the SC, where the average distance between an electron and a hole is the Bohr Radius ( $R_{\text{Bohr}}$ ). When the size of the semiconductor is smaller than the Bohr radius producing a crystalline matrix, the semiconductor is then called a nanocrystal quantum dot (NCQD) where its energy levels are quantized according to the Pauli's exclusion principle [24,25]. Due to its typical dimension at the nanorange (usually between 1-10 nm), a quantum dot nanocrystal becomes a set of atoms in a quasi-zero dimension, that have discrete energy levels with different quantum numbers at the band edges of the valence and conduction bands. In this case, the excitons are confined in all dimensions to a much smaller space due to few atoms present, thus the energy of the band gap increases with the decrease in the QDs size to exceed the coulombic interaction of the charge carriers, highlighting the "quantum confinement effect". The Bohr radius allows the examination of the influence of quantum confinement on the properties of the semiconductor [26]. At the nanoscale, the QDs properties could be tuned by changing its size, shape, composition, and surrounding environment [27,28]. The dependence on size is related to the high surface-to-volume ratio, and early was discovered, experimentally, by a group of scientists in semiconductor-doped glasses and in colloidal solutions [29–31]. Crystalline quantum dots are sometimes referred to as artificial atoms because, in fact, an atom complies with this criterion, but it is smaller in diameter. Scheme 1 illustrates the difference between bulk, QDs, and atomic energy gap theory, and the band gap evolution in relation to the size of semiconductor QDs. Nanocrystalline QDs are photostable, and they have wide absorption edges, in addition to narrow and tunable emission [32]. The emission color of the nanocrystals highly depends on the particle's size [33,34].

Several types of semiconductors, such as sulfides (ZnS, PbS, and CdS), selenides (GaSe, CdSe, and BiSe), and oxides (TiO<sub>2</sub>, WO<sub>3</sub>, ZnO, SnO<sub>2</sub>, and Fe<sub>2</sub>O<sub>3</sub>) are promising nanostructures for their diverse environmental applications [35,36].



Scheme 1 (a) Schematic energy level structure of (left) molecular dyes, (center) quantum dots and (right) bulk semiconductor. The dotted arrow indicates the electronic transition responsible for the luminescence [37]. (b) Illustration of the increasing energy gap by decreasing the size of the QDs. Adapted from ref. [38].

Mostly, SCs are considered as poor conducting materials due to the high excitonic recombination rate directly after excitation. They emit light instead of heat (favorable for light emitting diodes and fluorescence applications), resulting in high-energy loss and low photocatalytic activity [39–41]. Accordingly, it is a challenge to limit the recombination mechanisms in order to force the generated electrons and holes cooperate in other processes such as oxidation and reduction reactions. The redox reactions are valuable for photocatalytic behavior, which is a trendy subject in the photovoltaic and solar cells domains [42–45]. Moreover, semiconductors have a narrow spectral response range, and mostly their charge carriers could only be excited by UV light [46,47]. Therefore, most of the semiconductor nanostructures have a weak interaction with visible light, which is a considerable energy section in the solar spectrum.

To overcome these problems, several methods are adapted to increase the visible light response of wide bandgap semiconductors. Forming heterostructures is one of the solutions for this purpose [48,49]. Add to that, tuning the morphology [50,51], doping with metal or non-metal elements [52,53], or integrating semiconductors with plasmonic metals such as Cu, Pd, Pt, Ag, and Au could be beneficial [54–61]. The latter has attracted much attention within the scientific community due to exhibiting exclusive properties. Its preparation act as a director for the desired application (electronic, optical, or catalytic...), emerging in the area of research over the scientific world.

The doping process leads to an n-type or p-type semiconductors as a result to the electron oversupply (dopant is charge donor) or deficiency (dopant is charge acceptor) respectively, depending on the nature of the atomic properties, where these properties could be controlled

by adjusting the amount and positions of dopants in the semiconductor [62,63]. These impurities are considered as activators that confound the band structures by devising quantum states within the bandgaps, and will be auto-ionized due to the SC quantum confinement [32].

The metal/semiconductor (M/SC) link collects the semiconducting property along with the surface plasmon resonance (SPR), creating new behaviors of the combined system where the special band gap structures of semiconductors will be affected after the combination with noble metals. The metallic nanoparticles have enormous power to assist the SC in forming functional hybrids. Upon M/SC junction, the enhancement of the existing functionalities or exploring new ones is deeply highlighted. The SC properties will be influenced when adjoining MNPs. Similarly, the plasmonic properties of the metal will be also modified by the semiconductor component [64–68]. This progress will reinforce the catalytic reactions useful in the photodegradation of pollutants [69–71], production of hydrogen without the combustion process that is usually used for this aim [72,73], and CO<sub>2</sub> reduction to convert solar energy into chemical one indeed in energy storage [74,75]. The variation of properties after coupling relies on the ratio between components, their nature, and their energy levels and interactions.

To go further, after coupling between the semiconductor excitons and the plasmons of MNPs that will produce more charges, the generated charges will provoke the photocatalytic behavior by triggering the facial charges to participate in the redox reactions at the surface of the system [53,76]. At the M/SC interface, the separation of the electron-hole pairs will increase upon electrons irregularity after the formation of new electronic states in such systems. This will entitle us to talk about electron transfer between the semiconductor and the metal causing the production of current in the materials as well as enhancing the system's conductivity [77].

In the M/SC coupling nanosystems, it is worthy to take into account the three following terms: The work function of the components, their electronic affinity, and the Fermi levels in their electronic states. The work function is the minimum energy needed to remove an electron from a solid to a point in the vacuum outside the solid surface. The work function of a metal ( $e\Phi_m$ ) is the energy difference between vacuum energy and the Fermi level of the metal ( $E_{Fm}$ ) which is located in the band. However, for a semiconductor, the work function ( $e\Phi_s$ ) is the energy required to remove an electron from the semiconductor to the free vacuum level; it is the energy difference between the SC Fermi level ( $E_{Fs}$ ) and the vacuum level. The Fermi level in a solid indicates the chemical potential of the lowest energy of free electron or the highest

energy of free hole. In addition, the energy difference between the conduction band and vacuum level is the electron affinity.

When metals are coupled to semiconductors, two distinct types of connections could be observed; the Schottky and the Ohmic contacts. According to the work function of the metal and the semiconductor, and taking into account the type of the SC (n-type or p-type), the M/SC coupling is observed in different manners, where these junctions will reach an equilibrium after electron-hole exchanges [78]. This is shown in Figure 4.

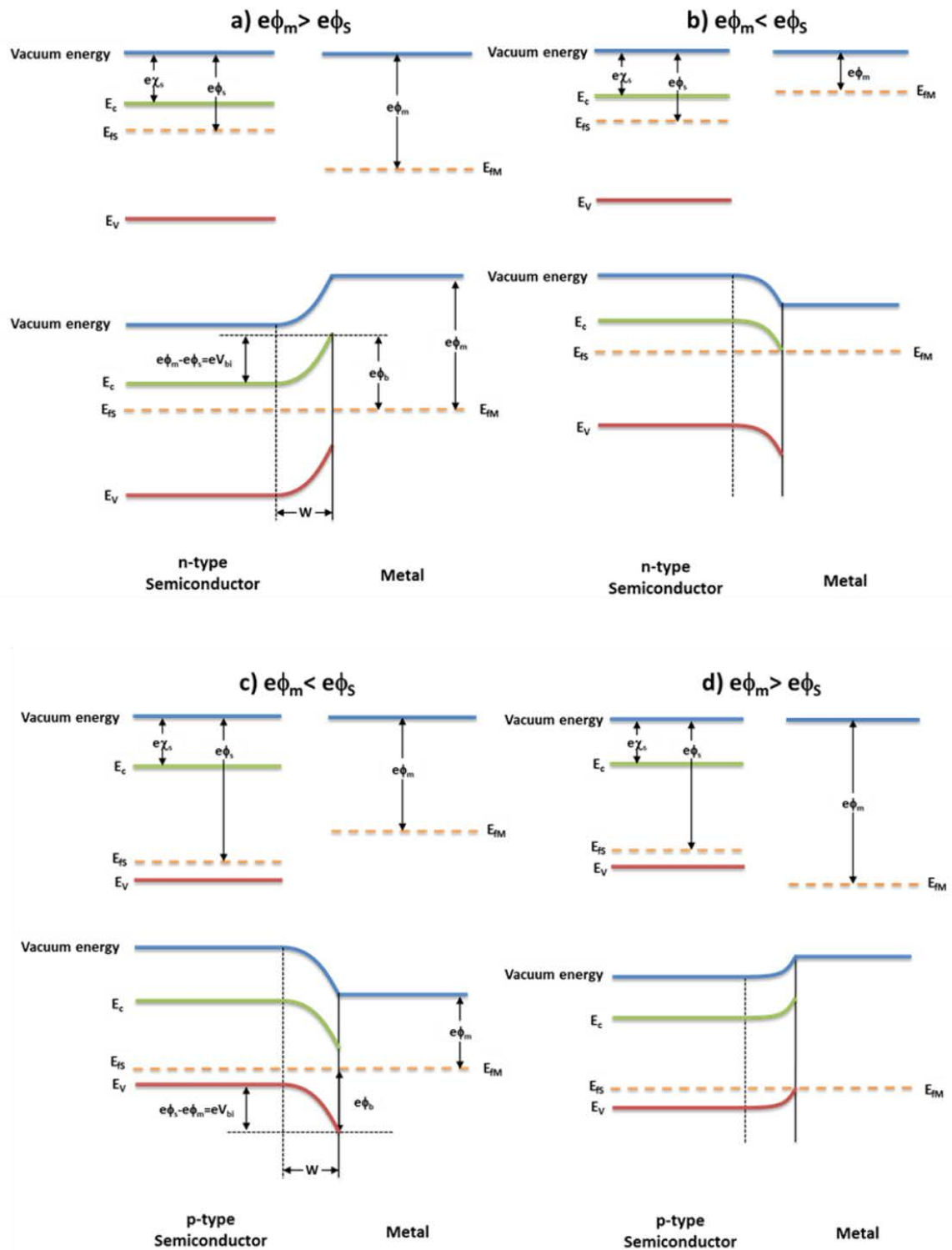


Figure 4 Band structures of metal–semiconductor junctions for (a,b) an n-type semiconductor and (c,d) a p-type semiconductor in thermodynamic equilibrium. Adapted from ref. [79].

1. In the n-type semiconductor with  $e\Phi_m > e\Phi_s$ , the fermi level of the metal is below that of the semiconductor, and thus, the metal's work function is larger than the SC electron affinity. Electrons will transfer from the semiconductor to the metal, leaving positively charged fixed dopants in the SC. This transfer provokes the redistribution of electron

densities to minimize the interface energy, resulting in equilibrium and alignment in the Fermi levels in the SC, in addition to dipole region at the interface. A depletion layer (W) in the semiconductor will be created stimulating a potential between the two constituents. In this type of junction, a Schottky barrier forms according to the classical Schottky model at the junction interface [80]. This barrier height is described as the difference between the work function of the metal and the electron affinity of the SC. In another words, it is the gap between the metal's Fermi level and the SC's conduction band at which the majority carriers reside [81]. The metal's fermi level does not change due to the massive free electron densities. The electrons transferring from the semiconductor to the metal face a barrier of  $eV_{bi}$  (Forward bias). On the other hand, due to existence of this barrier at the junction, the reverse translation (Reverse bias) needs more energy to move from the metallic to the semiconductor compound [82].

2. In another case, in n-type semiconductor, if  $e\Phi_m < e\Phi_s$ , the junction is Ohmic. Thus, the M/SC interface is barrier free. Therefore, the electrons can easily transfer from the metal to semiconductor where the junction acts as a resistor.
3. In the p-type semiconductor with  $e\Phi_m > e\Phi_s$ , the barrier in this junction does not exist. The metal acts as a charge that can produce more free space for charge transfer [82,83].
4. In p-type semiconductor, if  $e\Phi_m < e\Phi_s$ , the bands twist to form a barrier for the hole transport. The barrier height is given by the difference between the metal's fermi level and the SC valence band edge. Thus, electrons can transfer from the metal to the semiconductor in the junction to make a negative charge depletion layer.

The electronic mechanisms at the metal/SC interface is important to fully understand the coupling mechanism, which allow the control of the properties and functionalities of the applications relying on these hybrid material's junctions.

## **1.3 ZnO-Au: The studied plasmonic-semiconductor nanomaterial**

### **1.3.1 ZnO nanostructures**

Among various semiconductors, zinc oxide materials are special wurtzite n-type structures that have attracted much attention by research, thanks to their various electrical, optical, and physical traits. ZnO have a direct and a wide band gap besides the high exciton binding energy and rich defect chemistry structures [84–89]. Moreover, they adapt a strong oxidizing power and superior UV emission characteristics, in addition to their high stability and room temperature luminescence [90,91]. Experimentally available over different size ranges, ZnO is

one of the few metal oxides that exhibit quantum confinement effects [92]. These features show their promising and attractive materials that ensure efficient excitonic emission at room temperature, making it suitable for short wavelength optoelectronic applications as ultraviolet photodetectors, photovoltaic devices, sensors, solar cells, laser diodes and photocatalysis processes [93,94]. The contribution of ZnO in biological operations is due to the zinc element, since it is an essential feature for human beings, and its corresponding oxide (ZnO) is a biocompatible material of low toxicity, bio-safe, and can serve for biomedicine applications without further coatings [95,96].

Therefore, ZnO is considered as one of the most important promising nanomaterial classified as the 'future material'. The interest is concerned in the nanometric-sized particles that exhibit special traits as excellent physical and chemical properties distinct and superior to those of the bulk ZnO solids [97–101]. This difference is associated with quantum confinement effects and increased surface atoms of the solid materials at the level of the nano-scale [102]. As a result, a higher surface-to-volume ratio is attained with reducing the dimensions of the material, and the contributions of the nanoparticle's surface to physico-chemical properties become more important. Also, the defect contents and their optical properties are directly affected by the reduction and variation of the size into the nanoscale [103].

In particular, ZnO quantum dots (QDs) are extraordinary nanostructures considered as a new type of photocatalysts with a variation of utilization in the anti-bacteria, water purification fields and optoelectronic applications [97,104,105]. The control over the materials shape, size and crystal structure is crucial to manage the applications of ZnO quantum dots, and the synthesis of new and original nanostructures is intensively requested in the research fields [106].

Moreover, ZnO nanoparticles are characterized by their direct and wide bandgap. This property is seriously considered for using ZnO as an alternative to other semiconductors that were widely used before in optoelectronic domains as TiO<sub>2</sub> and GaN. ZnO has a band gap of value of 3.37 eV at room temperature and 3.44 eV at low temperatures [85]. This enables such nanostructures to be applicable in the field of optoelectronics over the UV region including photodetectors, lasers and light-emitting diodes (LED) [91,107–109].

The free-exciton binding energy in ZnO is 60 meV [110,111]. Its large value reveals efficient excitonic emission in ZnO at room temperatures and higher, making ZnO materials talented for optical devices that depend on excitonic effects.

Generally, ZnO photoemission bands are marked by two peaks: The first is a confined peak corresponding to the near band edge (NBE) emission in the ultraviolet region of the emission spectrum. This peak characterizes the exciton radiative recombination of the electrons and holes, and suggesting the formation of well-crystallized ZnO QDs [112]. The second peak is a large defect level band (DLB) in the visible zone [113–115]. Photoluminescence behaviors are highly dependent on the synthesis methods, crystallite size and structure, and the defect contents and surfaces [116–119]. Fonoberov *et al.* announced that the nanostructure's surface highly affects the UV and visible emission of ZnO QDs although the exact roles of the surface are still not clear [120]. Due to the strong luminescence in the UV and visible regions of the spectrum, ZnO is considered as an appropriate material for phosphor applications.

The UV emission of ZnO nanomaterials, normally at ~380 nm, represents a relaxed state of the excitons near the band edge, *i.e.* radiative recombination of electrons from the conduction band with the holes in the valence band. Thus it could be attributed to the near band edge emission or direct band-to-band transitions [112]. The nature of the UV-PL from ZnO QDs itself is still a matter of controversy because some reports have proved that the UV emission has a contribution with the surface impurities and defects [121], rather than the recombination of confined excitons [122]. However, its origin could distinguish between quantum confinement and surface-bound exciton states by measuring the radiative lifetime of the exciton [120,123–125]. In ZnO QDs, UV emissions are size dependent due to the quantum confinement by which their emission could be tuned as a function of the variation of size.

The origin and mechanism of the visible luminescence in ZnO QDs are not completely understood. They are associated to the charge transitions from the defect energy levels, and generally attributed to the oxygen vacancies [112,126,127], oxygen interstitials [128], zinc vacancies [127], zinc interstitials [129,130], in addition to oxygen and zinc antisites ( $O_{Zn}$  and  $Zn_O$ ) [127,131–135]. Zinc interstitials  $Zn_i$  and oxygen vacancies ( $V_O$ ) are the most cited prepositions for the visible emission in the literature, where the latest results from the recombination of electrons trapped in the singly ionized oxygen vacancy  $V_O^\bullet$  with the photoexcited holes [136]. Van Dijken *et al.* [126] assumed that the photogenerated holes are trapped at the surface, and then get back into the particle, to recombine with the trapped

electrons at  $V_O^\bullet$  center, resulting in the formation of double charged oxygen vacancy ( $V_O^{\bullet\bullet}$ ). When the holes trapped at  $V_O^{\bullet\bullet}$  center recombine with electrons in conduction band, the emission would be in the visible region. Another possibility for the visible emission observed is the surface (S) bonded to hydroxides (OH-S) as reported by Norberg *et al.* [137], in addition to donor-acceptor complex recorded by Reynolds *et al.* [138], and Studenikin *et al.* [139].

The different predictions of the origin of defect visible emission make ZnO luminescence as an argumentative subject that is considered as a matter of debate. Also, the emission mechanisms of the QDs in association to their photocatalytic activities are not yet clear. Table 1 shows some of the reported emission colors for ZnO nanostructures and their corresponding deep level transition.

Table 1 Reported emission colors from ZnO and deep level defect states responsible for this emission.

Luminescence color	Proposed $e^-$ transition	Reference
Violet	$Zn_i$ to VB	[129,130,138,140]
Blue	$Zn_i$ to $V_{Zn}$ CB to $V_{Zn}$	[129,130]
Green	CB to $V_{Zn}/V_O$ CB to $V_{Zn}$ & $V_O$	[112,127,141,142]
Yellow	CB to $O_i$ CB to $V_O/L_i$	[112,127,141–143]
Orange	$Zn_i$ to $O_i$ CB to $O_i$	[93,129,130,142]
Red	$V_{Zn}$ and $Zn_i$ induced lattice disorder along the c-axis	[127,129,130,144]

### 1.3.2 Gold nanoparticles

Metallic nanoparticles such as gold (Au), silver (Ag), copper (Cu), palladium (Pd), or platinum (Pt) are light interacting materials due to their surface plasmons [145]. They are highly developed in the current time due to their numerous applications in surface enhanced Raman scattering (SERS) [146], chemical and biological sensing [147], nanoscale lasing [148], plasmon enhanced fluorescence [149], amplification of non-linear optical signals [150], and photocatalysis [58].

GNPs are exclusive among all because they are easy to synthesize, highly stable, resistant to surface oxidation, and do not suffer from corrosion in photocatalysis processes. Thus, they are catalytically active. These traits, in addition to many other special characteristics, allow them to be used in several advantageous applications especially in the biomedical fields such as cancer therapy [151], DNA melting and assays [152], bio labeling [153], catalysis [154], drug delivery and other applications.

## **1.4 New/Enhanced features brought by plasmonic-semiconductor heterojunction**

The combination of two different materials into a single system enhances the characters of each component in addition to creating new traits. The difference in properties depends on the chemistry of the compounds in addition to the type of the interaction between them. Besides, inter-component structural or morphological characteristics of the constituents in the hybrid systems are also important in determining their features and performances. The SC characteristics depends on its energy band structures that will be affected after the combination with metals except at the M/SC interface where the band structures are bent together. Thus, the band gap energy of the SC could remain the same [22]. Contrarily, some main properties as emission and photocatalysis of the SC will be affected by SPR coupling. On the other hand, the hybridization of metals with a luminescent material will highly affect its plasmonic traits such as absorbance, scattering and catalysis. The M/SC combination leads to an important modification in their electronic, opto-electronic and magnetic properties [155–159]. Besides, inter-component structural or morphological features of the hybrid nanomaterials are also important in determining their properties and functionalities.

## **1.5 Tunable optical properties (absorption and fluorescence)**

### **1.5.1 Heterojunction modified absorption of both materials**

The creation of new electronic states in the M/SC interface and the electrodynamic effect will lead to the modulation in the absorption properties of both compounds. This property is highly affected by the distance between both constituents as described by He *et al.* in Figure 5 [160].

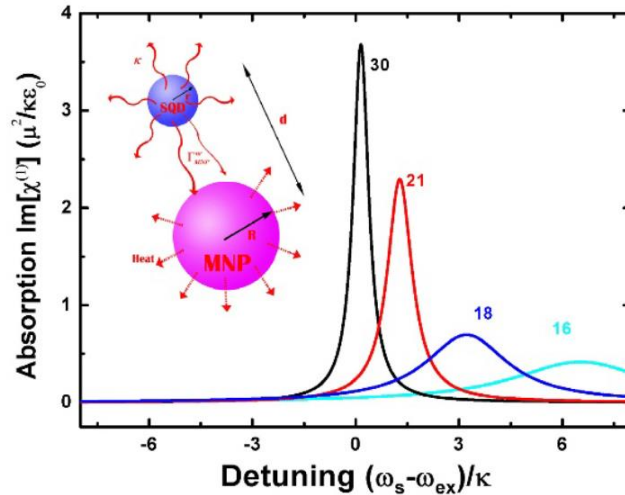


Figure 5 The signal light absorption spectrum of SQDs. The signal light absorption spectrum of SQDs for different distance  $d$ . The inset shows a complex system composed of a SQDs to a MNPs. A SQDs with radius  $r$  is placed in the vicinity of a MNPs with radius  $R$ . The center-to-center distance is  $d$ . Adapted from ref. [160].

As a result of the doping plasmonic metals in the semiconductor forming the M/SC junction, broadening and shifting in the plasmonic peak of the metal [161], as well as the excitonic absorption peak of the SC were previously observed [42]. (Figure 6)

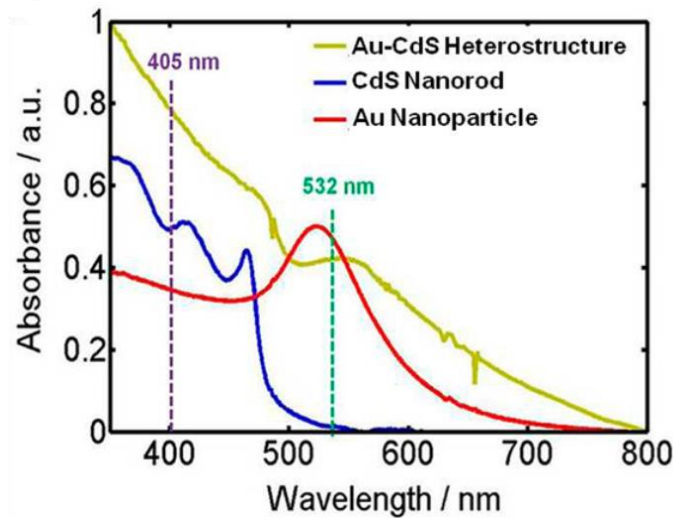


Figure 6 UV-vis absorption spectra of pure CdS nanorods (blue curve), Au nanoparticles (red curve), and high Au-CdS heterostructures (10.8 wt %, yellow curve). The green- and purple-dotted lines indicate the excitation source of a 532 nm laser and a 405 nm laser, respectively. Adapted from ref. [162].

In the ZnO QDs/Au system, Rahman *et al.* observed red shift in the absorbance peak of ZnO QDs in addition to the appearance of a weak peak in the visible region (Figure 7) [163]. The latter is attributed to the LSPR of the spherical GNPs [164]. The presence of this band affirms the presence of GNPs in the ZnO/Au hybrid system by which at smaller GNPs sizes this band

becomes blue shifted. The red shift of the ZnO QDs with conjoining GNPs indicates the interaction between ZnO and GNPs at the interface of the created heterostructures [165].

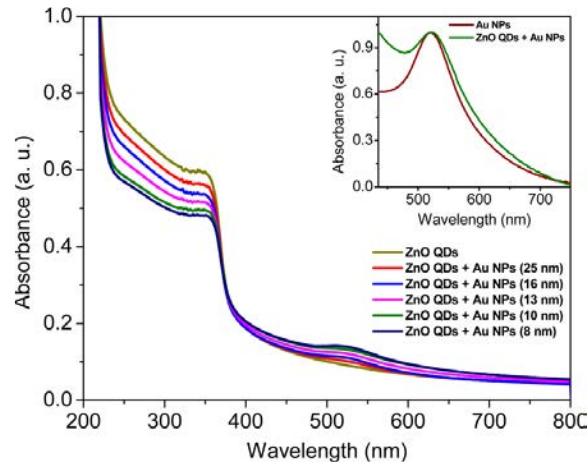


Figure 7 Absorption spectra of ZnO QDs (16.7  $\mu\text{M}$ ) in the absence and presence of Au NP (0.67  $\mu\text{M}$ ) of five different sizes. The inset shows the change in the surface plasmon band of Au NP upon interaction with the ZnO QDs. Adapted from ref. [163].

As shown in the above figure, the SPR peak of the GNPs was broadened and red shifted towards higher wavelengths as reported before in similar heterostructures [166,167]. Because metallic gold nanoparticles are considered as highly sensitive materials to the surrounding medium and the size of the NPs [168,169], the SPR peak will be influenced with its size, and after adding the ZnO QDs over. Since the refractive index of ZnO NPs ( $n_{\text{ZnO}}=2$ ) in the colloidal gold solution is higher than that of water ( $n_{\text{water}}=1.34$ ), the red shift in the SPR band is noticed.

### 1.5.2 Heterojunction modified SC's fluorescence

The optical properties of the SC will be highly affected in the presence of nearby metallic nanoparticles in one system. The M/SC interface has an inevitable role on the optical response of the SC nanoparticles, by which PL enhancement or quenching occurs at the metal's surface [170–174]. Mainly, there are two concepts stating the influence of the luminescence of the semiconductor when coupled to metals; the luminescence enhancement and quenching that has been generated since 1980's [175–177]. Viste *et al.* had studied the effect of local surface plasmon resonance of GNPs on the emission wavelengths of quantum dots [178]. The SC emission properties depend on the characteristics of the adjoining MNPs [22]. However, this influence is confusing and still under debate.

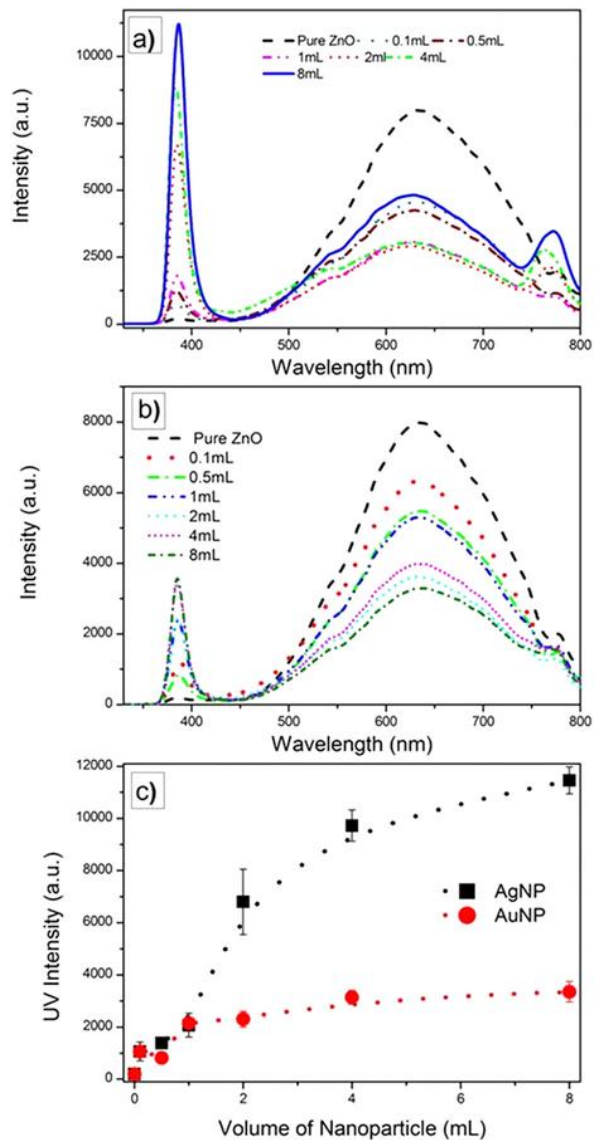
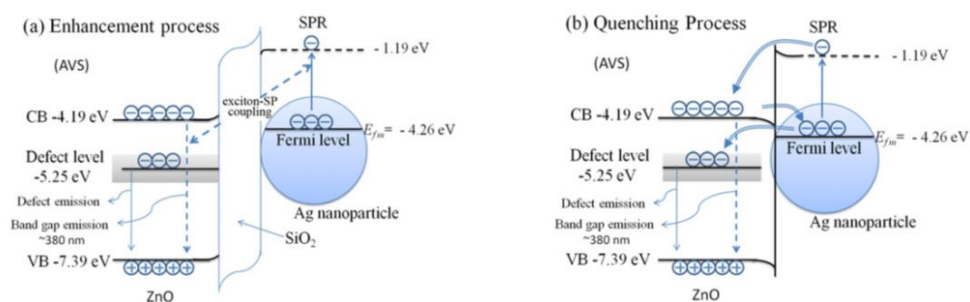


Figure 8 Photoluminescence spectra for the (a) ZnO/Ag and (b) ZnO/Au nanoparticles under excitation at 325 nm. (c) The ZnO UV-band intensity increases with increasing the metal nanoparticle concentration. Error bars represent the standard deviation for three separate measurements. Adapted from ref. [179].

The semiconductor's PL was enhanced in some studies due to its coupling to metallic nanoparticles [171,180,181] (Figure 8). In contrary cases, PL quenching was observed after metal doping of the semiconductor [164,182–185]. The enhancement and quenching in the PL after doping metals into semiconductors depends on the configuration of the interaction, and highly count on the competition between the modification of the radiative and non-radiative decay rates, and the enhancement of the local excitation fields [183,186]. Although, these two mechanisms are controversial issues that are still not well understood due to the complicated coupling process, which is still under discussion.

In general, the enhancement and quenching processes depend on the spectral compatibility between the emission and the SP energy in the SC and metal respectively [187,188]. The matching between energies lead to the effective resonant coupling which induces the PL enhancement [180,189]. These processes also count on the separation distance between the constituents [172,181,190,191], by which the enhancement process requires optimal distance between the M and the SC. At big distances between the MNPs and the SC, the surface plasmons are considered as fading waves that gradually collapse with distance, and thus the emission enhancement decreases proportionally with distance. Similarly, at shorter distances, the quenching by metal is superior to the semiconductor's emission. For that, a specific gap between the metal and the SC should be considered for SC emission evolution. The geometric configuration of the metallic nanoparticles (e.g. size and surface shape) also plays a major role in the SC's emission variation [192–195]. Generally, rough surface metals with bigger sizes enhances the luminescence of SC materials, whereas quenching luminescence occurs on smaller flat surface metallic NPs as reported by Matsuda *et al.* [195]. Mostly, three explanations justify the PL enhancement and quenching.

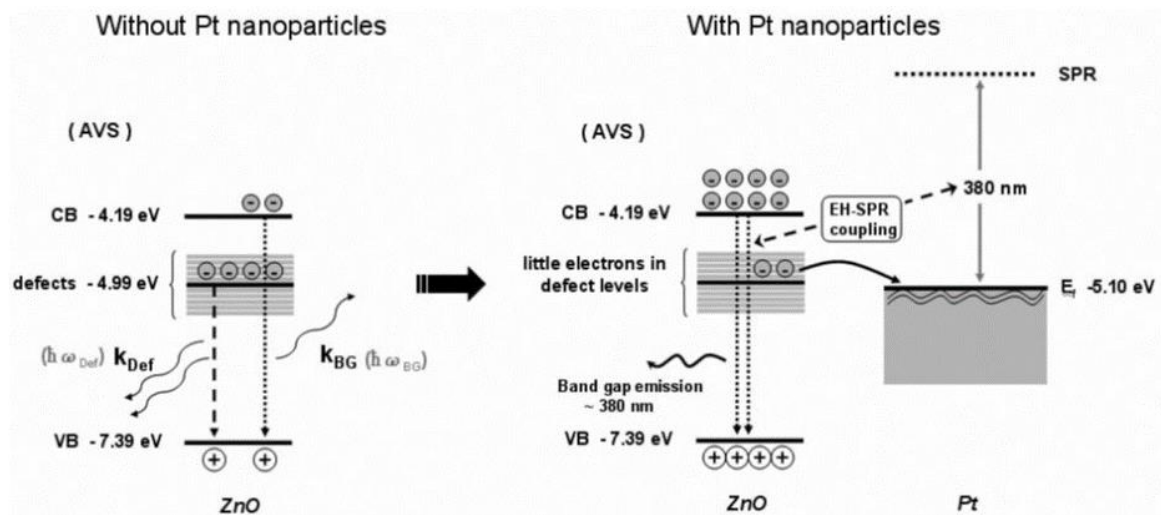
1. The scattering process of the plasmon resonance of the MNPs in the hybrid system enhances the luminescence, while its absorbance quenches the emission. This was proposed by Lacowicz *et al.* in the radiating plasmon model [193].
2. PL enhancement is due to the increased excitation and radiative recombination rates due to local field enhancement upon M/SC coupling, while the non-radiative energy transfer to the metal from the SC is the cause of PL quenching [171,190,194,195].
3. Electron transfer from metal to SC is the main cause of PL enhancement, while the reverse pathway (from SC to MNPs) is the origin of PL quenching [181,182,196].



Scheme 2 A schematic diagram showing the PL enhancement (a) and quenching (b) processes. Adapted from ref. [197].

Holding the attention on the SC's emission enhancement due to the favored circumstances applied in the field of science nowadays, MNPs can strongly amplify the band edge luminescence of the semiconductor when the optical transitions are improved. The enhancement in the PL upon coupling with plasmonic metal nanostructures is associated to the synergic resonant coupling interaction between the spontaneous recombination in the semiconductor and the SP arising from the metal [180].

Energy transfer between the system's constituents is a hypothesis for the exciton emission amplification upon coupling [180,189,198]. In the report of Jin *et al.*, they have announced the giant enhancement of the band edge luminescence of ZnO NR after Pt sputtering through energy transfer between the metal nanoparticles and the SC [199]. This mechanism is illustrated in Scheme 3.



Scheme 3 A schematic diagram for the coupling between bandgap and surface plasmon resonance, and carriers transfer between the defect level and the Pt Fermi level. It results in enhanced bandgap emission and suppressed defect emission. Adapted from ref. [199].

A strong resonant coupling takes place when the photon energy of the SC excitons matches that of the SPR of the metal, enhancing the spontaneous emission rate in the SC in addition to increasing the density of states. Thus, electrons in the CB and holes in the VB in the SC gain much energy enhancing the radiative band gap emission. The non-radiative recombination arising from the defect level to the valence band in such mechanism is altered by the interband transition from the defect level to the metal fermi level due to the mentioned resonant coupling. As reported by Lai *et al.*, a comparable enhancement strength was observed between silver and gold nanoparticles capped on ZnO films. It was reported that the Ag-capped sample showed larger emission enhancement than the Au-capped samples. The weak enhancement by gold was

referred to the reflection of the laser beam by the coating which doubles the excitation path, thus the enhancement is not significant as much as that observed in Ag-capped systems. The enhancement in PL after Ag capping was associated to the matching between the plasmon energy of Ag NPs with the emission band of the ZnO NPs creating a resonant coupling state that significantly enhances the spontaneous recombination rate in the SC [180].

Neogi *et al.* have explained in their study on InGaN quantum well that the rate of spontaneous emission is almost enhanced two orders of magnitude when coupled to a silver surface plasmon [200].

### **1.5.3 SERS enhancement**

The Raman scattering known as surface enhanced Raman scattering (SERS) effect support knowledge about the progress in the sensitivity of chemical, biological and environmental sensing devices by the increase in the Raman signals.

Indeed, the Raman scattering of the metallic nanoparticles could be adjusted in a way that helps these nanostructures more efficiently being active in molecular detection, and greatly effective in photovoltaics, solar cells, drug delivery, energy conversion and/or storage, in addition to biotechnological applications [201]. Conducting metallic NP are able to localize and powerfully enhance an incident electromagnetic field, which alter the charge density wave at the interface, modifying the electromagnetic field generated by the surface plasmon resonance [202]. These performances are outcomes of the producing carrier pairs by the surface plasmon resonance effect, in addition to the enhancement of the efficiency of the electron-hole separation, and increasing the light absorption [203,204]. Recently, SERS effects of different geometries of metallic nanoparticles (e.g. Au or Ag NPs) have been demonstrated [205–207]. The SERS measurements of Au NPs were highly manifested by different researchers [208,209]. The Raman spectroscopy of semiconducting materials as ZnO NPs has been also previously reported [210,211].

Thus, developing substrates that combine SC with SP with high sensitivity and localization of hot spots (regions where the electromagnetic field is locally concentrated), will induce high SERS enhancement that is also important in research fields nowadays.

Sakano *et al.* explained the surface enhanced Raman scattering properties using Au-coated ZnO nanorods hybrid systems [212]. They related the spatial configuration of the NP (size,

shape, and aspect ratio), and its aggregation activity to tailoring SERS characteristics (Figure 9). The Au-coated ZnO nanorod arrays showed a high SERS behavior due to the intense local electromagnetic fields stimulated by the surface plasmon polaritons at the surface of the MNPs, where increasing the SC's diameter further amplifies the SERS intensity validating better enhancement.

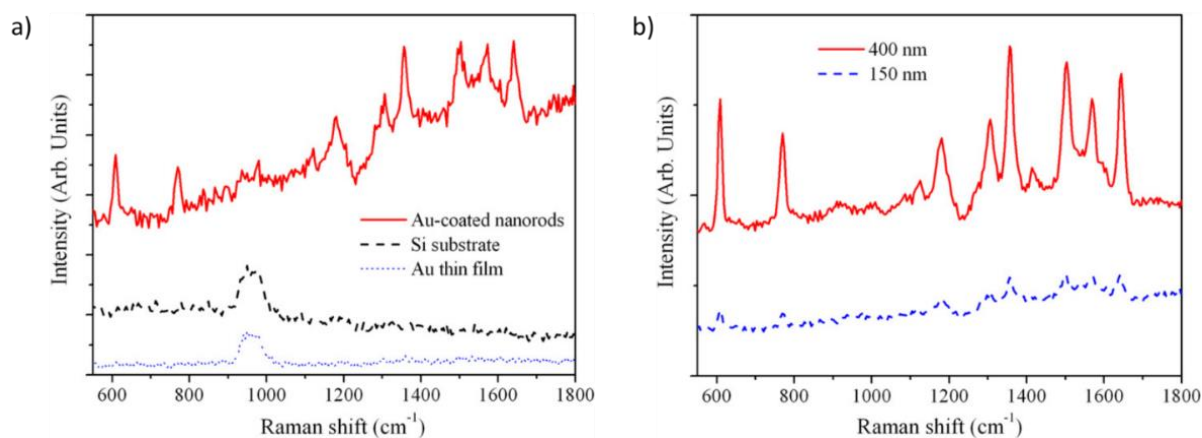
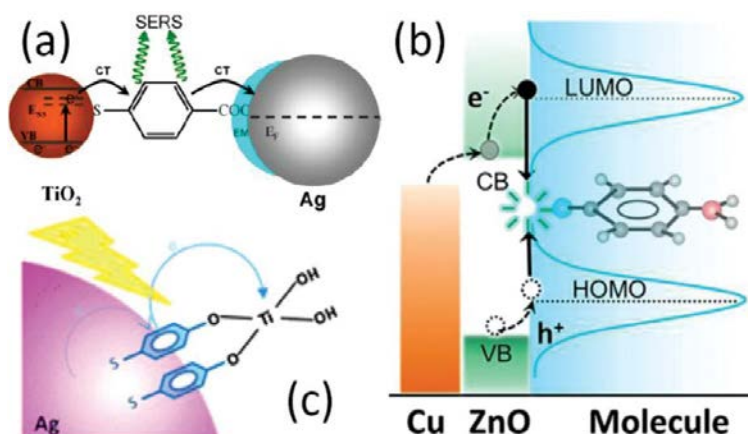


Figure 9 a) SERS spectra from Au-coated ZnO nanorods of 150 nm in diameter, Au thin film (5 nm thick), and a bare Si substrate with R6G of 1  $\mu$ M. b) Comparison of SERS spectra of Au-coated ZnO nanorods of diameter of 400 and 150 nm with R6G of 1  $\mu$ M. Adapted from ref. [212].

In another reports, Han *et al.* showed that the SERS of metallic nanoparticles (MNPs) is enhanced upon coupling with a semiconductor nanostructure improving the ability of detection of different chemical and biological species. This enhancement depends on the charge transfer (CT) mechanism between the metal and the semiconductor compounds. The charge transfer pathway highly depends on the type of the metal, electromagnetic field effect, the detected molecule, and the surrounding environment [213]. Scheme 4 represents the charge transfer in several hybrid systems.



Scheme 4 The CT pathways in semiconductor–metal heterostructures (a) semiconductor-to-molecule-to-metal, (b) metal-to-semiconductor-to molecule, (c) metal-to-molecule-to-semiconductor. Adapted from ref. [213].

In Au-CdSe spherical nanoparticles, similar comebacks considering SERS were observed. Govorov *et al.* showed that after coupling the GNPs with quantum emitter CdSe, the field enhancement factor was improved compared to that of single GNPs. This enhancement was shown to be widely affected by the size of the MNPs, their number, and distance between the metal and semiconductor [214]. This is illustrated in Figure 10.

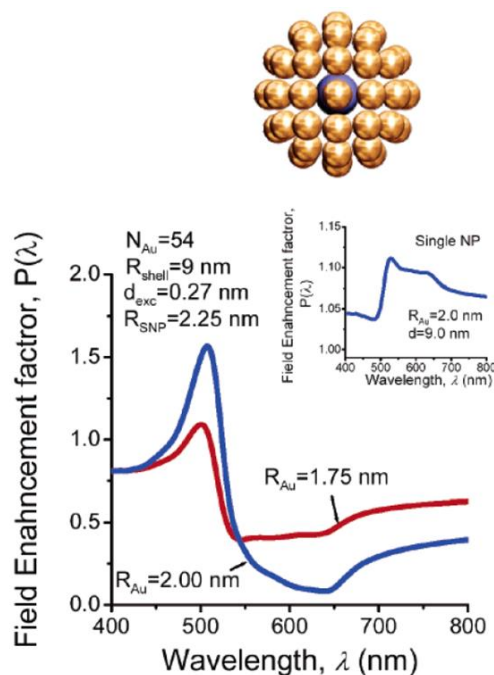


Figure 10 Optical characteristics of assemblies with 54 Au NP and 1 CdSe NP. Inset: field enhancement factor due to a single Au NP. Upper part: geometry of the complex. Adapted from ref. [214].

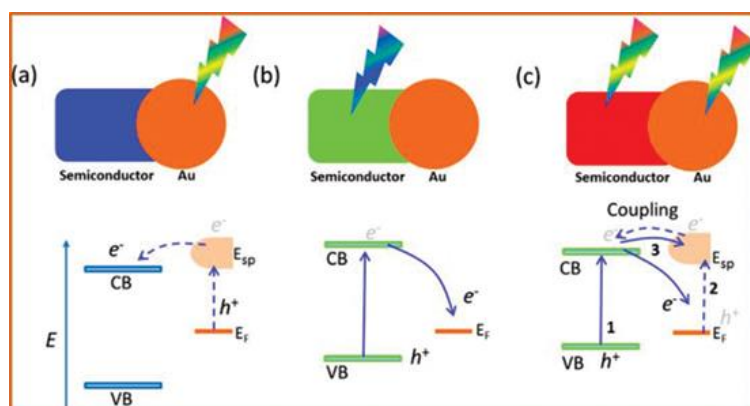
Another reports on the hybrid M/SC systems such as Au/CdSe nanowires (NW) junctions showed that the gold nanoparticles (GNPs) are arranged homogeneously after its nucleation at the lateral facets of the CdSe lattice defects, where SERS activity is notably enhanced upon plasmon generation [215].

#### 1.5.4 Stimulating charge transfer after photo-induced charge separation

The M/SC hybrid nanosystems have gained much attention by several researchers, where the hybrid nanostructure will endorse fast charge transfer upon light excitation, resulting in the charge separation.

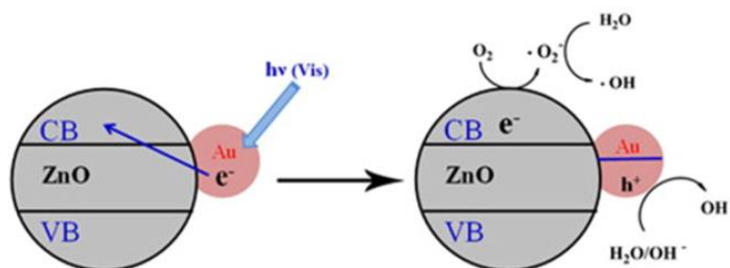
If the stimulating energy is in the visible range, the metallic nanoparticles will generate charges that will then transfer to the SC band gap [8,11,52,216,217]. Upon UV excitation, an

opposite proposition occurs where the photoexcited charges will transport from the semiconductor to the plasmonic metal systems, where only the semiconductor is excited [78,218]. After simultaneous excitations of both components, the semiconductor will use the SPR of the metal to enhance its light absorption, which is a valuable concept in photovoltaic and photocatalytic applications. This will be illustrated in Scheme 5.

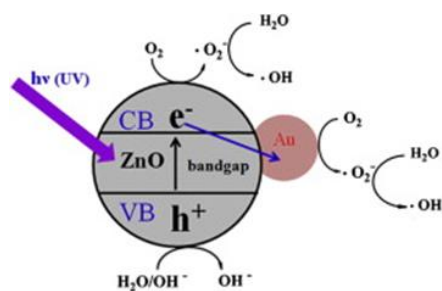


Scheme 5 Schematic presentation of the electron transfer processes in Au-semiconductor heterostructures. For Au-semiconductor heterostructure where (a) only Au is excited, (b) only semiconductor is excited, and (c) there are simultaneous excitations of both Au and semiconductor. The electron transfer path 1 refers for semiconductor excitation followed by electron transfer to Au, path 2 follows just the reverse process, and path 3 shows the coupling of exciton of the semiconductor and plasmon of Au. Here,  $E_{sp}$  refers to the Au surface plasmon state and  $E_f$  refers to the Au Fermi level. Adapted from ref. [219].

In the hybrid Au/ZnO systems, Yu *et al.* have examined the photocatalytic activity by the degradation of benzene molecules in two conditions. The first is under visible excitation of the gold nanoparticles (Scheme 6), and the second is under the UV excitation of the ZnO SC (Scheme 7) [65].



Scheme 6 Proposed mechanism of the photocatalysis of Au/ZnO nanostructures upon excitation of the visible light. Adapted from ref. [65].



Scheme 7 Proposed mechanism of the photocatalysis of Au/ZnO nanostructures under UV light irradiation. Adapted from ref. [65].

After visible excitation of the metal, the excited electrons will transfer from the GNPs into ZnO SC. The electron loss in GNPs will operate in forming active species (as HO radicals) to increase the photodegradation of benzene molecules. On the other hand, if the excitation is UV, the photoinduced electrons created in the ZnO conduction band will transfer into the metallic NPs, decreasing the  $e^-h^+$  recombination rate. This will stimulate high efficiency charge separation at the Au/ZnO interface, producing more reactive species that are further used in the degradation of benzene. Other hybrid M/SC systems used such mechanisms to degrade various molecules other than benzene such as Avans blue dye [163], methyl orange (MO) [220], and oxalic acid [221].

At the M/SC interface, the energy bands will arrange to be well aligned after excitation, facilitating the separated charge transfer between the metal and the SC according to the stimulation (Figure 11).

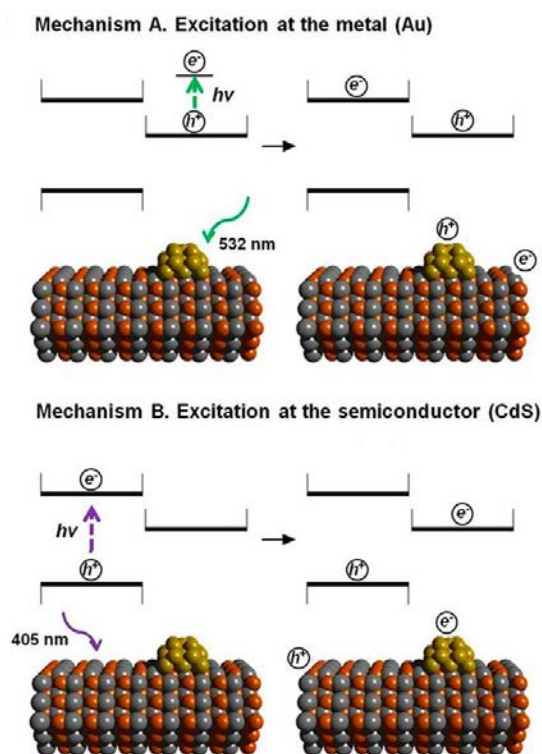


Figure 11 Two charge separation mechanisms in these hybrid heterostructures. Mechanism A starts by excitation at the metal at 532 nm, thus forming hot electrons ( $e^-$ ) and holes ( $h^+$ ) in the metal. The hot electrons are then transferred to the semiconductor's conduction band. Mechanism B starts with excitation at the semiconductor at 405 nm, thus forming electron-hole pairs at the semiconductor. Photogenerated electrons are then trapped by the gold. Adapted from ref. [162].

## 1.6 Applications of plasmonic-semiconductor heterojunctions

One of the motivations in implanting metallic nanoparticles into semiconducting materials is the ability to adjoin the functionalities of each compound creating new performances that are interesting outcome traits for light-involved applications.

### 1.6.1 Solar cells

Generation of electrical energy by the conversion of available solar energy using photovoltaic cells is considered as a prosperous technology nowadays [222]. The main goal in this process is to obtain the highest efficiency in a lower production cost. Hybrid M/SC such as Au/ZnO nanoparticles have been the dominant technology in the photovoltaic industry, where the process of material synthesis is often flexible, resulting in a high quantum yield and good stability nanomaterials. The surface plasmon resonance from Au nanoparticles was found to improve the photoresponse of ZnO due to enhanced charge separation, and facilitating the charge transport that are important mechanisms in solar cells. In addition, GNPs help in the visible absorption of light.

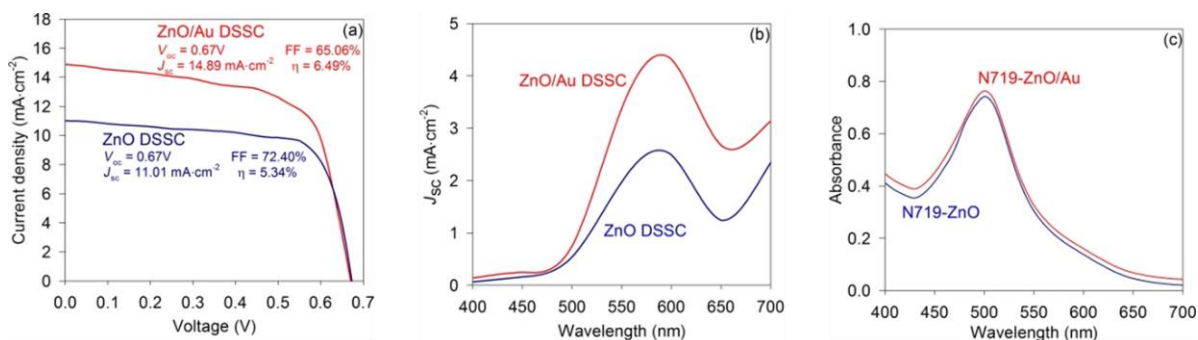


Figure 12 J–V characteristics of the bare ZnO-nanorod and ZnO/Au-hybrid DSSCs, measured at 1 sun, AM 1.5 G illumination, (b) short-circuit photocurrent density of the bare ZnO-nanorod and ZnO/Au-hybrid DSSCs measured at different incident wavelengths and (c) optical absorptions of dye N719 in 0.1 mM KOH aqueous solution for bare ZnO-nanorod and ZnO/Au-hybrid photoelectrodes. The optical absorption was measured by removing the dye molecules from the respective photoelectrodes (size = 1 cm<sup>2</sup>) by dipping them in a 0.1 mM KOH aqueous solution (2 mL) for 5 min. Adapted from ref. [80].

The best J-V characteristics is obtained in the hybrid systems, where the photocurrent is improved after GNPs incorporation due to the absorption by the SPs of the metallic NPs, and thus improving the overall power conversion efficiency. The improved performance could be referred due to the Schottky barrier at the M/SC interface that controls the charge transfer between constituents (Figure 12).

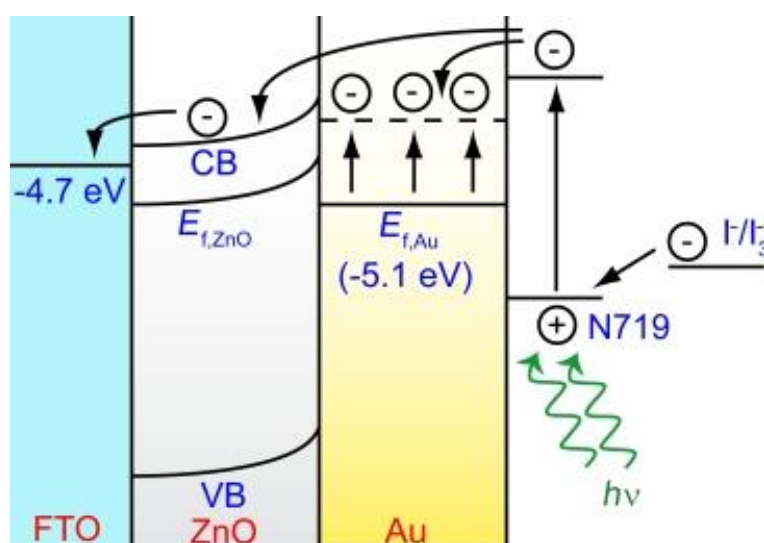
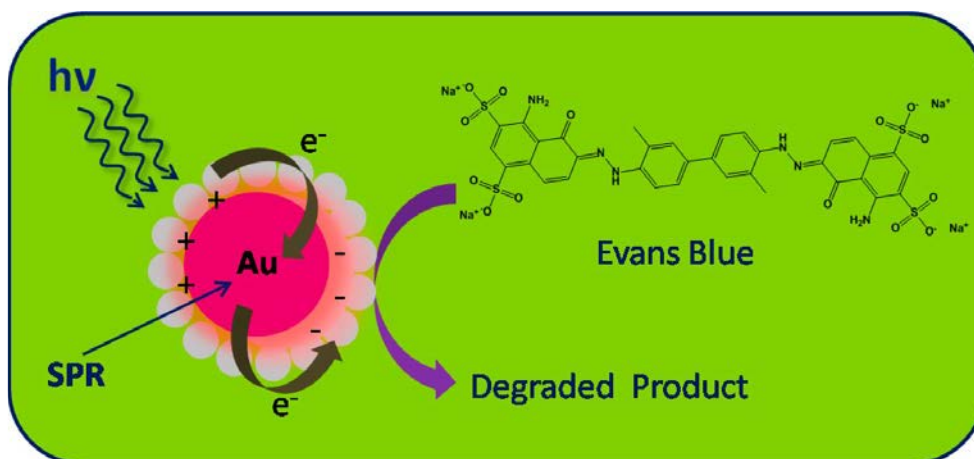


Figure 13 Energy-band diagram depicting the possible electron-transfer path in the ZnO/Au-hybrid DSSC, showing the Schottky barrier formed at the ZnO/Au interface. The dashed line in Au represents the position of the Fermi level of gold after electron injection from dye N719. Adapted from ref. [80].

Coupling will induce charge transfer from the excited dye molecules to the MNPs at the surface of the SC, to accumulate electrons in the GNPs, leading to the alignment which facilitates the charge transfer until reaching equilibrium [17,80] (Figure 13).

## 1.6.2 Catalysis-based applications

The hybrid heterostructures consisting of metal incorporated into semiconductor nanomaterials can highly improve the photocatalytic performance of the latter by the aid of the metal's SPR [54–57] Scheme 8.



Scheme 8 Schematic Presentation of the Photocatalytic Degradation of Evans Blue at the ZnO–Au Hybrids Surfaces. Adapted from ref. [163].

The metallic nanoparticles facilitate the charge separation through photoexcitation. Thus, the hybrid system could be used to amplify the degradation of organic pollutants used for water disinfection and air purification [223], photosynthesis of organic molecules arising from the hot-electron effect due to the plasmonic local heating [224], photocatalytic reduction of carbon dioxide by converting the solar energy into chemical one with the help of photocatalytic reactions using hydrogen molecules [225], and hydrogen production from water splitting highly needed issue in the future of energy [226].

In our work, we are interested in the photocatalytic activity of ZnO nanostructures and its evolution after attachment of gold nanoparticles to form Au/ZnO hybrids. This activity will be further discussed in the following chapters (2 and 3).

## 1.7 Engineering of plasmonic-semiconductor nanomaterials

As any given nanomaterial, hybrid nanoparticles are also synthesized by the two general approaches: the chemical bottom-up way, and physical top-down mode. As described above, based on the state of art about the plasmonic-semiconductor nanomaterials, three methods were mainly adapted to fabricate the M/SC hybrid systems [227–233]:

1. The first preparation is mixing the pre-grown semiconductor nanostructures into a metal salt solution, and then the addition of appropriate reducing agent is followed. By this strategy, the chemically reduced metal nanoparticles are supposed to be coupled to the semiconductor [17,65,232,234]. The shape and size of MNPs could be highly controlled through this process.
2. The second approach is the nucleation and growth of the oxide semiconductor (OSC) at the surface of the pre-existing metal nanoparticles. The oxide SC starting material is reduced, and then decomposed into OSC nanoparticles [155].
3. Another preparation method is the sequential approach, where coupling of the two constituents that are both already previously prepared is adapted. In some cases of this approach, additives as molecular linkers or stabilizers may be necessary to add [64,163].

On the basis of this chapter and particularly this final section that shows some disadvantages in the manufacturing of M/SC nanomaterials, we emphasize in the next chapters a new way to fabricate ZnO-Au NPs. Precisely, we describe a chemical approach allowing to control the coupling between Au and ZnO NPs in order to enhance both the optical and catalytic properties of ZnO nanostructures.

## 1.8 Conclusion

According to the state of art presented, it is observed that many research papers have been published on the fabrication of various aspects of metal oxides coupled to metallic nanoparticles, to produce multifunctional systems that are effective in wide fields of applications.

Since the last two decades, ZnO material was investigated in the scientific and technological applications such as optoelectronic devices, photocatalytic applications, in addition to piezoelectric and electronic devices as a fluorescent material.

ZnO is of high interest among all oxide semiconductors due to its low cost, low-toxicity, ease of synthesis and the ability of its growing on various kinds of substrates such as glass, ITO, Si/SiO<sub>2</sub>, etc.

As shown in the literature concerning ZnO nanomaterial and its coupling with noble metal, more precisely with gold nanoparticles due to its stability, this offers additional behaviors on

the ZnO nanostructures modulating its properties in a positive manner added on its special traits.

For that, this hybrid system (GNPs coupled to ZnO nanostructures) is chosen for our research study where the synthesis of ZnO nano-objects will be established through a simple process. The optimization of parametric conditions will be intensively varied and studied to obtain ultrasmall and pure ZnO NPs in an aqueous medium. The obtained nanoparticles will be thermally treated (annealed) after synthesis at various temperatures to obtain different sizes and morphologies of ZnO nanostructures. The emission properties of the fabricated ZnO will be studied and applied in photocatalysis through the degradation of an organic dye under different conditions (this will be discussed in details in chapter 2). Then, these particles will be coupled to different geometries of gold nanoparticles in different manners to modulate the optical properties of the crystalline ZnO NPs, where the luminescence enhancement and quenching mechanisms will be studied depending on each parametric condition. The photocatalytic activity will be investigated as well for the hybrid systems, to examine the influence of the GNPs on the ZnO photocatalytic activity (will be detailed in chapter 3). The different applications of the fabricated hybrid system will also be validated highlighting the importance of our hybrid systems for surface-based devices.

## 1.9 References

1. Carbone, L.; Cozzoli, P.D. Colloidal heterostructured nanocrystals: Synthesis and growth mechanisms. *Nano Today* **2010**, *5*, 449–493.
2. Lattuada, M.; Hatton, T.A. Synthesis, properties and applications of Janus nanoparticles. *Nano Today* **2011**, *3*, 286–308.
3. Kuo, C.-H.; Yang, Y.-C.; Gwo, S.; Huang, M.H. Facet-Dependent and Au Nanocrystal-Enhanced Electrical and Photocatalytic Properties of Au–Cu<sub>2</sub>O Core–Shell Heterostructures. *J. Am. Chem. Soc.* **2011**, *133*, 1052–1057.
4. Seh, Z.W.; Liu, S.; Han, M.-Y. Titania-Coated Metal Nanostructures. *Chem. Asian J.* **2012**, *7*, 2174–2184.
5. Liu, S.; Bai, S.-Q.; Zheng, Y.; Shah, K.W.; Han, M.-Y. Composite metal–oxide nanocatalysts. *ChemCatChem* **2012**, *4*, 1462–1484.
6. Zhang, Q.; Lee, I.; Joo, J.B.; Zaera, F.; Yin, Y. Core–shell nanostructured catalysts. *Acc. Chem. Res.* **2012**, *46*, 1816–1824.
7. Li, G.; Tang, Z. Noble metal nanoparticle@metal oxide core/yolk–shell nanostructures as catalysts: recent progress and perspective. *Nanoscale* **2014**, *6*, 3995–4011.

8. Clavero, C. Plasmon-induced hot-electron generation at nanoparticle/metal-oxide interfaces for photovoltaic and photocatalytic devices. *Nat. Photonics* **2014**, *8*, 95–103.
9. Zeng, J.; Wang, X.; G., J. Colloidal Hybrid Nanocrystals: Synthesis, Properties, and Perspectives. In *Nanocrystal*; Masuda, Y., Ed.; InTech, 2011 ISBN 978-953-307-199-2.
10. Park, K.-W.; Choi, J.-H.; Kwon, B.-K.; Lee, S.-A.; Sung, Y.-E.; Ha, H.-Y.; Hong, S.-A.; Kim, H.; Wieckowski, A. Chemical and Electronic Effects of Ni in Pt/Ni and Pt/Ru/Ni Alloy Nanoparticles in Methanol Electrooxidation. *J. Phys. Chem. B* **2002**, *106*, 1869–1877.
11. Wang, L.; Clavero, C.; Huba, Z.; Carroll, K.J.; Carpenter, E.E.; Gu, D.; Lukaszew, R.A. Plasmonics and Enhanced Magneto-Optics in Core–Shell Co–Ag Nanoparticles. *Nano Lett.* **2011**, *11*, 1237–1240.
12. Homaei, A.; Etemadipour, R. Improving the activity and stability of actinidin by immobilization on gold nanorods. *Int. J. Biol. Macromol.* **2015**, *72*, 1176–1181.
13. Fahmi, A.; Pietsch, T.; Mendoza, C.; Cheval, N. Functional hybrid materials. *Mater. Today* **2009**, *12*, 44–50.
14. Zhang, W.; Govorov, A.O.; Bryant, G.W. Semiconductor-Metal Nanoparticle Molecules: Hybrid Excitons and the Nonlinear Fano Effect. *Phys. Rev. Lett.* **2006**, *97*.
15. Manjavacas, A.; García de Abajo, F.J.; Nordlander, P. Quantum Plexcitonics: Strongly Interacting Plasmons and Excitons. *Nano Lett.* **2011**, *11*, 2318–2323.
16. Chen, X.-W.; Sandoghdar, V.; Agio, M. Coherent Interaction of Light with a Metallic Structure Coupled to a Single Quantum Emitter: From Superabsorption to Cloaking. *Phys. Rev. Lett.* **2013**, *110*.
17. Chen, Z.H.; Tang, Y.B.; Liu, C.P.; Leung, Y.H.; Yuan, G.D.; Chen, L.M.; Wang, Y.Q.; Bello, I.; Zapien, J.A.; Zhang, W.J.; et al. Vertically Aligned ZnO Nanorod Arrays Sensitized with Gold Nanoparticles for Schottky Barrier Photovoltaic Cells. *J. Phys. Chem. C* **2009**, *113*, 13433–13437.
18. Li, P.; Wei, Z.; Wu, T.; Peng, Q.; Li, Y. Au–ZnO Hybrid Nanopyramids and Their Photocatalytic Properties. *J. Am. Chem. Soc.* **2011**, *133*, 5660–5663.
19. Busch, G. Early history of the physics and chemistry of semiconductors—from doubts to fact in a hundred years. *Eur. J. Phys.* **1989**, *10*, 254–264.
20. Łukasiak, L.; Andrzej, J. History of semiconductors. *J. Telecommun. Inf. Technol.* **2010**, *3–9*.
21. Laeri, F., Schüth, F., Simon, U., Wark, M., Host-Guest-Systems Based on Nanoporous Crystals: LAERI: NANOPOROUS CRYSTALS O-BK; Eds.; Wiley-VCH Verlag GmbH & Co. KGaA: Weinheim, FRG, 2003; ISBN 978-3-527-60267-4.
22. Jiang, R.; Li, B.; Fang, C.; Wang, J. Metal/Semiconductor Hybrid Nanostructures for Plasmon-Enhanced Applications. *Adv. Mater.* **2014**, *26*, 5274–5309.

23. Yang, X. Yang, X. (2016). Synthesis and Characterization of Hybrid Metal-Metallic Oxide Composite Nanofibers by Electrospinning and Their Applications.
24. Bawendi, M.G.; Steigerwald, M.L.; Brus, L.E. The Quantum Mechanics of Larger Semiconductor Clusters (“Quantum Dots”). *Annu. Rev. Phys. Chem.* **1990**, *41*, 477–496.
25. Reimann, S.M.; Manninen, M. Electronic structure of quantum dots. *Rev. Mod. Phys.* **2002**, *74*, 1283–1342.
26. Koole, R.; Groeneveld, E.; Vanmaekelbergh, D.; Meijerink, A.; de Mello Donegá, C. Size Effects on Semiconductor Nanoparticles. In *Nanoparticles*; de Mello Donegá, C., Ed.; Springer Berlin Heidelberg: Berlin, Heidelberg, 2014; pp. 13–51 ISBN 978-3-662-44822-9.
27. Li, L.; Hu, J.; Yang, W.; Alivisatos, A.P. Band Gap Variation of Size- and Shape-Controlled Colloidal CdSe Quantum Rods. *Nano Lett.* **2001**, *1*, 349–351.
28. Hu, J. Linearly Polarized Emission from Colloidal Semiconductor Quantum Rods. *Science* **2001**, *292*, 2060–2063.
29. Ekimov, A.I.; Efros, A.L.; Onushchenko, A.A. Quantum size effect in semiconductor microcrystals. *Solid State Commun.* **1985**, *56*, 921–924.
30. Brus, L.E. A simple model for the ionization potential, electron affinity, and aqueous redox potentials of small semiconductor crystallites. *J. Chem. Phys.* **1983**, *79*, 5566–5571.
31. Brus, L. Quantum crystallites and nonlinear optics. *Appl. Phys. Solids Surf.* **1991**, *53*, 465–474.
32. Bera, D.; Qian, L.; Tseng, T.-K.; Holloway, P.H. Quantum Dots and Their Multimodal Applications: A Review. *Materials* **2010**, *3*, 2260–2345.
33. Efros, A.L.; Rosen, M. The Electronic Structure of Semiconductor Nanocrystals. *Annu. Rev. Mater. Sci.* **2000**, *30*, 475–521.
34. Schneider, R.; Balan, L.; Aldeek, F. Synthesis, Characterization and Biological Applications of Water-Soluble ZnO Quantum Dots. In *Nanomaterials*; Rahman, M., Ed.; InTech, 2011 ISBN 978-953-307-913-4.
35. Simeonidis, K.; Mourdikoudis, S.; Kaprara, E.; Mitrakas, M.; Polavarapu, L. Inorganic engineered nanoparticles in drinking water treatment: a critical review. *Environ. Sci. Water Res. Technol.* **2016**, *2*, 43–70.
36. Wang, H.; Zhang, L.; Chen, Z.; Hu, J.; Li, S.; Wang, Z.; Liu, J.; Wang, X. Semiconductor heterojunction photocatalysts: design, construction, and photocatalytic performances. *Chem. Soc. Rev.* **2014**, *43*, 5234.
37. O’Farrell, N.; Houlton, A.; Horrocks, B.R. Silicon nanoparticles: applications in cell biology and medicine. *Int. J. Nanomedicine* **2006**, *1*, 451–472.

38. Amini, P.; Dolatyari, M.; Rostami, G.; Rostami, A. High Throughput Quantum Dot Based LEDs. In *Energy Efficiency Improvements in Smart Grid Components*; Eissa, M.M., Ed.; InTech, 2015 ISBN 978-953-51-2038-4.
39. Kuriakose, S.; Choudhary, V.; Satpati, B.; Mohapatra, S. Facile synthesis of Ag–ZnO hybrid nanospindles for highly efficient photocatalytic degradation of methyl orange. *Phys. Chem. Chem. Phys.* **2014**, *16*, 17560.
40. Yıldırım, Ö.A.; Unalan, H.E.; Durucan, C. Highly Efficient Room Temperature Synthesis of Silver-Doped Zinc Oxide (ZnO:Ag) Nanoparticles: Structural, Optical, and Photocatalytic Properties. *J. Am. Ceram. Soc.* **2013**, *96*, 766–773.
41. Lu, Y.; Lin, Y.; Wang, D.; Wang, L.; Xie, T.; Jiang, T. Surface charge transfer properties of high-performance Ag-decorated ZnO photocatalysts. *J. Phys. Appl. Phys.* **2011**, *44*, 315502.
42. Manna, G.; Bose, R.; Pradhan, N. Photocatalytic Au-Bi<sub>2</sub>S<sub>3</sub> Heteronanostructures. *Angew. Chem. Int. Ed.* **2014**, *53*, 6743–6746.
43. Maeda, K.; Domen, K. Photocatalytic Water Splitting: Recent Progress and Future Challenges. *J. Phys. Chem. Lett.* **2010**, *1*, 2655–2661.
44. Zhao, J.; Osterloh, F.E. Photochemical Charge Separation in Nanocrystal Photocatalyst Films: Insights from Surface Photovoltage Spectroscopy. *J. Phys. Chem. Lett.* **2014**, *5*, 782–786.
45. Khon, E.; Lambright, K.; Khnayzer, R.S.; Moroz, P.; Perera, D.; Butaeva, E.; Lambright, S.; Castellano, F.N.; Zamkov, M. Improving the Catalytic Activity of Semiconductor Nanocrystals through Selective Domain Etching. *Nano Lett.* **2013**, *13*, 2016–2023.
46. Wang, Y.; Yang, Y.; Xi, L.; Zhang, X.; Jia, M.; Xu, H.; Wu, H. A simple hydrothermal synthesis of flower-like ZnO microspheres and their improved photocatalytic activity. *Mater. Lett.* **2016**, *180*, 55–58.
47. Kumar, S.G.; Rao, K.S.R.K. Zinc oxide based photocatalysis: tailoring surface-bulk structure and related interfacial charge carrier dynamics for better environmental applications. *RSC Adv.* **2015**, *5*, 3306–3351.
48. Woan, K.; Pyrgiotakis, G.; Sigmund, W. Photocatalytic Carbon-Nanotube-TiO<sub>2</sub> Composites. *Adv. Mater.* **2009**, *21*, 2233–2239.
49. Dai, G.; Yu, J.; Liu, G. Synthesis and Enhanced Visible-Light Photoelectrocatalytic Activity of *p* – *n* Junction BiOI/TiO<sub>2</sub> Nanotube Arrays. *J. Phys. Chem. C* **2011**, *115*, 7339–7346.
50. Rajeshwar, K.; de Tacconi, N.R. Solution combustion synthesis of oxide semiconductors for solar energy conversion and environmental remediation. *Chem. Soc. Rev.* **2009**, *38*, 1984.

51. Liu, S.; Yu, J.; Jaroniec, M. Tunable Photocatalytic Selectivity of Hollow TiO<sub>2</sub> Microspheres Composed of Anatase Polyhedra with Exposed {001} Facets. *J. Am. Chem. Soc.* **2010**, *132*, 11914–11916.
52. Xiang, Q.; Yu, J.; Wang, W.; Jaroniec, M. Nitrogen self-doped nanosized TiO<sub>2</sub> sheets with exposed {001} facets for enhanced visible-light photocatalytic activity. *Chem. Commun.* **2011**, *47*, 6906.
53. Xiang, Q.; Yu, J.; Jaroniec, M. Nitrogen and sulfur co-doped TiO<sub>2</sub> nanosheets with exposed {001} facets: synthesis, characterization and visible-light photocatalytic activity. *Phys Chem Chem Phys* **2011**, *13*, 4853–4861.
54. Linic, S.; Christopher, P.; Ingram, D.B. Plasmonic-metal nanostructures for efficient conversion of solar to chemical energy. *Nat. Mater.* **2011**, *10*, 911–921.
55. Zhou, X.; Liu, G.; Yu, J.; Fan, W. Surface plasmon resonance-mediated photocatalysis by noble metal-based composites under visible light. *J. Mater. Chem.* **2012**, *22*, 21337.
56. Wang, P.; Huang, B.; Dai, Y.; Whangbo, M.-H. Plasmonic photocatalysts: harvesting visible light with noble metal nanoparticles. *Phys. Chem. Chem. Phys.* **2012**, *14*, 9813.
57. Xiao, M.; Jiang, R.; Wang, F.; Fang, C.; Wang, J.; Yu, J.C. Plasmon-enhanced chemical reactions. *J. Mater. Chem. A* **2013**, *1*, 5790.
58. Hou, W.; Cronin, S.B. A Review of Surface Plasmon Resonance-Enhanced Photocatalysis. *Adv. Funct. Mater.* **2013**, *23*, 1612–1619.
59. Güy, N.; Çakar, S.; Özacar, M. Comparison of palladium/zinc oxide photocatalysts prepared by different palladium doping methods for congo red degradation. *J. Colloid Interface Sci.* **2016**, *466*, 128–137.
60. Morales-Flores, N.; Pal, U.; Sánchez Mora, E. Photocatalytic behavior of ZnO and Pt-incorporated ZnO nanoparticles in phenol degradation. *Appl. Catal. Gen.* **2011**, *394*, 269–275.
61. Méndez-Medrano, M.G.; Kowalska, E.; Lehoux, A.; Herissan, A.; Ohtani, B.; Bahena, D.; Briois, V.; Colbeau-Justin, C.; Rodríguez-López, J.L.; Remita, H. Surface Modification of TiO<sub>2</sub> with Ag Nanoparticles and CuO Nanoclusters for Application in Photocatalysis. *J. Phys. Chem. C* **2016**, *120*, 5143–5154.
62. Yang, H.; Santra, S.; Holloway, P.H. Syntheses and Applications of Mn-Doped II-VI Semiconductor Nanocrystals. *J. Nanosci. Nanotechnol.* **2005**, *5*, 1364–1375.
63. Yang, Y.; Chen, O.; Angerhofer, A.; Cao, Y.C. Radial-Position-Controlled Doping in CdS/ZnS Core/Shell Nanocrystals. *J. Am. Chem. Soc.* **2006**, *128*, 12428–12429.
64. Chen, H.M.; Chen, C.K.; Chen, C.-J.; Cheng, L.-C.; Wu, P.C.; Cheng, B.H.; Ho, Y.Z.; Tseng, M.L.; Hsu, Y.-Y.; Chan, T.-S.; et al. Plasmon Inducing Effects for Enhanced Photoelectrochemical Water Splitting: X-ray Absorption Approach to Electronic Structures. *ACS Nano* **2012**, *6*, 7362–7372.

65. Yu, H.; Ming, H.; Zhang, H.; Li, H.; Pan, K.; Liu, Y.; Wang, F.; Gong, J.; Kang, Z. Au/ZnO nanocomposites: Facile fabrication and enhanced photocatalytic activity for degradation of benzene. *Mater. Chem. Phys.* **2012**, *137*, 113–117.
66. Zhang, L.; Blom, D.A.; Wang, H. Au–Cu<sub>2</sub>O Core–Shell Nanoparticles: A Hybrid Metal–Semiconductor Heteronanostructure with Geometrically Tunable Optical Properties. *Chem. Mater.* **2011**, *23*, 4587–4598.
67. Meir, N.; Jen-La Plante, I.; Flomin, K.; Chockler, E.; Moshofsky, B.; Diab, M.; Volokh, M.; Mokari, T. Studying the chemical, optical and catalytic properties of noble metal (Pt, Pd, Ag, Au)–Cu<sub>2</sub>O core–shell nanostructures grown via a general approach. *J Mater Chem A* **2013**, *1*, 1763–1769.
68. Shanmugapriya, T.; Ramamurthy, P. Photoluminescence Enhancement of Nanogold Decorated CdS Quantum Dots. *J. Phys. Chem. C* **2013**, *117*, 12272–12278.
69. Zhang, P.; Shao, C.; Li, X.; Zhang, M.; Zhang, X.; Sun, Y.; Liu, Y. In situ assembly of well-dispersed Au nanoparticles on TiO<sub>2</sub>/ZnO nanofibers: A three-way synergistic heterostructure with enhanced photocatalytic activity. *J. Hazard. Mater.* **2012**, *237–238*, 331–338.
70. Zhang, N.; Liu, S.; Fu, X.; Xu, Y.-J. Synthesis of M@TiO<sub>2</sub> (M = Au, Pd, Pt) Core–Shell Nanocomposites with Tunable Photoreactivity. *J. Phys. Chem. C* **2011**, *115*, 9136–9145.
71. Ye, M.; Zhou, H.; Zhang, T.; Zhang, Y.; Shao, Y. Preparation of SiO<sub>2</sub>@Au@TiO<sub>2</sub> core–shell nanostructures and their photocatalytic activities under visible light irradiation. *Chem. Eng. J.* **2013**, *226*, 209–216.
72. Warren, S.C.; Thimsen, E. Plasmonic solar water splitting. *Energy Env. Sci* **2012**, *5*, 5133–5146.
73. Tachibana, Y.; Vayssieres, L.; Durrant, J.R. Artificial photosynthesis for solar water-splitting. *Nat. Photonics* **2012**, *6*, 511–518.
74. Dhakshinamoorthy, A.; Navalon, S.; Corma, A.; Garcia, H. Photocatalytic CO<sub>2</sub> reduction by TiO<sub>2</sub> and related titanium containing solids. *Energy Environ. Sci.* **2012**, *5*, 9217.
75. Navalón, S.; Dhakshinamoorthy, A.; Álvaro, M.; Garcia, H. Photocatalytic CO<sub>2</sub> Reduction using Non-Titanium Metal Oxides and Sulfides. *ChemSusChem* **2013**, *6*, 562–577.
76. Park, J.H.; Kim, S.; Bard, A.J. Novel Carbon-Doped TiO<sub>2</sub> Nanotube Arrays with High Aspect Ratios for Efficient Solar Water Splitting. *Nano Lett.* **2006**, *6*, 24–28.
77. Sarkar, S.; Makhal, A.; Bora, T.; Baruah, S.; Dutta, J.; Pal, S.K. Photosensitive excited state dynamics in ZnO–Au nanocomposites and their implications in photocatalysis and dye-sensitized solar cells. *Phys. Chem. Chem. Phys.* **2011**, *13*, 12488.
78. Potje-Kamloth, K. Semiconductor Junction Gas Sensors. *Chem. Rev.* **2008**, *108*, 367–399.

79. Esmaili, Z.K. *inc oxide based nano-composites for multifunctional applications*, RMIT University, 2014.
80. Bora, T.; Kyaw, H.H.; Sarkar, S.; Pal, S.K.; Dutta, J. Highly efficient ZnO/Au Schottky barrier dye-sensitized solar cells: Role of gold nanoparticles on the charge-transfer process. *Beilstein J. Nanotechnol.* **2011**, *2*, 681–690.
81. D'Amico, N.R.; Cantele, G.; Perroni, C.A.; Ninno, D. Electronic properties and Schottky barriers at ZnO–metal interfaces from first principles. *J. Phys. Condens. Matter* **2015**, *27*, 015006.
82. Mishra, U.K.; Singh, J. Structural Properties of Semiconductors. In *Semiconductor Device Physics and Design*; Springer Netherlands: Dordrecht, 2007; pp. 1–27 ISBN 978-1-4020-6480-7.
83. Hamaguchi, C. Energy Band Structures of Semiconductors. In *Basic Semiconductor Physics*; Springer International Publishing: Cham, 2017; pp. 1–63 ISBN 978-3-319-66859-8.
84. Thomas, D.G. The exciton spectrum of zinc oxide. *J. Phys. Chem. Solids* **1960**, *15*, 86–96.
85. Mang, A.; Reimann, K.; Rübenacke, S. Band gaps, crystal-field splitting, spin-orbit coupling, and exciton binding energies in ZnO under hydrostatic pressure. *Solid State Commun.* **1995**, *94*, 251–254.
86. Reynolds, D.C.; Look, D.C.; Jogai, B.; Litton, C.W.; Cantwell, G.; Harsch, W.C. Valence-band ordering in ZnO. *Phys. Rev. B* **1999**, *60*, 2340–2344.
87. Chen, Y.; Bagnall, D.M.; Koh, H.; Park, K.; Hiraga, K.; Zhu, Z.; Yao, T. Plasma assisted molecular beam epitaxy of ZnO on *c*-plane sapphire: Growth and characterization. *J. Appl. Phys.* **1998**, *84*, 3912–3918.
88. Srikant, V.; Clarke, D.R. On the optical band gap of zinc oxide. *J. Appl. Phys.* **1998**, *83*, 5447–5451.
89. Schmidt-Mende, L.; MacManus-Driscoll, J.L. ZnO – nanostructures, defects, and devices. *Mater. Today* **2007**, *10*, 40–48.
90. Gupta, T.K. Application of Zinc Oxide Varistors. *J. Am. Ceram. Soc.* **1990**, *73*, 1817–1840.
91. Look, D.C. Recent advances in ZnO materials and devices. *Mater. Sci. Eng. B* **2001**, *80*, 383–387.
92. Lee, J.; Easteal, A.J.; Pal, U.; Bhattacharyya, D. Evolution of ZnO nanostructures in sol–gel synthesis. *Curr. Appl. Phys.* **2009**, *9*, 792–796.
93. Djurišić, A.B.; Leung, Y.H. Optical Properties of ZnO Nanostructures. *Small* **2006**, *2*, 944–961.

94. Wang, Z.-S.; Huang, C.-H.; Huang, Y.-Y.; Hou, Y.-J.; Xie, P.-H.; Zhang, B.-W.; Cheng, H.-M. A Highly Efficient Solar Cell Made from a Dye-Modified ZnO-Covered TiO<sub>2</sub> Nanoporous Electrode. *Chem. Mater.* **2001**, *13*, 678–682.
95. Salman, M.S.; Riaz, A.; Iqbal, A.; Zulfiqar, S.; Sarwar, M.I.; Shabbir, S. Design and fabrication of covalently linked PEGylated nanohybrids of ZnO quantum dots with preserved and tunable fluorescence. *Mater. Des.* **2017**, *131*, 156–166.
96. Rasmussen, J.W.; Martinez, E.; Louka, P.; Wingett, D.G. Zinc oxide nanoparticles for selective destruction of tumor cells and potential for drug delivery applications. *Expert Opin. Drug Deliv.* **2010**, *7*, 1063–1077.
97. Li, H.; Zhang, Y.; Pan, X.; Zhang, H.; Wang, T.; Xie, E. Effects of In and Mg doping on properties of ZnO nanoparticles by flame spray synthesis. *J. Nanoparticle Res.* **2009**, *11*, 917–921.
98. Jian-Feng, Y.; You-Ming, L.; Hong-Wei, L.; Yi-Chun, L.; Bing-Hui, L.; Xi-Wu, F.; Jun-Ming, Z. Growth and properties of ZnO nanotubes grown on Si(111) substrate by plasma-assisted molecular beam epitaxy. *J. Cryst. Growth* **2005**, *280*, 206–211.
99. Zhao, Q.X.; Willander, M.; Morjan, R.E.; Hu, Q.-H.; Campbell, E.E.B. Optical recombination of ZnO nanowires grown on sapphire and Si substrates. *Appl. Phys. Lett.* **2003**, *83*, 165–167.
100. Meulenkamp, E.A. Synthesis and Growth of ZnO Nanoparticles. *J. Phys. Chem. B* **1998**, *102*, 5566–5572.
101. Roy, V.A.L.; Djurišić, A.B.; Chan, W.K.; Gao, J.; Lui, H.F.; Surya, C. Luminescent and structural properties of ZnO nanorods prepared under different conditions. *Appl. Phys. Lett.* **2003**, *83*, 141–143.
102. Bang, J.; Yang, H.; Holloway, P.H. Enhanced and stable green emission of ZnO nanoparticles by surface segregation of Mg. *Nanotechnology* **2006**, *17*, 973–978.
103. Singh, L.R.; Ningthoujam, R.S.; Singh, S.D. Tuning of ultra-violet to green emission by choosing suitable excitation wavelength in ZnO: Quantum dot, nanocrystals and bulk. *J. Alloys Compd.* **2009**, *487*, 466–471.
104. Ullah, R.; Dutta, J. Photocatalytic degradation of organic dyes with manganese-doped ZnO nanoparticles. *J. Hazard. Mater.* **2008**, *156*, 194–200.
105. Sawai, J.; Igarashi, H.; Hashimoto, A.; Kokugan, T.; Shimizu, M. Evaluation of growth inhibitory effect of ceramics powder slurry on bacteria by conductance method. *J. Chem. Eng. Jpn.* **1995**, *28*, 288–293.
106. Li, G.-R.; Lu, X.-H.; Su, C.-Y.; Tong, Y.-X. Facile Synthesis of Hierarchical ZnO:Tb<sup>3+</sup> Nanorod Bundles and Their Optical and Magnetic Properties. *J. Phys. Chem. C* **2008**, *112*, 2927–2933.

107. Özgür, Ü.; Alivov, Y.I.; Liu, C.; Teke, A.; Reshchikov, M.A.; Doğan, S.; Avrutin, V.; Cho, S.-J.; Morkoç, H. A comprehensive review of ZnO materials and devices. *J. Appl. Phys.* **2005**, *98*, 041301.
108. Soci, C.; Zhang, A.; Xiang, B.; Dayeh, S.A.; Aplin, D.P.R.; Park, J.; Bao, X.Y.; Lo, Y.H.; Wang, D. ZnO Nanowire UV Photodetectors with High Internal Gain. *Nano Lett.* **2007**, *7*, 1003–1009.
109. Ryu, Y.; Lee, T.-S.; Lubguban, J.A.; White, H.W.; Kim, B.-J.; Park, Y.-S.; Youn, C.-J. Next generation of oxide photonic devices: ZnO-based ultraviolet light emitting diodes. *Appl. Phys. Lett.* **2006**, *88*, 241108.
110. Reynolds, D.C.; Look, D.C.; Jogai, B. Optically pumped ultraviolet lasing from ZnO. *Solid State Commun.* **1996**, *99*, 873–875.
111. Bagnall, D.M.; Chen, Y.F.; Zhu, Z.; Yao, T.; Koyama, S.; Shen, M.Y.; Goto, T. Optically pumped lasing of ZnO at room temperature. *Appl. Phys. Lett.* **1997**, *70*, 2230–2232.
112. Vanheusden, K.; Warren, W.L.; Seager, C.H.; Tallant, D.R.; Voigt, J.A.; Gnade, B.E. Mechanisms behind green photoluminescence in ZnO phosphor powders. *J. Appl. Phys.* **1996**, *79*, 7983–7990.
113. Wu, L.; Wu, Y.; Pan, X.; Kong, F. Synthesis of ZnO nanorod and the annealing effect on its photoluminescence property. *Opt. Mater.* **2006**, *28*, 418–422.
114. Li, J.; Zhao, D.; Meng, X.; Zhang, Z.; Zhang, J.; Shen, D.; Lu, Y.; Fan, X. Enhanced Ultraviolet Emission from ZnS-Coated ZnO Nanowires Fabricated by Self-Assembling Method. *J. Phys. Chem. B* **2006**, *110*, 14685–14687.
115. Lee, W.-J.; Kang, J.; Chang, K.J. Defect properties and p -type doping efficiency in phosphorus-doped ZnO. *Phys. Rev. B* **2006**, *73*.
116. Zhou, H.; Alves, H.; Hofmann, D.M.; Kriegseis, W.; Meyer, B.K.; Kaczmarczyk, G.; Hoffmann, A. Behind the weak excitonic emission of ZnO quantum dots: ZnO/Zn(OH)<sub>2</sub> core-shell structure. *Appl. Phys. Lett.* **2002**, *80*, 210–212.
117. Hong, S.; Joo, T.; Park, W.I.; Jun, Y.H.; Yi, G.-C. Time-resolved photoluminescence of the size-controlled ZnO nanorods. *Appl. Phys. Lett.* **2003**, *83*, 4157–4159.
118. Hirai, T.; Harada, Y.; Hashimoto, S.; Itoh, T.; Ohno, N. Luminescence of excitons in mesoscopic ZnO particles. *J. Lumin.* **2005**, *112*, 196–199.
119. Gu, Y.; Kuskovsky, I.L.; Yin, M.; O'Brien, S.; Neumark, G.F. Quantum confinement in ZnO nanorods. *Appl. Phys. Lett.* **2004**, *85*, 3833–3835.
120. Fonoberov, V.A.; Balandin, A.A. Origin of ultraviolet photoluminescence in ZnO quantum dots: Confined excitons versus surface-bound impurity exciton complexes. *Appl. Phys. Lett.* **2004**, *85*, 5971–5973.

121. Guo, L.; Yang, S.; Yang, C.; Yu, P.; Wang, J.; Ge, W.; Wong, G.K.L. Highly monodisperse polymer-capped ZnO nanoparticles: Preparation and optical properties. *Appl. Phys. Lett.* **2000**, *76*, 2901–2903.
122. Bahnemann, D.W.; Kormann, C.; Hoffmann, M.R. Preparation and characterization of quantum size zinc oxide: a detailed spectroscopic study. *J. Phys. Chem.* **1987**, *91*, 3789–3798.
123. Fonoberov, V.A.; Alim, K.A.; Balandin, A.A.; Xiu, F.; Liu, J. Photoluminescence investigation of the carrier recombination processes in ZnO quantum dots and nanocrystals. *Phys. Rev. B* **2006**, *73*.
124. Fonoberov, V.A.; Balandin, A.A. Radiative lifetime of excitons in ZnO nanocrystals: The dead-layer effect. *Phys. Rev. B* **2004**, *70*.
125. Alim, K.A.; Fonoberov, V.A.; Balandin, A.A. Origin of the optical phonon frequency shifts in ZnO quantum dots. *Appl. Phys. Lett.* **2005**, *86*, 053103.
126. van Dijken, A.; Meulenkaamp, E.A.; Vanmaekelbergh, D.; Meijerink, A. Identification of the transition responsible for the visible emission in ZnO using quantum size effects. *J. Lumin.* **2000**, *90*, 123–128.
127. Klason, P.; Moe Børseth, T.; Zhao, Q.X.; Svensson, B.G.; Kuznetsov, A.Y.; Bergman, P.J.; Willander, M. Temperature dependence and decay times of zinc and oxygen vacancy related photoluminescence bands in zinc oxide. *Solid State Commun.* **2008**, *145*, 321–326.
128. Li, D.; Leung, Y.H.; Djurišić, A.B.; Liu, Z.T.; Xie, M.H.; Shi, S.L.; Xu, S.J.; Chan, W.K. Different origins of visible luminescence in ZnO nanostructures fabricated by the chemical and evaporation methods. *Appl. Phys. Lett.* **2004**, *85*, 1601–1603.
129. Yang, Q.; Tang, K.; Zuo, J.; Qian, Y. Synthesis and luminescent property of single-crystal ZnO nanobelts by a simple low temperature evaporation route. *Appl. Phys. A* **2004**, *79*, 1847–1851.
130. Lin, B.; Fu, Z.; Jia, Y. Green luminescent center in undoped zinc oxide films deposited on silicon substrates. *Appl. Phys. Lett.* **2001**, *79*, 943–945.
131. Mishra, S.K.; Srivastava, R.K.; Prakash, S.G.; Yadav, R.S.; Panday, A.C. Photoluminescence and photoconductive characteristics of hydrothermally synthesized ZnO nanoparticles. *Opto-Electron. Rev.* **2010**, *18*.
132. Yin, J.; Gao, F.; Wei, C.; Lu, Q. Water Amount Dependence on Morphologies and Properties of ZnO nanostructures in Double-solvent System. *Sci. Rep.* **2015**, *4*.
133. Guo, L.; Yang, S.; Yang, C.; Yu, P.; Wang, J.; Ge, W.; Wong, G.K.L. Synthesis and Characterization of Poly(vinylpyrrolidone)-Modified Zinc Oxide Nanoparticles. *Chem. Mater.* **2000**, *12*, 2268–2274.
134. Manzano, C.V.; Alegre, D.; Caballero-Calero, O.; Alén, B.; Martín-González, M.S. Synthesis and luminescence properties of electrodeposited ZnO films. *J. Appl. Phys.* **2011**, *110*, 043538.

135. Pandey, S.K.; Pandey, S.K.; Mukherjee, C.; Mishra, P.; Gupta, M.; Barman, S.R.; D'Souza, S.W.; Mukherjee, S. Effect of growth temperature on structural, electrical and optical properties of dual ion beam sputtered ZnO thin films. *J. Mater. Sci. Mater. Electron.* **2013**, *24*, 2541–2547.
136. Sadaf, J.R.; Israr, M.Q.; Kishwar, S.; Nur, O.; Willander, M. White Electroluminescence Using ZnO Nanotubes/GaN Heterostructure Light-Emitting Diode. *Nanoscale Res. Lett.* **2010**, *5*, 957–960.
137. Norberg, N.S.; Gamelin, D.R. Influence of Surface Modification on the Luminescence of Colloidal ZnO Nanocrystals. *J. Phys. Chem. B* **2005**, *109*, 20810–20816.
138. Reynolds, D.C.; Look, D.C.; Jogai, B. Fine structure on the green band in ZnO. *J. Appl. Phys.* **2001**, *89*, 6189–6191.
139. Studenikin, S.A.; Cocivera, M. Time-resolved luminescence and photoconductivity of polycrystalline ZnO films. *J. Appl. Phys.* **2002**, *91*, 5060–5065.
140. Zeng, H.; Duan, G.; Li, Y.; Yang, S.; Xu, X.; Cai, W. Blue Luminescence of ZnO Nanoparticles Based on Non-Equilibrium Processes: Defect Origins and Emission Controls. *Adv. Funct. Mater.* **2010**, *20*, 561–572.
141. van Dijken, A.; Meulenkaamp, E.A.; Vanmaekelbergh, D.; Meijerink, A. The Kinetics of the Radiative and Nonradiative Processes in Nanocrystalline ZnO Particles upon Photoexcitation. *J. Phys. Chem. B* **2000**, *104*, 1715–1723.
142. Studenikin, S.A.; Golego, N.; Cocivera, M. Fabrication of green and orange photoluminescent, undoped ZnO films using spray pyrolysis. *J. Appl. Phys.* **1998**, *84*, 2287–2294.
143. Chand, P.; Gaur, A.; Kumar, A. Structural, optical and ferroelectric behavior of hydrothermally grown ZnO nanostructures. *Superlattices Microstruct.* **2013**, *64*, 331–342.
144. Morfa, A.J.; Gibson, B.C.; Karg, M.; Karle, T.J.; Greentree, A.D.; Mulvaney, P.; Tomljenovic-Hanic, S. Single-Photon Emission and Quantum Characterization of Zinc Oxide Defects. *Nano Lett.* **2012**, *12*, 949–954.
145. Stockman, M.I. Nanoplasmonics: The physics behind the applications. *Phys. Today* **2011**, *64*, 39–44.
146. Moskovits, M. Surface-enhanced Raman spectroscopy: a brief retrospective. *J. Raman Spectrosc.* **2005**, *36*, 485–496.
147. Stewart, M.E.; Anderton, C.R.; Thompson, L.B.; Maria, J.; Gray, S.K.; Rogers, J.A.; Nuzzo, R.G. Nanostructured Plasmonic Sensors. *Chem. Rev.* **2008**, *108*, 494–521.
148. Zhou, W.; Dridi, M.; Suh, J.Y.; Kim, C.H.; Co, D.T.; Wasielewski, M.R.; Schatz, G.C.; Odom, T.W. Lasing action in strongly coupled plasmonic nanocavity arrays. *Nat. Nanotechnol.* **2013**, *8*, 506–511.

149. Lakowicz, J.R.; Ray, K.; Chowdhury, M.; Szmecinski, H.; Fu, Y.; Zhang, J.; Nowaczyk, K. Plasmon-controlled fluorescence: a new paradigm in fluorescence spectroscopy. *The Analyst* **2008**, *133*, 1308.
150. Zakharko, Y.; Nychyporuk, T.; Bonacina, L.; Lemiti, M.; Lysenko, V. Plasmon-enhanced nonlinear optical properties of SiC nanoparticles. *Nanotechnology* **2013**, *24*, 055703.
151. Jain, P.K.; El-Sayed, I.H.; El-Sayed, M.A. Au nanoparticles target cancer. *Nano Today* **2007**, *2*, 18–29.
152. Jin, R.; Wu, G.; Li, Z.; Mirkin, C.A.; Schatz, G.C. What Controls the Melting Properties of DNA-Linked Gold Nanoparticle Assemblies? *J. Am. Chem. Soc.* **2003**, *125*, 1643–1654.
153. Daniel, M.-C.; Astruc, D. Gold nanoparticles: assembly, supramolecular chemistry, quantum-size-related properties, and applications toward biology, catalysis, and nanotechnology. *Chem. Rev.* **2004**, *104*, 293–346.
154. Chen, M.; Goodman, D.W. Catalytically Active Gold: From Nanoparticles to Ultrathin Films. *Acc. Chem. Res.* **2006**, *39*, 739–746.
155. Lee, M.-K.; Kim, T.G.; Kim, W.; Sung, Y.-M. Surface Plasmon Resonance (SPR) Electron and Energy Transfer in Noble Metal–Zinc Oxide Composite Nanocrystals. *J. Phys. Chem. C* **2008**, *112*, 10079–10082.
156. Cheng, C.W.; Sie, E.J.; Liu, B.; Huan, C.H.A.; Sum, T.C.; Sun, H.D.; Fan, H.J. Surface plasmon enhanced band edge luminescence of ZnO nanorods by capping Au nanoparticles. *Appl. Phys. Lett.* **2010**, *96*, 071107.
157. Bera, A.; Basak, D. Pd-nanoparticle-decorated ZnO nanowires: ultraviolet photosensitivity and photoluminescence properties. *Nanotechnology* **2011**, *22*, 265501.
158. Wang, J.Q.; Luo, J.; Fan, Q.; Suzuki, M.; Suzuki, I.S.; Engelhard, M.H.; Lin, Y.; Kim, N.; Zhong, C.-J. Monodispersed Core–Shell Fe<sub>3</sub>O<sub>4</sub>@Au Nanoparticles. *J. Phys. Chem. B* **2005**, *109*, 21593–21601.
159. Banerjee, S.; Raja, S.O.; Sardar, M.; Gayathri, N.; Ghosh, B.; Dasgupta, A. Iron oxide nanoparticles coated with gold: Enhanced magnetic moment due to interfacial effects. *J. Appl. Phys.* **2011**, *109*, 123902.
160. He, Y.; Zhu, K.-D. Strong coupling among semiconductor quantum dots induced by a metal nanoparticle. *Nanoscale Res. Lett.* **2012**, *7*.
161. Sun, Z.; Yang, Z.; Zhou, J.; Yeung, M.H.; Ni, W.; Wu, H.; Wang, J. A General Approach to the Synthesis of Gold-Metal Sulfide Core-Shell and Heterostructures. *Angew. Chem. Int. Ed.* **2009**, *48*, 2881–2885.
162. Ha, J.W.; Ruberu, T.P.A.; Han, R.; Dong, B.; Vela, J.; Fang, N. Super-Resolution Mapping of Photogenerated Electron and Hole Separation in Single Metal–Semiconductor Nanocatalysts. *J. Am. Chem. Soc.* **2014**, *136*, 1398–1408.

163. Rahman, D.S.; Ghosh, S.K. Manipulating Electron Transfer in Hybrid ZnO–Au Nanostructures: Size of Gold Matters. *J. Phys. Chem. C* **2016**, *120*, 14906–14917.
164. Eustis, S.; El-Sayed, M.A. Why gold nanoparticles are more precious than pretty gold: Noble metal surface plasmon resonance and its enhancement of the radiative and nonradiative properties of nanocrystals of different shapes. *Chem Soc Rev* **2006**, *35*, 209–217.
165. Ingram, D.B.; Linic, S. Water Splitting on Composite Plasmonic-Metal/Semiconductor Photoelectrodes: Evidence for Selective Plasmon-Induced Formation of Charge Carriers near the Semiconductor Surface. *J. Am. Chem. Soc.* **2011**, *133*, 5202–5205.
166. Wang, X.; Kong, X.; Yu, Y.; Zhang, H. Synthesis and Characterization of Water-Soluble and Bifunctional ZnO–Au Nanocomposites. *J. Phys. Chem. C* **2007**, *111*, 3836–3841.
167. Sukharev, M.; Day, P.N.; Pachter, R. Optical Response of Hybrid Plasmon–Exciton Nanomaterials in the Presence of Overlapping Resonances. *ACS Photonics* **2015**, *2*, 935–941.
168. Storhoff, J.J.; Lazarides, A.A.; Mucic, R.C.; Mirkin, C.A.; Letsinger, R.L.; Schatz, G.C. What Controls the Optical Properties of DNA-Linked Gold Nanoparticle Assemblies? *J. Am. Chem. Soc.* **2000**, *122*, 4640–4650.
169. Lee, K.-S.; El-Sayed, M.A. Gold and Silver Nanoparticles in Sensing and Imaging: Sensitivity of Plasmon Response to Size, Shape, and Metal Composition. *J. Phys. Chem. B* **2006**, *110*, 19220–19225.
170. Shimizu, K.T.; Woo, W.K.; Fisher, B.R.; Eisler, H.J.; Bawendi, M.G. Surface-Enhanced Emission from Single Semiconductor Nanocrystals. *Phys. Rev. Lett.* **2002**, *89*.
171. Kulakovich, O.; Strelak, N.; Yaroshevich, A.; Maskevich, S.; Gaponenko, S.; Nabiev, I.; Woggon, U.; Artemyev, M. Enhanced Luminescence of CdSe Quantum Dots on Gold Colloids. *Nano Lett.* **2002**, *2*, 1449–1452.
172. Song, J.-H.; Atay, T.; Shi, S.; Urabe, H.; Nurmikko, A.V. Large enhancement of fluorescence efficiency from CdSe/ZnS quantum dots induced by resonant coupling to spatially controlled surface plasmons. *Nano Lett.* **2005**, *5*, 1557–1561.
173. Biteen, J.S.; Pacifici, D.; Lewis, N.S.; Atwater, H.A. Enhanced Radiative Emission Rate and Quantum Efficiency in Coupled Silicon Nanocrystal-Nanostructured Gold Emitters. *Nano Lett.* **2005**, *5*, 1768–1773.
174. Gersten, J.; Nitzan, A. Electromagnetic theory of enhanced Raman scattering by molecules adsorbed on rough surfaces. *J. Chem. Phys.* **1980**, *73*, 3023–3037.
175. Champion, A.; Gallo, A.R.; Harris, C.B.; Robota, H.J.; Whitmore, P.M. Electronic energy transfer to metal surfaces: a test of classical image dipole theory at short distances. *Chem. Phys. Lett.* **1980**, *73*, 447–450.
176. Hayakawa, T.; Selvan, S.T.; Nogami, M. Field enhancement effect of small Ag particles on the fluorescence from Eu<sup>3+</sup>-doped SiO<sub>2</sub> glass. *Appl. Phys. Lett.* **1999**, *74*, 1513–1515.

177. Das, P.; Metiu, H. Enhancement of molecular fluorescence and photochemistry by small metal particles. *J. Phys. Chem.* **1985**, *89*, 4680–4687.
178. Viste, P.; Plain, J.; Jaffiol, R.; Vial, A.; Adam, P.M.; Royer, P. Enhancement and Quenching Regimes in Metal–Semiconductor Hybrid Optical Nanosources. *ACS Nano* **2010**, *4*, 759–764.
179. Guidelli, E.J.; Baffa, O.; Clarke, D.R. Enhanced UV Emission From Silver/ZnO And Gold/ZnO Core-Shell Nanoparticles: Photoluminescence, Radioluminescence, And Optically Stimulated Luminescence. *Sci. Rep.* **2015**, *5*.
180. Lai, C.W.; An, J.; Ong, H.C. Surface-plasmon-mediated emission from metal-capped ZnO thin films. *Appl. Phys. Lett.* **2005**, *86*, 251105.
181. Chen, C.W.; Wang, C.H.; Wei, C.M.; Chen, Y.F. Tunable emission based on the composite of Au nanoparticles and CdSe quantum dots deposited on elastomeric film. *Appl. Phys. Lett.* **2009**, *94*, 071906.
182. Nikoobakht, B.; Burda, C.; Braun, M.; Hun, M.; El-Sayed, M.A. The Quenching of CdSe Quantum Dots Photoluminescence by Gold Nanoparticles in Solution¶. *Photochem. Photobiol.* **2007**, *75*, 591–597.
183. Gueroui, Z.; Libchaber, A. Single-Molecule Measurements of Gold-Quenched Quantum Dots. *Phys. Rev. Lett.* **2004**, *93*.
184. Anger, P.; Bharadwaj, P.; Novotny, L. Enhancement and Quenching of Single-Molecule Fluorescence. *Phys. Rev. Lett.* **2006**, *96*.
185. Thomas, M.; Greffet, J.-J.; Carminati, R.; Arias-Gonzalez, J.R. Single-molecule spontaneous emission close to absorbing nanostructures. *Appl. Phys. Lett.* **2004**, *85*, 3863–3865.
186. Pompa, P.P.; Martiradonna, L.; Torre, A.D.; Sala, F.D.; Manna, L.; De Vittorio, M.; Calabi, F.; Cingolani, R.; Rinaldi, R. Metal-enhanced fluorescence of colloidal nanocrystals with nanoscale control. *Nat. Nanotechnol.* **2006**, *1*, 126–130.
187. Chen, Y.; Munechika, K.; Ginger, D.S. Dependence of Fluorescence Intensity on the Spectral Overlap between Fluorophores and Plasmon Resonant Single Silver Nanoparticles. *Nano Lett.* **2007**, *7*, 690–696.
188. Munechika, K.; Chen, Y.; Tillack, A.F.; Kulkarni, A.P.; Plante, I.J.-L.; Munro, A.M.; Ginger, D.S. Spectral Control of Plasmonic Emission Enhancement from Quantum Dots near Single Silver Nanoprisms. *Nano Lett.* **2010**, *10*, 2598–2603.
189. Okamoto, K.; Niki, I.; Shvartser, A.; Narukawa, Y.; Mukai, T.; Scherer, A. Surface-plasmon-enhanced light emitters based on InGaN quantum wells. *Nat. Mater.* **2004**, *3*, 601–605.
190. Ni, W.H.; An, J.; Lai, C.W.; Ong, H.C.; Xu, J.B. Emission enhancement from metallodielectric-capped ZnO films. *J. Appl. Phys.* **2006**, *100*, 026103.

191. Cheng, D.; Xu, Q.-H. Separation distance dependent fluorescence enhancement of fluorescein isothiocyanate by silver nanoparticles. *Chem Commun* **2007**, 248–250.
192. Cheng, P.; Li, D.; Yuan, Z.; Chen, P.; Yang, D. Enhancement of ZnO light emission via coupling with localized surface plasmon of Ag island film. *Appl. Phys. Lett.* **2008**, *92*, 041119.
193. Lakowicz, J.R. Radiative decay engineering 5: metal-enhanced fluorescence and plasmon emission. *Anal. Biochem.* **2005**, *337*, 171–194.
194. Ito, Y.; Matsuda, K.; Kanemitsu, Y. Mechanism of photoluminescence enhancement in single semiconductor nanocrystals on metal surfaces. *Phys. Rev. B* **2007**, *75*.
195. Matsuda, K.; Ito, Y.; Kanemitsu, Y. Photoluminescence enhancement and quenching of single CdSe/ZnS nanocrystals on metal surfaces dominated by plasmon resonant energy transfer. *Appl. Phys. Lett.* **2008**, *92*, 211911.
196. Hsieh, Y.-P.; Liang, C.-T.; Chen, Y.-F.; Lai, C.-W.; Chou, P.-T. Mechanism of giant enhancement of light emission from Au/CdSe nanocomposites. *Nanotechnology* **2007**, *18*, 415707.
197. Zhou, X.D.; Xiao, X.H.; Xu, J.X.; Cai, G.X.; Ren, F.; Jiang, C.Z. Mechanism of the enhancement and quenching of ZnO photoluminescence by ZnO-Ag coupling. *EPL Europhys. Lett.* **2011**, *93*, 57009.
198. Okamoto, K.; Niki, I.; Scherer, A.; Narukawa, Y.; Mukai, T.; Kawakami, Y. Surface plasmon enhanced spontaneous emission rate of InGaN/GaN quantum wells probed by time-resolved photoluminescence spectroscopy. *Appl. Phys. Lett.* **2005**, *87*, 071102.
199. Lin, J.M.; Lin, H.Y.; Cheng, C.L.; Chen, Y.F. Giant enhancement of bandgap emission of ZnO nanorods by platinum nanoparticles. *Nanotechnology* **2006**, *17*, 4391–4394.
200. Neogi, A.; Lee, C.-W.; Everitt, H.O.; Kuroda, T.; Tackeuchi, A.; Yablonovitch, E. Enhancement of spontaneous recombination rate in a quantum well by resonant surface plasmon coupling. *Phys. Rev. B* **2002**, *66*.
201. Asok, A.; Kulkarni, A.R.; Gandhi, M.N. Defect rich seed mediated growth: a novel synthesis method to enhance defect emission in nanocrystals. *J Mater Chem C* **2014**, *2*, 1691–1697.
202. Zhang, D.; Wang, P.; Murakami, R.; Song, X. Effect of an interface charge density wave on surface plasmon resonance in ZnO/Ag/ZnO thin films. *Appl. Phys. Lett.* **2010**, *96*, 233114.
203. He, W.; Kim, H.-K.; Wamer, W.G.; Melka, D.; Callahan, J.H.; Yin, J.-J. Photogenerated Charge Carriers and Reactive Oxygen Species in ZnO/Au Hybrid Nanostructures with Enhanced Photocatalytic and Antibacterial Activity. *J. Am. Chem. Soc.* **2014**, *136*, 750–757.

204. Rummyantseva, A.; Kostcheev, S.; Adam, P.-M.; Gaponenko, S.V.; Vaschenko, S.V.; Kulakovich, O.S.; Ramanenka, A.A.; Guzatov, D.V.; Korbutyak, D.; Dzhagan, V.; et al. Nonresonant Surface-Enhanced Raman Scattering of ZnO Quantum Dots with Au and Ag Nanoparticles. *ACS Nano* **2013**, *7*, 3420–3426.
205. Duan, G.; Cai, W.; Luo, Y.; Li, Z.; Li, Y. Electrochemically induced flowerlike gold nanoarchitectures and their strong surface-enhanced Raman scattering effect. *Appl. Phys. Lett.* **2006**, *89*, 211905.
206. Qian, L.H.; Yan, X.Q.; Fujita, T.; Inoue, A.; Chen, M.W. Surface enhanced Raman scattering of nanoporous gold: Smaller pore sizes stronger enhancements. *Appl. Phys. Lett.* **2007**, *90*, 153120.
207. Lee, S.J.; Morrill, A.R.; Moskovits, M. Hot Spots in Silver Nanowire Bundles for Surface-Enhanced Raman Spectroscopy. *J. Am. Chem. Soc.* **2006**, *128*, 2200–2201.
208. Félidj, N.; Aubard, J.; Lévi, G.; Krenn, J.R.; Hohenau, A.; Schider, G.; Leitner, A.; Aussenegg, F.R. Optimized surface-enhanced Raman scattering on gold nanoparticle arrays. *Appl. Phys. Lett.* **2003**, *82*, 3095–3097.
209. Duan, G.; Cai, W.; Luo, Y.; Li, Y.; Lei, Y. Hierarchical surface rough ordered Au particle arrays and their surface enhanced Raman scattering. *Appl. Phys. Lett.* **2006**, *89*, 181918.
210. Damen, T.C.; Porto, S.P.S.; Tell, B. Raman Effect in Zinc Oxide. *Phys. Rev.* **1966**, *142*, 570–574.
211. Scott, J.F. uv Resonant Raman Scattering in ZnO. *Phys. Rev. B* **1970**, *2*, 1209–1211.
212. Sakano, T.; Tanaka, Y.; Nishimura, R.; Nedyalkov, N.N.; Atanasov, P.A.; Saiki, T.; Obara, M. Surface enhanced Raman scattering properties using Au-coated ZnO nanorods grown by two-step, off-axis pulsed laser deposition. *J. Phys. Appl. Phys.* **2008**, *41*, 235304.
213. Han, X.X.; Ji, W.; Zhao, B.; Ozaki, Y. Semiconductor-enhanced Raman scattering: active nanomaterials and applications. *Nanoscale* **2017**, *9*, 4847–4861.
214. Govorov, A.O.; Bryant, G.W.; Zhang, W.; Skeini, T.; Lee, J.; Kotov, N.A.; Slocik, J.M.; Naik, R.R. Exciton–Plasmon Interaction and Hybrid Excitons in Semiconductor–Metal Nanoparticle Assemblies. *Nano Lett.* **2006**, *6*, 984–994.
215. Das, G.; Chakraborty, R.; Gopalakrishnan, A.; Baranov, D.; Di Fabrizio, E.; Krahne, R. A new route to produce efficient surface-enhanced Raman spectroscopy substrates: gold-decorated CdSe nanowires. *J. Nanoparticle Res.* **2013**, *15*.
216. Selinsky, R.S.; Ding, Q.; Faber, M.S.; Wright, J.C.; Jin, S. Quantum dot nanoscale heterostructures for solar energy conversion. *Chem Soc Rev* **2013**, *42*, 2963–2985.
217. Yu, J.; Xiang, Q.; Zhou, M. Preparation, characterization and visible-light-driven photocatalytic activity of Fe-doped titania nanorods and first-principles study for electronic structures. *Appl. Catal. B Environ.* **2009**, *90*, 595–602.

218. Lesnyak, V.; Gaponik, N.; Eychmüller, A. Colloidal semiconductor nanocrystals: the aqueous approach. *Chem Soc Rev* **2013**, *42*, 2905–2929.
219. Mishra, N. Metal–Semiconductor Hybrid Nano-Heterostructures for Photocatalysis Application. In *Semiconductor Photocatalysis - Materials, Mechanisms and Applications*; Cao, W., Ed.; InTech, 2016 ISBN 978-953-51-2484-9.
220. Zheng, Y.; Chen, C.; Zhan, Y.; Lin, X.; Zheng, Q.; Wei, K.; Zhu, J. Photocatalytic Activity of Ag/ZnO Heterostructure Nanocatalyst: Correlation between Structure and Property. *J. Phys. Chem. C* **2008**, *112*, 10773–10777.
221. Iliev, V.; Tomova, D.; Bilyarska, L.; Eliyas, A.; Petrov, L. Photocatalytic properties of TiO<sub>2</sub> modified with platinum and silver nanoparticles in the degradation of oxalic acid in aqueous solution. *Appl. Catal. B Environ.* **2006**, *63*, 266–271.
222. Green, M.A. Third generation photovoltaics: comparative evaluation of advanced solar conversion options. In Proceedings of the Conference Record of the Twenty-Ninth IEEE Photovoltaic Specialists Conference, 2002.; IEEE: New Orleans, LA, USA, 2002; pp. 1330–1334.
223. Hoffmann, M.R.; Martin, S.T.; Choi, W.; Bahnemann, D.W. Environmental Applications of Semiconductor Photocatalysis. *Chem. Rev.* **1995**, *95*, 69–96.
224. Gao, Z.-D.; Liu, H.-F.; Li, C.-Y.; Song, Y.-Y. Biotemplated synthesis of Au nanoparticles–TiO<sub>2</sub> nanotube junctions for enhanced direct electrochemistry of heme proteins. *Chem Commun* **2013**, *49*, 774–776.
225. Zhang, X.; Li, J.; Lu, X.; Tang, C.; Lu, G. Visible light induced CO<sub>2</sub> reduction and Rh B decolorization over electrostatic-assembled AgBr/palygorskite. *J. Colloid Interface Sci.* **2012**, *377*, 277–283.
226. Seh, Z.W.; Liu, S.; Low, M.; Zhang, S.-Y.; Liu, Z.; Mlayah, A.; Han, M.-Y. Janus Au-TiO<sub>2</sub> Photocatalysts with Strong Localization of Plasmonic Near-Fields for Efficient Visible-Light Hydrogen Generation. *Adv. Mater.* **2012**, *24*, 2310–2314.
227. Cozzoli, P.D.; Comparelli, R.; Fanizza, E.; Curri, M.L.; Agostiano, A.; Laub, D. Photocatalytic Synthesis of Silver Nanoparticles Stabilized by TiO<sub>2</sub> Nanorods: A Semiconductor/Metal Nanocomposite in Homogeneous Nonpolar Solution. *J. Am. Chem. Soc.* **2004**, *126*, 3868–3879.
228. Zheng, Y.; Zheng, L.; Zhan, Y.; Lin, X.; Zheng, Q.; Wei, K. Ag/ZnO Heterostructure Nanocrystals: Synthesis, Characterization, and Photocatalysis. *Inorg. Chem.* **2007**, *46*, 6980–6986.
229. Gu, C.; Cheng, C.; Huang, H.; Wong, T.; Wang, N.; Zhang, T.-Y. Growth and Photocatalytic Activity of Dendrite-like ZnO@Ag Heterostructure Nanocrystals. *Cryst. Growth Des.* **2009**, *9*, 3278–3285.
230. Peh, C.K.N.; Ke, L.; Ho, G.W. Modification of ZnO nanorods through Au nanoparticles surface coating for dye-sensitized solar cells applications. *Mater. Lett.* **2010**, *64*, 1372–1375.

231. George, C.; Genovese, A.; Qiao, F.; Korobchevskaya, K.; Comin, A.; Falqui, A.; Marras, S.; Roig, A.; Zhang, Y.; Krahn, R.; et al. Optical and electrical properties of colloidal (spherical Au)-(spinel ferrite nanorod) heterostructures. *Nanoscale* **2011**, *3*, 4647.
232. Mahanti, M.; Basak, D. Highly enhanced UV emission due to surface plasmon resonance in Ag-ZnO nanorods. *Chem. Phys. Lett.* **2012**, *542*, 110–116.
233. Zhang, Z.; Zhang, L.; Hedhili, M.N.; Zhang, H.; Wang, P. Plasmonic Gold Nanocrystals Coupled with Photonic Crystal Seamlessly on TiO<sub>2</sub> Nanotube Photoelectrodes for Efficient Visible Light Photoelectrochemical Water Splitting. *Nano Lett.* **2013**, *13*, 14–20.
234. Bian, J.-C.; Yang, F.; Li, Z.; Zeng, J.-L.; Zhang, X.-W.; Chen, Z.-D.; Tan, J.Z.Y.; Peng, R.-Q.; He, H.-Y.; Wang, J. Mechanisms in photoluminescence enhancement of ZnO nanorod arrays by the localized surface plasmons of Ag nanoparticles. *Appl. Surf. Sci.* **2012**, *258*, 8548–8551.

## 2. Chapter 2 Synthesis and characterization of pure ZnO nanostructures highly efficient for photocatalysis

### 2.1 Introduction

In recent years, the fabrication of ZnO QDs with an efficient photocatalytic activity has been emerging at the level of science and technology due to their unusual photonic functions, triggering them to have valuable roles in fundamental studies and technical applications [1]. These semiconducting nano-scaled systems have received growing interest due to their optical and electronic traits [2–5]. They have enhanced quantum efficiency and a tunable band gap [6], which enable them to participate in wide fields of applications, favoring the catalytic, optoelectronic and biomedical operations [7–9]. Also, luminescent QDs can be used as chemical sensors, responding selectively to many influential metal cations and anions after conjugating the QDs surface with a suitable ligand [10].

Many synthesis pathways were adapted to fabricate ZnO QDs. Some of these methods are tabulated in Table 2.

Table 2 List of some synthesis methods for crystalline ZnO nanostructures

Synthesis Method	Reference
Vapor phase oxidation	[11]
Thermal vapor transport and condensation (TVTC)	[12,13]
Micro-emulsion	[14]
Polyol methods	[15]
Sol-gel method	[1,16–18]
Sonochemical or microwave-assisted synthesis	[19–23]
Spray pyrolysis	[24]
Chemical vapor deposition	[25,26]
Thermal decomposition of organic precursor	[27]
Direct precipitation	[28]
Double solvothermal method	[29]
Hydrothermal synthesis	[30–36]

Although these methods are very useful, yet most of these approaches require complicated processes. They also involve complex and sophisticated equipment, toxic reactants such as lithium hydroxide (LiOH) as an oxygen source [23,37], and deteriorating organic solvents such as methanol, 2-methoxyethanol, or chloroform- instead of water. The synthesis of ZnO nanostructures in alcoholic media has received extensive acceptance because of the faster nucleation and growth of NPs in such solvents as compared to water. The latter was generally avoided because it facilitates the transfer of the excited charge carriers of the corresponding NPs to the surrounding molecules leading to its luminescence quenching. Due to the high surface tension of ZnO QDs, surfactant-assisted synthesis that required capping or stabilizing agents such as poly vinyl pyridine (PVP), polyethylene glycol (PEG), etc., were used in order to obtain small, spherical, and non-aggregated nanoparticles [38,39]. The utilization of these additives induces large amount of organic impurities complexing the chemistry of the reaction, and restricting the accessibility to the nanocrystal surface. Hu *et al.* used the vapor-phase oxidation method to synthesize ZnO whiskers [11]. This process involves multi-steps to achieve the final product, as well as hard reaction conditions that require high temperatures and pressures to obtain ZnO nanostructures. This process is energy consuming, and the control over the size of the produced nanocrystals is found to be difficult at such conditions. In another reports, Rani *et al.* have used methanol solvent through the sol-gel method to produce ZnO nanocrystals [16]. This solvent is environmentally non-friendly as it is considered flammable and poisonous chemical. Moreover, it is corrosive to some metals which bothers the doping of the synthesized NCs by metals to enhance their luminescence or improve their applications. On the other hand, Asok *et al.* have used microwave assisted synthesis to produce ZnO QDs [23]. Although this process is time saving and could be achieved in few minutes, yet the starting material LiOH used as an oxygen precursor is a toxic reagent, by which the lithium atom is considered as highly reactive and flammable, especially under high power reactions as in the microwave synthesis. Add to that, the high power synthesis stimulates the increase in the heating rate resulting in the reaction overheating. This will lack the control over the temperature, ending up in the formation of unstable products.

Among all the cited synthesis techniques, the hydrothermal method is a promising synthetic pathway, because it is a simple apparatus process that could be carried out under moderate conditions. Its obtained products more likely have different properties from those obtained at high temperatures and pressures. Furthermore, it is economical, catalyst-free, and environmentally the less hazardous synthesis protocol. Moreover, it is an easy way to control

over the particle's size and morphology, by which the nano-scaled particles of different morphology forms could be realized by adjusting the reaction conditions, in the time where the size and shape control has raised an extensive interest.

Lu *et al.* hydrothermally prepared crystalline ZnO powder using zinc nitrate and ammonia at different temperatures. The effect of growth temperature and pH was studied, and the obtained particles transformed from spherical to rod like microstructures with increasing the pH in the reaction mixture. The small nanometric scaled particles were difficult to attain [33]. Baruwati *et al.* have reported the aqueous synthesis of ZnO in an autoclave at a temperature of 120°C using ammonium hydroxide to adjust the pH [32]. The supported method is relatively time consuming since it needs an overnight drying to obtain the desired final product. Chen *et al.* have synthesized different morphologies of ZnO nanoparticles using ZnCl<sub>2</sub> and NaOH in a hydrothermal growth process, using several organic templates to control the size of the obtained nanostructures [34]. Different morphologies of ZnO powders were synthesized by Wirunmongkol *et al.*, and the obtained particles were prism-like shape with hexagonal phase of a large size about 0.3-0.5 μm in width, and 0.5-0.7 μm in length [35]. 10 to 20 nm ZnO nanoparticles were precipitated at room temperature by Musić *et al.* through the addition of TMAH to an ethanolic solution of zinc acetate dehydrate. The pH of the reaction was indeed high (~14) to obtain the desired size and shape [36]. Moussodia *et al.* have modified the ZnO NPs surface by the silanization method in order to obtain a water soluble and stable product useful for biological labels [40]. They covalently linked the ZnO surface by a PEG-siloxane where the aim of the surface modification was to maintain the surface luminescence properties of the synthesized ZnO QDs that may be struck and destroyed by the water molecules. However, the initial synthesis was carried out in alcoholic medium, and the final obtained product was not absolutely pure as they introduced organic molecules throughout the fabrication process, in the time homogeneous and pure nanomaterials are needed as a result for various applications. In another reports concerning the fabrication of water soluble ZnO QDs, Fu *et al.* have synthesized water-stable ZnO QDs. The addition of oleic acid and/or diethanoamine (DEA) was indeed to adopt high stability and water dispersion availability preserving the intensity fluorescence property [41].

Despite the excessive efforts to fabricate ultra-small, efficient catalyst and luminescent quantum dots in aqueous solutions, no research has so far achieved this performant product of nanocrystalline ZnO QDs, *via* simple synthesis route and under soft conditions including

temperature, pressure, time, equipment used, and materials. Precisely, “aqueous solution-based” hydrothermal methods are commercially profitable for massive production with good consistency and can be manipulated at easy settings. The hydrothermal aqueous route represents a simple way for large-scale particles production at low cost without requiring expensive and toxic raw materials or complex equipment. It is an attractive method of fabrication because it is easy to perform, and allows tailoring the morphology of the desired particles in a facile, cheap, and eco-friendly approach for ZnO QDs synthesis. Moreover, previous reports have shown that nanocrystalline ZnO have two faults which limit their functional applications [42]. They have proved that due to their large specific area and surface activity, ZnO nanocrystals are unstable and have the ability to highly aggregate. Another disadvantage was that the suspended nanocrystals could be quickly lost during the reaction making the ZnO NCs not accessible for practical operations. Consequently, still scattered reports of hydrothermal synthesis of stable ZnO QDs in aqueous medium are available in the literature.

In most current fabrication methods, a high temperature procedure, either at high temperature fabrication process or high temperature post-synthesis treatment of the ZnO is needed for attaining good quality material [43]. On the other hand, applied science is currently recommending plastics and flexible electronics [44–46], which emphasizes on the necessity of adapting alternate treatment processes that ensure the synthesis of well crystalline ZnO nanostructures keeping the temperature at the low value [47].

In the present research study, small, uniform and highly stable ZnO NPs were fabricated using water as a non-contaminating solvent that acts as a self-capping, stabilizing and directing agent, where the nanocrystals’ shape and size could be controlled. This method is a promising alternative guide for preparation of pure ZnO NPs at a relatively low temperature using soft conditions. It is simple, green, and high throughput method, in addition to the good stability and purity of products, where these properties are necessary for photocatalytic and biological purposes

Although, ZnO luminescence has been the subject of studies for several decades where the mechanisms responsible for many of its emission properties in relation to its photocatalytic activity are still a matter of discussion. To our knowledge, no reports in the literature have succeeded to aqueously fabricate highly luminescent ZnO NPs with high photocatalytic activities, since the photocatalysis (PC) and the photoluminescence (PL) are two processes that

depend respectively on the separation and recombination of the photo-induced charge carriers which are competitive mechanisms. In this work, we efficiently describe how imprinting procedures can be adapted for ZnO NPs synthesis, serving as a model system for other oxide nanostructures synthesized in water, and the optical characterizations could be successfully attained.

## **2.2 Experimental part**

In quantum mechanics, the optical and electronic characteristics of ZnO QDs are obviously determined by the experimental conditions used in the fabrication method as the solvent, heating temperature, time of the reaction, precursor's concentrations, etc. These parameters highly affect the final structure of the products (size, morphology, surface structure, etc.), tailoring the materials properties. The aim of the present work is to investigate the influence of synthesis procedures on the formation and properties of ZnO NCs with evident exciton emission. Therefore the photoluminescence measurements were the guideline of setting up the starting conditions of our reaction.

The characterization techniques are described in details in Appendix-B in chapter 5.

### **2.2.1 Synthesis process**

The chemical reagents adapted as starting materials for the formation of ZnO QDs in this synthesis process were zinc nitrate hexahydrate, 98% extra pure ( $\text{Zn}(\text{NO}_3)_2 \cdot 6\text{H}_2\text{O}$ ) as zinc precursor, and sodium hydroxide (NaOH) as an oxygen source purchased from ACROS ORGANICS and FISHER SCIENTIFIC respectively. All these chemicals were used as purchased without further purification. The water used throughout all the experiments was adapted from a water purification system Milli-Di (9V-1W) as deionized water ( $> 1\text{M}\Omega \cdot \text{cm}$  @25°C).

#### **2.2.1.1 Preparation of stock solutions (Zn and O sources)**

The zinc nitrate stock solution and the sodium hydroxide stock solution were prepared in deionized water. Three molar concentrations (0.1, 0.5 and 1 M) of each stock solution was prepared. These aqueous solutions were prepared by constant stirring at 350 rpm using magnetic stirrer without any heating step for ~30 min to completely achieve the suspension of the precursors and to obtain clear and transparent solutions.

### 2.2.1.2 Preparation of ZnO QDs seeds

Equal volumes of equimolar stock solutions were added up together in a flask, *i.e.* a volume of 0.1 M NaOH is added to the same volume of 0.1 M  $\text{Zn}(\text{NO}_3)_2 \cdot 6\text{H}_2\text{O}$  to form the seed solution A1'. The same process is repeated with the 0.5 M and 1 M for the seed solution A2' and A3', respectively, which contain equal molarities and volumes of  $\text{Zn}(\text{NO}_3)_2 \cdot 6\text{H}_2\text{O}$  and NaOH stock solutions. After the addition of NaOH to the zinc nitrate solution, a direct formation of white precipitate was observed. Then, the solution separated into two phases: a white bottom layer including ZnO clusters embedded in a complex structure, and an upper suspension that was nearly transparent including very small quantity of ZnO QDs. The quantity of the white precipitate in A3' was larger than that in A2' and A1' where the latter had a very low quantity which was difficult to collect. This is related to the concentrations of the stock solutions used by which the highest concentrations lead to the high production of ZnO powders. The samples A1', A2', and A3' were heated at 80°C for 20 min with stirring at 350 rpm on a normal heating plate. During the reaction, the solutions were covered to prevent the oxygen of the atmospheric air to contribute in the reaction, minimizing the excess formation of defects in the crystal structures. Annealing of the ZnO product after cooling to room temperature was indeed in order to crystallize ZnO. The post-thermal treatment was achieved for 1 hr at 150°C even before filtration of the obtained powders or after (see discussion part). The final obtained annealed raw material solutions (before filtration) of initial starting materials concentrations of 0.1, 0.5, and 1 M were named A1, A2, and A3, respectively. Figure 14 shows an image of the suspension A3 obtained to clarify the different supernatant and precipitate phases obtained in the reaction.

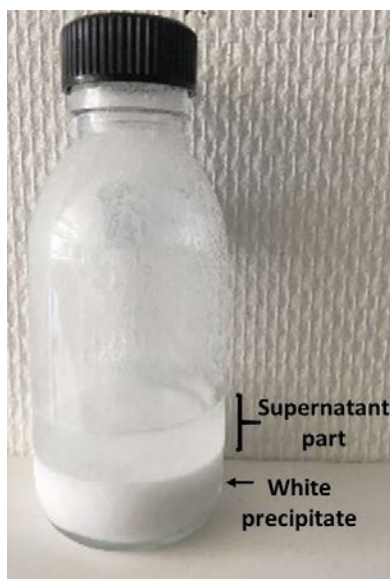
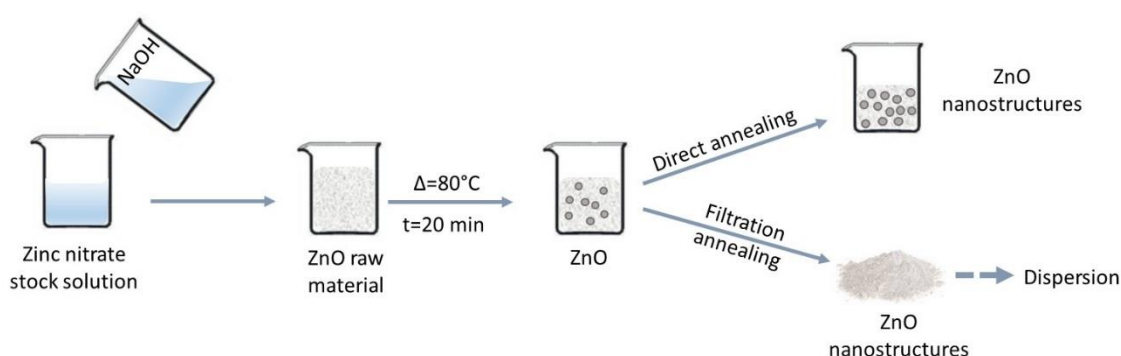


Figure 14 Image of the solution A3 after post-thermal treatment solution of as-synthesized QDs showing the two separated gradations: the transparent supernatant phase and the bottom white precipitate.

The raw powders were extracted by filtration before any annealing of the solution. After washing several times with D.I. water and isopropanol, the collected powders were annealed at different temperatures to gain more purity, increase the number of the synthesized ZnO nanostructures, and to enhance their crystallinity. The annealing was carried in an oven, for 1 hr and under air. The overall achieved powders were able to be embedded in several solvents such as water, isopropanol, ethanol, and others..., depending on the desired application. Through our study, the collected ZnO powders were dispersed in water. The whole synthesis process is illustrated in Scheme 9.



Scheme 9 Schematic diagram of the synthesis of ZnO NCs.

## 2.3 Results and discussion

### 2.3.1 Optimization of the synthesis reaction parameters

The interaction of materials with light is an important issue to study in order to qualify the studied material. Light absorption and emission (either spontaneous or stimulated) were intensively studied in quantum mechanics to optically characterize the transitions in the studied material. Exclusively, photoluminescence could serve as interesting candidate for this purpose because the luminescence is very sensitive to its surface state [48]. On this basis, our synthesis process was optimized according to the PL measurements that could be beneficial for characterizing the produced ZnO nanostructures. This process could supply a full study about the investigated materials, and gives valuable information about the morphology, as well as the optical and electronic properties of the materials. Add to that, it is useful in the field of

photocatalysis by supplying information about the surface of the materials (defects, oxygen vacancies, and recombination of photogenerated charge carriers...).

The photoemission study was aimed to examine the effects of the precursor concentrations, reaction time, and reaction temperature on the particle size and structure of ZnO nanocrystals.

### 2.3.1.1 Effect of raw materials concentration

As mentioned in the synthesis process, different yield production was obtained using different concentrations of zinc nitrate and sodium hydroxide as stock solutions. The simple conventional heating at 80°C for 20 min of the starting materials did not allow the observation of the exciton emission of the fabricated quantum dots (not shown here), unless an annealing step of the solutions was applied. The PL measurements of the post-thermally treated solutions are shown in Figure 15.

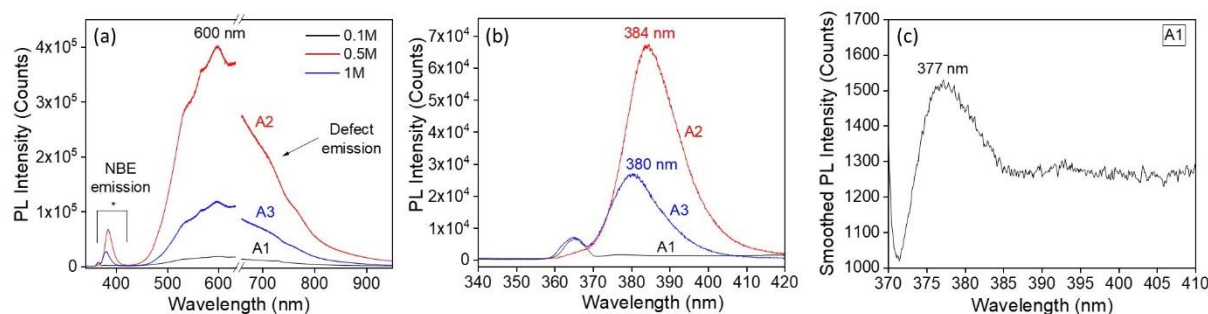


Figure 15 Photoluminescence measurements of different samples of ZnO QDs solutions (A1, A2 and A3) after annealing at 150°C (a) the full PL spectrum showing break line at the missing data points over the region of the second order of the laser. (b) ZnO UV region of the PL spectrum, (c) zoom in the UV-region of the smoothed PL spectrum of the solution A1 (0.1 M raw materials).

Figure 15 shows the typical PL spectra of different synthesized ZnO samples (A1, A2, and A3). From the PL results, it is clearly observed that the UV and visible PL intensities differs from one solution to another. Accordingly, each sample adapts a particular size, number, surface, and distribution of fabricated quantum dots. A2 has the highest emission intensities among all, where A3 has intermediate luminescence intensities, and A1 showed the lowest intensities.

ZnO photoluminescence here is marked by two regions. While the first is a confined peak corresponding to the near band edge (NBE) emission in the ultraviolet region of the emission spectrum, characterizing the exciton radiative recombination of the electrons and holes. The second is a large intense defect level band (DLB) in the visible zone [49–51]. All solutions

showed a broad peak in the visible region ranging from the green section to the orange zone of the visible area, and centered at ~600 nm. The contributions of the green luminescence is referred to the recombination of electrons in the singly ionized oxygen vacancies with photo-excited holes in the valence band [52–54]. Whereas the orange luminescence is attributed to the transition of electrons from the conduction band to the oxygen interstitials above the valence band [55]. The visible emission includes the yellow luminescence also, which is related to the presence of Zn(OH)<sub>2</sub> impurities at the surface of the NPs [56]. The presence of compounds other than pure ZnO is indeed in our raw material solutions (Zn<sub>5</sub>(NO<sub>3</sub>)<sub>2</sub>(OH)<sub>8</sub>.2H<sub>2</sub>O in our case) since the interacting precursors did not transform completely into ZnO, in addition, purification of the solutions was not carried on.

As shown in Figure 15(b), the intensity and position of UV emission was found to increase with increasing precursor concentrations up to 0.5 M, beyond which the intensity and positions diminishes for 1M precursor's concentrations. Kumar *et al.* has related the increase in the UV emission intensity to the reduction in the size of the particles whereby smaller nanoparticles involves more surface atoms that increases the rate of trapping of the photogenerated holes at the surface enhancing the emission intensity [54].

A2 have the most intense and wider UV emission, indicating the heterogeneous forms of the nanostructures. In addition, this sample showed the highest visible luminescence, thus it is the richest in defects among all. Although, solution A3 exhibits a clear exciton emission blue shifted with respect to that of A2 solution, in addition to moderate visible emission intensities corresponding to moderate defect levels in the fabricated particles. The blue shift in the exciton emission is referred to the size decrease. The smaller the nanoparticles are, the higher surface-to-volume ratio they have, leading to novel applications in electro-optical devices, chemical sensors, and making them more interesting in catalysis applications, where the photocatalytic degradation behaviors become much efficient for active and smaller sized particles.

Add to that, the powders produced in the solution A3 were the highest among all, which allowed the collection of more powders after filtration of the samples for further solid characterization indicating that sample A3 has the highest yield of production.

These output characters were the motive to adapt the synthesis of ZnO nanocrystal quantum dots using 1M stock solution precursor concentrations as starting materials. These conditions will be used in the coming studies and in the hybrids in the next chapters.

### 2.3.1.2 Role of synthesis time, temperature, and post-thermal treatment

Figure 16 displays typical UV photoluminescence spectra of the ZnO QDs formed when 1M  $\text{Zn}(\text{NO}_3)_2 \cdot 6\text{H}_2\text{O}$  and NaOH stock solutions are the starting materials in the synthesis process.

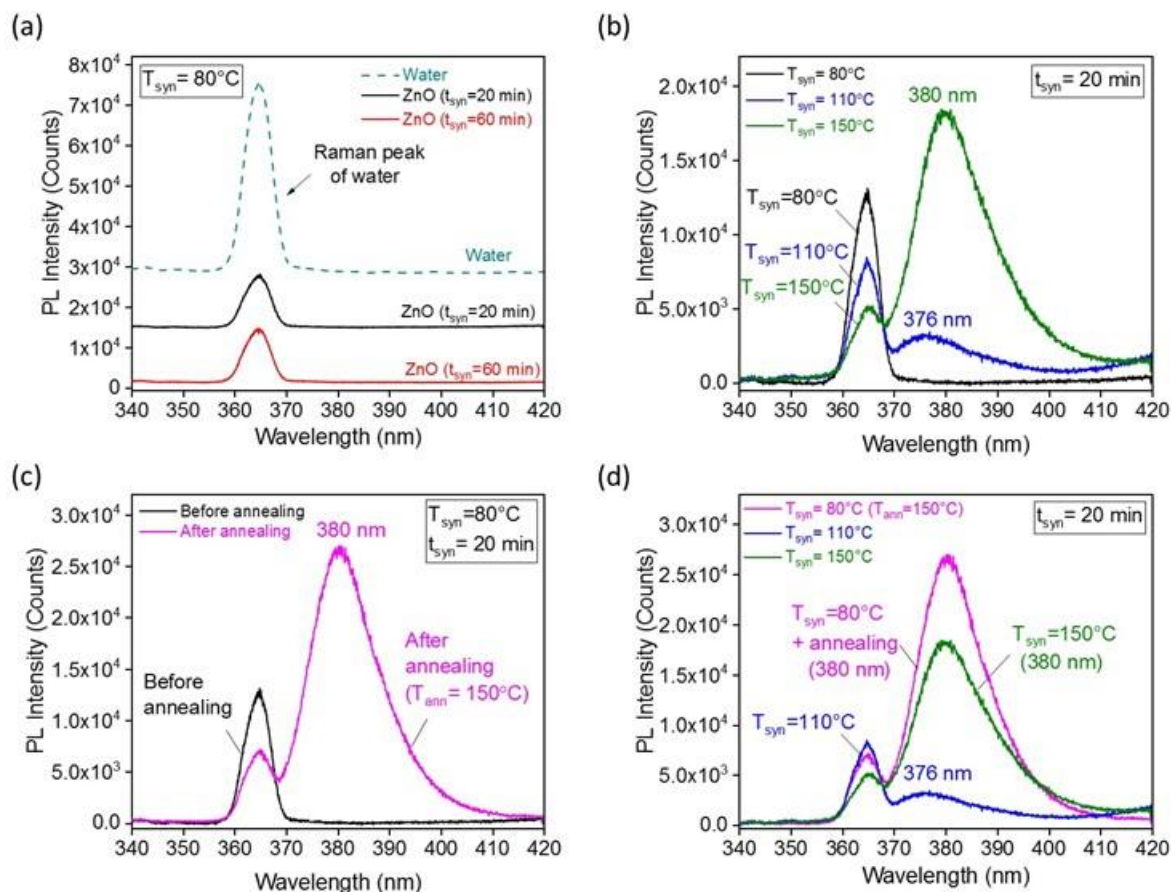


Figure 16 UV zone of the photoluminescence spectra of ZnO nanostructures in solution (a) effect of the time of the reaction carried on at 80°C, (b) Effect of the reaction temperature on the ZnO UV-emission lasting for 20 minutes, (c) Effect of 150°C annealing on the ZnO synthesis reaction done at 80°C for 20 minutes, (d) Sum-up of the reaction temperature conditions to obtain UV-exciton emission.

### 2.3.1.3 Effects of synthesis time

For examining the reaction time on the nanostructures of ZnO, the reaction temperature was fixed at 80°C, and the reaction time was prolonged from 20 min to 1 h, where the UV exciton luminescence of the ZnO nanostructures was examined.

The PL measurements of the as-synthesized NPs prepared at 80°C during 20 and 60 min reaction time show no obvious UV emission relative to the exciton luminescence in either condition. The only observed peak in the UV region is the Raman scattering of the water

solvent at  $\sim 365$  nm ( $3372$   $\text{cm}^{-1}$ ) while no emission band for ZnO NPs was observed (Figure 16 (a)). The peak located at 365 nm was identified to be a Raman signature of water, since this peak was also detected even from the deionized water alone. Therefore, extending the reaction time does not enhance the crystal growth of ZnO nanostructures to evidence their exciton emission. Energy transfer could also take place quenching the ZnO exciton emission, by which the water molecules may highly react with the NCs in the solution, transforming all the excitation energy between the surface water units to obtain the Raman scattering, preventing the ZnO electron excitation process as well as its luminescence. Consequently, the absence of this peak has been attributed to the overlapping of the Raman of the -OH group of the water solvent with the exciton of the ZnO NPs preventing its luminescence. In addition, ZnO NPs are considered as donors because they normally have luminescence in the UV-Vis region, while water is considered as an acceptor because it absorbs in the UV-Vis-NIR region. As reported by Meyer *et al.* and Dulub *et al.*, electron-hole pairs are generated in ZnO nanostructures upon UV illumination in the photoluminescence measurements, where the water molecules are physisorbed on the surface of the particles. The nearby water molecules on each neighboring ZnO NCs create a hydrogen bond between them, stimulating the dissociation of water units, which in turn capture these pairs at the same moment, leading to the decrease in the carrier density in the ZnO NPs. As a result, a gradual decay of the current through the charge transfer occurs, preventing the emission of the nanostructures [57–59]. In this context, the major concern in ZnO NPs is the diminishing luminescence of the nanoparticles due to the effect of the water solvent where the exchange of the ionic species at the oxygen defect levels in ZnO NPs leads to a slow photo-response [60]. Mahamuni *et al.* and Jin *et al.* referred the quenching of UV luminescence to the poor crystalline quality of the as-synthesized nanoparticles [61,62]. Vanheusden *et al.* and Hosono *et al.* also attributed that the UV-PL quenching is resulting from the poor quality of ZnO nanostructures [63,64].

In conclusion, the reaction time in our experiments has no considerable effects on building up ZnO NCs to differentiate its photoluminescence in such conditions.

#### **2.3.1.4 Effects of synthesis temperature**

In fact,  $80^\circ\text{C}$  temperature is below the normal boiling temperature of water ( $100^\circ\text{C}$ ). For that, higher synthesis temperatures were adapted in order to decrease the effect of water molecules on the ZnO luminescence. Two curing temperatures above  $100^\circ\text{C}$  ( $110^\circ\text{C}$  and

150°C) were investigated to test its effect on the luminescence of the as-prepared nanostructures through similar synthesis processes lasting for 20 min.

As shown in the PL results in Figure 16(b), increasing the synthesis temperatures allowed us to identify the ZnO exciton luminescence peak. Obviously, it could be identified that by increasing the reaction temperature from 80°C to 150°C passing through 110°C, the Raman peak intensity of water decreased while ZnO peak prevails, thus the exciton emission becomes more and more clear. As a result, it could be concluded that the temperature is a key factor in our reaction, where the effect of adsorbing solvent is less effective with increasing temperatures. We also suggest that, temperature increase allows the formation of ZnO nanostructures of better crystallinity. TEM images over the supernatant obtained by 80°C and 150°C reaction temperatures (without annealing) highlighting the sizes of the particles are shown in Figure 17. The particles seem to grow and become more crystalline and organized for higher synthesis temperatures.

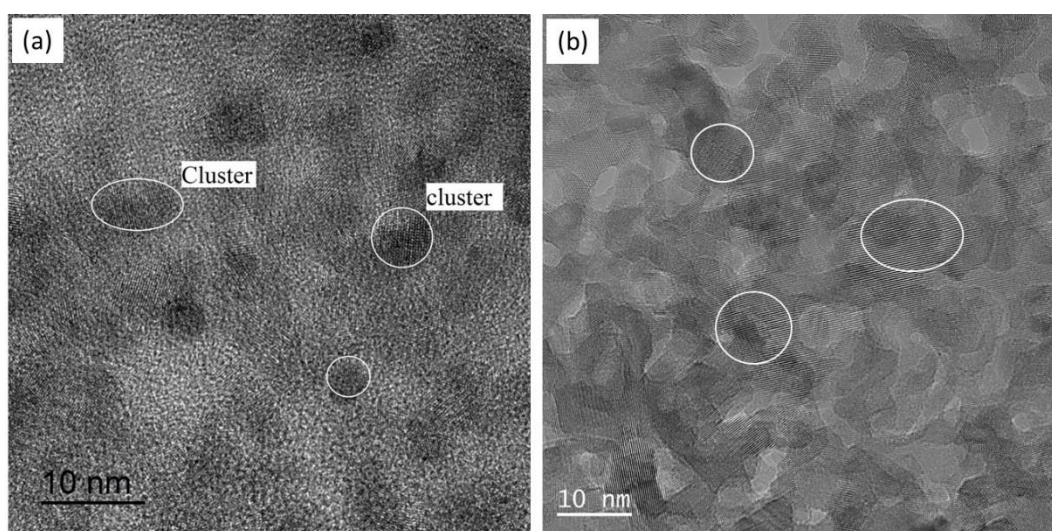


Figure 17 TEM images on for the supernatant part of the solutions synthesized at (a) 80°C, (b) 150°C.

Concerning the effect of the reaction time and that of the temperature on the desired reaction, we found that boosting the reaction time at 80°C had no significant influence on the characteristics of the obtained ZnO nanostructures, however raising the reaction temperature had.

Although, it is well known that with increasing temperature and/or time of the reaction results in unfavorable grain growth of the particles, increasing the average crystallite size of the reaction products [65]. Yet, the smaller the nanoparticles are, the more interesting they are in catalysis applications where the photocatalytic degradation behaviors become much efficient

at smaller sizes, by which the active surface atoms increases triggering the surface to gain much tension, and therefore offering higher catalytic efficiency [66–68]. Also, the low reaction temperatures make the products attractive for microelectronics and plastic electronics applications [69]. For this reason, ZnO NPs obtained in our reaction at lower temperatures might be more interesting, dealing with smaller nanocrystals. As an indication of the smaller NPs sizes obtained at 80°C temperature reaction is the quenching UV luminescence, referring to Biju *et al.* whom they reported that smaller NPs will have higher surface over volume ratio favoring the quenching effect [70,71].

Thus, to avoid exciton emission quenching of the small sized ZnO nanostructures synthesized at 80°C, the bond between the hydroxide of the solvent with the NPs should be broken. For this aim, the solution was annealed for one hour at a temperature 150°C on a normal heating plate. As a result of the annealing process, the excess solvent is evaporated, and thus the quenching effect is eliminated. Add to that, the crystallinity of the NPs is enhanced.

PL measurements applied on the annealed solutions are shown in Figure 16(c), stating the emergence of the excitonic peak at ~380 nm after post thermal treatment of the particles. Consequently, the quenching luminescence of the small sized NPs synthesized at 80°C is avoided after post-thermal treatment.

Accordingly, to detect the exciton emission of small ZnO NPs synthesized in water, the synthesis should be adapted by two conditions: even at a temperature smaller than the normal boiling temperature of the solvent with a post-thermal treatment ( $T=80^{\circ}\text{C} + \text{annealing}$ ), or at a temperature higher than the solvent's boiling temperature without any further operations. It is worth to note that the exciton emission of the annealed ZnO synthesized at 80°C shown in Figure 16(d) exhibits the most intense UV peak among others. This is referred to the fact that the annealing process promotes the removal of additional complex impurities in solution by transforming the residual  $\text{Zn}(\text{OH})_2$  and  $\text{ZnNO}_3$  complexes into ZnO nanoparticles. Thereby, increasing the latter's density number in solution. The resulted small red shift in the exciton emission may be linked to the slight aggregation caused by annealing.

In this simple strategy, the characteristics of the ZnO nanoparticles could be controlled throughout the synthesis process according to the aimed appliances.

## 2.3.2 Structural properties

Tuning the physical and chemical properties of the fabricated ZnO nanostructures through the chemical reaction synthesis has gained attention and reported by adapting different ways such as controlling the ZnO growth using dopants, or by thermal annealing of the pure ZnO nanostructures [72,73]. This latter is favorable since the physical and optical properties of the initial synthesized nanostructures could be mainly conserved. Thus the effect of annealing process on the as-synthesized ZnO samples was examined.

### 2.3.2.1 TGA Analysis

Thermogravimetric analysis of the synthesized ZnO powders at 80°C for 20 min before annealing has been investigated to examine their thermal behavior by probing the thermal decomposition and stability of our product with temperature. The chemical and physical manners could also be examined by TGA.

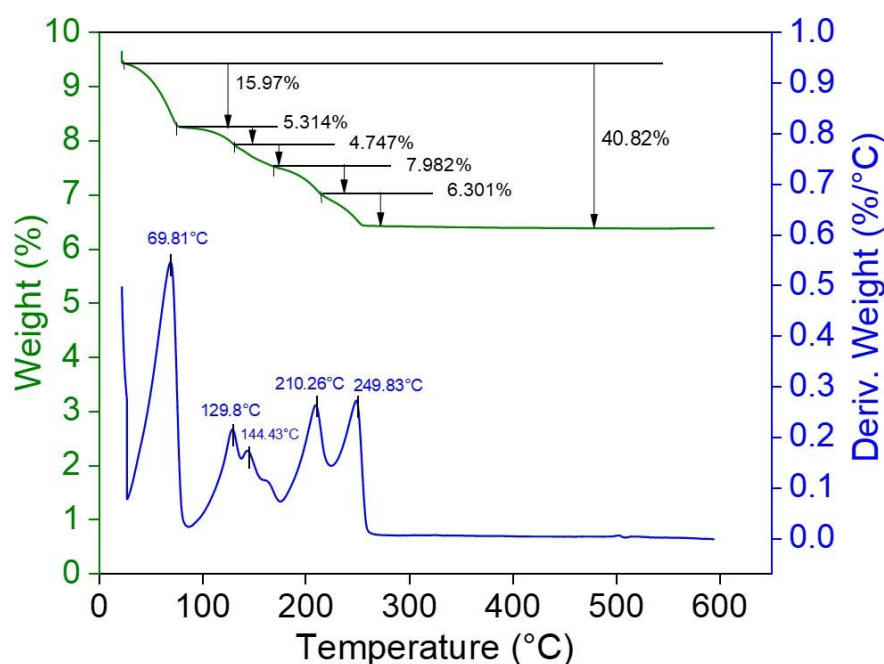


Figure 18 TGA measurements of the powders synthesized at 80°C representing the percentage of weight loss with its corresponding derivative.

The TGA profile shown in Figure 18 states a continuous loss of weight with five alterations occurring at approximately 70, 130, 144, 210, and 250°C, followed by almost a flat terrain up to 600°C. Heating up to 250°C distracts nearly 41% of the total mass. Hence, annealing at

250°C could be considered as an optimum temperature for annealing which will help to guarantee the formation of stable ZnO nanostructures.

Therefore, the obtained powders were annealed at different temperatures below (at 80, 100 and 150°C) and beyond 250°C (at 500 and 800°C) to examine the annealing effect on the progress of the synthesized nanostructures.

### **2.3.2.2 XRD analysis**

It is known that XRD pattern analysis allows the identification of various material properties. On this basis, XRD measurements were performed for ZnO powders synthesized at 80°C and annealed at various temperatures in order to investigate their structures and crystallinity. The corresponding XRD patterns are shown in Figure 19. Table 3 showed that the raw synthesis product is mainly composed of  $Zn_5(NO_3)_2(OH)_8 \cdot 2H_2O$  crystalline structure, which is embedded with only 9% of amorphous nanoparticles. The formation of nanoparticles and the amorphous feature can be attributed to both broadness and weakness of peak intensities in the  $2\theta$  range 10-18 Degree (Figure 19(a)). Subsequently, a thermal annealing allowed the destruction of  $Zn_5(NO_3)_2(OH)_8 \cdot 2H_2O$  phase and a complete disappearance above 250°C giving rise to 100% ZnO nanoparticles. Thus, the ZnO percentage in the obtained powders increased from 9% without post-thermal annealing into 10, 30, 75, and 99% for the following annealing at 80, 100, 150, and 250°C, respectively. Moreover, with increasing the annealing temperatures, the amorphous ZnO became crystalline, in relation with the appearance of narrow, intense peaks, which were attributed to ZnO crystalline nanostructures.

Table 3 Percentage of ZnO composition in the raw synthesis product and the lattice parameters (a, b and c) of ZnO samples before and after annealing at different temperatures.

<b>ZnO annealing temperature (°C)</b>	<b>XRD</b>		
	<b>%ZnO</b>	<b>a=b (nm)</b>	<b>c (nm)</b>
<b>Bulk ZnO [75]</b>		<b>0.3249</b>	<b>0.5206</b>
<b>n/a</b>	9%	0.3313	0.5273
<b>80</b>	10%	0.3248	0.5195
<b>100</b>	30%	0.3252	0.5207
<b>150</b>	75%	0.3251	0.5209
<b>250</b>	99%	0.3247	0.5202
<b>500</b>	100%	0.3246	0.5201
<b>800</b>	100%	0.3243	0.5197

In addition, the ZnO phase displayed the same structure for all the samples. Precisely, the five observed diffraction peaks after annealing including (100), (002), (101), (102) and (110), match well the wurtzite hexagonal structure of the ZnO NPs, having predominantly (101) preferred orientation as a result of minimizing the internal stress and surface energy through this plane [74]. After raising the annealing temperatures beyond 150°C, no peaks corresponding to impurities were observed in the patterns, confirming the high phase purity of the samples due to the deduction of chemical residues and impurities.

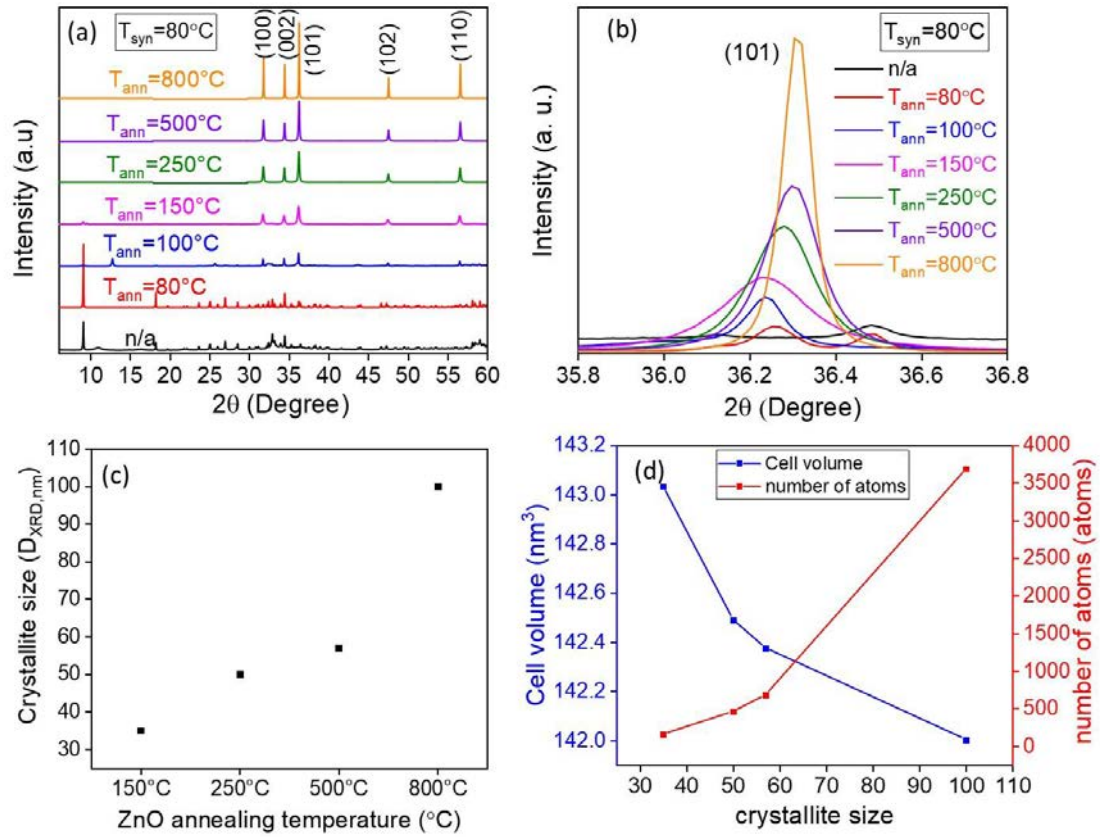


Figure 19 XRD measurements of the powdered ZnO NPs synthesized at 80°C and annealed at different temperatures: (a) XRD patterns, (b) the variation of the (101) plane peak intensity and position with increasing the annealing temperatures, (c) the evolution of the crystallite size as a function of annealing temperature, (d) illustration of the variation of the cell volume and number of atoms per unit cell as a function of crystallite size.

The lattice constants "a", "b" and "c" were assessed from the hkl Miller indices in the XRD patterns using the formula associated to the hexagonal systems:

$$1/d^2 = 4/3 ((h^2 + hk + k^2)/a^2) + l^2/c^2 \quad (1)$$

Using Bragg's law

$$n\lambda = 2d \sin\theta \quad (2)$$

with the first order approximation  $n = 1$ , and assessing  $\theta$  for each plane from the XRD patterns, then,

$$d = \lambda / 2 \sin\theta \quad (3)$$

Hence, the lattice constant "a" for the (100) plane is calculated by:

$$a = 2d / \sqrt{3} \quad (4)$$

For the (002) plane, the lattice constant "c" was calculated by:

$$c = 2d \quad (5)$$

The obtained values of “a” and “c” of the different ZnO samples correspond to ZnO bulk structure [75], as shown in Table 3.

Figure 19(b) illustrates the evolution of the (101) preferred lattice plane of the ZnO nano-objects (before and after annealing at different temperatures). As the annealing temperature rises, a slight increase in the  $2\theta$  position of the (101) plane was observed with an increased peak intensity, in relation with better crystallinity and higher amount of crystalline ZnO nanoparticles oriented at this plane direction as assessed before.

The variation of the full width half maximum (FWHM) obtained from the XRD measurements gives a reflection of the structural distribution, in addition to the surface state of the material related to the grain distortion, dislocation density and residual stresses. Tung *et al.* refers the linear increase of the FWHM is an implication of the increased point defects and hardness which in turns affects the crystallinity and grain boundary (2D defects) mobility of the particles [76]. In other reports, Kim *et al.* stated that defect rich materials with structural disorder widen the XRD peaks [77].

The crystallite size of the mostly crystalline nanoparticles annealed at 150, 250, 500 and 800°C depicted in Figure 19(c) were estimated using the Scherrer equation:

$$D = \frac{K\lambda}{\beta \cos \theta} \quad (6)$$

where  $D$  is the crystallite size,  $K$  is a numerical factor referred to the crystallite-shape constant (0.94),  $\lambda$  is the wavelength of the X-rays,  $\beta$  is the full-width at half-maximum (FWHM) for the most intense peak (101) in radians and  $\theta$  is the Bragg angle. The crystallite sizes were 35, 50, and 57 nm for the samples annealed at 150, 250, and 500°C respectively, to reach a size higher than 100 nm, after annealing at 800°C.

The cell volume and the number of atoms for the ZnO samples with hexagonal form depicted in Figure 19(d) were estimated using the following respective equations [78]:

$$V = \frac{3\sqrt{3}}{2} a^2 c \quad (7)$$

$$n = \frac{4\pi}{3V} \left(\frac{D}{2}\right)^3 \quad (8)$$

As the crystallite size increased, the cell volumes decreased followed by the increase in the number of atoms. These theoretical results are in agreement with the percentage composition

measurements (derived from the XRD) of crystalline ZnO with respect to the complex structures initially obtained after synthesis.

### 2.3.2.3 XPS analysis

The surface structures of the ZnO nanocrystal samples before and after annealing at 250°C were investigated by XPS, and the corresponding experimental results are shown in the XPS spectra show that the nanoparticles were composed of zinc (Zn) and oxygen (O) atoms.

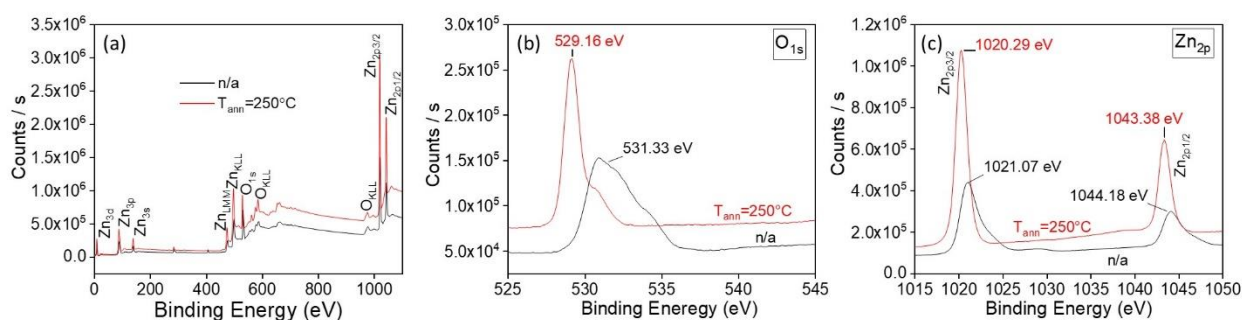


Figure 20 (a) XPS measurements of the synthesized ZnO NCs before (black curve) and after annealing at 250°C (red curve), (b)  $O_{1s}$  spectrum, (c)  $Zn_{2p}$  spectrum.

The XPS survey spectrum of ZnO NCs before and after annealing at 250°C are illustrated in Figure 20.

Figure 20(a) displays Zn and O peaks [79]. The binding energies at 531.33 and 529.16 eV were attributed to  $O_{1s}$  relative to the ZnO (Zn-O bonding) before and after annealing at 250°C, respectively [80]. The small red shift in the Zn-O bonding for the non-annealed powders may be attributed to the presence of bound oxygens such as hydroxyl groups or  $O^{2-}$  ions in the regions that are deficit in oxygen [81]. Whereas, the peaks located at 1021.07 and 1044.18 eV for non-annealed ZnO, and at 1020.29 and 1043.38 eV for 250°C annealed ZnO NCs, are respective peaks referred to  $Zn_{2p_{3/2}}$  and  $Zn_{2p_{1/2}}$ . The transformation of the  $Zn_{2p_{3/2}}$  into lone and sharp peak after annealing confirms that the Zn group is in the completely oxidized state [82].

### 2.3.2.4 SEM analysis

Scanning electron microscopy were performed to overview the morphology of the synthesized nanostructures. Indeed, after the deposition of the samples on a conductive substrate, the nanoparticles will be slightly aggregated due to the change in their surrounding environment.

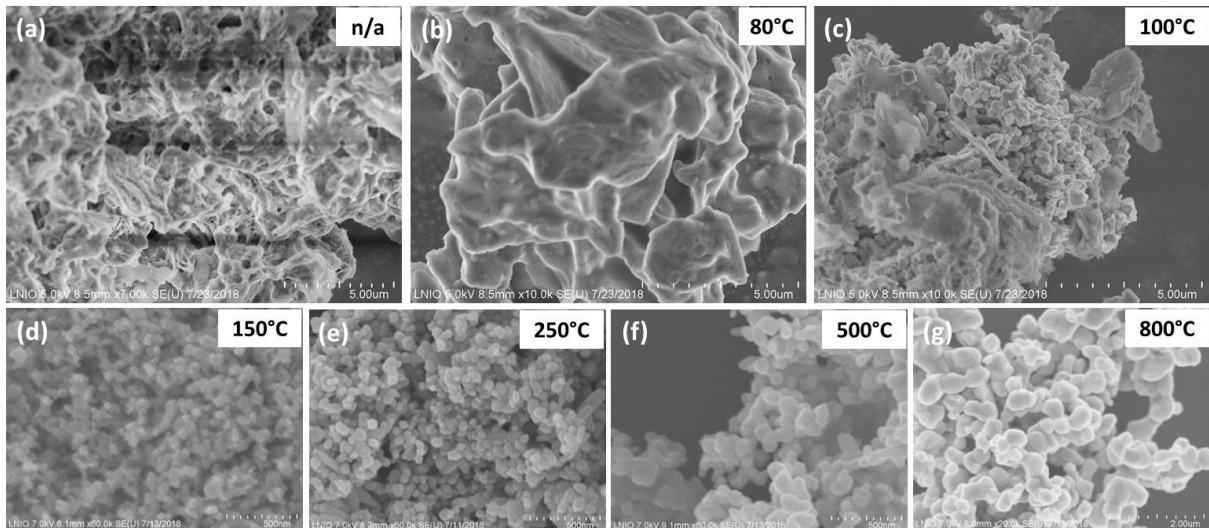


Figure 21 SEM images of the synthesized ZnO NCs: (a) before annealing (n/a), annealed at (b-g) 80, 100, 150, 250, 500 and 800°C, respectively. The scale bar in images (a-c) is 5  $\mu\text{m}$ , (d-f) 500 nm, and (g) 2  $\mu\text{m}$ .

Figure 21 shows the SEM morphologies of the samples before and after annealing at different temperatures (from 80°C to 800°C). SEM images also confirm the increase of ZnO nanoparticles size with increasing the annealing temperature. Indeed, without annealing we only observe the  $\text{Zn}_5(\text{NO}_3)_2(\text{OH})_8 \cdot 2\text{H}_2\text{O}$  microstructure. ZnO nanostructures are very small at this condition and they are embedded inside. When the temperature increases,  $\text{Zn}_5(\text{NO}_3)_2(\text{OH})_8 \cdot 2\text{H}_2\text{O}$  is annealed. We can observe ZnO as small nano-objects on the surface of melted microstructure in Figure 21(b). From Figure 21(b) until Figure 21(g), only ZnO nanoparticles appeared with a continuous increased size respectively.

Precisely, the nanoparticles became gradually more numerous, crystalline and bigger when annealed. After excessive increase in the annealing temperatures to 500°C and 800°C, the size further increased, whereas the density of particles started to decrease. This may be linked to the effect of sintering of the nanoparticles at high temperatures. At 800°C, coalescence of the nanostructures could occur, ending up in bigger nanoparticles (larger than 100 nm). At the same time, 500 and 800°C could be high enough to recrystallize the nanoparticles, retaining the high crystallinity behavior observed by XRD.

### 2.3.2.5 TEM analysis

For a better investigation of ZnO photoluminescence characteristics, in addition to SEM, samples were also observed by TEM. Subsequently, their absorption spectra were then collected by UV-Vis spectrophotometry measurements. Figure 22 shows the TEM micrographs

of the ZnO nanostructures. The nanoparticles are necessarily little aggregated after deposition on the TEM grid.

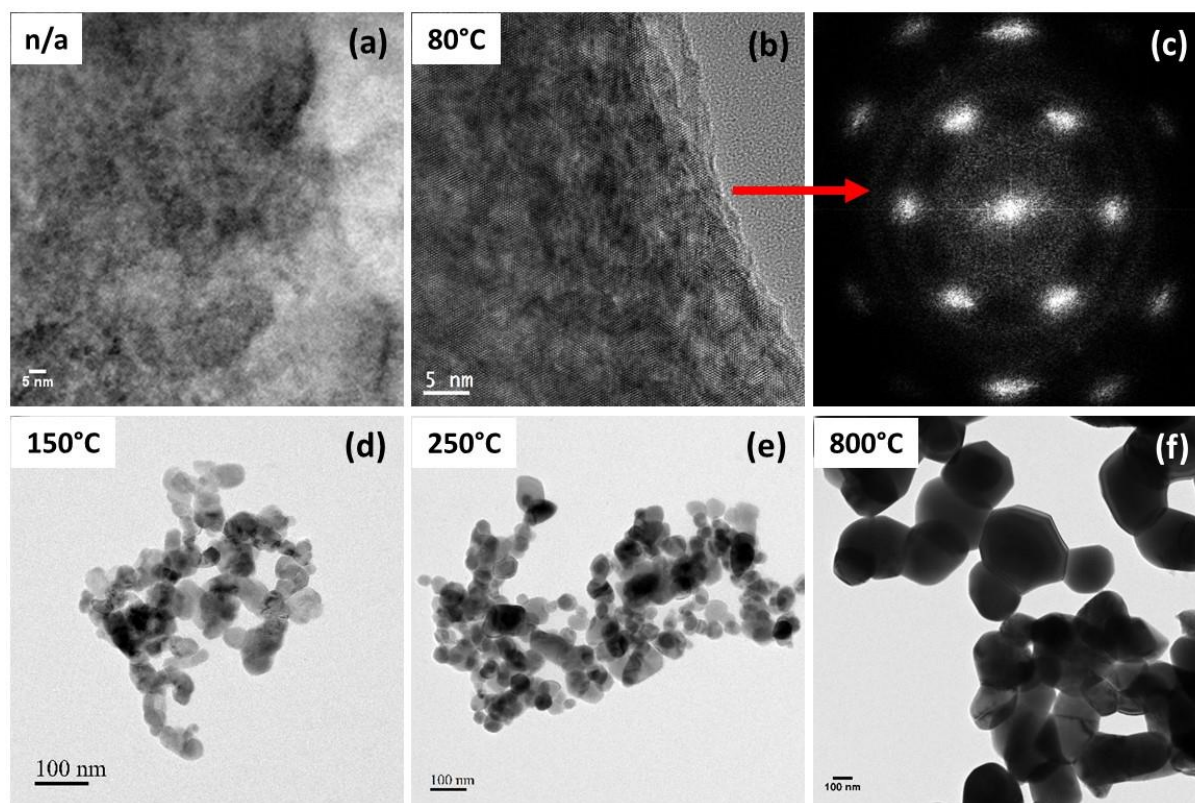


Figure 22 (a) Bright field TEM image of the as-prepared ZnO NCs before annealing. ZnO sample annealed at 80°C (b) TEM image (c) Diffraction of the crystal, (d-f) TEM images of the annealed samples 150,250, and 800°C respectively. The scale bar in images (a-b) is 5 nm and in (d-f) is 100 nm.

In Figure 22(a), the non-annealed sample showed the  $Zn_5(NO_3)_2(OH)_8 \cdot 2H_2O$  microstructure as observed and discussed before in the SEM images of Figure 21(a). We can guess the presence of ZnO nanostructures of very small size ( $< 1$  nm) as black dots doping the microstructure. After post-thermal treatment at 80°C, the TEM image of the corresponding sample shown in Figure 22(b) revealed an increase in the crystallinity that was also significant in the crystal diffraction image in Figure 22(c). The as-synthesized and annealed sample at 80°C showed a very small sized particles ( $< 1$  nm). Here, we can talk about ZnO nanoclusters. Above 80°C as annealing condition, the nanocrystals started growing until reaching the nanoscale. Thus, the produced nanoparticles gradually coalesced and aggregated as temperature increased until reaching a large size of  $\sim 200$  nm at 800°C. The observed evolution in size here is in consistent with the trend observed in the XRD and SEM measurements.

### 2.3.3 Optical properties

To complete the insight over the characteristics of our products, further examination of the synthesized products as solutions was carried on. To make it possible, the synthesized powders were dispersed in water to adapt a suitable environment for characterization with an ultrasonic aid to achieve un-aggregated and homogeneous nanostructures.

#### 2.3.3.1 Absorption measurements

UV-Vis absorption measurements were performed on the as-synthesized samples of Figure 21. Figure 23(a) shows an absorption (Abs.) band centered at 365 nm for the non-annealed sample, which is a characteristic peak of ZnO NPs (blue shifted with respect to the value of bulk ZnO “385 nm” might be due to a high quantum confinement effects) [83]. After annealing at 80, 100, 150, 250, and 500°C, the absorption peaks of the samples shifted to 375, 378, 371, 375, and 378 nm, respectively. One can note the Abs. band broadness at 800°C due to the non-homogenous size presence. From there, we conclude that the thermal annealing is a critical parameter that mainly affects both the structural and optical properties of ZnO nanoparticles [84].

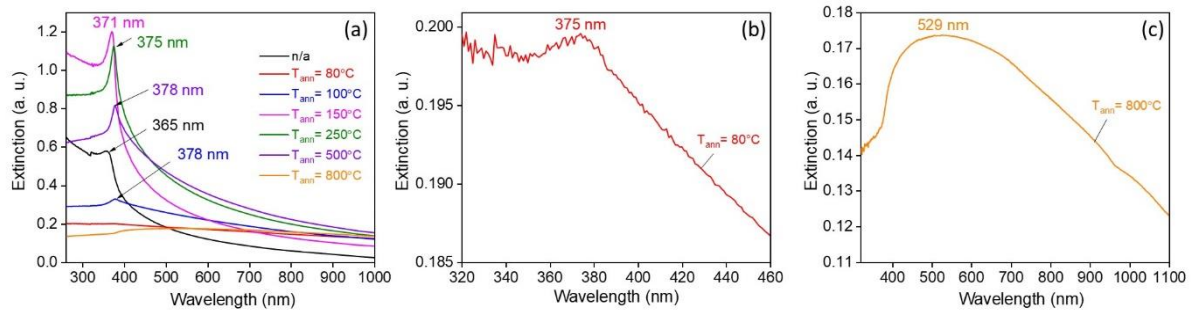


Figure 23 (a) UV-Vis absorption spectroscopy of the as-prepared non-annealed (n/a) ZnO NPs and after annealing at different temperatures, (b) zoom in the UV region of the ZnO nanocrystals annealed at 80°C, and (c) magnification of the UV-Vis absorption spectra of the ZnO nanocrystals annealed at 800°C.

When the electrons of the material absorb light energy at specific wavelength, they will go to the excited state with respect to their ground state with an energy equals to their band gap energy which can be determined by the absorption wavelength.

Based on the Abs. band, we calculated the optical band gap energy according to the relation of photon energy in quantum mechanics through the following relation:

$$E_g = \frac{hc}{\lambda} \quad (9)$$

where  $E_g$  is the optical band gap energy (in eV),  $h$  is Plank's constant ( $6.626 \times 10^{-34}$  J.s),  $c$  is the velocity of light ( $2.99 \times 10^8$  m.s<sup>-1</sup>) and  $\lambda$  is the wavelength absorption peak value (in nm). The optical band gap energies are listed in Table 4.

Table 4 Absorption peak position and the optical band gap energy of the ZnO samples without and with annealing at different temperatures.

<b>ZnO annealing temperature (°C)</b>	<b>UV-Vis Absorption</b>	
	<b>Wavelength absorption peak (nm)</b>	<b>Optical band gap (eV)</b>
<b>n/a</b>	365	3.40
<b>80</b>	375	3.31
<b>100</b>	378	3.28
<b>150</b>	371	3.34
<b>250</b>	375	3.31
<b>500</b>	378	3.28

A gradual decrease of  $E_g$  from 3.4 to 3.28 eV is observed with increasing annealing temperatures. The highest value of 3.4 eV determined at 80°C, is higher than the theoretical  $E_g$  value of ZnO (3.34 eV). This result could indicate the quantum confinement that appears when the nanoparticle's size matches or it is lower than the Bohr radius of the material as assessed before. The band gap energy of the ZnO NPs annealed at 800°C could not be determined due to the largely wide absorption band that does not allow a precise determination of the band gap energy.

### 2.3.3.2 Photoluminescence measurements

After Abs. measurements, the photoemission of the samples (with the same annealing parameters) was tested under 365 nm UV-lamp and the images are shown in Figure 24. One can observe UV and visible emission of ZnO nanoparticles in the images.

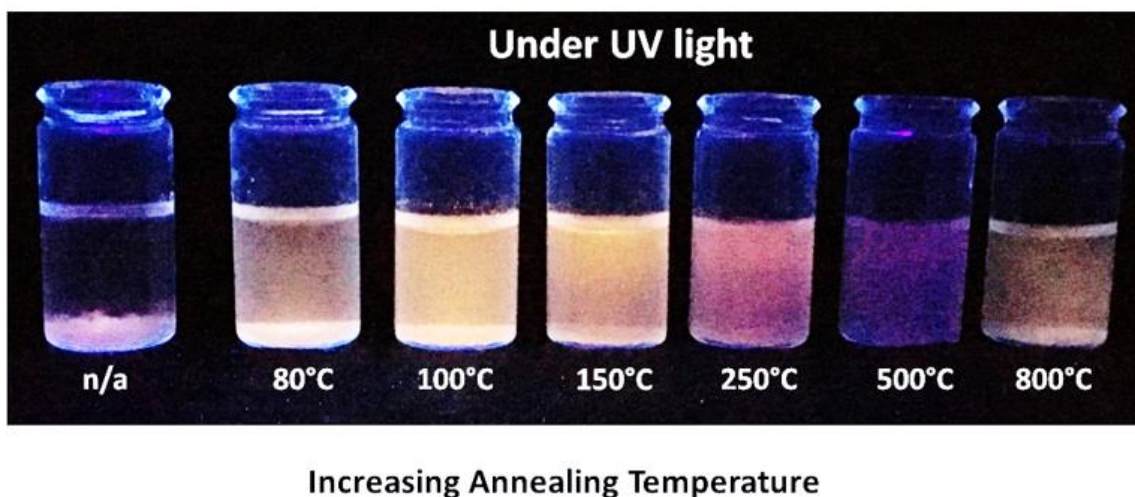


Figure 24 Photoemission colors under 365 nm UV lamp light of ZnO NCs annealed at different temperatures.

In a research work concerning the importance of water soluble ZnO QDs combined into biological systems, Lu *et al.* have recommended the different color emission of the QDs rather than the blue emission [85]. Since the UV irradiation of the biological cells reveals a blue light [85,86], it is worth to introduce different color emitters in such systems in order to distinguish between the obtained emissions. This results in enhanced investigations in biological labeling applications. The different colours obtained by our fabricated products reveal various optical properties, in relation with different dimensions of the nanoparticles. This could highly serve the above mentioned application as well as many other operations.

The UV energy belongs to the band gap emission in ZnO referring to the recombination in the near band edge (NBE), where the visible emission mainly originates from the intrinsic defect energy levels. Similarly, for our fabricated samples, ZnO nanostructures exhibited an intense UV peak accompanied by a broad visible peak as shown in Figure 25(a).

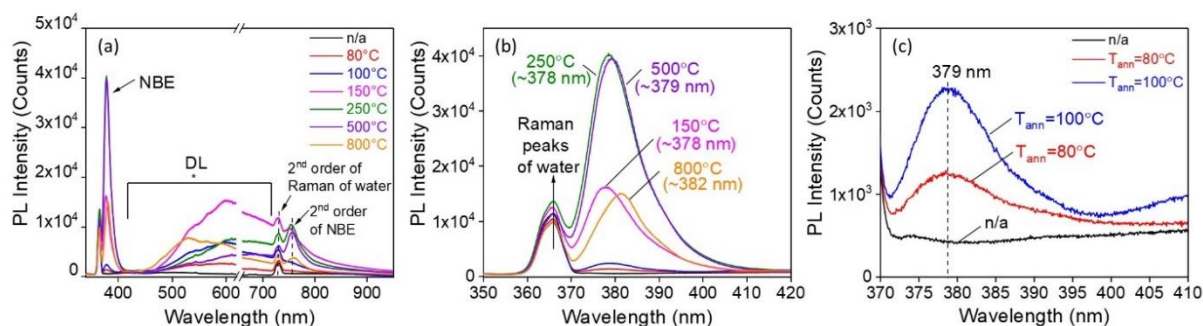


Figure 25 Photoluminescence of ZnO NPs dispersed in water: (a) the full PL spectrum of all samples before and after annealing and showing break line at the missing data points over the region of the second order of the laser, (b) a zoom in the ZnO UV region of the PL spectrum showing the maximum position of the UV emission wavelength, (c) a zoom in the ZnO UV region of the PL spectrum of the non-annealed (n/a) ZnO and the annealed ZnO at 80 and 100°C.

The above PL measurements showed no considerable UV peak for the non-annealed sample due to its amorphous structure in addition to the Raman peak of water as discussed above. However, the UV luminescence was clearly identified after annealing of the powders revealing the exciton emission of ZnO nanoparticles (Figure 25(c)). Upon annealing, the PL band position shifted from ~378 nm to ~381 nm, indicating a gradual increase in size.

One can also see in Figure 25(b) an increase of the intensity of UV emission band when temperature increased from 80°C until 250°C. Above this value, the intensity gradually decreased. The emergence in the UV-PL intensity with the annealing temperatures up to 250°C is attributed to the annealing process, which acts as impurity removal and then increase the ZnO amount in the dispersed powder, increasing the radiative recombination of their excitons. However, it was previously shown in the TGA measurements in Figure 18 that no mass loss was observed above 250°C, thus higher annealing temperatures will have no deal with the purification of the particles or transforming complexes into nanostructures. Therefore, the excessive increase in the annealing temperatures increase the particle's size, affect the crystal itself, and deform its structure until coalescence as shown in TEM and SEM images. As a result, the radiative recombination decreases, which reflects weaker UV emission band.

The broad visible PL band related to the defects in all samples, is ranged from green to orange emission regions with different intensities depending on the annealing temperature. The small shoulders included in the defect level band contributes to the noise interference and the technical imperfections.

As assigned before, the green emission corresponds to the intrinsic defect energy levels (oxygen vacancies  $V_O$  resulting from the recombination of photo-generated hole with the singly ionized charge state of this defect, and/or zinc vacancies  $V_{Zn}$ ). Green defect emission peaks were also observed in comparable synthesis [29]. The orange emission is related to the excess of oxygen as interstitial defects [87–90], in addition to zinc interstitials and surface dislocations [91,92]. In some reports, yellow emissions were also observed and attributed to the oxygen interstitial defects as well as to the presence of  $Zn(OH)_2$  and other impurities at the surface of the NPs [56].

In our case, the defect level peak position was approximately the same for samples annealed in the range 80-500°C, which indicates the constant local environment of the defect centers in our samples [93,94]. Annealing at 800°C showed a slightly different contribution of the defects which is related to the variation in the crystal environment due to the fusion of nanoparticles at

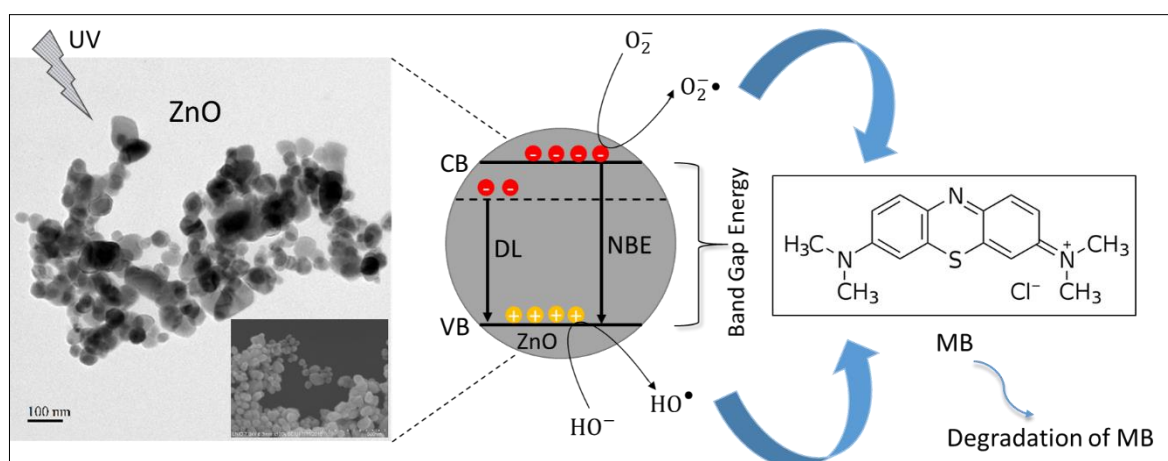
this temperature. We could also expect the distortion of the atomic distribution inside the crystal at high temperature, which caused such defect evolution.

The present small peaks at 730 nm and the other at  $\sim 755$  nm correspond to the second order of the water solvent peak and the UV emission of the ZnO nanoparticles, respectively. The latest peak was also reported by Tonon *et al.* [95].

As a conclusion, the thermal annealing is necessary to obtain crystalline and efficiently photoluminescent ZnO nanostructures. Nevertheless, the temperatures must be ranged between 250 and 500°C holding proper purity and size of the NPs.

### 2.3.3.3 Photocatalytic activity

The purpose of the current study is to degrade different kinds of organic pollutants. For this aim, we used methylene blue (MB) dye as a model pollutant.



Scheme 10 Schematic representation of the photocatalytic activity of the ZnO NPs by degradation of methylene blue (MB) dye. (The photoluminescence of ZnO NPs is also indicated). The TEM image corresponds to the synthesized ZnO NPs annealed at 250°C. The inset in the TEM image is the SEM image of the same sample.

Due to the small size of ZnO nanoparticles ( $< 1$  nm at 80°C), that we were able to fabricate in the present work, which is required in photocatalysis analysis, we investigate here the performance of our samples as catalysis. The catalyst was mixed with MB aqueous solution, then irradiated with a wavelength of 365 nm at various time intervals. In the absence of the ZnO photocatalyst, the irradiated MB solution was found to be stable even after 120 min and the color of the MB solution remained the same. The corresponding absorption spectra of MB alone under UV irradiation is shown in Figure 26(a).

Knowing that each annealing temperature corresponds to a critical size and number of ZnO nanoparticles, the degradation efficiency was estimated by measuring the absorbance of MB in the presence of ZnO (before and after annealing). After the addition of ZnO nanoparticles, the solutions exhibited various photocatalytic activities. The height of the MB absorbance band centered at 664 nm decreased, which indicates the contribution of ZnO to the degradation of MB. At the end of reaction, the solutions turned colorless indicating the total consumption of MB in the dispersions. The MB degradation in the presence of the various ZnO samples studied before, are represented in Figure 26(b-h).

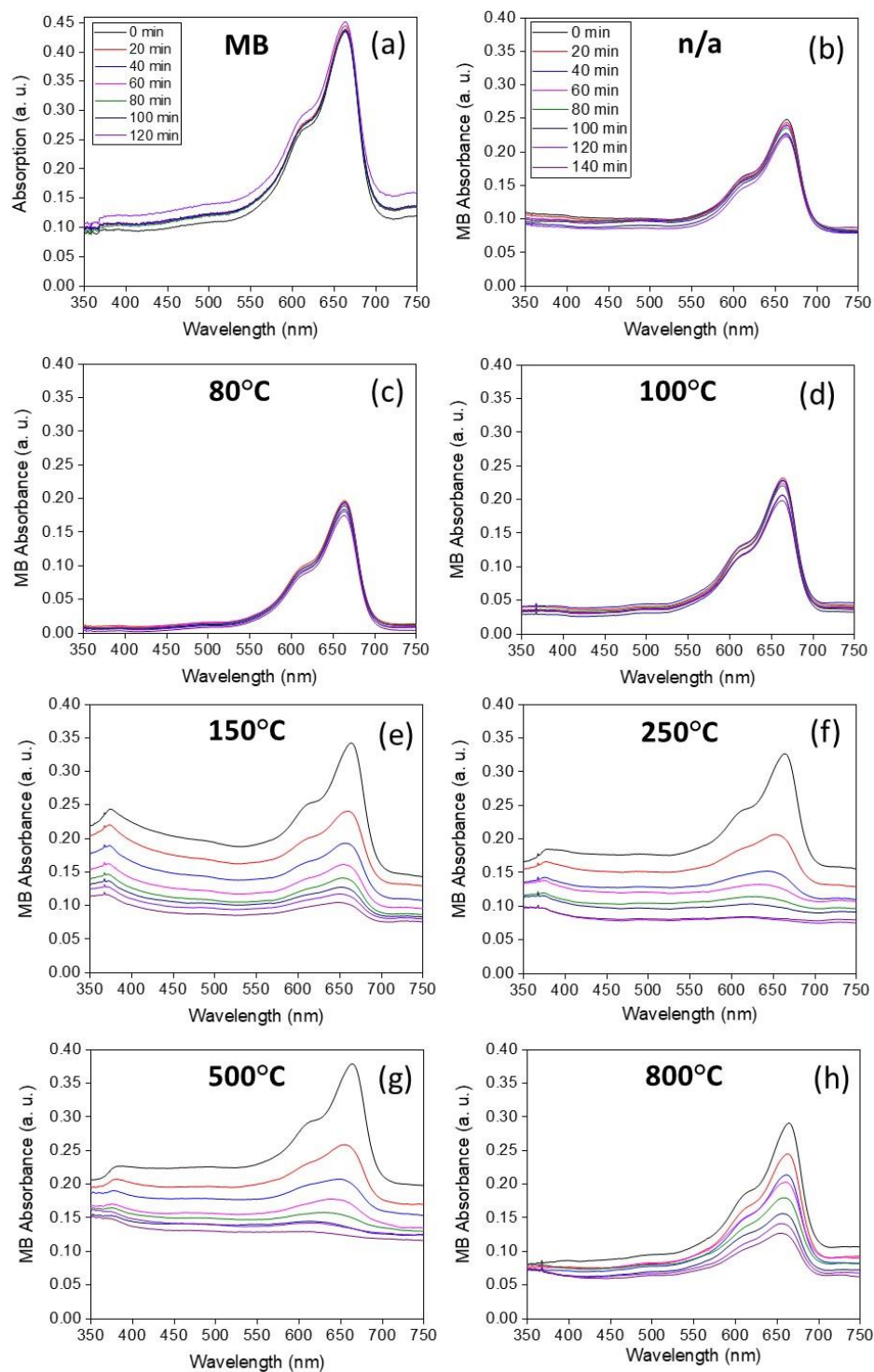


Figure 26 Optical absorption spectra showing (a) the evolution of MB absorption in the absence of a catalyst under different irradiation times until 120 min, the inset shows the different irradiation times, (b-h) the degradation of MB using ZnO NPs at different irradiation times until 140 min: (b) non-annealed (n/a) ZnO NPs, the legend in (a) shows different irradiation times of the MB/ZnO solution and belongs to the other curves, (c-h) annealed ZnO NCs at 80, 100, 150, 250, 500, 800°C, respectively.

The photocatalytic efficiency of these samples is illustrated *via* the percentage of degradation of MB dye and calculated using the following equation:

$$\text{Degradation (\%)} = \left( \frac{Abs_{t_0} - Abs_{t_f}}{Abs_{t_0}} \right) \times 100 \quad (10)$$

where  $Abs_{t_0}$  is the absorbance value of MB at  $t=0$  min of the photo-reaction, and  $Abs_{t_f}$  is the value of absorbance at the final time of the reaction  $t=140$  min. The results are tabulated in Table 5.

The amount of the ZnO catalyst was 4 mg in all the samples, the percentage of ZnO weight in the powders used was estimated from the percentages obtained through the XRD measurement, and the results are listed in Table 5.

Table 5 Photocatalytic activity of ZnO samples representing the percentage of degradation of MB with the photodegradation rate and the relative regression coefficient.

<b>ZnO annealing temperature (°C)</b>	<b>Photocatalysis</b>			
	<b>mass of ZnO (mg)</b>	<b>% of MB degradation</b>	<b>Photodegradation rate (min<sup>-1</sup>)</b>	<b>Regression coefficient (R<sup>2</sup>)</b>
<b>n/a</b>	0.36	13.69774	$1.18 \times 10^{-3}$	0.92254
<b>80</b>	0.4	6.578583	$8.02138 \times 10^{-4}$	0.91903
<b>100</b>	1.2	16.81652	$1.13 \times 10^{-3}$	0.87755
<b>150</b>	3	86.2676	$8.22 \times 10^{-3}$	0.9416
<b>250</b>	3.96	98.0041	$9.38 \times 10^{-3}$	0.89676
<b>500</b>	4	94.90976	$7.39 \times 10^{-3}$	0.88006
<b>800</b>	4	66.97948	$5.99 \times 10^{-3}$	0.99313

The decrease in the MB absorbance became more efficient when the annealing temperature increases up to 250°C. Beyond this temperature, the degradation of MB started to decrease.

Referring to the photocatalysis concept of ZnO, electrons and holes are generated on the conduction and valence bands, respectively, after illumination with sufficient UV light (equation 11), where the efficiency of the photo-induced charge carriers count on the intensity of incident photons with energy higher than or equals to the ZnO bandgap energy [96]. At the surface of the ZnO, oxygen acceptors could be reduced at the conduction band resulting in the

formation of superoxide radical anion ( $O_2^{\bullet-}$ ), which may produce hydroxyl radicals ( $HO^\bullet$ ) (see equations 12 and 13). While the holes in the valence band react with the adsorbed water to form reactive hydroxyl radicals ( $HO^\bullet$ ) (equation 14). The resulted radicals can directly oxidize the organic pollutants and have a powerful ability to degrade an organic dye of MB (equation 15) [97,98]. The mentioned reactions are summarized below:



As a result, the nanocrystals with smaller sizes have more energetic surface electrons and should have better photocatalytic activity. At the same time, the sample containing more of well dispersed and non-aggregated nanoparticles can absorb more light, which increases the photocatalytic activity. On this basis, ZnO nanoparticles annealed at 250°C showed the highest photocatalytic activity, in relation with high number of well dispersed nanoparticles in this case. On the other hand, at higher annealing temperature, the size increase lead to the decrease in the photocatalytic activity.

The photocatalytic degradation kinetics of MB in the presence of ZnO follows Langmuir-Hinshelwood kinetic model [99]:

$$r = \frac{dc}{dt} = [kKc/(1 + Kc)] \quad (16)$$

where r is the photodegradation rate, C is the reactant concentration at irradiation time t, k is the reactant rate constant and K is the adsorption coefficient of the reactant. Kc is nearly 1 at very small c leading to pseudo-first order kinetics equation, and therefore the rate expression is given by the equation:

$$\ln \frac{C_0}{C} = K_{app}t \quad (17)$$

where  $C_0$  is the equilibrium concentration of MB (t=0 min) and C is the concentration at time t, and  $K_{app}$  is the apparent pseudo-first order rate constant. The plot of the kinetic analysis of the ZnO NPs annealed at different temperatures is shown in Figure 27(a) stating a linear relationship between the MB concentration and the irradiation time.

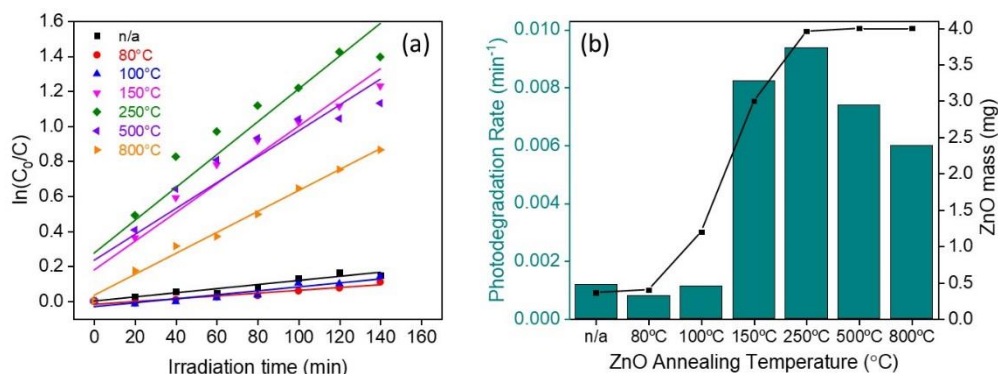


Figure 27 (a) 1<sup>st</sup> order equation of the kinetic reaction of different sizes of ZnO NPs annealed at different temperatures plotted by  $\ln(C_0/C)$  versus irradiation time and (b) comparative photodegradation rates of MB dye with different sizes of ZnO NPs annealed at various temperatures.

The photodegradation rate is computed as a function of increasing annealing temperature of ZnO in Figure 27(b). It is observed that the degradation rate is similar for the non-annealed and both the annealed ZnO ones at 80 and 100°C. Further increase in the annealing temperatures significantly increased the photodegradation rate to reach its maximum at 250°C. After this temperature, the photodegradation rate decreased. The kinetic rate constant and the linear regression coefficient ( $R^2$ ) of all ZnO NPs are also listed in Table 5.

To better understand these observations, we tried to discuss the relation between ZnO photocatalytic efficiency and its amount in the powder dispersed in water for analysis. To make it possible, we described the ZnO mass change as a function of annealing temperature in relation to the photodegradation rate in the following manner:

- (i) Without and with annealing at 80°C, ~9% (0.36 mg ZnO/4 mg) of ZnO nanostructures are present in the powder sample.
- (ii) Annealing at 80 to 250°C, ZnO percentage increased from 10% (0.4mg ZnO/ 4mg) to ~99% (3.96 mg).
- (iii) From 250 to 800°C, ZnO percentage reached 100% (4 mg ZnO/4 mg) and remains constant.

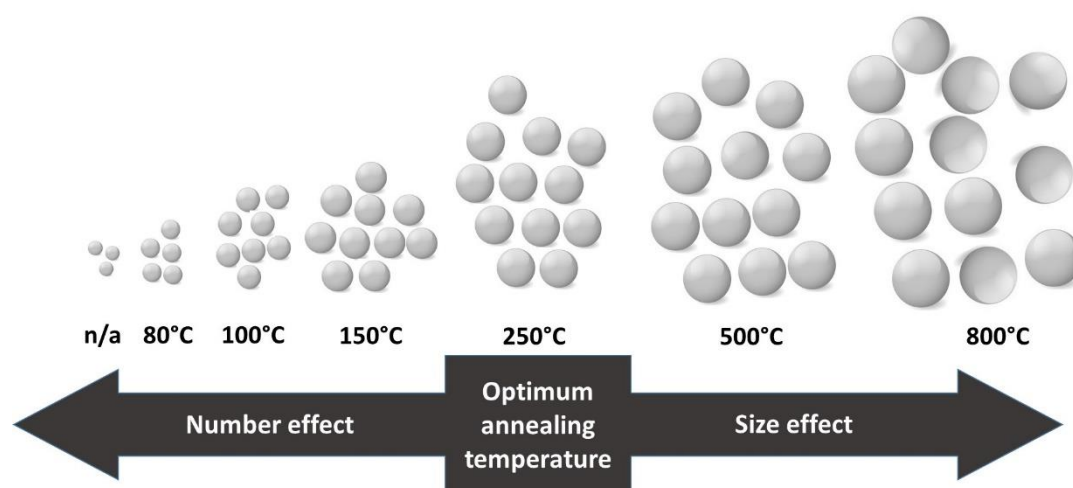
Therefore, the PC activity of all samples could be discussed according to these three zones.

In the first range (i), knowing that the non-annealed samples are smaller in size, they allowed higher % of MB degradation than those annealed at 80°C due to higher surface area.

In the second zone (ii), when the annealing temperature was raised, both the size and the number of nanoparticles increased, creating a competitive role between the dimension effect and the volume fraction effect; bigger nanoparticles should have less photocatalytic activity. In contrast, a dispersion containing higher concentration of nanoparticles should have higher one. In our experiments, we observed an increase in the PC activity until reaching nearly an ideal photodegradation (100%) at an annealing temperature 250°C. Here, the density effect dominated the size effect leading to better photocatalytic activity.

In the last region (iii), the amount of ZnO nanoparticles is the same (4 mg), while their size increased with annealing effect. Due to the size effect at a constant number of particles, the photocatalytic activity gradually decreased.

Scheme 11 shows the simplified illustration of the number and size of ZnO nanostructures at each annealing temperature to relate with the photocatalytic efficiency of the ZnO NCs. Each gray sphere corresponds to a particle of the ZnO NCs.



Scheme 11 Schematic representation of the ZnO nanocrystals with annealing temperatures showing the size and number effect on the photocatalytic activity. The gray spheres represents the ZnO NCs.

In most photocatalysis studies, TiO<sub>2</sub> is widely used for this aim. However, ZnO is an effective alternative due to its comparative band gap energy and lower cost of fabrication [100,101]. In addition, ZnO is considered higher photoactive than TiO<sub>2</sub> as reported by several scientist [102–105]. The higher photoactivity is referred to the higher efficiency to provoke the formation of photoexcited charge carriers [100,106]. The photocatalytic activity highly depends on the exposed surfaces of the catalyst which enhance its degradation efficiency [107,108]. Since the contaminant molecules to be degraded should adsorb on the catalyst surface for the above mentioned reactions to occur. Therefore the catalyst surface area plays a

decisive role for the photocatalyst's efficiency, which is determined through the method of preparation of the catalyst. Previously, few reports were investigated using ZnO nanostructures aiming for the degradation of methylene blue under irradiation of UV light [109–112]. Talebian *et al.* reported the efficient photocatalytic activity of ZnO thin films by the degradation of MB dye after UV light illumination for 240 min [109]. Delgado *et al.* reported the synthesis of ZnO thin film by sol–gel process. The photocatalytic activity of ZnO over the degradation of MB was achieved within 5 h of UV light irradiation [112].

As the nanoparticles adapt higher surface to volume ratio compared to nanowires and thin films that are widely used in photocatalysis, ZnO NPs could be appropriate applicant for the adsorption of contaminants to achieve higher degradation rates with less irradiation times compared to other morphologies. This was evidence in our samples where the MB was completely degraded using the proper ZnO catalyst annealed at 250°C adapting the best surface, size, number and crystallinity of particles. ZnO here exhibited a high photodegradation rate within ~100 min UV light irradiation to completely degrade the MB due in the solution.

Based on all the previous studies over the ZnO NCs stated that 250°C is the perfect annealing temperature for which highly luminescent and catalytically active pure ZnO NCs, where all previous studies over the ZnO NCs stated that 250°C is the perfect annealing temperature to obtain highly luminescent and catalytically active ZnO NCs.

## 2.4 Conclusion

In this work, we have profitably synthesized highly confined, photo-stable, and regular ZnO nanocrystals by a facile, low cost, free-additives, and ecological synthesis method, where the dimensions and the configuration of the produced nanoparticles are well supervised to a high extent by the annealing process. This synthesis could be derived by adapting two synthesis temperatures, a lower one from the boiling temperature (T) of the solvent with a post-thermal treatment, or a temperature higher than the solvent's boiling T. XRD results confirm the formation of ZnO NC with hexagonal wurtzite structure. The application of the as-synthesized particles could be controlled by the post-thermal treatment, where the obtained crystalline NPs can be greatly used in a wide fields of biological, photocatalytic, optical, and electronic applications. The post-thermally treated particles exhibit different emissions according to the size of the nanocrystal. The PL spectra give peaks at the UV region corresponding to NBE emission and visible emission peaks at green to orange luminescence regions corresponding to

various defect levels in ZnO nanoparticles. The annealing at 250°C guarantees the formation of high density number of homogeneous NCs with a strong UV emission. The photocatalytic activity of the synthesized NCs was enhanced after annealing of the particles (annealing enhances crystallinity). The samples annealed at 250°C also adapted the highest photodegradation activity (~98%) with the highest rate of degradation ( $0.00938 \text{ min}^{-1}$ ) among all other samples.

The as-synthesized particles will be coupled to metallic gold nanoparticles in order to examine the evolution of the optical properties of the synthesized nanocrystallines after the exciton interaction with different composition content of the metal plasmons. This will be discussed in chapter 3. The effect of gold nanoparticles morphology on the hybrid interaction is going to be investigated. The inter-planar distance between the exciton and plasmon in the hybrid system will be controlled by a chemical way apart from the modelled theories.

We trust that our approach can be accommodated as a reference strategy for the fabrication of other semiconducting nanoparticles with such controllability and efficacy.

## 2.5 References

1. Lin, K.-F.; Cheng, H.-M.; Hsu, H.-C.; Lin, L.-J.; Hsieh, W.-F. Band gap variation of size-controlled ZnO quantum dots synthesized by sol-gel method. *Chem. Phys. Lett.* **2005**, *409*, 208–211.
2. Wang, Y.; Herron, N. Quantum size effects on the exciton energy of CdS clusters. *Phys. Rev. B* **1990**, *42*, 7253–7255.
3. Nanda, J.; Kuruvilla, B.A.; Sarma, D.D. Photoelectron spectroscopic study of CdS nanocrystallites. *Phys. Rev. B* **1999**, *59*, 7473–7479.
4. Brus, L.E. Electron-electron and electron-hole interactions in small semiconductor crystallites: The size dependence of the lowest excited electronic state. *J. Chem. Phys.* **1984**, *80*, 4403–4409.
5. Sapa, S.; Sarma, D.D. Evolution of the electronic structure with size in II-VI semiconductor nanocrystals. *Phys. Rev. B* **2004**, *69*.
6. Mishra, S.K.; Srivastava, R.K.; Prakash, S.G.; Yadav, R.S.; Panday, A.C. Photoluminescence and photoconductive characteristics of hydrothermally synthesized ZnO nanoparticles. *Opto-Electron. Rev.* **2010**, *18*.
7. Gouvêa, C.A.K.; Wypych, F.; Moraes, S.G.; Durán, N.; Nagata, N.; Peralta-Zamora, P. Semiconductor-assisted photocatalytic degradation of reactive dyes in aqueous solution. *Chemosphere* **2000**, *40*, 433–440.

8. Kumar, Y.; Kumar, H.; Mukherjee, B.; Rawat, G.; Kumar, C.; Pal, B.N.; Jit, S. Visible-Blind Au/ZnO Quantum Dots-Based Highly Sensitive and Spectrum Selective Schottky Photodiode. *IEEE Trans. Electron Devices* **2017**, *64*, 2874–2880.
9. Gao, X.; Cui, Y.; Levenson, R.M.; Chung, L.W.K.; Nie, S. In vivo cancer targeting and imaging with semiconductor quantum dots. *Nat. Biotechnol.* **2004**, *22*, 969–976.
10. Frasco, M.; Chaniotakis, N. Semiconductor Quantum Dots in Chemical Sensors and Biosensors. *Sensors* **2009**, *9*, 7266–7286.
11. Hu, J.Q.; Li, Q.; Wong, N.B.; Lee, C.S.; Lee, S.T. Synthesis of Uniform Hexagonal Prismatic ZnO Whiskers. *Chem. Mater.* **2002**, *14*, 1216–1219.
12. Lao, J.Y.; Huang, J.Y.; Wang, D.Z.; Ren, Z.F. ZnO Nanobridges and Nanonails. *Nano Lett.* **2003**, *3*, 235–238.
13. Lao, J.Y.; Wen, J.G.; Ren, Z.F. Hierarchical ZnO Nanostructures. *Nano Lett.* **2002**, *2*, 1287–1291.
14. Guo, L.; Ji, Y.L.; Xu, H.; Simon, P.; Wu, Z. Regularly Shaped, Single-Crystalline ZnO Nanorods with Wurtzite Structure. *J. Am. Chem. Soc.* **2002**, *124*, 14864–14865.
15. Bouropoulos, N.; Tsiaoussis, I.; Pouloupoulos, P.; Roditis, P.; Baskoutas, S. ZnO controllable sized quantum dots produced by polyol method: An experimental and theoretical study. *Mater. Lett.* **2008**, *62*, 3533–3535.
16. Rani, S.; Suri, P.; Shishodia, P.; Mehra, R. Synthesis of nanocrystalline ZnO powder via sol–gel route for dye-sensitized solar cells. *Sol. Energy Mater. Sol. Cells* **2008**, *92*, 1639–1645.
17. Ristić, M.; Musić, S.; Ivanda, M.; Popović, S. Sol–gel synthesis and characterization of nanocrystalline ZnO powders. *J. Alloys Compd.* **2005**, *397*, L1–L4.
18. Paul, G.; Bandyopadhyay, S.; Sen, S.; Sen, S. Structural, optical and electrical studies on sol–gel deposited Zr doped ZnO films. *Mater. Chem. Phys.* **2003**, *79*, 71–75.
19. Qian, D.; Jiang, J.Z.; Lenvig Hansen, P. Preparation of ZnO nanocrystals via ultrasonic irradiation. *Chem. Commun.* **2003**, 1078–1079.
20. Yu, W.; Li, X.; Gao, X. Catalytic Synthesis and Structural Characteristics of High-Quality Tetrapod-Like ZnO Nanocrystals by a Modified Vapor Transport Process. *Cryst. Growth Des.* **2005**, *5*, 151–155.
21. Banerjee, P.; Chakrabarti, S.; Maitra, S.; Dutta, B.K. Zinc oxide nano-particles – Sonochemical synthesis, characterization and application for photo-remediation of heavy metal. *Ultrason. Sonochem.* **2012**, *19*, 85–93.
22. Hu, X.-L.; Zhu, Y.-J.; Wang, S.-W. Sonochemical and microwave-assisted synthesis of linked single-crystalline ZnO rods. *Mater. Chem. Phys.* **2004**, *88*, 421–426.

23. Asok, A.; Kulkarni, A.R.; Gandhi, M.N. Defect rich seed mediated growth: a novel synthesis method to enhance defect emission in nanocrystals. *J Mater Chem C* **2014**, *2*, 1691–1697.
24. Aranovich, J.; Ortiz, A.; Bube, R.H. Optical and electrical properties of ZnO films prepared by spray pyrolysis for solar cell applications. *J. Vac. Sci. Technol.* **1979**, *16*, 994–1003.
25. Natsume, Y.; Sakata, H.; Hirayama, T.; Yanagida, H. Low-temperature conductivity of ZnO films prepared by chemical vapor deposition. *J. Appl. Phys.* **1992**, *72*, 4203–4207.
26. Yao, B.D.; Chan, Y.F.; Wang, N. Formation of ZnO nanostructures by a simple way of thermal evaporation. *Appl. Phys. Lett.* **2002**, *81*, 757–759.
27. Rataboul, F.; Nayral, C.; Casanove, M.-J.; Maisonnat, A.; Chaudret, B. Synthesis and characterization of monodisperse zinc and zinc oxide nanoparticles from the organometallic precursor [Zn(C<sub>6</sub>H<sub>11</sub>)<sub>2</sub>]. *J. Organomet. Chem.* **2002**, *643–644*, 307–312.
28. Wang, J.; Gao, L. Synthesis and characterization of ZnO nanoparticles assembled in one-dimensional order. *Inorg. Chem. Commun.* **2003**, *6*, 877–881.
29. Yin, J.; Gao, F.; Wei, C.; Lu, Q. Water Amount Dependence on Morphologies and Properties of ZnO nanostructures in Double-solvent System. *Sci. Rep.* **2015**, *4*.
30. Cheng, B.; Samulski, E.T. Hydrothermal synthesis of one-dimensional ZnO nanostructures with different aspect ratios. *Chem. Commun.* **2004**, 986.
31. Madathil, A.N.P.; Vanaja, K.A.; Jayaraj, M.K. Synthesis of ZnO nanoparticles by hydrothermal method. In Proceedings of the Nanophotonic Materials IV; International Society for Optics and Photonics, 2007; Vol. 6639, p. 66390J.
32. Baruwati, B.; Kumar, D.K.; Manorama, S.V. Hydrothermal synthesis of highly crystalline ZnO nanoparticles: A competitive sensor for LPG and EtOH. *Sens. Actuators B Chem.* **2006**, *119*, 676–682.
33. Lu, C.-H.; Yeh, C.-H. Influence of hydrothermal conditions on the morphology and particle size of zinc oxide powder. *Ceram. Int.* **2000**, *26*, 351–357.
34. Chen, D.; Jiao, X.; Cheng, G. Hydrothermal synthesis of zinc oxide powders with different morphologies. *Solid State Commun.* **1999**, *113*, 363–366.
35. Wirunmongkol, T.; O-Charoen, N.; Pavasupree, S. Simple Hydrothermal Preparation of Zinc Oxide Powders Using Thai Autoclave Unit. *Energy Procedia* **2013**, *34*, 801–807.
36. Musić, S.; Popović, S.; Maljković, M.; Dragčević, Đ. Influence of synthesis procedure on the formation and properties of zinc oxide. *J. Alloys Compd.* **2002**, *347*, 324–332.
37. Liu, D.-P.; Li, G.-D.; Su, Y.; Chen, J.-S. Highly Luminescent ZnO Nanocrystals Stabilized by Ionic-Liquid Components. *Angew. Chem. Int. Ed.* **2006**, *45*, 7370–7373.

38. Yang, C.L.; Wang, J.N.; Ge, W.K.; Guo, L.; Yang, S.H.; Shen, D.Z. Enhanced ultraviolet emission and optical properties in polyvinyl pyrrolidone surface modified ZnO quantum dots. *J. Appl. Phys.* **2001**, *90*, 4489–4493.
39. Gupta, A.; Bhatti, H.S.; Kumar, D.; Verma, N.K.; Tandon, dan R. Nano and bulk crystals of ZnO: synthesis and characterization. *Dig. Int J Nanomat Biostruct* **2006**, *1*, 1–9.
40. Moussodia, R.-O.; Balan, L.; Schneider, R. Synthesis and characterization of water-soluble ZnO quantum dots prepared through PEG-siloxane coating. *New J. Chem.* **2008**, *32*, 1388.
41. Fu, Y.-S.; Du, X.-W.; Kulinich, S.A.; Qiu, J.-S.; Qin, W.-J.; Li, R.; Sun, J.; Liu, J. Stable Aqueous Dispersion of ZnO Quantum Dots with Strong Blue Emission via Simple Solution Route. *J. Am. Chem. Soc.* **2007**, *129*, 16029–16033.
42. Zhang, X.; Shao, C.; Zhang, Z.; Li, J.; Zhang, P.; Zhang, M.; Mu, J.; Guo, Z.; Liang, P.; Liu, Y. In situ Generation of Well-Dispersed ZnO Quantum Dots on Electrospun Silica Nanotubes with High Photocatalytic Activity. *ACS Appl. Mater. Interfaces* **2012**, *4*, 785–790.
43. Hsieh, P.-T.; Chen, Y.-C.; Wang, C.-M.; Tsai, Y.-Z.; Hu, C.-C. Structural and photoluminescence characteristics of ZnO films by room temperature sputtering and rapid thermal annealing process. *Appl. Phys. A* **2006**, *84*, 345–349.
44. Petti, L.; Münzenrieder, N.; Vogt, C.; Faber, H.; Büthe, L.; Cantarella, G.; Bottacchi, F.; Anthopoulos, T.D.; Tröster, G. Metal oxide semiconductor thin-film transistors for flexible electronics. *Appl. Phys. Rev.* **2016**, *3*, 021303.
45. Nathan, A.; Ahnood, A.; Cole, M.T.; Sungsik Lee; Suzuki, Y.; Hiralal, P.; Bonaccorso, F.; Hasan, T.; Garcia-Gancedo, L.; Dyadyusha, A.; et al. Flexible Electronics: The Next Ubiquitous Platform. *Proc. IEEE* **2012**, *100*, 1486–1517.
46. Moonen, P.F.; Yakimets, I.; Huskens, J. Fabrication of Transistors on Flexible Substrates: from Mass-Printing to High-Resolution Alternative Lithography Strategies. *Adv. Mater.* **2012**, *24*, 5526–5541.
47. Yang, S.; Bak, J.Y.; Yoon, S.-M.; Ryu, M.K.; Oh, H.; Hwang, C.-S.; Kim, G.H.; Park, S.-H.K.; Jang, J. Low-Temperature Processed Flexible In–Ga–Zn–O Thin-Film Transistors Exhibiting High Electrical Performance. *IEEE Electron Device Lett.* **2011**, *32*, 1692–1694.
48. Yao, B.; Shi, H.; Bi, H.; Zhang, L. Optical properties of ZnO loaded in mesoporous silica. *J. Phys. Condens. Matter* **2000**, *12*, 6265–6270.
49. Wu, L.; Wu, Y.; Pan, X.; Kong, F. Synthesis of ZnO nanorod and the annealing effect on its photoluminescence property. *Opt. Mater.* **2006**, *28*, 418–422.
50. Li, J.; Zhao, D.; Meng, X.; Zhang, Z.; Zhang, J.; Shen, D.; Lu, Y.; Fan, X. Enhanced Ultraviolet Emission from ZnS-Coated ZnO Nanowires Fabricated by Self-Assembling Method. *J. Phys. Chem. B* **2006**, *110*, 14685–14687.

51. Lee, W.-J.; Kang, J.; Chang, K.J. Defect properties and p -type doping efficiency in phosphorus-doped ZnO. *Phys. Rev. B* **2006**, *73*.
52. Zeng, H.; Duan, G.; Li, Y.; Yang, S.; Xu, X.; Cai, W. Blue Luminescence of ZnO Nanoparticles Based on Non-Equilibrium Processes: Defect Origins and Emission Controls. *Adv. Funct. Mater.* **2010**, *20*, 561–572.
53. Teke, A.; Özgür, Ü.; Doğan, S.; Gu, X.; Morkoç, H.; Nemeth, B.; Nause, J.; Everitt, H.O. Excitonic fine structure and recombination dynamics in single-crystalline ZnO. *Phys. Rev. B* **2004**, *70*.
54. Kumar, V.B.; Kumar, K.; Gedanken, A.; Paik, P. Facile synthesis of self-assembled spherical and mesoporous dandelion capsules of ZnO: efficient carrier for DNA and anti-cancer drugs. *J Mater Chem B* **2014**, *2*, 3956–3964.
55. Djurišić, A.B.; Leung, Y.H. Optical Properties of ZnO Nanostructures. *Small* **2006**, *2*, 944–961.
56. Zhou, H.; Alves, H.; Hofmann, D.M.; Kriegseis, W.; Meyer, B.K.; Kaczmarczyk, G.; Hoffmann, A. Behind the weak excitonic emission of ZnO quantum dots: ZnO/Zn(OH)<sub>2</sub> core-shell structure. *Appl. Phys. Lett.* **2002**, *80*, 210–212.
57. Li, Y.; Della Valle, F.; Simonnet, M.; Yamada, I.; Delaunay, J.-J. Competitive surface effects of oxygen and water on UV photoresponse of ZnO nanowires. *Appl. Phys. Lett.* **2009**, *94*, 023110.
58. Meyer, B.; Marx, D.; Dulub, O.; Diebold, U.; Kunat, M.; Langenberg, D.; Wöll, C. Partial Dissociation of Water Leads to Stable Superstructures on the Surface of Zinc Oxide. *Angew. Chem. Int. Ed.* **2004**, *43*, 6641–6645.
59. Dulub, O.; Meyer, B.; Diebold, U. Observation of the Dynamical Change in a Water Monolayer Adsorbed on a ZnO Surface. *Phys. Rev. Lett.* **2005**, *95*.
60. Ahn, S.-E.; Ji, H.J.; Kim, K.; Kim, G.T.; Bae, C.H.; Park, S.M.; Kim, Y.-K.; Ha, J.S. Origin of the slow photoresponse in an individual sol-gel synthesized ZnO nanowire. *Appl. Phys. Lett.* **2007**, *90*, 153106.
61. Mahamuni, S.; Borgohain, K.; Bendre, B.S.; Leppert, V.J.; Risbud, S.H. Spectroscopic and structural characterization of electrochemically grown ZnO quantum dots. *J. Appl. Phys.* **1999**, *85*, 2861–2865.
62. Jin, B.; Im, S.; Lee, S.. Violet and UV luminescence emitted from ZnO thin films grown on sapphire by pulsed laser deposition. *Thin Solid Films* **2000**, *366*, 107–110.
63. Vanheusden, K.; Warren, W.L.; Seager, C.H.; Tallant, D.R.; Voigt, J.A.; Gnade, B.E. Mechanisms behind green photoluminescence in ZnO phosphor powders. *J. Appl. Phys.* **1996**, *79*, 7983–7990.
64. Hosono, E.; Fujihara, S.; Kimura, T.; Imai, H. Non-Basic Solution Routes to Prepare ZnO Nanoparticles. *J. Sol-Gel Sci. Technol.* **2004**, *29*, 71–79.

65. Yu, J.; Wang, G.; Cheng, B.; Zhou, M. Effects of hydrothermal temperature and time on the photocatalytic activity and microstructures of bimodal mesoporous TiO<sub>2</sub> powders. *Appl. Catal. B Environ.* **2007**, *69*, 171–180.
66. Narayanan, R.; El-Sayed, M.A. Effect of Catalysis on the Stability of Metallic Nanoparticles: Suzuki Reaction Catalyzed by PVP-Palladium Nanoparticles. *J. Am. Chem. Soc.* **2003**, *125*, 8340–8347.
67. Ye, C.; Bando, Y.; Shen, G.; Golberg, D. Thickness-Dependent Photocatalytic Performance of ZnO Nanoplatelets. *J. Phys. Chem. B* **2006**, *110*, 15146–15151.
68. Pradhan, N.; Pal, A.; Pal, T. Catalytic Reduction of Aromatic Nitro Compounds by Coinage Metal Nanoparticles. *Langmuir* **2001**, *17*, 1800–1802.
69. Lee, C.Y.; Tseng, T.Y.; Li, S.Y.; Lin, P. Effect of phosphorus dopant on photoluminescence and field-emission characteristics of Mg<sub>0.1</sub>Zn<sub>0.9</sub>O nanowires. *J. Appl. Phys.* **2006**, *99*, 024303.
70. Biju, V.; Itoh, T.; Baba, Y.; Ishikawa, M. Quenching of Photoluminescence in Conjugates of Quantum Dots and Single-Walled Carbon Nanotube. *J. Phys. Chem. B* **2006**, *110*, 26068–26074.
71. Biju, V.; Makita, Y.; Sonoda, A.; Yokoyama, H.; Baba, Y.; Ishikawa, M. Temperature-Sensitive Photoluminescence of CdSe Quantum Dot Clusters. *J. Phys. Chem. B* **2005**, *109*, 13899–13905.
72. Lee, S.; Jeong, S.; Kim, D.; Hwang, S.; Jeon, M.; Moon, J. ZnO nanoparticles with controlled shapes and sizes prepared using a simple polyol synthesis. *Superlattices Microstruct.* **2008**, *43*, 330–339.
73. Sowri Babu, K.; Ramachandra Reddy, A.; Sujatha, C.; Reddy, K.V.G.; Mallika, A.N. Annealing effects on photoluminescence of ZnO nanoparticles. *Mater. Lett.* **2013**, *110*, 10–12.
74. Bao, D.; Gu, H.; Kuang, A. Sol-gel-derived c-axis oriented ZnO thin films. *Thin Solid Films* **1998**, *312*, 37–39.
75. Mathew, J.P.; Varghese, G.; Mathew, J. Effect of post-thermal annealing on the structural and optical properties of ZnO thin films prepared from a polymer precursor. *Chin. Phys. B* **2012**, *21*, 078104.
76. Tung, H.-M.; Huang, J.-H.; Tsai, D.-G.; Ai, C.-F.; Yu, G.-P. Hardness and residual stress in nanocrystalline ZrN films: Effect of bias voltage and heat treatment. *Mater. Sci. Eng. A* **2009**, *500*, 104–108.
77. Kim, J.-M.; Chung, H.-T. Electrochemical characteristics of orthorhombic LiMnO<sub>2</sub> with different degrees of stacking faults. *J. Power Sources* **2003**, *115*, 125–130.
78. Raji, R.; Gopchandran, K.G. ZnO nanostructures with tunable visible luminescence: Effects of kinetics of chemical reduction and annealing. *J. Sci. Adv. Mater. Devices* **2017**, *2*, 51–58.

79. Yuvakkumar, R.; Suresh, J.; Nathanael, A.J.; Sundrarajan, M.; Hong, S.I. Novel green synthetic strategy to prepare ZnO nanocrystals using rambutan (*Nephelium lappaceum* L.) peel extract and its antibacterial applications. *Mater. Sci. Eng. C* **2014**, *41*, 17–27.
80. Bora, T.; Myint, M.T.Z.; Al-Harhi, S.H.; Dutta, J. Role of surface defects on visible light enabled plasmonic photocatalysis in Au–ZnO nanocatalysts. *RSC Adv.* **2015**, *5*, 96670–96680.
81. Song, X.; Liu, Y.; Zheng, Y.; Ding, K.; Nie, S.; Yang, P. Synthesis of butterfly-like ZnO nanostructures and study of their self-reducing ability toward Au<sup>3+</sup> ions for enhanced photocatalytic efficiency. *Phys. Chem. Chem. Phys.* **2016**, *18*, 4577–4584.
82. Wang, X.; Huo, K.; Zhang, F.; Hu, Z.; Chu, P.K.; Tao, H.; Wu, Q.; Hu, Y.; Zhu, J. Structural Regulation and Optical Properties of One-Dimensional ZnO Nanomaterials in Situ Grown from and on Brass Substrates. *J. Phys. Chem. C* **2009**, *113*, 170–173.
83. Moghaddam, F.M.; Saeidian, H. Controlled microwave-assisted synthesis of ZnO nanopowder and its catalytic activity for O-acylation of alcohol and phenol. *Mater. Sci. Eng. B* **2007**, *139*, 265–269.
84. Raoufi, D. Synthesis and photoluminescence characterization of ZnO nanoparticles. *J. Lumin.* **2013**, *134*, 213–219.
85. Lu, P.; Zhang, H.; Satoh, T.; Ohkubo, T.; Yamazaki, A.; Takano, K.; Kamiya, T.; Zhu, L.; Huang, Y.; Jiang, Z.; et al. Investigation on the stability of water-soluble ZnO quantum dots in KB cells by X-ray fluorescence and absorption methods. *Nucl. Instrum. Methods Phys. Res. Sect. B Beam Interact. Mater. At.* **2011**, *269*, 1940–1943.
86. Schneider, R.; Balan, L.; Aldeek, F. Synthesis, Characterization and Biological Applications of Water-Soluble ZnO Quantum Dots. In *Nanomaterials*; Rahman, M., Ed.; InTech, 2011 ISBN 978-953-307-913-4.
87. Studenikin, S.A.; Golego, N.; Cocivera, M. Fabrication of green and orange photoluminescent, undoped ZnO films using spray pyrolysis. *J. Appl. Phys.* **1998**, *84*, 2287–2294.
88. Kwok, W.M.; Djurišić, A.B.; Leung, Y.H.; Chan, W.K.; Phillips, D.L. Time-resolved photoluminescence study of the stimulated emission in ZnO nanoneedles. *Appl. Phys. Lett.* **2005**, *87*, 093108.
89. Cross, R.B.M.; Souza, M.M.D.; Narayanan, E.M.S. A low temperature combination method for the production of ZnO nanowires. *Nanotechnology* **2005**, *16*, 2188–2192.
90. Liu, X.; Wu, X.; Cao, H.; Chang, R.P.H. Growth mechanism and properties of ZnO nanorods synthesized by plasma-enhanced chemical vapor deposition. *J. Appl. Phys.* **2004**, *95*, 3141–3147.
91. Fan, H.J.; Scholz, R.; Kolb, F.M.; Zacharias, M.; Gösele, U.; Heyroth, F.; Eisenschmidt, C.; Hempel, T.; Christen, J. On the growth mechanism and optical properties of ZnO multi-layer nanosheets. *Appl. Phys. A* **2004**, *79*, 1895–1900.

92. Gomi, M.; Oohira, N.; Ozaki, K.; Koyano, M. Photoluminescent and Structural Properties of Precipitated ZnO Fine Particles. *Jpn. J. Appl. Phys.* **2003**, *42*, 481–485.
93. Özgür, Ü.; Alivov, Y.I.; Liu, C.; Teke, A.; Reshchikov, M.A.; Doğan, S.; Avrutin, V.; Cho, S.-J.; Morkoç, H. A comprehensive review of ZnO materials and devices. *J. Appl. Phys.* **2005**, *98*, 041301.
94. Lin, B.; Fu, Z.; Jia, Y. Green luminescent center in undoped zinc oxide films deposited on silicon substrates. *Appl. Phys. Lett.* **2001**, *79*, 943–945.
95. Tonon, C.; Duvignacq, C.; Teyssedre, G.; Dinguirard, M. Degradation of the optical properties of ZnO-based thermal control coatings in simulated space environment. *J. Phys. Appl. Phys.* **2001**, *34*, 124–130.
96. Yatmaz, H.C.; Akyol, A.; Bayramoglu, M. Kinetics of the Photocatalytic Decolorization of an Azo Reactive Dye in Aqueous ZnO Suspensions. *Ind. Eng. Chem. Res.* **2004**, *43*, 6035–6039.
97. Xiong, H.-M.; Shchukin, D.G.; Möhwald, H.; Xu, Y.; Xia, Y.-Y. Sonochemical Synthesis of Highly Luminescent Zinc Oxide Nanoparticles Doped with Magnesium(II). *Angew. Chem. Int. Ed.* **2009**, *48*, 2727–2731.
98. Ghosh, S.; Priyam, A.; Bhattacharya, S.C.; Saha, A. Mechanistic Aspects of Quantum Dot Based Probing of Cu (II) Ions: Role of Dendrimer in Sensor Efficiency. *J. Fluoresc.* **2009**, *19*, 723–731.
99. Xiaohong, W.; Wei, Q.; Weidong, H. Thin bismuth oxide films prepared through the sol–gel method as photocatalyst. *J. Mol. Catal. Chem.* **2007**, *261*, 167–171.
100. Wang, X.; Zhang, S.; Peng, B.; Wang, H.; Yu, H.; Peng, F. Enhancing the photocatalytic efficiency of TiO<sub>2</sub> nanotube arrays for H<sub>2</sub> production by using non-noble metal cobalt as co-catalyst. *Mater. Lett.* **2016**, *165*, 37–40.
101. Jimenez-Cadena, G.; Comini, E.; Ferroni, M.; Vomiero, A.; Sberveglieri, G. Synthesis of different ZnO nanostructures by modified PVD process and potential use for dye-sensitized solar cells. *Mater. Chem. Phys.* **2010**, *124*, 694–698.
102. Ng, S.M.; Wong, D.S.N.; Phung, J.H.C.; Chua, H.S. Integrated miniature fluorescent probe to leverage the sensing potential of ZnO quantum dots for the detection of copper (II) ions. *Talanta* **2013**, *116*, 514–519.
103. Desai, A.V.; Haque, M.A. Mechanical properties of ZnO nanowires. *Sens. Actuators Phys.* **2007**, *134*, 169–176.
104. Zavar, S. A novel three component synthesis of 2-amino-4H-chromenes derivatives using nano ZnO catalyst. *Arab. J. Chem.* **2017**, *10*, S67–S70.
105. Hassan, N.K.; Hashim, M.R.; Bououdina, M. One-dimensional ZnO nanostructure growth prepared by thermal evaporation on different substrates: Ultraviolet emission as a function of size and dimensionality. *Ceram. Int.* **2013**, *39*, 7439–7444.

106. Ju, D.; Xu, H.; Zhang, J.; Guo, J.; Cao, B. Direct hydrothermal growth of ZnO nanosheets on electrode for ethanol sensing. *Sens. Actuators B Chem.* **2014**, *201*, 444–451.
107. Jang, E.S.; Won, J.-H.; Hwang, S.-J.; Choy, J.-H. Fine Tuning of the Face Orientation of ZnO Crystals to Optimize Their Photocatalytic Activity. *Adv. Mater.* **2006**, *18*, 3309–3312.
108. McLaren, A.; Valdes-Solis, T.; Li, G.; Tsang, S.C. Shape and Size Effects of ZnO Nanocrystals on Photocatalytic Activity. *J. Am. Chem. Soc.* **2009**, *131*, 12540–12541.
109. Talebian, N.; Nilforoushan, M.R. Comparative study of the structural, optical and photocatalytic properties of semiconductor metal oxides toward degradation of methylene blue. *Thin Solid Films* **2010**, *518*, 2210–2215.
110. Amornpitoksuk, P.; Suwanboon, S.; Sangkanu, S.; Sukhoom, A.; Wudtipan, J.; Srijan, K.; Kaewtaro, S. Synthesis, photocatalytic and antibacterial activities of ZnO particles modified by diblock copolymer. *Powder Technol.* **2011**, *212*, 432–438.
111. Kim, S.-J.; Park, D.-W. Preparation of ZnO nanopowders by thermal plasma and characterization of photo-catalytic property. *Appl. Surf. Sci.* **2009**, *255*, 5363–5367.
112. Torres Delgado, G.; Zúñiga Romero, C.I.; Mayén Hernández, S.A.; Castanedo Pérez, R.; Zelaya Angel, O. Optical and structural properties of the sol–gel-prepared ZnO thin films and their effect on the photocatalytic activity. *Sol. Energy Mater. Sol. Cells* **2009**, *93*, 55–59.

### **3. Chapter 3 ZnO-Au heterojunction enhanced the fluorescence and photocatalytic properties of ZnO NPs**

#### **3.1 Introduction**

Nowadays, hybrid nanomaterials especially plasmonic-semiconductor ones show unique and enhanced performances as the metallic and metal-oxide nanoparticles [1–6]. Thus, the addition of impurities into the ZnO nano-objects leads to the evolution of its structural, photoelectric, and photocatalytic properties [7–10]. Coupling the ZnO photocatalysts with other semiconductors [11–13], addition of carbon materials [14–18], or loading the ZnO with metals [19–24], are examples of doped impurities into ZnO.

Metallic nanoparticles are characterized by their surface plasmon resonance (SPR), which highly affect the exciton abilities of a semiconductor. Therefore, SPR-mediated emission has been effectively emerging, and commit to expand highly the fields of nanomaterials, especially the nano-optics research field. This is due to the collective oscillations of the free electrons relative to the metallic nanoparticles, which possess great potentials to enhance the efficiencies of semiconductor materials and devices. Plasmonic metals in combination with light emitters provide one of the important designs of functional nanomaterials that harmoniously interact by various mechanisms. Upon this interaction, the physical properties of the metallic nanoparticles could be modified, characterized by the SPR shift, and conversely, the photoemitter characteristics could be tuned, such as luminescence enhancement or quenching as a result of surface plasmon-mediated emission interaction, as well as the photocatalytic activity of the whole system. Therefore, the properties of both constituents may be modified, resulting in new characteristics that differs from the traits acquired by each material alone. The advanced and new functionalities make these hybrid systems useful in diverse domains, most importantly in photocatalysis [25–27], optoelectronics [28,29], biomedicine [30], etc. So far, Linsebigler *et al.* [31] have proved that the coupling of an exciton with SPR materials would affect the separation, pathways and the recombination rates of the photoexcited charges due to the formation of the Schottky barriers at the metal/semiconductor (M/SC) interface. These barriers are resulted from different band alignment and diverse work functions of both constituents. On this basis, the harmonious exciton/plasmon mixture is an important scientific concern, which investigates particular morphology and composition dependent properties, and often exhibits

multiple performances in addition to tunable and novel physical and chemical characteristics [32–34].

As they are highly stable nanomaterials, and acquire unique potentials in electronics, catalysis, chemical sensing, optics and biology [35–38], gold nanoparticles after coupling to ZnO nanostructures produce an effective hybrid system based on the exciton-plasmon cooperation. The coupling interaction between gold nanoparticles and ZnO nanostructures have been studied by several researchers, mainly to examine the sensor applications [39–43], as well as the photocatalytic activity of the hybrid systems [44–51]. This exciton-plasmon interaction was also found to highly affect the near band edge (NBE) emission efficiency of the semiconductor, where previously, PL enhancement or quenching was observed after doping metallic nanoparticles (e.g. Au, Ag) to ZnO [33,52–54].

The extent to which the exciton-plasmon coupling could be cooperative is found to be distance dependence in a way that the enhanced electric field near the metal nanoparticles can fade with junction length between the two materials [55–58]. Thus, the inter-distance between SC and metal nanoparticles was believed to manage the competition between enhancing and quenching the PL of the SC. Kulakovich *et al.* [59] and Chen *et al.* [60] have reported that a space of 10 nm between the semiconducting material and the metal is an optimal gap. At short distances, the metal quenches the PL. Whereas, at larger pathways, the SP of the metal decays since it is considered as a fading wave, which vanishes with distance, and thus, quenching may occur. In this context, based on many theoretical researches, the gap distance (heterojunction) separating the metal from the semiconductor has been widely studied to optimize a suitable distance allowing to obtain the highest PL enhancement required in the technology of optoelectronic devices [61,62]. Researchers working on the development of the semiconductor's emission have introduced a spacer into the hybrid system to supply the suitable length in order to boost the SC's photoluminescence [33,52,63]. As an example, Lawrie *et al.* have imported MgO spacer layers between GNPs and ZnO to control the latter's NBE emission enhancement. Chen *et al.* also included polystyrene-block-polyacrylic acid (PS154-*b*-PAA60) to augment the ZnO PL through citrate-capped GNPs. However, the attachment of additional molecules (organic/inorganic) into the hybrid system seems to influence the properties of the materials, and paves the way of possible side reactions to occur in the system. These additives are unfavorable, which bothers some applications based on the hybrid systems, indeed to be composed of pure components, especially in the biomedical applications where less chemical input is required.

In our work, we aimed to extend the absorption of the hybrid system into the visible region through the SPR effect of gold nanoparticles. They act as “antennas” for light, where at the nanoparticle’s surface, they afford fluctuate electric fields oscillating with similar frequency of the incident light under resonance conditions, and adapting higher intensities by several magnitudes [64,65]. This results in an improved band gap emission of the ZnO nanostructures without further addition of organic linkers or spacers, as well as deriving efficient photocatalytic activity. Moreover, the PL property was highly dependent on the characteristics of the GNPs used. The effect of the interfacial gap between the coupled nanomaterials has been devised chemically, *i.e.* by changing the surfactant type used in the GNPs synthesis, which alters the heterojunction distance without the addition of any supplementary molecules. Since the surfactant acts as a capping agent, it forms a shell-like around the nanoparticles, and therefore creates a specific distance between ZnO and GNPs nano-objects. To our knowledge, no work was reported in literature for ZnO-GNPs coupling based on the effect of regulating the used capping agent as a beneficial spacer for better PL enhancement.

The present study provides an efficient chemical way to fabricate plasmon-mediated exciton of ZnO-GNPs systems that could control the photoemission of the semiconductor to a high extent as well as its photocatalytic properties, creating an opportunity to apply our products in various applications.

## **3.2 Experimental part**

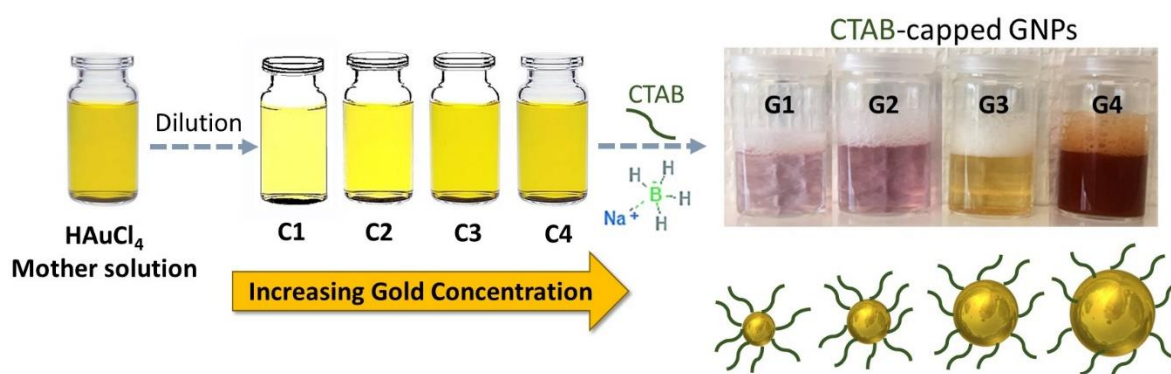
### **3.2.1 Reagents**

In this current work, all the purchased reagents were used without any further purification. Hydrogen tetrachloroaurate (III) trihydrate 99.99% ( $\text{HAuCl}_4 \cdot 3\text{H}_2\text{O}$ ) and (1-hexadecyl) trimethyl-ammonium bromide 98% ( $\text{CH}_3(\text{CH}_2)_{15}\text{N}(\text{CH}_3)_3\text{Br}$ ) was purchased from Alfa Aesar. However, sodium borohydride ( $\text{NaBH}_4$ ) was purchased from Merck KGaA.

### **3.2.2 Synthesis of gold nanoparticles (GNPs)**

The colloidal synthesis of CTAB-capped gold NP seeds in solution was established by the chemical reduction method [66], using  $\text{NaBH}_4$  as a reducing agent and CTAB surfactant. In the simple synthesis, four different sizes of GNPs were prepared by the subsequent

modification of the ratio of common tetrachloroauric acid gold precursor ( $\text{HAuCl}_4$ ) to the other used reagents. Different aqueous acidic gold concentrations of  $5 \times 10^{-5} \text{ M}$ ,  $8 \times 10^{-5} \text{ M}$ ,  $10^{-3} \text{ M}$  and  $10^{-2} \text{ M}$  were prepared by gentle stirring. After their total dissolving, the obtained solutions were added directly into 0.2 M of CTAB aqueous solution and stirred well to guarantee the total capping of the gold solution with CTAB surfactant molecules. Finally, a fresh solution of 0.01 M of  $\text{NaBH}_4$  was added to the CTAB-capped gold solutions, in order to obtain final GNPs of significantly different sizes of respective names; (G1, G2, G3 and G4). These solutions were settle down at room temperature for at least three hours in order to reach a complete reduction. The synthesis pathway is illustrated in Scheme 12. The obtained suspensions have different colors indicating the difference sized GNPs.



Scheme 12 Schematic representation of the synthesis of the CTAB-capped gold nanoparticles of different sizes using  $5 \times 10^{-5} \text{ M}$ ,  $8 \times 10^{-5} \text{ M}$ ,  $10^{-3} \text{ M}$  and  $10^{-2} \text{ M}$  of gold precursor concentration for G1, G2, G3 and G4 respectively.

According to this synthesis method, G1 was synthesized in different ways, yet conserving the volumes of the constituents as before. Gold nanoparticles were obtained after modifying the order of addition of the capping and reducing agents into the gold precursor. CTAB-free gold nanoparticles were synthesized through the direct reduction of the gold precursor by  $\text{NaBH}_4$ , in the absence of the capping agent, following by the capping of CTAB after being reduced.

### 3.2.3 Coupling ZnO to GNPs

The hybrid exciton-plasmon nanostructures have been synthesized by mixing the ZnO and GNPs solutions for 1 hour at 350 rpm. The previously prepared ZnO NPs were coupled into:

1. CTAB-capped gold nanoparticles of different sizes.
2. CTAB-capped gold precursor of concentration  $5 \times 10^{-5} \text{ M}$ , reduced by  $\text{NaBH}_4$  after coupling.

3. CTAB-free gold nanoparticles of precursor concentration  $5 \times 10^{-5}$  M.
4. CTAB-capped GNPs of precursor concentration  $5 \times 10^{-5}$  M after being reduced by  $\text{NaBH}_4$ .

Since some characterization techniques such as photoluminescence measurements depend on the number of the detected particles of the SC (section 5.1.1 in Appendix-A), the volume of ZnO NPs dispersion solutions was fixed in all the experiments as 1 ml. Then, the GNPs were added in different volumes in order to obtain a proportional ratio (R) with ZnO NPs, where  $R = V_{\text{GNPs}}/V_{\text{ZnO}}$ . The GNPs/ZnO ratio was varied by 0.1, 0.5, 1 & 2, representing the respective addition of 0.1, 0.5, 1, and 2 ml of GNPs to 1 ml of ZnO dispersion. This leads to loading the ZnO NPs dispersions with 10%, 50%, 100% and 200% GNPs, respectively. At the end, a compensating amounts of deionized water were added to reach a total final volume of the solution (3 ml), to avoid any effect of concentration-dependent analysis (not in all studies).

### 3.3 Results and discussion

#### 3.3.1 Role of the semiconductor part (ZnO size) in the interaction with GNPs

In order to understand the effects of ZnO properties in the coupling, as first investigations, the fabricated CTAB-capped gold nanoparticles (G1) were coupled to ZnO nanoparticles of different sizes *i.e.* ZnO nanocrystals annealed at different temperatures, according to the previous chapter. The coupling between ZnO and G1 was attained in a volume ratio of  $R_{\text{G1/ZnO}} = 0.1$ . Therefore, the ZnO solution was embedded by 10% of gold G1. The different ZnO samples annealed at temperatures ranging from 80 to 800°C and introduced into G1 solution were then studied by photoluminescence measurements. For these samples, no significant change in the ZnO visible emission was observed after addition of GNPs. Therefore, we only focused on the changes in the ZnO UV emission. The modification of the NBE emission intensity of the Au/ZnO samples with respect to the bare ZnO was highlighted by the modification factor (F) and was represented by:

$$F = \Delta I_h / \Delta I_{\text{ZnO}} \quad (18)$$

where  $\Delta I_h$  is the maximum UV-PL height intensity of the hybrid solution contained the GNPs loaded ZnO ( $[I_{\text{max(UV)}} - I_0]$  of the hybrid system), and  $\Delta I_{\text{ZnO}}$  is the maximum UV-PL height intensity of the pure ZnO without any addition of GNPs ( $[I_{\text{max(UV)}} - I_0]$  of the bare ZnO used).

Therefore,  $F=1$  is the characteristic factor for ZnO before the addition of Au NPs ( $R=0$ ). If  $F>1$ , we can consider that the ZnO exciton emission is enhanced by GNPs, whereas, if  $F<1$ , then the emission is quenched.

The UV-PL modification factor ( $F$ ) of different ZnO NPs coupled into G1 was estimated from their relative PL spectra of each hybrid sample, and the results are illustrated in Figure 28.

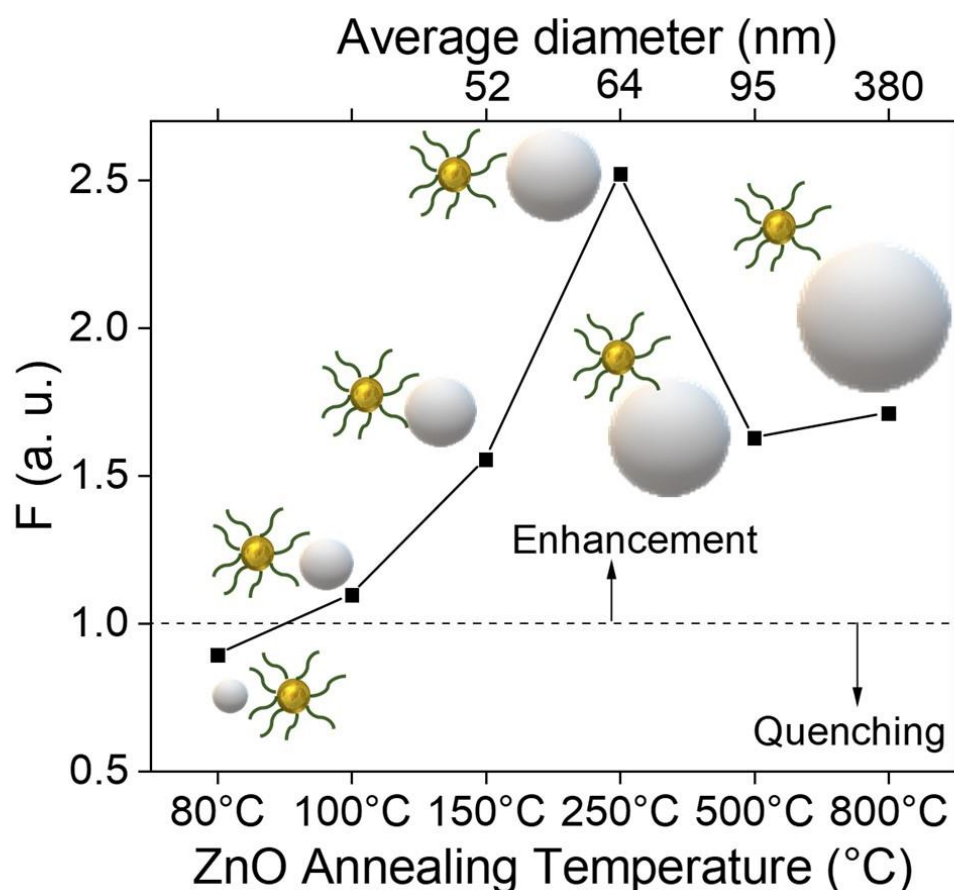


Figure 28 UV-PL modification factor of the hybrids after the addition of G1 in a ratio  $R_{G1/ZnO}=0.1$  to ZnO nanoparticles of different sizes. The different sized gray spheres represent ZnO NPs of specific size and the gold spheres capped with the green shell represent the gold nanoparticles capped by the CTAB respectively. Only one sphere from each hybrid system is represented for simplification. ZnO NPs of different sizes were obtained by annealing ZnO nanocrystals of small size at different temperatures ranging from 80 to 800°C.

As observed in Figure 28, the enhancement efficiency increased with boosting the annealing temperatures up to 250°C. Above this value, the enhancement started decreasing with the excessive annealing above 250°C. GNPs quenched the 80°C annealed ZnO emission, however, increasing the annealing temperatures into 100°C induced the GNPs to slightly enhance the ZnO emission. Due to the presence of the hydroxynitrate microstructures that encapsulate ZnO nanocrystals (as seen in chapter 2, figures 21 and 22) when annealed at 80 and 100°C, we

weren't able to determine ZnO size at these 2 points. For this reason, we didn't show in figure 28 the diameter of ZnO below 150°C.

On this basis, we can divide our analysis into three behavior ranges:

1. The quenching at the smallest ZnO nanoparticle size, *i.e.* at low annealing temperatures <100°C.
2. The raised enhancement efficiency at 100-250°C.
3. The drop down enhancement efficiency at 500-800°C.

These preliminary results can be explained based on a state of art summary of the literature on plasmon-exciton interaction in the following manner:

During the PL measurements, the excitation wavelength (325 nm) is sufficient to induce electrons from the valence band (VB) of ZnO NPs into the conduction band (CB), leaving behind positively charged holes, and creating electron-hole pairs, which could spontaneously recombine, represented by the NBE exciton emission.

On the other hand, it is well known that gold nanoparticles have localized surface plasmon resonance in the visible region of the electromagnetic spectrum [67]. They are considered as an electron reservoir that have a big ability to accept electrons. Consequently, the photo-excited electrons presented in the CB of the ZnO NPs can easily transfer to the attached gold nanoparticles. We expect that the corresponding charge pathway could be in competition with the exciton radiative emission.

As stated before in chapter 1, the contact between the semiconductors and metal nanoparticles is either Schottky or Ohmic, depending on the type of the semiconductor, and the work functions of both constituents [68]. Normally, when materials having different work functions are coupled together, a Schottky barrier will form, and the electrons will transfer from the lower work function material to the higher work function material [69–73]. The work function of ZnO nanoparticles is 4.2 [74], and for GNPs is 5.1-5.2 [75,76]. Therefore, after excitation, the charge is proposed to transfer from ZnO into GNPs, which proposes the quenching of the ZnO luminescence. Fageria *et al.* reported that the fermi level of GNPs is higher than that of ZnO NPs due to its larger work function. Under UV radiation, the electrons flow from the CB of ZnO NPs into the surface of attached GNPs after inhibition of the  $e^-h^+$  recombination in the ZnO, so that PL quenching could be observed [23].

On another hand, Wei *et al.* assumed that the surface plasmons from metallic nanoparticles can excite semiconductors, and the inverse is correct [77]. The absorption of gold nanoparticles

involves components from the excitation of both the interband transitions and surface plasmons at wavelengths less than 500 nm, while surface plasmons apart, dominantly absorb at wavelengths longer than 500 nm. Add to that, gold nanoparticles have a filled d-level in their electronic configuration (Au<sup>0</sup>: 1s<sup>2</sup> 2s<sup>2</sup> 2p<sup>6</sup> 3s<sup>2</sup> 3p<sup>6</sup> 4s<sup>2</sup> 3d<sup>10</sup> 4p<sup>6</sup> 5s<sup>2</sup> 4d<sup>10</sup> 5p<sup>6</sup> 6s<sup>1</sup> 4f<sup>14</sup> 5d<sup>10</sup>). This filled d-orbital below the fermi level supports a big number of electrons for the interband transitions under UV excitation [78,79]. Therefore, 3.81 eV is enough to excite the GNPs interband. However, for the metal to couple with a semiconductor, the resonant frequencies must match each other. Thus, the photon absorption of the metal nanoparticle must be correlated with respect to that of the semiconductor in order to investigate their spectral overlap. The visible emission of the ZnO NPs here (500-800 nm) is indeed overlapped with the absorption of the SPR of the GNPs.

In this context, GNPs can be charge donors, as well as charge acceptor materials depending on the interaction conditions with the coupled molecules. This allow the possibility of either PL enhancement of the linked ZnO NPs or PL quenching phenomena, after exciton-plasmon interaction.

After UV excitation of the hybrids, GNPs are induced to loose e<sup>-</sup> and release them in the solution, to become positively charged. They will also have the affinity to acquire electrons in order to attain their equilibrium state, as they have a great ability to gain electrons [80].

As reported by Lai *et al.*, the enhancement in the UV-PL intensity in the SC is associated to the increase in the concentration of the free carriers, resulting from the resonant coupling between the radiative recombination in the semiconductor and the SP arising from the metal. In addition, PL enhancement could be resulted from the charge and/or energy transfer between the plasmon of the metal and the exciton of the semiconductor used [63]. The latest hypothesis can be explained as a result of increased light absorption by ZnO due to the scattering by GNPs explained by Atwater *et al.* [81]. Moreover, in the presence of photo-excited charges on the CB of the ZnO NPs, an efficient energy transfer could take place between ZnO NPs and GNPs by exciton-SP resonant coupling, that accumulate the surface electron density within GNPs [82]. As a result, hot electrons presenting on high energy states of the GNPs can highly transfer into the CB of the ZnO NPs, thereby increasing the number of photo-excited electrons, which involve the high emission represented by the PL enhancement [83].

Furthermore, the quenching of the exciton emission could be attributed to the destruction of electron-hole recombination in the ZnO nanostructures. The photoexcited electrons present at the conduction band (CB) of ZnO could easily transfer into the gold nanoparticles, and the

exciton recombination in ZnO NPs decreases, leading to the PL quenching. Moreover, the surface electrons in the GNPs can easily trap the holes in the ZnO NPs, and therefore, charge carrier recombination in ZnO would reduce as reported by Jin *et al.* [84].

In the previous chapter, the XRD measurements showed that the purity of the ZnO NPs is different depending on the annealing temperature, while before annealing,  $\text{Zn}_5(\text{NO}_3)_2(\text{OH})_8 \cdot 2\text{H}_2\text{O}$  crystalline structure was the major composition of the product, that contain only 9% of amorphous ZnO nanoparticles. Consequently, annealing supported the sintering and elimination of the microstructure phase to completely vanish above 250°C indicating 100% pure ZnO NPs. This is the temperature threshold by which the excessive annealing can lead to the sintering of the nanoparticles, thus increasing their final size. The presence of the complexes acts as a barrier for the complete coupling of the ZnO to the GNPs. For that, ZnO annealed at 80°C showing 90% of the microstructures that could be at a large distance from the attached GNPs in addition to the distance honored by the CTAB capping the GNPs. The large distance lead to the fading of the PR wave, and thus, quenching of the ZnO luminescence was obtained. This was obvious after coupling the gold nanoparticles into the synthesis raw material of ZnO NPs explained in Figure 52 in section 5.1.4 of Appendix-A.

Increasing the annealing temperature into 250°C have proportionally decreased the composition of the complex microstructures till total disappearance, and therefore the distance created by the complex was also decreased. Herein, a harmonious coupling between GNPs and ZnO NPs is proposed, resulted from the Schottky Au–ZnO contact that enables the injection of electrons from gold to ZnO nanostructures. This results in an enhancement of the ZnO luminescence. Moreover, as the annealing temperature increased to 250°C, the quantity of the microstructures as well as the ZnO-GNPs separation distance decreased. Then, the coupling between the materials in the hybrid becomes more synergic. Proportionally, the PL enhancement increases.

ZnO samples annealed above 250°C presents 100% pure ZnO NPs (no presence of the microstructures). Increasing the annealing temperatures have greatly increased the size of the ZnO. Therefore, in this range, the enhancement evolution is controlled by the size effect. As the size of the ZnO increases, the surface to volume ratio decreases. Therefore, surface recombination of the charges becomes weaker as the photoexcited charges become far from the surface, facilitating the interfacial charge transfer into the GNPs, which in turns decreases the enhancement efficiency of the ZnO exciton emission. Moreover, as the size of ZnO NPs increases, their absorption peak position is red-shifted into higher wavelengths as observed in

chapter 2. Hence, the absorption peak becomes far from the excitation wavelength, decreasing the initial radiative recombination of pure ZnO as well as that after coupling with G1.

From all the above results, it could be concluded that for better PL enhancement of ZnO NPs, gold nanoparticles must be coupled into 100% pure ZnO NPs with a moderate size. Here, annealing the ZnO nanostructures at 250°C ended up into the smallest 100% pure materials, where the post-thermal treatment decreased the raw material microstructures and yielded in proper sized ZnO NPs, which aids in the enhancement of the ZnO PL.

On this basis, different ways of exciton-plasmon interactions will be studied using the pure ZnO samples annealed at 250°C due to the high PL enhancement that they provided.

### 3.3.2 Role of the plasmonic part (GNPs size or number, capping) in the interaction with ZnO nanocrystals

Due to the proper size and purity in addition to high photoluminescence and best photocatalytic activity, ZnO NPs annealed at 250°C was selected to be coupled to gold nanospheres of different diameters to elucidate the surface plasmons effects in the plasmon-exciton interaction. Then, for all GNPs sizes, different routes of coupling were adapted to monitor the ZnO PL quenching/enhancement. Figure 29 represents the SEM and TEM images for the selected ZnO NPs for coupling, as well as their extinction and the PL spectra.

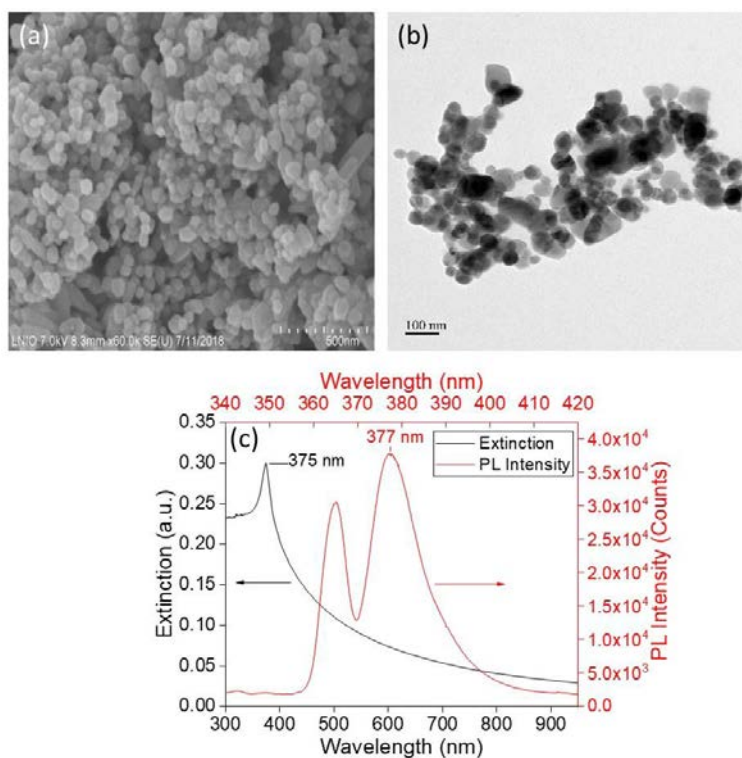


Figure 29 ZnO NPs annealed at 250°C (a) SEM-FEG image and (b) TEM image and (c) extinction (black) and average photoluminescence (red) of three PL spectrum measured separately (laser power is slightly different).

The UV-Vis absorption of a water solution of ZnO was recorded, before and after loading the solution with gold nanoparticles. As formerly explained in chapter 2, the extinction spectrum of the bare ZnO NPs (before the addition of GNPs) indicates a sharp absorption peak at 375 nm. This peak is correlated to the exciton band (ground excitonic state) of ZnO nanostructures [85]. Additionally, photoluminescence (PL) was measured with a UV excitation wavelength of 325 nm. ZnO photoluminescence showed two UV emissions, one at ~366 nm that was attributed to the Raman peak of the water solvent (see section 2.3.1.3 in chapter 2), and the other is positioned at 377 nm. The latter peak was referred to the exciton radiative recombination (see section 2.3.1.4 in chapter 2).

On the other hand, the synthesis of different sizes of GNPs was achieved, as assessed in the experimental part. The obtained solutions are named G1, G2, G3 and G4 corresponding to the initial gold precursors concentrations  $5 \times 10^{-5}$  M,  $8 \times 10^{-5}$  M,  $10^{-3}$  M &  $10^{-2}$  M proportionally, marked by different colors previously observed in Scheme 12.

SEM images for the CTAB-capped GNPs were examined after centrifugation of the NPs in order to remove the CTAB from the samples. The pure NPs were then dispersed in water, and further diluted in order to deposit the GNPs on Si-substrates by spin-coating, to be ready for imaging. 10  $\mu$ L of each solution were spin-coated at a speed of 1000 rpm and acceleration 3000 rpm/sec. The SEM images for the four different samples are shown in Figure 30. All nanoparticles show spherical morphology. Some aggregations are indeed observed after the extraction of the nanoparticles from a solution medium, and their deposition on substrates.

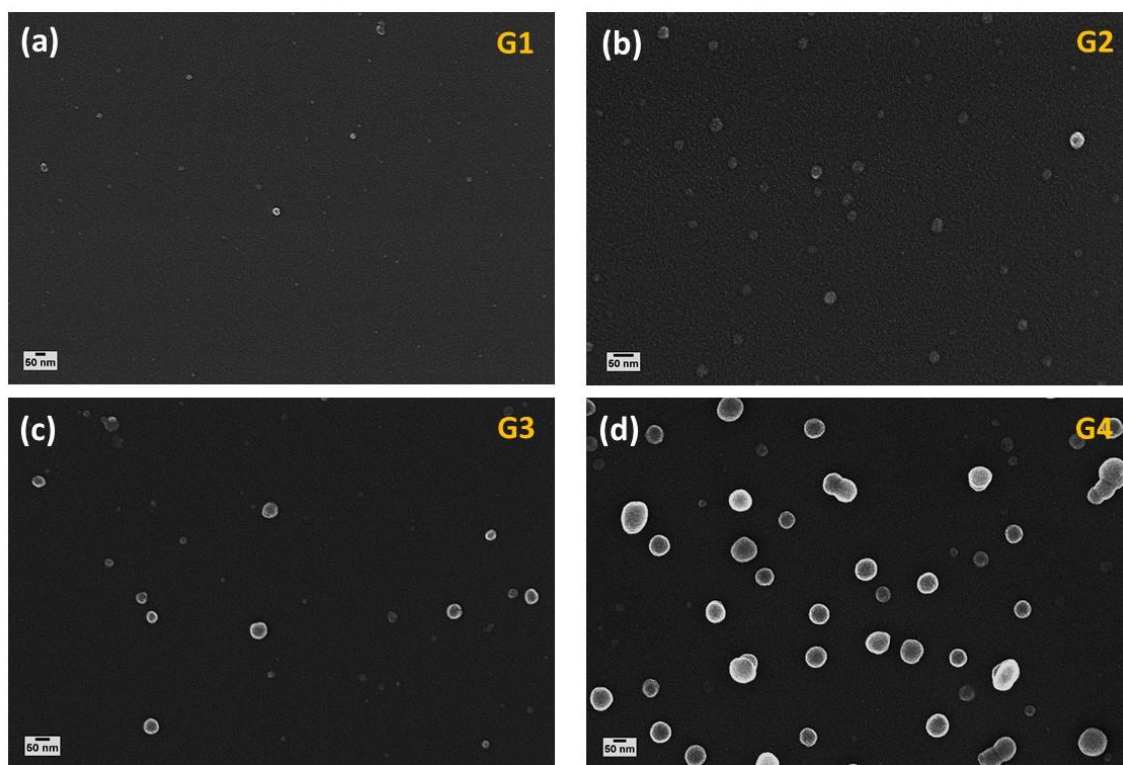


Figure 30 SEM images of the fabricated gold nanoparticles after centrifugation and dispersion in water (a) G1, (b) G2, (c) G3, (d) G4. The scale in all images is 200 nm.

One can see the gradual increase of the GNPs size from G1 until G4. The average size estimated from the SEM images relative to G1, G2, G3 and G4, is respectively 25 nm, 29 nm, 66 nm, and 77 nm.

The extinction spectra of G1, G2, G3 and G4 are also shown in Figure 31.

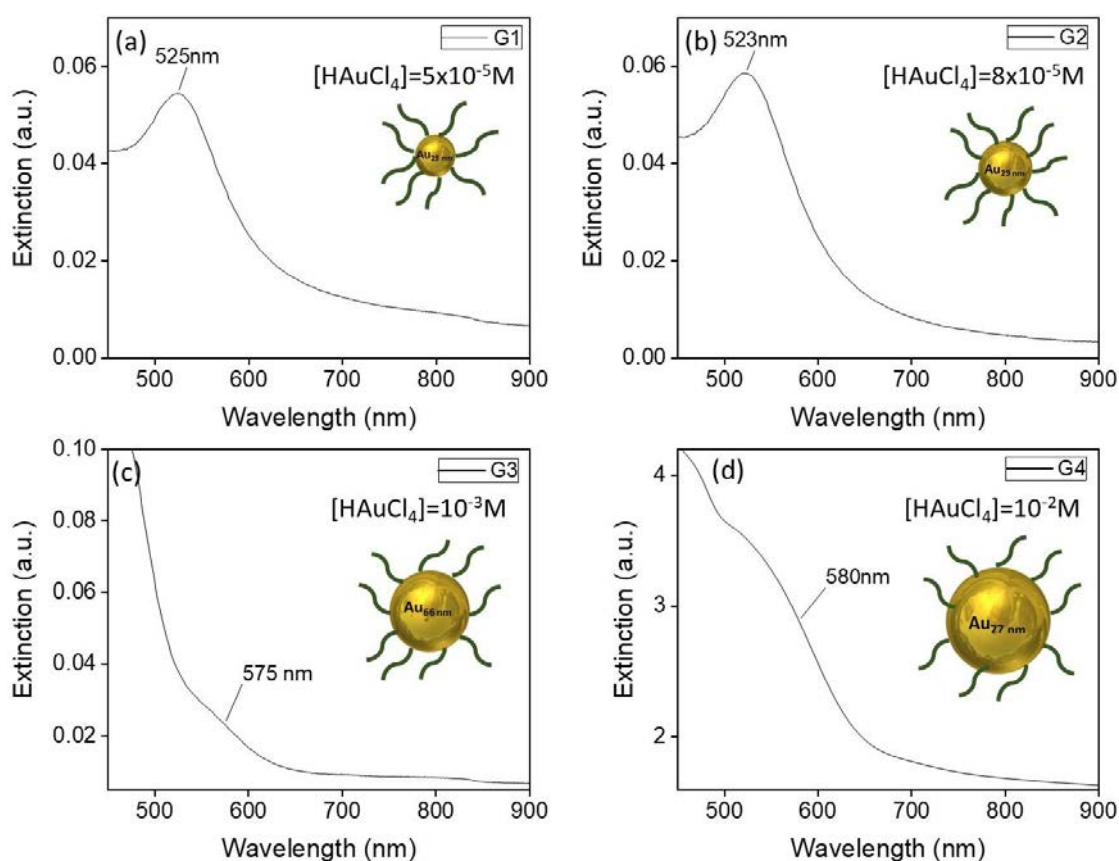
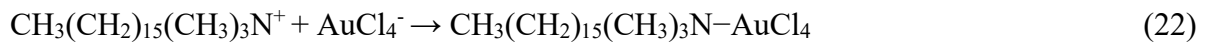
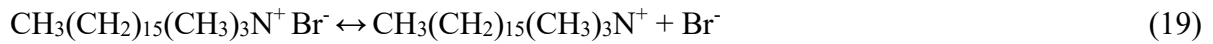


Figure 31 Extinction spectra of the CTAB-capped gold nanoparticles produced using 0.2 M of CTAB as a capping agent (a) G1 of  $[HAuCl_4] = 5 \times 10^{-5} M$ , (b) G2 of  $[HAuCl_4] = 8 \times 10^{-5} M$ , (c) G3 of  $[HAuCl_4] = 10^{-3} M$ , (d) G4 of  $[HAuCl_4] = 10^{-2} M$  (smoothed curve).

The visible absorption represents the surface plasmon resonance (SPR) band of the fabricated GNPs that are sensitive to the morphology of metals. The surface plasmons (SP) of G1 and G2 are nearly similar of respective values 525 nm and 523 nm lying in the spherical morphology zone of the absorption spectrum which is confirmed by their SEM images in Figure 30(a and b). Referring to Mie theory, the SPR position and intensity highly depend on the size, shape, composition, and dielectric constant at metal surface, which will affect the electron charge density on particle surface [86]. After increasing the concentrations of the gold precursor ( $[HAuCl_4]$ ), the size of the GNPs is supposed to increase conserving the spherical morphology at a constant CTAB concentration. A gradual increase in the intensities of absorption, and a red shift in the position of the SPR peaks was observed. For G3 and G4, SPR bands changed to a broad shoulder instead of a peak absorbing at 575 nm and 580 nm, respectively. The size increase of spherical gold nanoparticles was obvious in the SEM images illustrated in Figure 30 and can explain this peaks broadness. The highest concentrations of gold precursors yielded in the appearance of a sharp peak and a shoulder one, correspondingly

at 395 nm and 485 nm for G3, and at 390 nm and 460 nm for G4 (not shown in the extinction spectra for an obvious observation of the plasmon band, see Figure 51 of Appendix-A for the complete spectra). The formation of these new peaks were attributed to the complexation formed between the positive head group of the CTAB surfactant ( $\text{N}^+(\text{CH}_3)_3$ ) and the ionized species of the acid gold precursor ( $\text{AuCl}_4^-$ ) by electrostatic interaction. The formation of  $[\text{AuBr}_4^-]$  complexes were also resulted after the solution became oversaturated. As shown in Scheme 12, G1 and G2 exhibited a transparent pink color solutions with G2 is slightly more intense than G1. Yet, G3 displayed a transparent dark yellow color, and G4 showed a turbid dark orange-to brownish solution. Nikoobakht *et al.* [87] and Khan *et al.* [88] have reported the formation of these peaks. Khan *et al.* assigned that the formed CTA- $\text{AuCl}_4$  complex capped inside the CTAB micelles is insoluble in water, which leads to the formation of the yellow color and the surfactant-gold ions precipitate. Moreover, Pérez-Juste *et al.* correlated the color and the formed precipitate to the adsorbed  $\text{AuCl}_4^-$  onto the CTAB head [89]. The formation mechanisms of the resulted complexes from the interaction between  $\text{HAuCl}_4$  and CTAB through ligand exchange reactions are summarized as follows.



Equation (21) is a fast reaction that produces  $[\text{AuBr}_4^-]$  responsible for the orange color by a multi-step ligand exchange reaction that occurs in less than a minute [90].

Subsequently, the obtained GNPs were added into a constant solution volume of the ZnO NPs shown in Figure 36. The volume of the added GNPs was varied in all sets to obtain a GNPs/ZnO volume ratio of 0.1, 0.5, 1 and 2. Therefore, 16 different hybrid samples were obtained. The extinction and the PL behavior of the hybrid nanosystems were studied. The results are depicted in Figure 32.

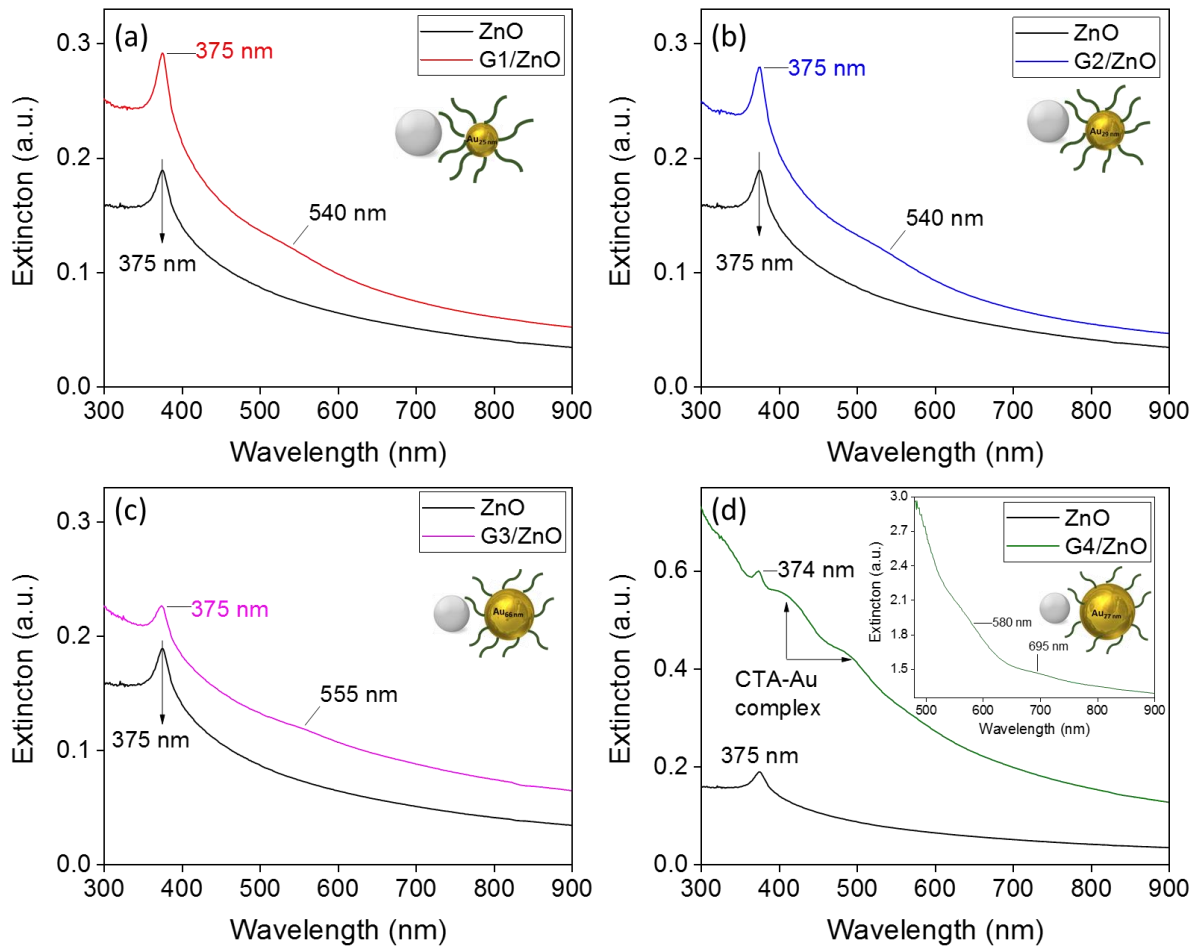


Figure 32 Extinction spectra of ZnO NPs solution before and after the addition of GNPs (a) G1 ( $R_{G1/ZnO}=2$ ), (b) G2 ( $R_{G2/ZnO}=2$ ), (c) G3 ( $R_{G3/ZnO}=2$ ), (g) G4 ( $R_{G4/ZnO}=0.1$ ), the inset in (d) is the zoom in UV region of the extinction spectrum of coupling G4 to ZnO NPs in a ratio  $R_{G4/ZnO}=2$ .

To examine the contribution of the peak corresponding to GNPs absorption in the hybrid systems, only the hybrid having  $R_{GNPs/ZnO}=2$  for coupling ZnO with G1, G2 and G3 are represented. The extinction spectrum of the hybrid system corresponding to G4 coupled to ZnO is represented by the hybrid ratio  $R=0.1$  in order to identify the position of the peak related to ZnO NPs absorption, and  $R=2$  (inset of the figure) to clarify the SPR absorption peaks.

After the addition of four different sizes of GNPs onto the ZnO NPs dispersions, the extinction spectra displayed new behaviors in correlation to bare GNPs (previously illustrated in Figure 31) and ZnO ones. The evolution in the absorption peaks of the hybrid results from the interface interaction between GNPs and ZnO NPs, in addition to the novel size and structure of the hybrid constituents [91,92]. This revealed a successful hybridization, *i.e.* strong plasmon-exciton coupling.

The SPR of G1 and G2 in the hybrid interaction transformed into a broad shoulder instead of a peak, red-shifted with respect to that of pure gold, both located at 540 nm. Concerning G3,

the CTA-AuCl<sub>4</sub> complex band disappeared after coupling and the SPR of G3 blue-shifted by 20 nm to absorb at 555 nm. Finally, G4 exhibited a red shift in the CTA-AuCl<sub>4</sub> complex, preserving the 580 nm absorption peak, accompanied by a new shoulder at 695 nm. The evolution of the SPR bands relative to the GNPs is attributed to change in its local environment due to ZnO presence in its surrounding medium. This shift confirms the surface modification of GNPs by ZnO NPs. The ZnO corresponding absorption peak intensity was enhanced through the addition of G1, where increasing the GNPs size lead to its gradual decrease.

As assessed before, ZnO emission has a confined peak located in the UV and visible regions. The UV emission corresponds to the near band edge (NBE) emission, whereas the visible broad emission refers to the defect luminescence. The UV emission of the ZnO NPs is ranging in the absorption region of the GNPs interband, and the visible emission of the ZnO NPs is overlapped with the absorption of the SPR of the GNPs. Thus, the interaction lead to the synergic coupling between the exciton of the ZnO and the SPR of GNPs that could resonantly absorb the ZnO visible emission, resulting in plasmon excited gold nanoparticles. This entitles us to talk about charge and/or energy transfer between the ZnO GNPs that cause the modification of ZnO luminescence.

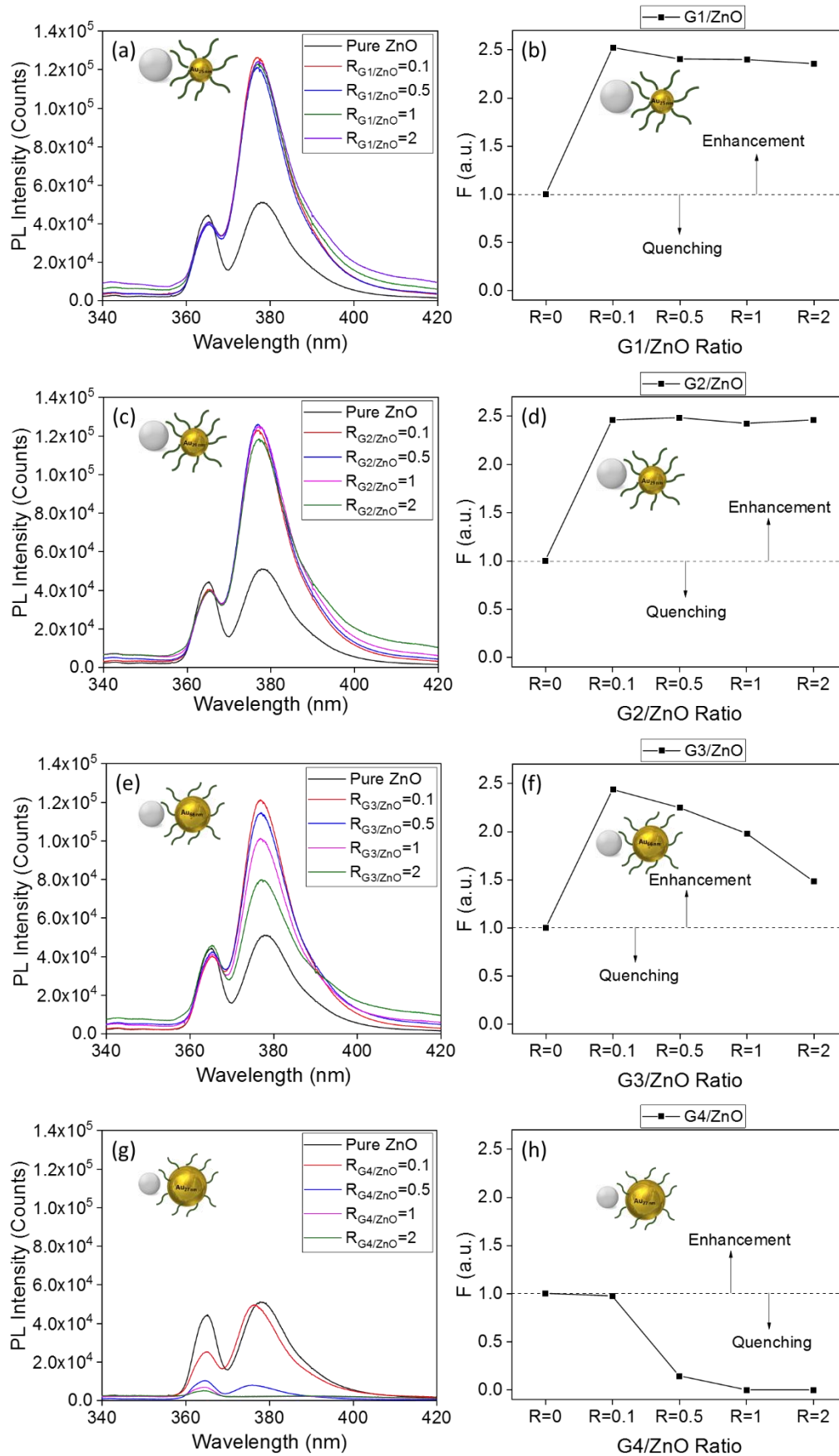


Figure 33 UV-zone of the PL spectra (right), and the UV-PL modification factor (left) of ZnO NPs solutions before and after the addition of (a,b) G1, (c,d) G2, (e,f) G3, and (g,h) G4.

The PL observations in Figure 33 (a, c, e and g) showed that coupling ZnO NPs with gold nanoparticles, in all ratios for all GNPs sizes, are found to enhance the ZnO UV emission compared to that of the pure ZnO, except for G4 which had opposite response. However, using G1 and G2 nanoparticles, the intensity of the ZnO UV-band remained nearly constant after raising the volume ratio of GNPs in the hybrid solutions above 0.1. Yet, increased loading of G3 gold nanoparticles into ZnO resulted in the decrease of the PL Intensity. On the other side, embedding ZnO with G4, having the highest size among all GNPs, the UV-PL at R=0.1 was similar to that of pure ZnO (inconsiderable decrease in the exciton emission). The further increase in G4 gold NP content leads to the quenching of the UV emission of ZnO to reach a complete suppression of the UV luminescence to the noise level.

Figure 33 (b, d, f and h) represents the UV-PL modification factor of ZnO NPs upon adding GNPs respectively, G1, G2, G3 and G4 in different numbers (Ratios). G1 and G2 showed nearly similar responses of non-affected enhancement efficiency upon increasing the GNPs content. This indicates that there is a threshold of recombination in the ZnO NPs that can not be exceeded. Contrarily, increasing G3 number in the hybrid solution negatively affects the UV-PL enhancement factor in the enhancement zone. Individually, increasing G4 loading quenched the ZnO exciton emission. This phenomena is due to the fact that larger GNPs are deficit in  $e^-$ , and cannot serve them into ZnO NPs to enhance their PL, which in turns may acquire their deficiency in electrons from the ZnO NPs when loaded in high quantities.

To summarize, GNPs of small dimensions ( $< 70$  nm) and present in small amounts in ZnO-Au hybrid systems gave rise to PL enhancement. From there, it may be expected that charge transfer from small GNPs to ZnO is behind this successful coupling.

It is worthy to note that the hypothesis of the possibility that the UV-PL enhancement emission is induced by the stabilizing agent CTAB is excluded because we measured the PL of ZnO NPs solution in the presence of CTAB without GNPs. The results in section 5.1.5 of Appendix-A show that CTAB solution alone prevents the ZnO NPs to even absorb or emit light. As a result, the enhancement was not resulted from the contribution of CTAB, but from the SPR effects of the GNPs.

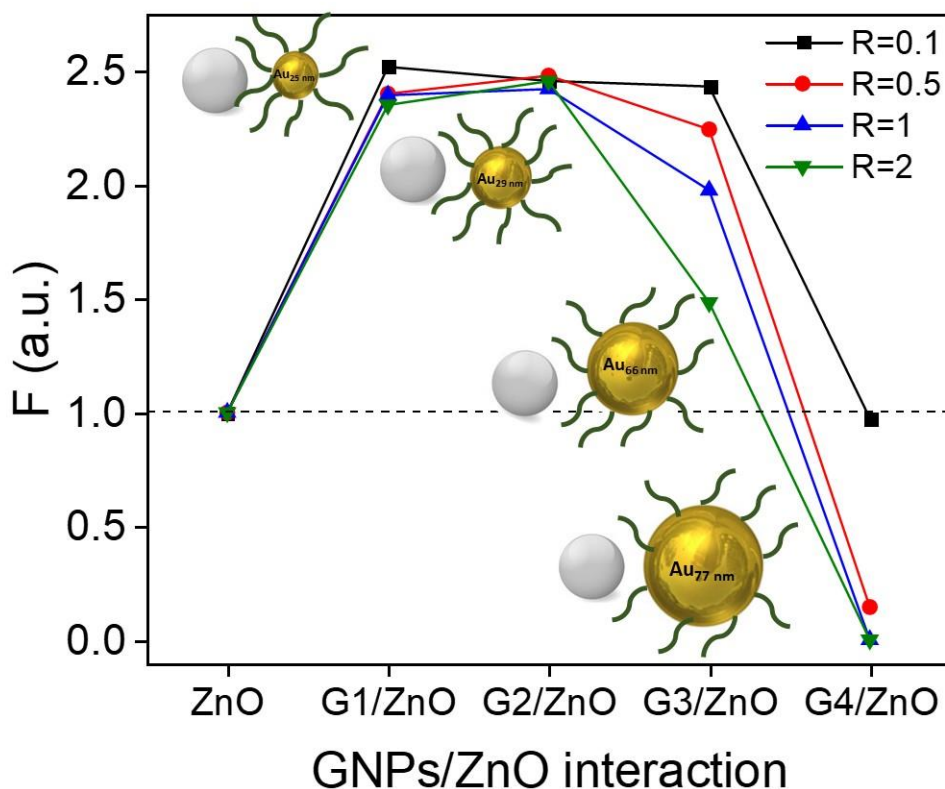


Figure 34 UV-PL modification factor of ZnO NPs solutions before and after the addition of increased sizes GNPs G1, G2, G3, and G4 for all GNPs/ZnO ratios.

These findings may be attributed to the lower absorption of the GNPs with increasing their size. When the light absorption is weaker than scattering, the electron transfer from GNP to ZnO becomes lower, leading to less radiative recombinations as reported by Mahanti *et al.* [93], and thus the PL enhancement decreases with GNPs size, till quenching at G4. After the GNPs become larger, their surface energy (surface/volume ratio) drop down with size. Consequently, the number and mobility of the GNPs surface electrons will decrease with GNPs size. Therefore, less electrons are transferred into the CB of ZnO NPs. This will minimize the latest exciton recombination, to finally decrease the enhancement efficiency. In addition, G1 and G2 are relatively similar in size (25 nm and 29 nm respectively, derived from the SEM images). Their small sizes allow these GNPs to attach totally over the ZnO surface. Herein, at small GNPs sizes, and taking into consideration the spectral overlap between ZnO emission and GNPs absorption mentioned before, when the light of the exciton emission from ZnO is incident on the GNPs, the high-density electrons in the small GNPs form an electron cloud and fluctuate. The electrons then concentrate at the interface between the metal and ZnO, proceeded by a band bending in ZnO side. Consequently, an easy electron transfer from the GNPs to ZnO

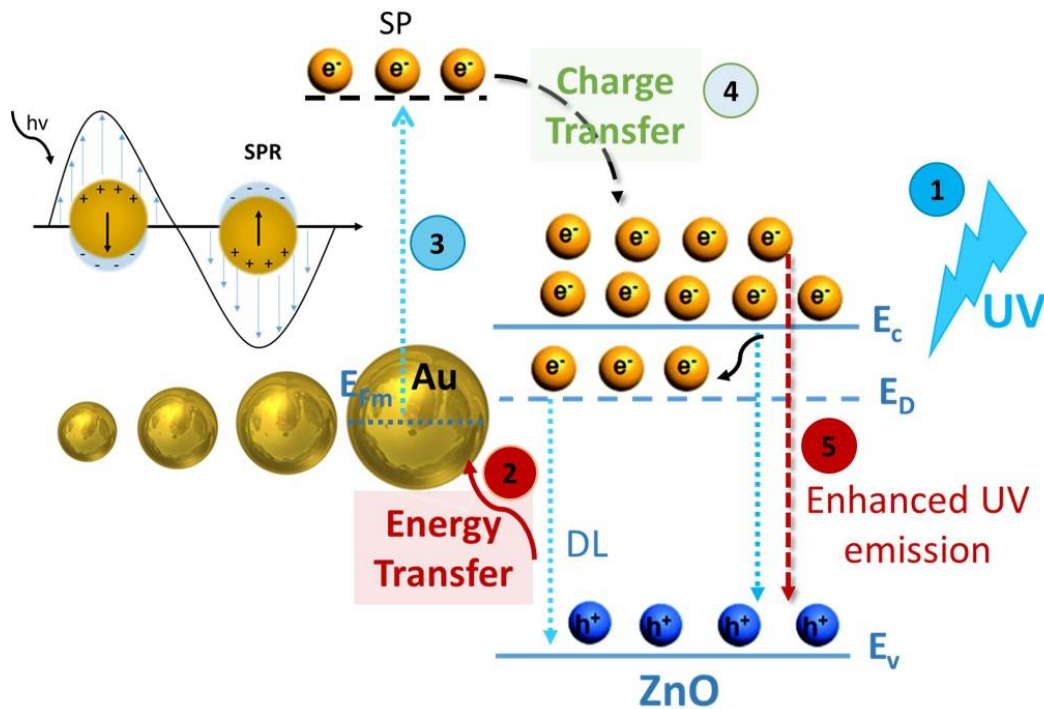
NPs could occur. After boosting the volumes (number) of G1 and G2 in the hybrids, no significant impact over the charge transfer into ZnO surface is observed. Thus, PL enhancement is not affected. Therefore, ZnO has a threshold emission satisfied by the small quantity of GNPs which induced the saturated recombination in the hybrid samples, after which the further addition of GNPs could no more enhance the NBE emission.

Adding to the fact of G3 that has less surface electrons than G1 and G2 due to its bigger size, then less electrons could be transferred into ZnO compared to G1 and G2. Augmenting the number of G3 could lead to a competitive mechanism between the charge transfer from GNPs into ZnO, and the inverse pathway to return the electrons into GNPs. Therefore, the PL enhancement efficiency decreases with G3's number.

The exaggerated increase in the size of G4 let the NPs have very weak surface electrons which could not transfer into the ZnO NPs. At small ratios, the presence of GNPs has no impact over the ZnO emission. At higher G4 numbers, with small surface energy, the GNPs could highly be able to gain electrons, and thus these electrons could be acquired from the ZnO CB after excitation. Add to that, as the number of GNPs increases, the CTAB quantity will increase with respect to the content of the whole solution. Thus, the possibility to prevent ZnO NPs from absorbing and emitting light increases. Moreover, big sized GNPs could trap the holes in the ZnO surfaces. All these factors lead to favoring the charge transfer from ZnO CB into GNPs, resulting in a quenching of its luminescence.

The charge transfer from GNPs into ZnO NPs is induced by the energy transfer from ZnO NP into GNPs. In another words, ZnO NPs have a visible luminescence referring to the defect emissions ranging from 500 nm to 800 nm (see section 2.3.3.2). This emission range is overlapped with the absorption range of the loaded GNPs. Consequently, the visible luminescence could be absorbed by the GNPs. The absorption of GNPs to the visible luminescence could act as an internal visible excitation of the GNPs, leading to the generation of the hot electrons over the surface of the GNPs, which could be transferred into the CB of the ZnO NPs, and thus, increasing the radiative recombination in the ZnO NPs reflected by the PL enhancement. This phenomena is known by the PIRET effect (Plasmon Induced Resonance Energy Transfer).

The enhancement of the UV PL by GNPs under UV irradiation is illustrated in Scheme 13.



Scheme 13 The mechanism of the UV-PL enhancement of ZnO NPs by GNPs under UV-irradiation.

As the size of GNPs increases, the interfacial interaction between ZnO and GNPs decreases, and thus, less energy is absorbed by the GNPs, and therefore less PL enhancement is observed. In the PIRET effect, five process will occur to enhance the the PL of ZnO NPs by the GNPs:

1. Under UV irradiation, UV and visible luminescence will be results in the ZnO NPs, related to the exciton and defect luminescence respectively.
2. The defect luminescence will be absorbed by the GNPs (energy transfer).
3. SPR will be generated over the surface of the GNPs.
4. The SP could be transferred into the CB of the ZnO NPs to increase the number of e<sup>-</sup> in this band.
5. Radiative recombination will increase in the ZnO NPs due to the higher number of e<sup>-</sup> in the ZnO NPs, and thus, PL is enhanced.

This enhancement effect is validated by the distance between GNPs and ZnO NPs created by the CTAB capping agent, which weakens the schottky barrier effect (previously explained), to allow the indirect charge transfer from GNPs into ZnO NPs under UV irradiation, through the energy transfer.

The distribution of the CTAB-capped gold nanoparticles loaded over ZnO NPs was evaluated by SEM imaging (Figure 35). The image clarifies the distance created by the CTAB between AuNPs and ZnO NPs. The small particles corresponds to the GNPs, and the larger ones correspond to the ZnO NPs since the ZnO NPs used have larger size than the GNPs used.

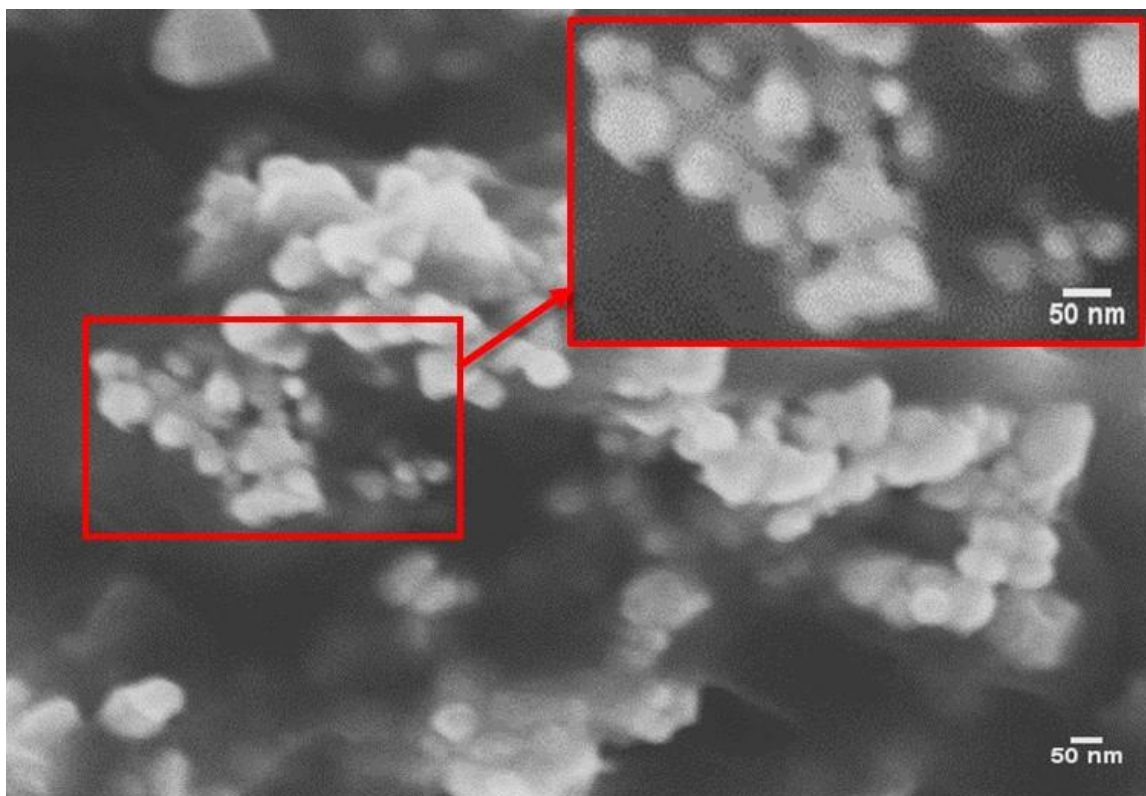


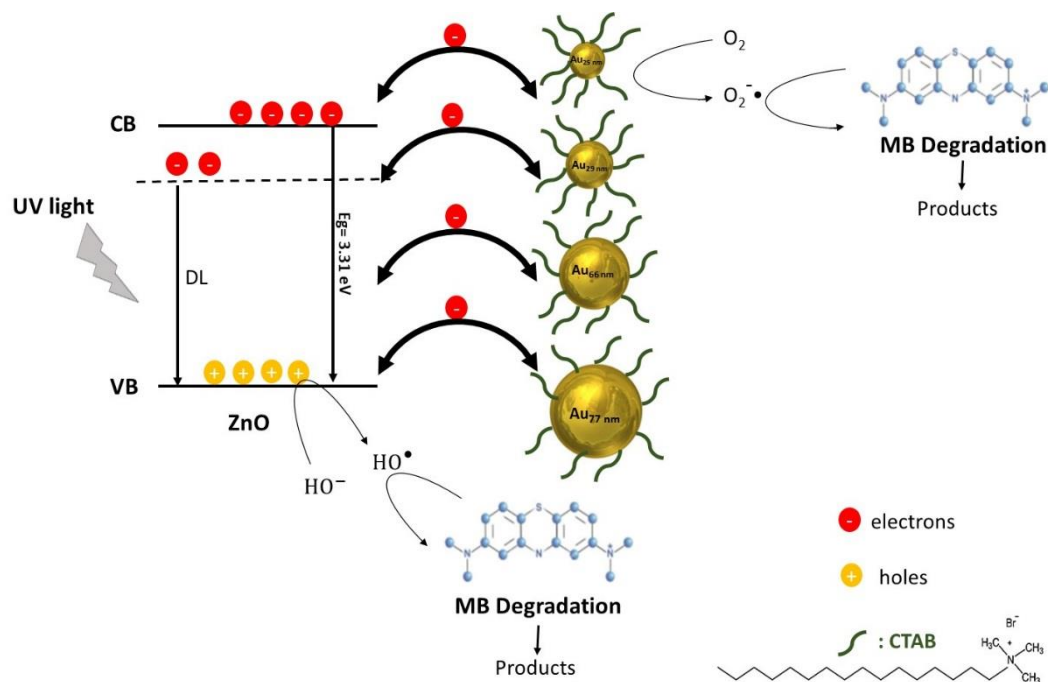
Figure 35 SEM image of the CTAB-capped GNPs loaded over ZnO NPs (annealed at 250°C). The inset shows a zoom in a specific region to clarify the contact between ZnO NPs and capped gold NPs.

In view of this, we could conclude that the coupling ZnO NPs with the smallest size of CTAB-capped GNPs ( $[HAuCl_4] = 5 \times 10^{-5} \text{ M}$ ) in a ratio  $R_{GNPs/ZnO} = 0.1$ , are the best experimental parameters to adapt a suitable binding aspect between ZnO NPs and GNPs surfaces and to enhance the ZnO emission better. However, increasing the size and number of GNPs in the hybrid solutions negatively affects the PL enhancement especially at very high GNPs sizes which suppresses the luminescence of ZnO NPs.

### 3.3.3 Photocatalytic performance of ZnO-GNPs

For a better understanding of the optical properties of the studied hybrid systems and also to evaluate their performance as catalysts, the samples were evaluated by photocatalysis. The main objective behind this study was to elucidate the merit of the plasmon-exciton junction in the photocatalysis activity of ZnO. To make it possible, we measured the ability of the ZnO

NPs before and after coupling with GNPs to degrade methylene blue (MB) dye, under UV light irradiation (365 nm). The photocatalytic (PC) process was well described previously in chapter 2, and the charge transfer between ZnO and GNPs was also detailed. The charge transfer and PC activity is illustrated in scheme 13.



Scheme 14 Schematic representation of the charge transfer and the photocatalytic activity of CTAB-capped gold nanoparticles of different sizes loaded into ZnO NPs (DL: defect luminescence).

It is worth to note that the concentration of the used catalyst here (in the hybrid systems) is two times diluted with respect to that used in chapter 2 due to the additional solutions of GNPs and compensating water. The comparison of the photocatalytic activities between both concentrations of the same ZnO catalyst (annealed at 250°C) is illustrated in Figure 36.

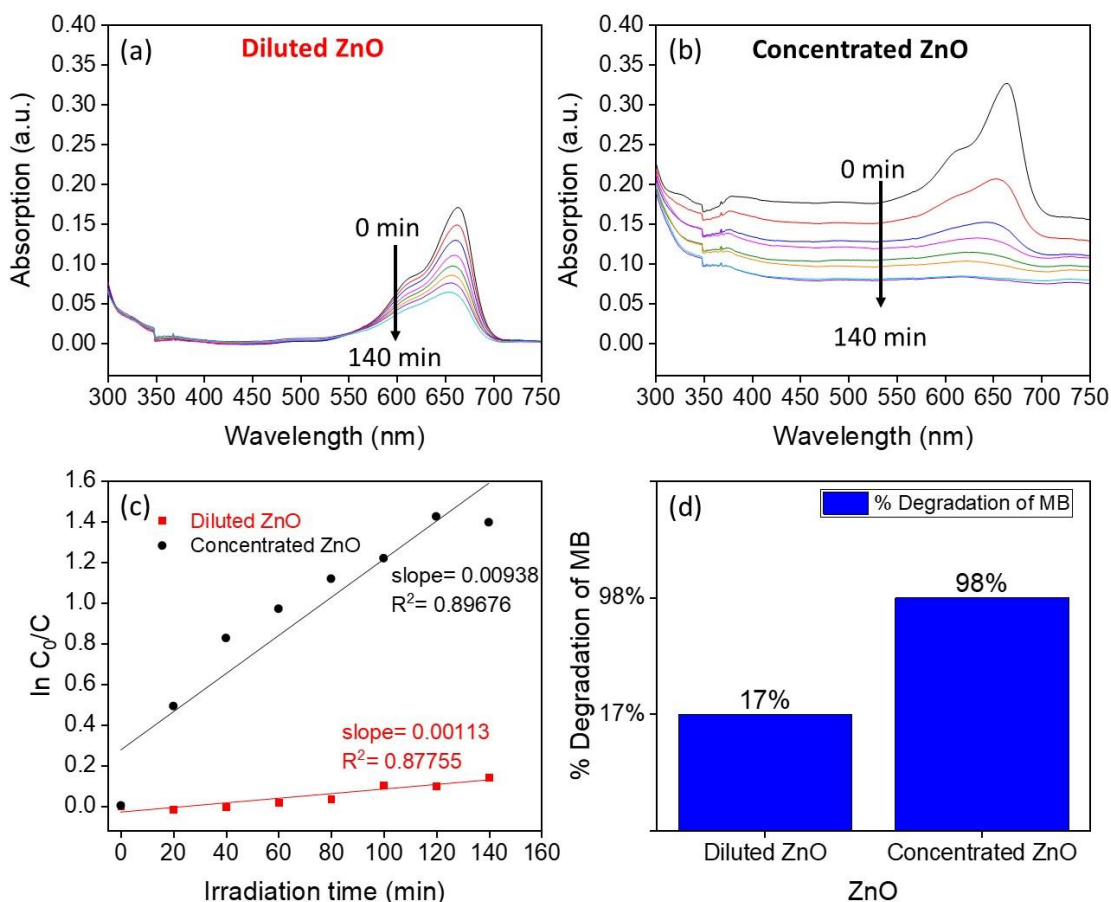


Figure 36 Absorption of ZnO ( $T_{\text{ann}}=250^\circ\text{C}$ )-MB mixture with UV irradiation for different irradiation time intervals lasting for 140 min using (a) diluted solution of ZnO catalyst, and (b) concentrated solution of the same ZnO catalyst, (c) the variation of  $\ln C_0/C$  of both catalysts concentrations with irradiation time lasting for 140 min, (d) % degradation of MB by different concentrations of ZnO catalyst.

The ZnO catalyst is diluted by water (no GNPs), and in this case, the MB molecules were slowly degraded. This is shown in Figure 36(a) by the small decrease of the absorption intensity of the MB in the presence of diluted ZnO NPs at 664 nm, which corresponds to the absorption wavelength of the MB dye. The degradation percentage of MB observed in Figure 36(d) has decreased from 98% using the concentrated solution of the ZnO catalyst until 17% after dilution. This indicates that the photocatalytic activity depends on the concentration of the catalyst used.

Subsequently, ZnO catalyst was then loaded by the fabricated GNPs. As a result, ZnO catalyst was diluted by the GNPs and water in the same factor. The photocatalytic activities of ZnO/CTAB-capped GNPs hybrid systems were also evaluated through the degradation of MB under UV irradiation. In particular, the photocatalytic activities of GNPs/ZnO were investigated considering the four different sizes of the CTAB-capped gold nanoparticles (G1, G2, G3 and G4), deposited in different volume fractions on ZnO, to obtain various GNPs/ZnO

ratios (taking into consideration the addition of compensating volume of water to reach an equal total volume for all samples). The photocatalytic experiments were carried in the same way proceeded for the non-modified ZnO, that were previously studied in chapter 2.

The results in terms of MB degradation assembled by the G1/ZnO-MB mixture absorption, as a function of irradiation time were reported in Figure 37.

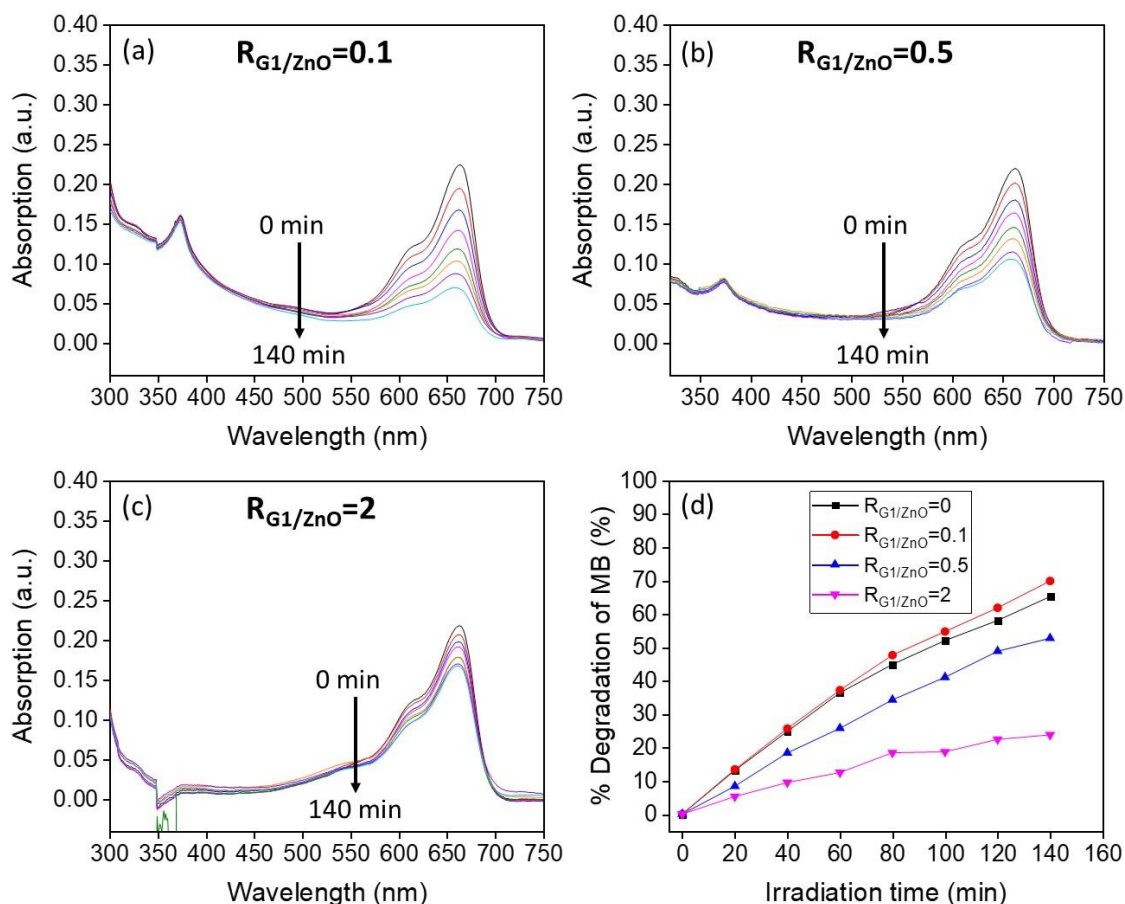


Figure 37 Absorption of G1-loaded ZnO ( $T_{\text{ann}}=250^{\circ}\text{C}$ )-MB mixture with UV irradiation for different irradiation time intervals lasting for 140 min at different GNPs/ZnO ratios (a)  $R_{\text{G1/ZnO}}=0.1$ , (b)  $R_{\text{G1/ZnO}}=0.5$ , (c)  $R_{\text{G1/ZnO}}=2$ , (d) % degradation of MB using the three ratios G1/ZnO mixed with MB as a function of irradiation time.

The absorption intensity at 664 nm relative to the MB absorption slightly decreased with UV irradiation in all ratios as seen in Figure 37(a, b and c). Moreover, the % of degradation of MB investigated in Figure 37(d) shows that the photocatalytic activity of the G1/ZnO catalyst decreased in comparison to that of bare ZnO catalyst for all G1/ZnO ratios except for  $R=0.1$  which was nearly similar to the bare ZnO. The decrease of the % degradation of MB was more efficient with increasing the loading content of G1, where the MB degradation decreased further after increasing ratios from  $R=0.1$  up to  $R=2$ . Therefore, G1 nanoparticles suppressed the ZnO photoactivity with increasing the volume fraction of G1 in solution.

This may be attributed to the fact that the higher amount of the GNPs is, the more doping species are creating chemical or physical defects in the nanocrystal. These defects could act as trapping sites for the photogenerated electron-hole pairs, which in turn reduce the photocatalytic activity that depends on the separation of these charges. The decreased separations of the photoexcited charges means the recombination of these charges. This was confirmed by the enhanced photoluminescence of the hybrid using G1 (Figure 33 (a and b)).

G2 NPs were also loaded into the same ZnO in four different ratios, and the hybrid's photoactivity against MB dye was also evaluated. The results are shown in Figure 38. As observed in Figure 38(a, b, c and d), the four hybrids were able to make degradation of the MB dye where its absorbance was decreasing with increasing the irradiation time. The % degradation of the hybrids were lower than that of the bare ZnO NPs. One can also observe that the % degradation of MB is similar to that of bare ZnO NP when loaded in a ratio 0.1, 0.5 and 1. This % decreased with the further increase in G2 NPs in the solution to R=2. The main reason here is similar to that explained using G1, and could also be referred using G2. Also, the relative PL activities that showed enhancement of the ZnO photoemission in the presence of G2, confirm the proposed hypothesis.

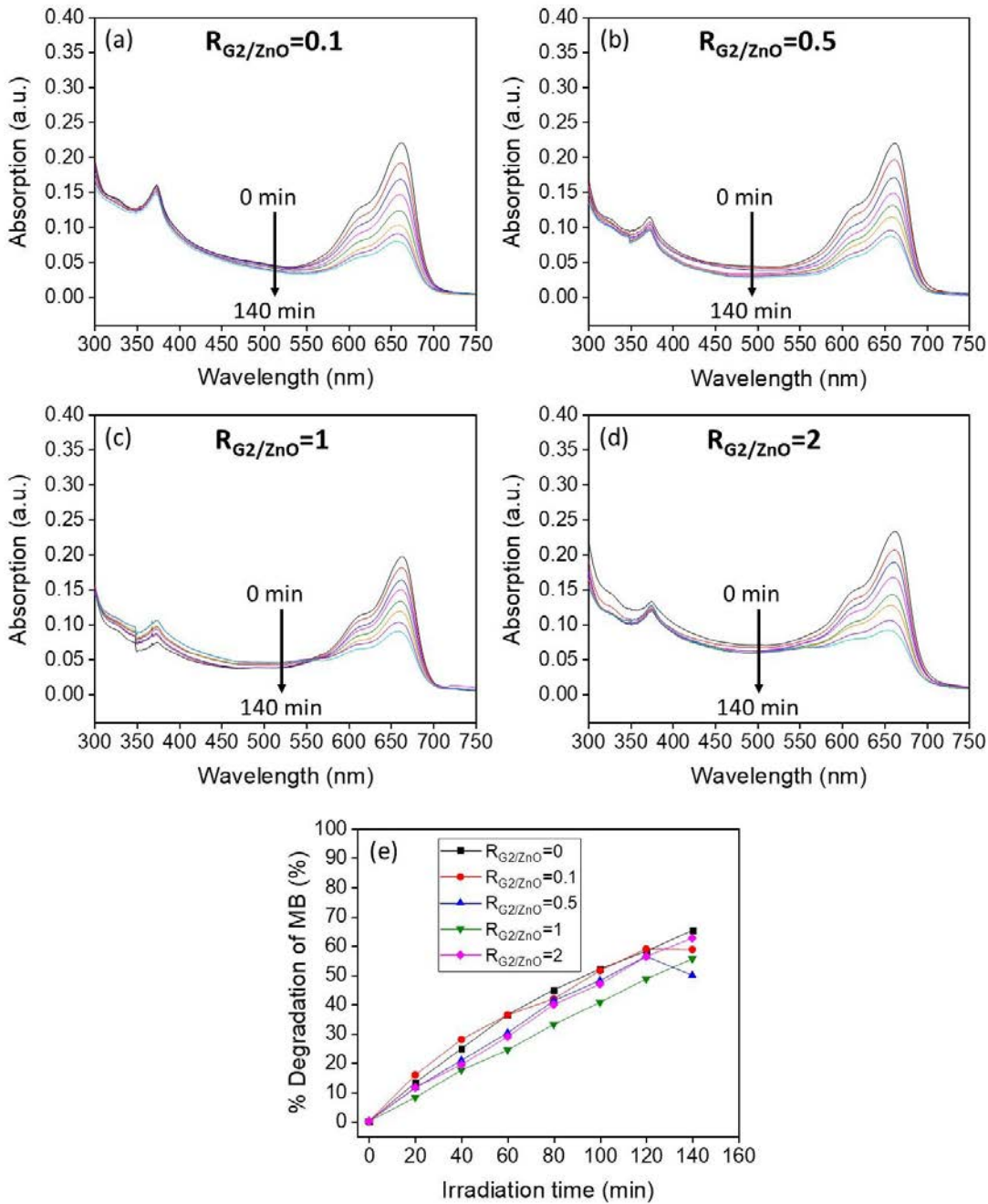


Figure 38 Absorption of G2-loaded ZnO ( $T_{ann}=250^{\circ}\text{C}$ )-MB mixture with UV irradiation for different irradiation time intervals lasting for 140 min at different GNPs/ZnO ratios (a)  $R_{G2/ZnO}=0.1$ , (b)  $R_{G2/ZnO}=0.5$ , (c)  $R_{G2/ZnO}=1$ , (d)  $R_{G2/ZnO}=2$ , (e) % degradation of MB using the four ratios G2/ZnO mixed with MB as a function of irradiation time.

The photoactivity of G3-loaded ZnO NPs was also studied and shown in Figure 39.

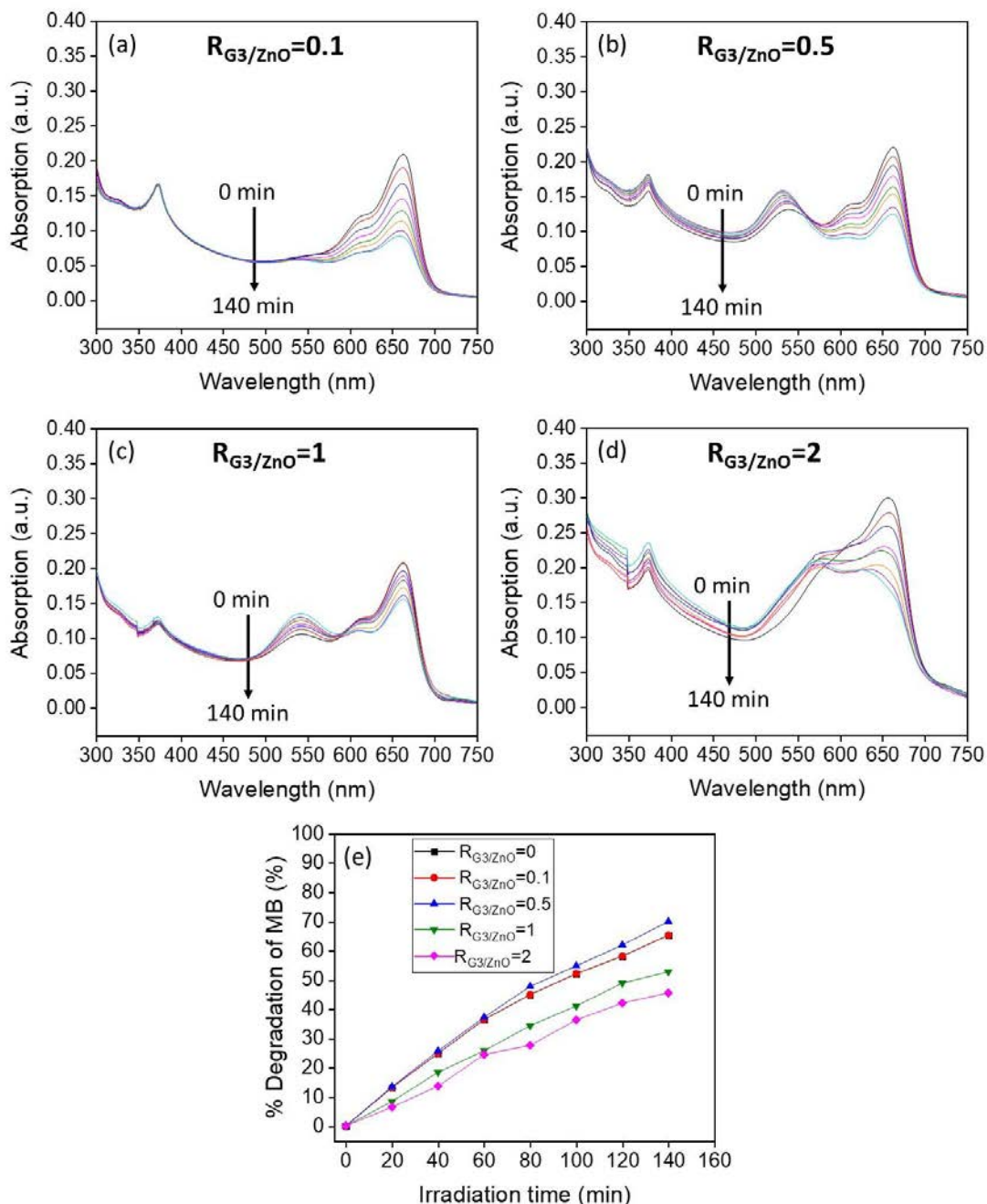


Figure 39 Absorption of G3-loaded ZnO ( $T_{\text{ann}}=250^{\circ}\text{C}$ )-MB mixture with UV irradiation for different irradiation time intervals lasting for 140 min at different GNPs/ZnO ratios (a)  $R_{\text{G3/ZnO}}=0.1$ , (b)  $R_{\text{G3/ZnO}}=0.5$ , (c)  $R_{\text{G3/ZnO}}=1$ , (d)  $R_{\text{G3/ZnO}}=2$ , (e) % degradation of MB using the four ratios G3/ZnO mixed with MB as a function of irradiation time.

The MB absorption at 664 nm observed in Figure 39(a, b, c and d) also decreased with UV irradiation in the presence of the four hybrids (four different G3/ZnO ratios). The % degradation of MB at  $R=0.1$  and  $R=0.5$  are similar to that of bare ZnO, which decreases with the further increase of gold NPs contents.

The study of the G4-loaded ZnO NPs photoactivity of was also shown in Figure 40.

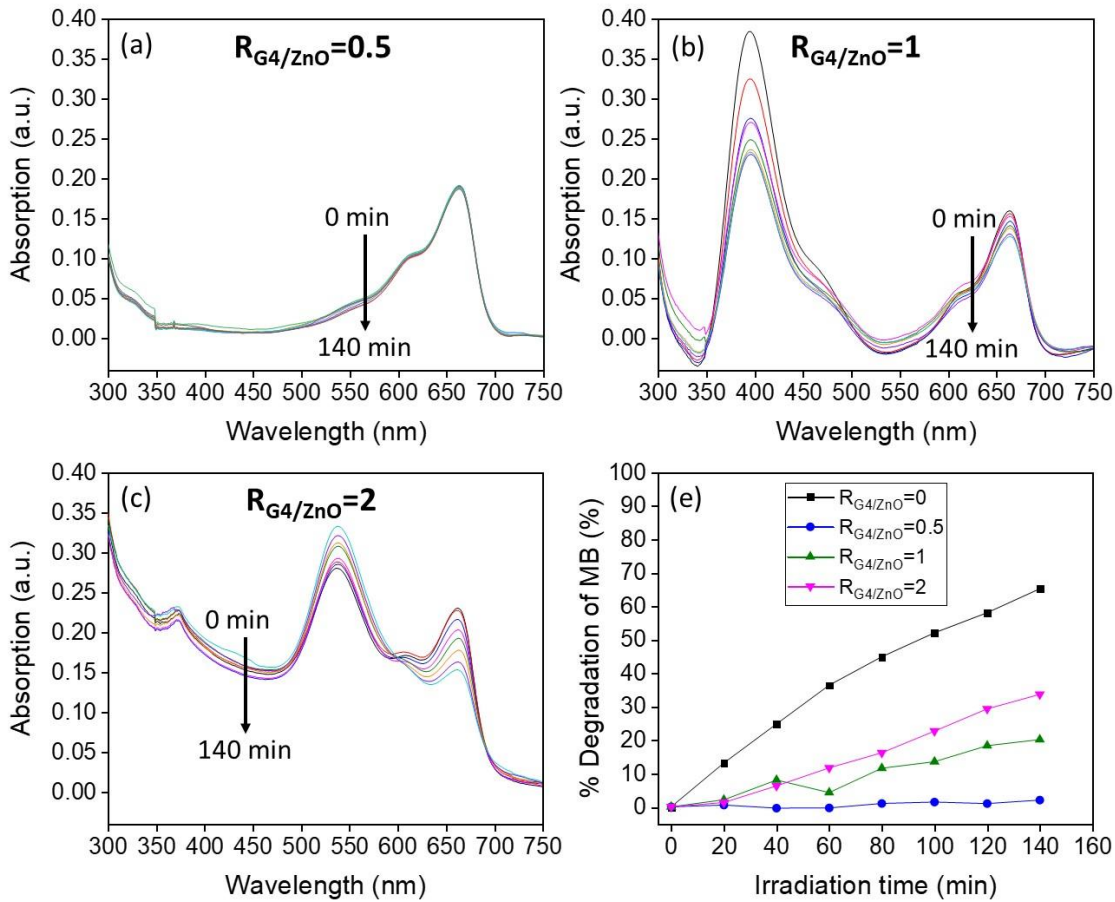


Figure 40 Absorption of G4-loaded ZnO ( $T_{ann}=250^{\circ}\text{C}$ )-MB mixture with UV irradiation for different irradiation time intervals lasting for 140 min at different GNPs/ZnO ratios (a)  $R_{G4/ZnO}=0.5$ , (b)  $R_{G4/ZnO}=1$ , (c)  $R_{G4/ZnO}=2$ , (d) % degradation of MB using the three ratios G4/ZnO mixed with MB as a function of irradiation time.

It is clearly observed that the G4 NPs quenched the ZnO photoactivity for all ratios. However, raising the quantity of G4 NPs has increased the photoactivity of the hybrids. This was shown by the augmented % degradation of MB with G4/ZnO ratios.

The photodegradation rates of the hybrids were shown for each GNP size as a function of golds loading contents. The results are depicted in Figure 41.

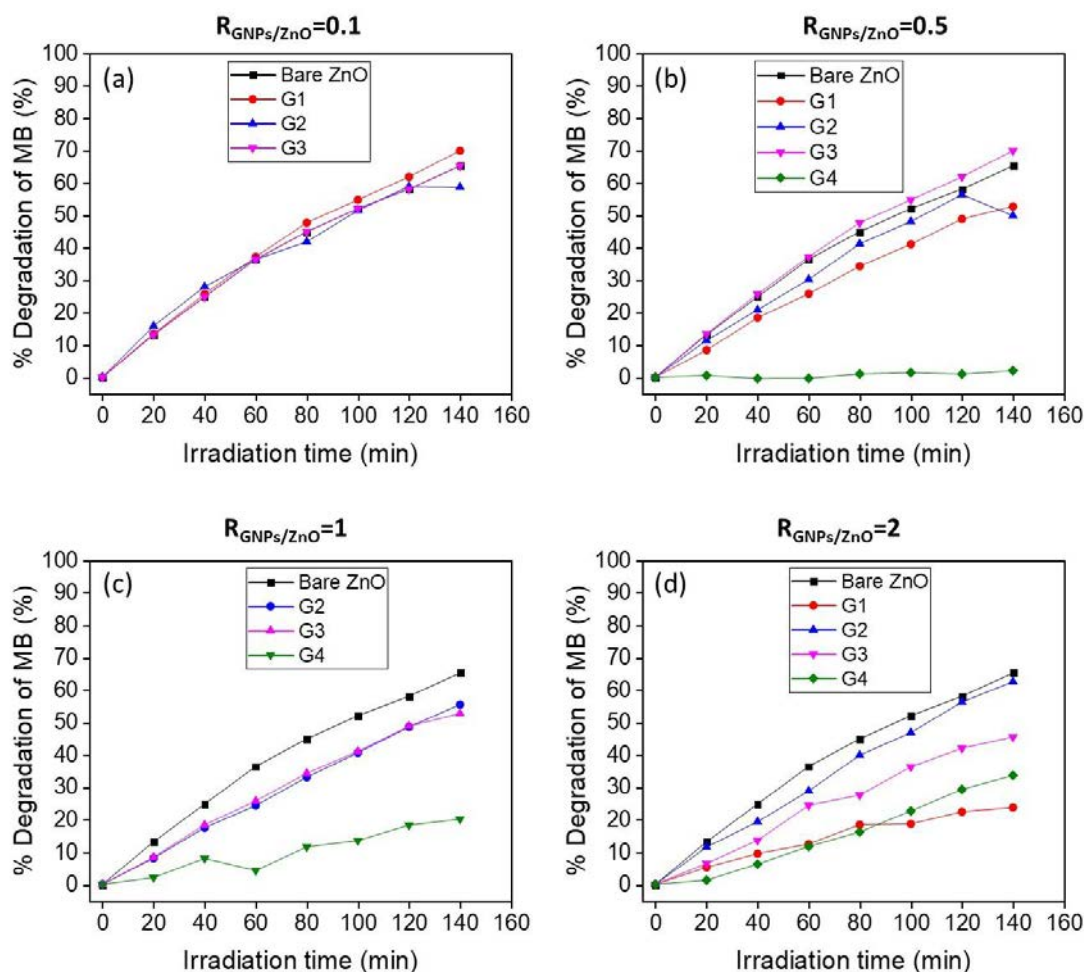


Figure 41 % degradation of MB using GNPs/ZnO catalyst in different sizes at (a)  $R_{\text{GNPs/ZnO}}=0.1$ , (b)  $R_{\text{GNPs/ZnO}}=0.5$ , (c)  $R_{\text{GNPs/ZnO}}=1$ , (d)  $R_{\text{GNPs/ZnO}}=2$ .

At low GNPs contents, *i.e.*  $R=0.1$  shown in Figure 41(a), the photoactivity was nearly similar before and after the addition of the fabricated GNPs, since we observe a non-considerable change in the % degradation of MB.

Intensifying the amount of GNPs in the solution to reach  $R=0.5$  (Figure 41(b)), lead to similar results except for G4 which showed a high quenching of the photocatalytic activity after its addition into the ZnO solution.

Boosting the GNPs number into the solution to have  $R=1$  adapts the same results, but with enhanced activity of G4 in comparison to the same hybrid of  $R=0.5$ .

The enhancement of the G4 was more clear after the increase of the GNPs amount into the solution at  $R=2$ .

Therefore, increasing the GNPs amount in the solution could not enhance the photocatalytic activity of the ZnO catalyst. Yet, the photoactivity of the hybrids is markedly affected. It is likely that the GNPs surrounding the ZnO nanoparticles hinders the reaction between  $O_2$  or OH

species on the hybrids surfaces and the photogenerated charges. CTAB-capped GNPs could also act as barrier between ZnO and the surrounding media to reduce the generation of O<sub>2</sub> or OH species, causing the limitation of the PC activity. These hybrid nanoparticles would significantly expand the applications of ZnO for the UV protection of a wide range of materials by empowering the effectiveness of the blocking UV radiation useful in cosmetic domains.

### 3.3.4 Other strategies of plasmon-exciton coupling

#### 3.3.4.1 Real-time synthesis of GNPs over ZnO NPs: real-time interaction

The gold precursor of concentration of  $5 \times 10^{-5}$  M is capped with CTAB, then attached into ZnO NPs in the solution. The solution containing HAuCl<sub>4</sub> and CTAB only (before reduction) was added into the ZnO NPs solution in different volumes to reach the volume ratios 0.1, 0.5, 1 and 2 with respect to ZnO. The solutions were stirred well to guarantee the attachment of the HAuCl<sub>4</sub> and CTAB mixed solution into ZnO. Then, the reducing agent NaBH<sub>4</sub> was added into the whole solution to reduce the gold precursor loaded in the ZnO into the nanoparticles form to reduce the GNPs attached over the surface of ZnO NPs. This method allows the increase of the size of the GNPs over ZnO surfaces. The size of the GNPs increases with increasing the volume of the HAuCl<sub>4</sub>-CTAB complex solution over ZnO. The fabricated GNPs are finally named S1, S2, S3 and S4 of respective size increase. The obtained hybrids were examined by UV-Vis spectrophotometry in addition to the photoluminescence measurements. The results are shown in Figure 42.

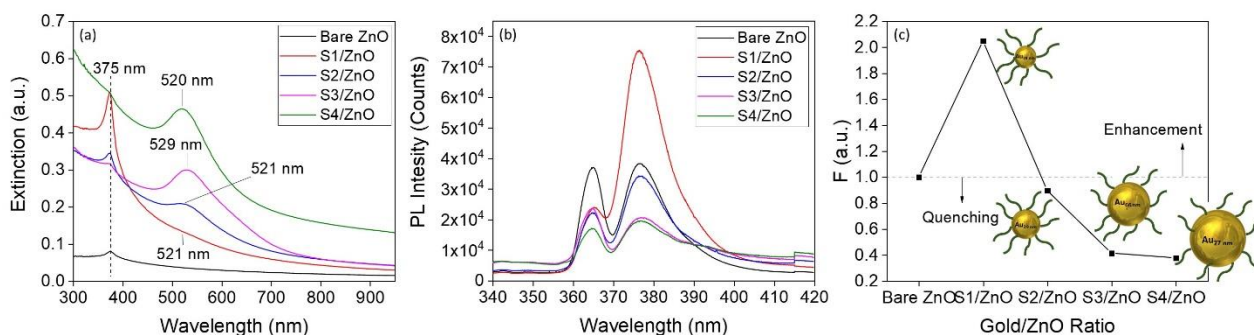


Figure 42 Different sizes of GNPs (S1, S2, S3 and S4) coupled into ZnO surfaces in real time, obtained by the reduction of the CTAB-capped gold precursor after being loaded into ZnO NPs (a) extinction spectrum, (b) UV region of the PL spectrum and (c) UV-PL modification factor. The different dimensions of the green shell capped-golden spheres represents the CTAB-capped GNPs of different sizes.

Figure 42(a) represents the extinction spectrum of different sizes of the hybrid. For the smallest obtained GNPs (S1) on ZnO surfaces (S1/ZnO), an intense peak at 375 nm corresponding to the absorption of ZnO NPs was observed in addition to a very weak shoulder at 521 nm associated to the PR peak of S1. The intensity of the ZnO peak is higher in comparison to bare ZnO. This intensity decreased with increasing GNPs size to reach a very small and broad shoulder for S4/ZnO, conserving its maximum at 375 nm, whereas the intensity of the PR peak increased with ratio. The PR peak position revealed to the spherical morphology of the obtained GNPs. As the GNPs size increased for S2 in the hybrid, the PR peak is red shifted into 529 nm. The further increase in the gold nanoparticle's size blue shifted the PR peak into smaller wavelengths with increasing amplitude, indicating the quantum confinement of the GNPs obtained. The evolution of the extinction spectra after reducing the gold precursor over ZnO indicates the successful coupling between GNPs and ZnO NPs.

As observed in Figure 42(b), the photoemission of ZnO was both enhanced and quenched depending on the GNPs size. The enhancement was only observed at the smallest gold size (S1), where higher GNPs sizes quenched the ZnO luminescence. As the size of the GNPs increases, the surface effect controls the charge transfer in the hybrids. Therefore, at small sized GNPs (S1), more energetic electrons are present over S1 surface due to their high mobility resulted from the decreased surface-to-volume ratio. This could increase the probability of transferring the excited electrons from the GNPs surface and interband into ZnO NPs leading to NBE emission enhancement. Whereas at higher gold sizes, the probability of transferring electrons from GNPs into ZnO decreases, which become in competition with transferring the electrons from ZnO surfaces into GNPs due to the mentioned surface effect. Therefore, the photoexcited charges transfer from the ZnO CB into the attached GNPs to reach an equilibrium state, leading to increased quenching with boosting ratios.

Since the conditions of the excitation source was constant during all the PL measurements here, the observed evolution in the PL intensity for the different samples can be referred to the change in the properties of the gold loaded ZnO NPs, indicating their evolution of size.

#### **3.3.4.2 Capping GNPs after reduction**

The pure GNPs without CTAB (named Au1) were then capped by CTAB after being reduced. The modified GNPs were attached into ZnO NPs at R= 0.1. The extinction and PL measurements were performed (Figure 43 (a&b) respectively). The UV-PL modification factor in comparison to uncapped GNPs (Au1) was examined after coupling into ZnO (Figure 43 (c)).

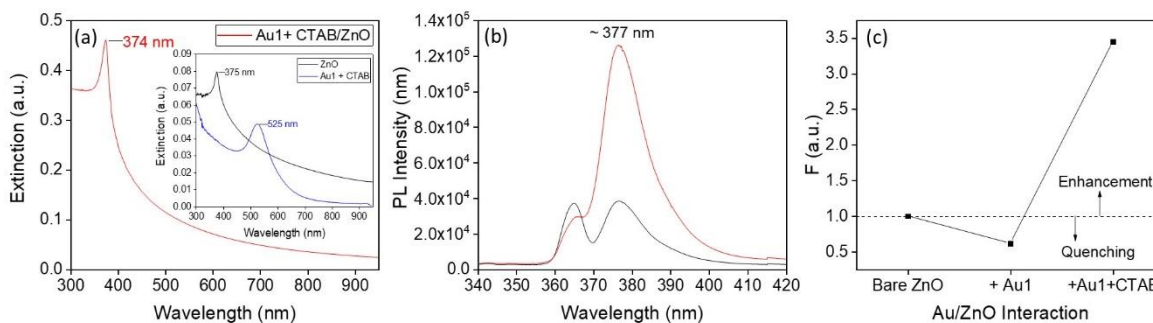


Figure 43 CTAB-capped Au1 (modified Au1) coupled into ZnO at R=0.1; (a) Extinction spectra, the inset represents the extinction spectra of bare ZnO as well as the bare gold nanoparticles used (Au1=CTAB), (b) UV zone of the PL spectrum, (c) evolution of the UV-PL modification factor (F) with respect to ZnO after the addition of Au1 with and without CTAB capping.

As shown in Figure 43(a), the absorption peak relative to the ZnO NPs was more intense than that of pure ZnO. Which means that the GNPs forces the ZnO to absorb more in the UV region. In addition, the ZnO exciton emission was highly enhanced in the presence of the Au1 capped by CTAB, as observed in Figure 43(b). Therefore, charge and/or energy were transferred from GNPs into the CB of the ZnO NPs, increasing the latter's radiative recombination, which in turns increases the ZnO PL. Therefore, the presence of the CTAB molecules was crucial in the ZnO luminescence enhancement. This was clearly observed in Figure 43(c), stating the comparison of the UV-PL modification of the coupled Au1 into ZnO NPs before and after addition of the CTAB into the GNPs. To be accurate, the quenching of the ZnO was observed in the absence of CTAB molecules. Whereas, the addition of the CTAB highly induces the enhancement of the ZnO UV emission.

Subsequently, as a connection platform between ZnO NPs surfaces and GNPs, the capping agent for GNPs has a crucial function in the charge transfer between the nanoparticles in the hybrid system. Several researchers studied the exciton-plasmon distance [59,60]. Thus, it is important to understand the effect of these agents on the luminescence of ZnO NPs, and the chemical control of the proper distance between the ZnO and GNPs to obtain a higher enhancement.

### 3.3.4.3 Tailoring the heterojunction distance between ZnO and GNPs: Free capping hybrid nanoparticles

The smaller sized GNPs (of initial precursor concentration  $5 \times 10^{-5}$  M) was now synthesized in the absence of CTAB. The SEM image of the obtained pure nanoparticles is shown in Figure 44.

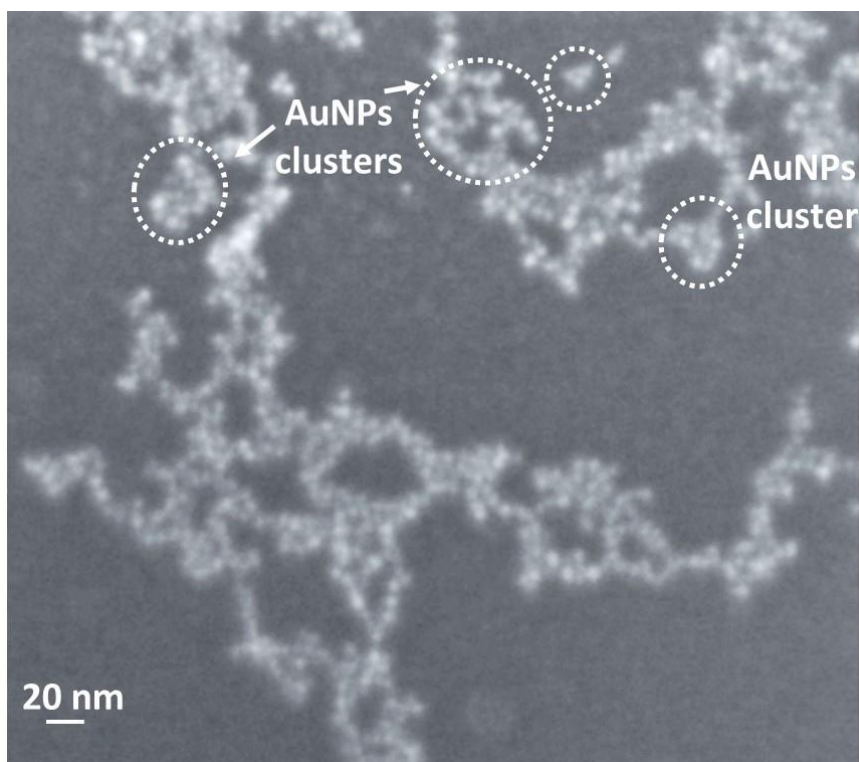


Figure 44 SEM image of the fabricated pure GNPs (Au1).

The SEM image reveals the spherical morphology of small sized GNPs (Au1) arranged in clusters.

The extinction spectrum of the fabricated pure GNPs named Au1 is also given in Figure 45(a). Different amounts of pure Au1 NP were loaded into ZnO NPs to obtain different Au1/ZnO ratios, and their influence on the ZnO behavior was examined by measuring the extinction and photoluminescence activities of the hybrids illustrated in Figure 45(b, c, d).

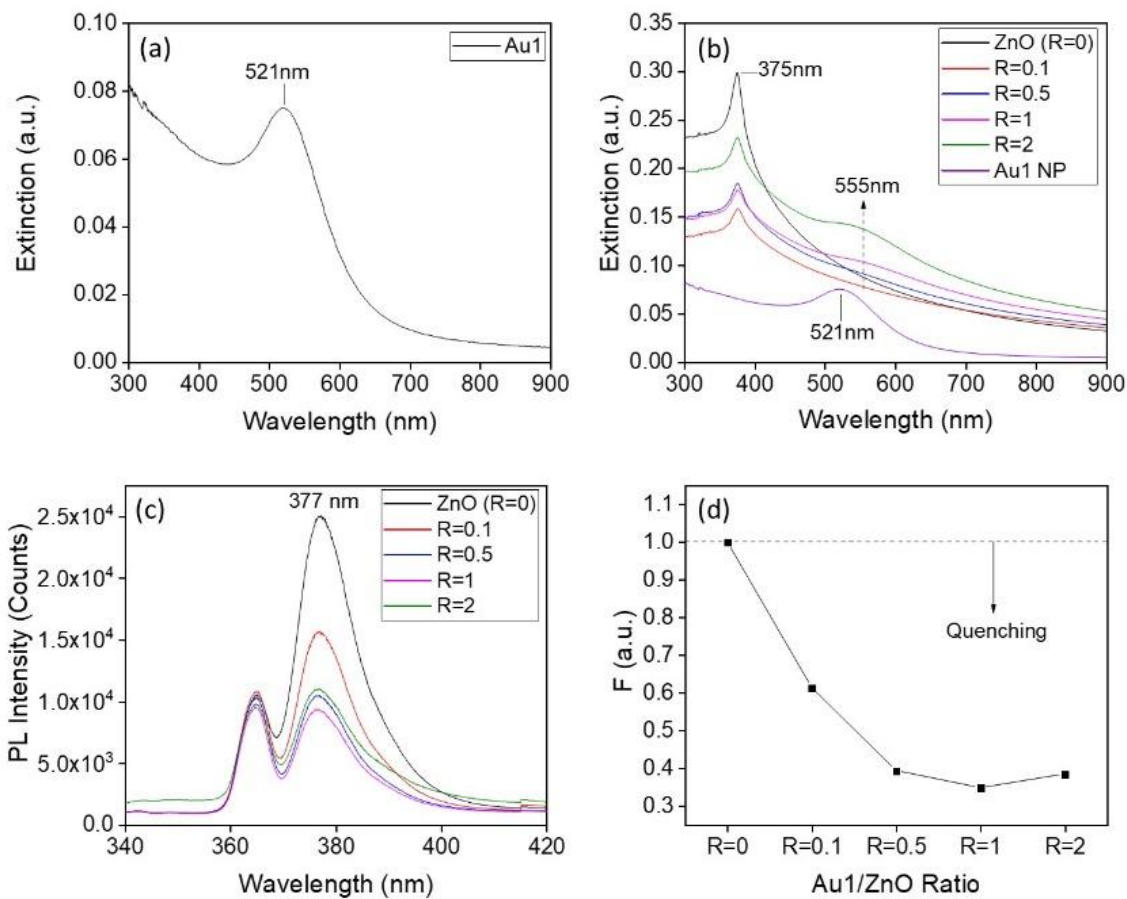


Figure 45 (a) Extinction spectrum of the synthesized pure gold nanoparticles Au1 of initial gold precursor concentration  $[HAuCl_4] = 5 \times 10^{-5}$  M, hybrids after loading the ZnO NPs with different densities of pure GNPs (Au1) to have consecutive ratios of  $R=0.1, 0.5, 1$  and  $2$  ( $R=0$  represents the bare ZnO NPs without any addition of GNPs) (b) Extinction spectra, (c) UV-zone of the photoluminescence spectra and (d) UV-PL modification factor.

Au1 have a SPR absorption at 521 nm (Figure 45(a)), which signifies a spherical morphology of the obtained NP. In this case, the synthesized gold nanoparticles as well as ZnO NPs are pure. Therefore, both constituents may be in direct contact to each other in the absence of ligands or any molecular linkers between them. Hence, no space is present between ZnO NPs surfaces and the attached GNPs, facilitating the charge transfer between both constituents.

As shown in Figure 45(b), in comparison to the absorption of bare ZnO, the hybrids show importantly a weaker extinction that conserves its maximum at 375 nm regardless of the GNPs loading content. This implies that the addition of this GNPs does not affect the absorption of ZnO. The weak peak at 555 nm is referred to the PR corresponding to the GNPs, which is broader and red shifted with respect to that of the used GNPs (Au1). GNPs are considered as highly sensitive materials to the surrounding medium. After the addition of the ZnO NPs solution, initially having a refractive index different from that of the water solvent containing the GNPs, ZnO will change the surrounding environment of the GNPs, resulting in a

modification of the medium's dielectric constant. Consequently, the SPR will be surely modified, transforming into weaker and broader band [94]. The intensity of the SPR peak in the hybrids decreased with decreasing the Au1 loading content (number) to disappear at  $R=0.1$ . This is due to the dilution effect that prevents the identification of this peak.

Figure 45(c) illustrates the UV photoemission spectra of ZnO NPs before and after the addition of different quantities of Au1. The effect of Au1 amount (Au1/ZnO ratio) on the ZnO photoemission behavior was studied by measuring the photoluminescence of the hybrids. All hybrid nanostructures yielded in weaker emission profiles compared to bare ZnO. The UV-PL modification factor (F) was estimated from the PL spectra (Figure 45(d)). As assessed before,  $F=1$  is the characteristic factor for ZnO before the addition of Au NP. After adding Au1 in different ratios, F decreased continuously with increasing Au1/ZnO ratio until reaching values smaller than 1 indicating the luminescence quenching effect.

After UV irradiation, ZnO NPs have photoexcited electrons in the CB. GNPs interband is also excited, inducing GNPs to release electrons in the solution and become positively charged after losing electrons in the medium. As the number of excited and positively charged GNPs attached into ZnO NPs increased, more electrons are transferred from ZnO to these GNPs. Besides, the probability of GNPs trapped holes in ZnO nanostructures due to direct contact is emerged, leading to increased quenching.

The decrease in the quenching efficiency after further addition (200%) of GNPs into the solution is referred to the increase of released electrons in the solution excited from the GNPs interband, and thus, ZnO may acquire these electrons to make recombination with its holes, and therefore, the radiative recombination probability increases, decreasing the quenching efficiency.

Herein, another reason for quenching is the lack of separating distance between the surfaces of both constituents, which allow the charge transfer from ZnO NPs into GNPs, which elaborated the probability of the PL quenching. The direct contact between Au1 and ZnO NPs is clearly observed through the SEM image of a hybrid sample showing the coupling of pure GNPs (Au1) with ZnO NPs.

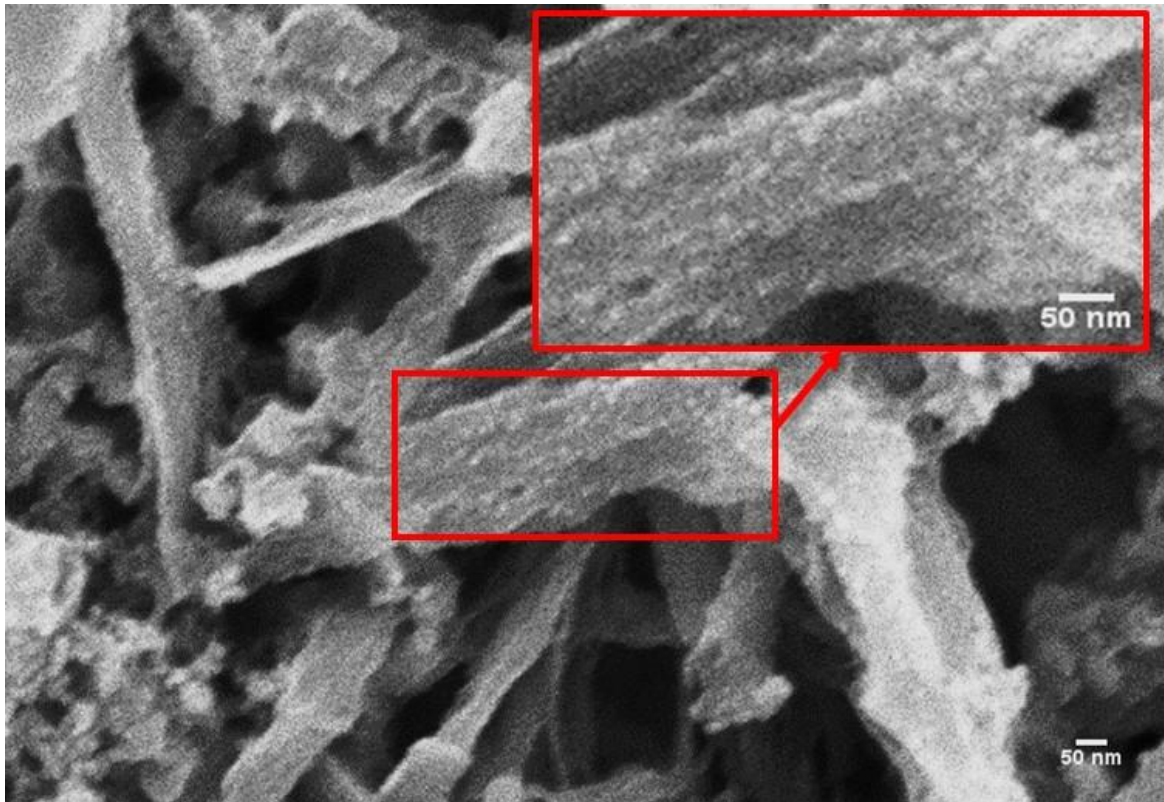


Figure 46 SEM images of the Au1 loaded over ZnO NPs annealed at 250°C (R=0.5). The inset shows a zoom in over a specific zone of the Au1 loaded over ZnO.

One can see the direct contact of the small spherical gold nanoparticles over the ZnO nanostructures. Pure AuNPs modify the morphology of ZnO NPs over substrates, changing their initial structures.

### 3.4 Conclusion

In this chapter, a chemical route to design plasmon-exciton junction in ZnO-Au NPs was described. The optical characterization of the obtained hybrid systems was investigated by UV-Vis absorption, and photoluminescence measurements. By a simple loading of different sizes and quantities of GNPs in a solution, we have realized a controlled emission of ZnO NPs of well-known size and distribution. The SPR of GNPs mediating the exciton emission of the ZnO NPs play an important role in the enhancement and quenching of the UV luminescence of ZnO semiconductor. It is necessary to purify the ZnO NPs to obtain enhanced luminescence after coupling with GNPs, by which the raw material synthesis inhibits the synergic interaction between the GNPs and ZnO NPs, thus quenching the latter's emission. Moreover, the distance separating the GNPs from the surface of the ZnO NPs is also a key factor in controlling the enhancement of the ZnO exciton emission. This inter-distance could be controlled by the size of the capping agent molecule used through the synthesis of GNPs. During the experimental

work, the PL alteration was highly influenced by the size and number of GNPs, in addition to the order of addition of the gold's capping and reducing agents. Assembly of small sized GNPs capped after the reduction of the gold precursor into the formed nanoparticle, and coupled into pure ZnO (annealed at 250°C to obtain optimum size and number), has led to the best enhancement efficiency at a volume ratio of  $R_{\text{GNPs/ZnO}}=0.1$ .

Further experimental studies are necessary in the future to better control the coupling mechanism. As a perspective, the effect of the morphology of GNPs could be investigated. Tuning the heterojunction distance via other ways, working on other plasmonic materials could be promising for the present study.

### 3.5 References

1. Claridge, S.A.; Castleman Jr, A.W.; Khanna, S.N.; Murray, C.B.; Sen, A.; Weiss, P.S. Cluster-assembled materials. *ACS Nano* **2009**, *3*, 244–255.
2. Glotzer, S.C.; Solomon, M.J. Anisotropy of building blocks and their assembly into complex structures. *Nat. Mater.* **2007**, *6*, 557.
3. Grzelczak, M.; Vermant, J.; Furst, E.M.; Liz-Marzan, L.M. Directed self-assembly of nanoparticles. *ACS Nano* **2010**, *4*, 3591–3605.
4. Mann, S. Self-assembly and transformation of hybrid nano-objects and nanostructures under equilibrium and non-equilibrium conditions. *Nat. Mater.* **2009**, *8*, 781.
5. Nie, Z.; Petukhova, A.; Kumacheva, E. Properties and emerging applications of self-assembled structures made from inorganic nanoparticles. *Nat. Nanotechnol.* **2010**, *5*, 15.
6. Srivastava, S.; Kotov, N.A. Nanoparticle assembly for 1D and 2D ordered structures. *Soft Matter* **2009**, *5*, 1146–1156.
7. Shi, X.-F.; Xia, X.-Y.; Cui, G.-W.; Deng, N.; Zhao, Y.-Q.; Zhuo, L.-H.; Tang, B. Multiple exciton generation application of PbS quantum dots in ZnO@PbS/graphene oxide for enhanced photocatalytic activity. *Appl. Catal. B Environ.* **2015**, *163*, 123–128.
8. Li, L.; Yang, S.; Jing, W.; Jiang, Z.; Han, F. Enhanced photocurrent gain by CdTe quantum dot modified ZnO nanowire. *Sens. Actuators Phys.* **2015**, *232*, 292–298.
9. Majumder, T.; Mondal, S.P. Advantages of nitrogen-doped graphene quantum dots as a green sensitizer with ZnO nanorod based photoanodes for solar energy conversion. *J. Electroanal. Chem.* **2016**, *769*, 48–52.
10. Hmar, J.J.L.; Majumder, T.; Dhar, S.; Mondal, S.P. Sulfur and Nitrogen co-doped graphene quantum dot decorated ZnO nanorod/polymer hybrid flexible device for photosensing applications. *Thin Solid Films* **2016**, *612*, 274–283.

11. Xiao, F.-X. Construction of highly ordered ZnO–TiO<sub>2</sub> nanotube arrays (ZnO/TNTs) heterostructure for photocatalytic application. *ACS Appl. Mater. Interfaces* **2012**, *4*, 7055–7063.
12. Chen, S.; Zhao, W.; Liu, W.; Zhang, S. Preparation, characterization and activity evaluation of p–n junction photocatalyst p-ZnO/n-TiO<sub>2</sub>. *Appl. Surf. Sci.* **2008**, *255*, 2478–2484.
13. Tak, Y.; Hong, S.J.; Lee, J.S.; Yong, K. Fabrication of ZnO/CdS core/shell nanowire arrays for efficient solar energy conversion. *J. Mater. Chem.* **2009**, *19*, 5945–5951.
14. Zhang, X.; Qin, J.; Hao, R.; Wang, L.; Shen, X.; Yu, R.; Limpanart, S.; Ma, M.; Liu, R. Carbon-doped ZnO nanostructures: facile synthesis and visible light photocatalytic applications. *J. Phys. Chem. C* **2015**, *119*, 20544–20554.
15. Fu, H.; Xu, T.; Zhu, S.; Zhu, Y. Photocorrosion inhibition and enhancement of photocatalytic activity for ZnO via hybridization with C<sub>60</sub>. *Environ. Sci. Technol.* **2008**, *42*, 8064–8069.
16. Ahmad, M.; Ahmed, E.; Hong, Z.L.; Jiao, X.L.; Abbas, T.; Khalid, N.R. Enhancement in visible light-responsive photocatalytic activity by embedding Cu-doped ZnO nanoparticles on multi-walled carbon nanotubes. *Appl. Surf. Sci.* **2013**, *285*, 702–712.
17. Saleh, T.A.; Gondal, M.A.; Drmosh, Q.A. Preparation of a MWCNT/ZnO nanocomposite and its photocatalytic activity for the removal of cyanide from water using a laser. *Nanotechnology* **2010**, *21*, 495705.
18. Fan, H.; Zhao, X.; Yang, J.; Shan, X.; Yang, L.; Zhang, Y.; Li, X.; Gao, M. ZnO–graphene composite for photocatalytic degradation of methylene blue dye. *Catal. Commun.* **2012**, *29*, 29–34.
19. Bandara, J.; Tennakone, K.; Jayatilaka, P.P.B. Composite Tin and Zinc oxide nanocrystalline particles for enhanced charge separation in sensitized degradation of dyes. *Chemosphere* **2002**, *49*, 439–445.
20. Liqiang, J.; Baiqi, W.; Baifu, X.; Shudan, L.; Keying, S.; Weimin, C.; Honggang, F. Investigations on the surface modification of ZnO nanoparticle photocatalyst by depositing Pd. *J. Solid State Chem.* **2004**, *177*, 4221–4227.
21. Xu, J.; Chang, Y.; Zhang, Y.; Ma, S.; Qu, Y.; Xu, C. Effect of silver ions on the structure of ZnO and photocatalytic performance of Ag/ZnO composites. *Appl. Surf. Sci.* **2008**, *255*, 1996–1999.
22. Lee, J.; Shim, H.S.; Lee, M.; Song, J.K.; Lee, D. Size-controlled electron transfer and photocatalytic activity of ZnO–Au nanoparticle composites. *J. Phys. Chem. Lett.* **2011**, *2*, 2840–2845.
23. Fageria, P.; Gangopadhyay, S.; Pande, S. Synthesis of ZnO/Au and ZnO/Ag nanoparticles and their photocatalytic application using UV and visible light. *RSC Adv* **2014**, *4*, 24962–24972.

24. Li, P.; Wei, Z.; Wu, T.; Peng, Q.; Li, Y. Au–ZnO Hybrid Nanopyramids and Their Photocatalytic Properties. *J. Am. Chem. Soc.* **2011**, *133*, 5660–5663.
25. Chen, Y.; Zeng, D.; Zhang, K.; Lu, A.; Wang, L.; Peng, D.-L. Au–ZnO hybrid nanoflowers, nanomultipods and nanopyramids: one-pot reaction synthesis and photocatalytic properties. *Nanoscale* **2014**, *6*, 874–881.
26. Tahir, M.N.; Natalio, F.; Cambaz, M.A.; Panthöfer, M.; Branscheid, R.; Kolb, U.; Tremel, W. Controlled synthesis of linear and branched Au@ZnO hybrid nanocrystals and their photocatalytic properties. *Nanoscale* **2013**, *5*, 9944.
27. Zeng, H.; Liu, P.; Cai, W.; Yang, S.; Xu, X. Controllable Pt/ZnO Porous Nanocages with Improved Photocatalytic Activity. *J. Phys. Chem. C* **2008**, *112*, 19620–19624.
28. Liu, J.; Li, Y.; Ding, R.; Jiang, J.; Hu, Y.; Ji, X.; Chi, Q.; Zhu, Z.; Huang, X. Carbon/ZnO Nanorod Array Electrode with Significantly Improved Lithium Storage Capability. *J. Phys. Chem. C* **2009**, *113*, 5336–5339.
29. He, J.H.; Chang, P.H.; Chen, C.Y.; Tsai, K.T. Electrical and optoelectronic characterization of a ZnO nanowire contacted by focused-ion-beam-deposited Pt. *Nanotechnology* **2009**, *20*, 135701.
30. Chen, T.; Zhao, T.; Wei, D.; Wei, Y.; Li, Y.; Zhang, H. Core–shell nanocarriers with ZnO quantum dots-conjugated Au nanoparticle for tumor-targeted drug delivery. *Carbohydr. Polym.* **2013**, *92*, 1124–1132.
31. Linsebigler, A.L.; Lu, G.; Yates, J.T. Photocatalysis on TiO<sub>2</sub> Surfaces: Principles, Mechanisms, and Selected Results. *Chem. Rev.* **1995**, *95*, 735–758.
32. Hocheppied, J.F.; Pileni, M.P. Magnetic properties of mixed cobalt–zinc ferrite nanoparticles. *J. Appl. Phys.* **2000**, *87*, 2472–2478.
33. Chen, T.; Xing, G.Z.; Zhang, Z.; Chen, H.Y.; Wu, T. Tailoring the photoluminescence of ZnO nanowires using Au nanoparticles. *Nanotechnology* **2008**, *19*, 435711.
34. Milliron, D.J.; Hughes, S.M.; Cui, Y.; Manna, L.; Li, J.; Wang, L.-W.; Paul Alivisatos, A. Colloidal nanocrystal heterostructures with linear and branched topology. *Nature* **2004**, *430*, 190–195.
35. Luo, S.; Xu, J.; Zhang, Y.; Liu, S.; Wu, C. Double Hydrophilic Block Copolymer Monolayer Protected Hybrid Gold Nanoparticles and Their Shell Cross-Linking. *J. Phys. Chem. B* **2005**, *109*, 22159–22166.
36. Prabakaran, M.; Grailer, J.J.; Pilla, S.; Steeber, D.A.; Gong, S. Gold nanoparticles with a monolayer of doxorubicin-conjugated amphiphilic block copolymer for tumor-targeted drug delivery. *Biomaterials* **2009**, *30*, 6065–6075.
37. Thompson, D.T. Using gold nanoparticles for catalysis. *Nano Today* **2007**, *2*, 40–43.

38. Daniel, M.-C.; Astruc, D. Gold nanoparticles: assembly, supramolecular chemistry, quantum-size-related properties, and applications toward biology, catalysis, and nanotechnology. *Chem. Rev.* **2004**, *104*, 293–346.
39. Chang, C.M.; Hon, M.H.; Leu, I.C. Influence of Size and Density of Au Nanoparticles on ZnO Nanorod Arrays for Sensing Reducing Gases. *J. Electrochem. Soc.* **2013**, *160*, B170–B176.
40. Guo, J.; Zhang, J.; Zhu, M.; Ju, D.; Xu, H.; Cao, B. High-performance gas sensor based on ZnO nanowires functionalized by Au nanoparticles. *Sens. Actuators B Chem.* **2014**, *199*, 339–345.
41. Han, X.; Sun, Y.; Feng, Z.; Zhang, G.; Chen, Z.; Zhan, J. Au-deposited porous single-crystalline ZnO nanoplates for gas sensing detection of total volatile organic compounds. *RSC Adv.* **2016**, *6*, 37750–37756.
42. Li, X.; Zhou, X.; Guo, H.; Wang, C.; Liu, J.; Sun, P.; Liu, F.; Lu, G. Design of Au@ZnO Yolk–Shell Nanospheres with Enhanced Gas Sensing Properties. *ACS Appl. Mater. Interfaces* **2014**, *6*, 18661–18667.
43. Chung, F.-C.; Zhu, Z.; Luo, P.-Y.; Wu, R.-J.; Li, W. Au@ZnO core–shell structure for gaseous formaldehyde sensing at room temperature. *Sens. Actuators B Chem.* **2014**, *199*, 314–319.
44. Aguirre, M.E.; Custo, G.; Goes, M.S.; Bueno, P.R.; Zampieri, G.; Grela, M.A. Critical Water Effect on the Plasmon Band and Visible Light Activity of Au/ZnO Nanocomposites. *J. Phys. Chem. C* **2014**, *118*, 2018–2027.
45. Ahmad, M.; Yingying, S.; Nisar, A.; Sun, H.; Shen, W.; Wei, M.; Zhu, J. Synthesis of hierarchical flower-like ZnO nanostructures and their functionalization by Au nanoparticles for improved photocatalytic and high performance Li-ion battery anodes. *J. Mater. Chem.* **2011**, *21*, 7723.
46. Bora, T.; Myint, M.T.Z.; Al-Harhi, S.H.; Dutta, J. Role of surface defects on visible light enabled plasmonic photocatalysis in Au–ZnO nanocatalysts. *RSC Adv.* **2015**, *5*, 96670–96680.
47. He, W.; Kim, H.-K.; Wamer, W.G.; Melka, D.; Callahan, J.H.; Yin, J.-J. Photogenerated Charge Carriers and Reactive Oxygen Species in ZnO/Au Hybrid Nanostructures with Enhanced Photocatalytic and Antibacterial Activity. *J. Am. Chem. Soc.* **2014**, *136*, 750–757.
48. Mondal, C.; Pal, J.; Ganguly, M.; Sinha, A.K.; Jana, J.; Pal, T. A one pot synthesis of Au–ZnO nanocomposites for plasmon-enhanced sunlight driven photocatalytic activity. *New J. Chem.* **2014**, *38*, 2999.
49. Ruiz Peralta, M.D.L.; Pal, U.; Zeferino, R.S. Photoluminescence (PL) Quenching and Enhanced Photocatalytic Activity of Au-Decorated ZnO Nanorods Fabricated through Microwave-Assisted Chemical Synthesis. *ACS Appl. Mater. Interfaces* **2012**, *4*, 4807–4816.

50. Yu, H.; Ming, H.; Zhang, H.; Li, H.; Pan, K.; Liu, Y.; Wang, F.; Gong, J.; Kang, Z. Au/ZnO nanocomposites: Facile fabrication and enhanced photocatalytic activity for degradation of benzene. *Mater. Chem. Phys.* **2012**, *137*, 113–117.
51. Yoon, M.; Lee, J.-E.; Jang, Y.J.; Lim, J.W.; Rani, A.; Kim, D.H. Comprehensive Study on the Controlled Plasmon-Enhanced Photocatalytic Activity of Hybrid Au/ZnO Systems Mediated by Thermoresponsive Polymer Linkers. *ACS Appl. Mater. Interfaces* **2015**, *7*, 21073–21081.
52. Lawrie, B.J.; Haglund Jr., R.F.; Mu, R. Enhancement of ZnO photoluminescence by localized and propagating surface plasmons. *Opt. Express* **2009**, *17*, 2565.
53. Guidelli, E.J.; Baffa, O.; Clarke, D.R. Enhanced UV Emission From Silver/ZnO And Gold/ZnO Core-Shell Nanoparticles: Photoluminescence, Radioluminescence, And Optically Stimulated Luminescence. *Sci. Rep.* **2015**, *5*.
54. Rahman, D.S.; Ghosh, S.K. Manipulating Electron Transfer in Hybrid ZnO–Au Nanostructures: Size of Gold Matters. *J. Phys. Chem. C* **2016**, *120*, 14906–14917.
55. Pala, R.A.; White, J.; Barnard, E.; Liu, J.; Brongersma, M.L. Design of Plasmonic Thin-Film Solar Cells with Broadband Absorption Enhancements. *Adv. Mater.* **2009**, *21*, 3504–3509.
56. Standridge, S.D.; Schatz, G.C.; Hupp, J.T. Distance Dependence of Plasmon-Enhanced Photocurrent in Dye-Sensitized Solar Cells. *J. Am. Chem. Soc.* **2009**, *131*, 8407–8409.
57. Anger, P.; Bharadwaj, P.; Novotny, L. Enhancement and Quenching of Single-Molecule Fluorescence. *Phys. Rev. Lett.* **2006**, *96*.
58. Praveena, M.; Mukherjee, A.; Venkatapathi, M.; Basu, J.K. Plasmon-mediated emergence of collective emission and enhanced quantum efficiency in quantum dot films. *Phys. Rev. B* **2015**, *92*.
59. Kulakovich, O.; Strelak, N.; Yaroshevich, A.; Maskevich, S.; Gaponenko, S.; Nabiev, I.; Woggon, U.; Artemyev, M. Enhanced Luminescence of CdSe Quantum Dots on Gold Colloids. *Nano Lett.* **2002**, *2*, 1449–1452.
60. Chen, C.W.; Wang, C.H.; Wei, C.M.; Chen, Y.F. Tunable emission based on the composite of Au nanoparticles and CdSe quantum dots deposited on elastomeric film. *Appl. Phys. Lett.* **2009**, *94*, 071906.
61. Mertens, H.; Koenderink, A.F.; Polman, A. Plasmon-enhanced luminescence near noble-metal nanospheres: Comparison of exact theory and an improved Gersten and Nitzan model. *Phys. Rev. B* **2007**, *76*.
62. Vandembem, C.; Brayer, D.; Froufe-Pérez, L.S.; Carminati, R. Controlling the quantum yield of a dipole emitter with coupled plasmonic modes. *Phys. Rev. B* **2010**, *81*.
63. Lai, C.W.; An, J.; Ong, H.C. Surface-plasmon-mediated emission from metal-capped ZnO thin films. *Appl. Phys. Lett.* **2005**, *86*, 251105.

64. Wessel, J. Surface-enhanced optical microscopy. *J. Opt. Soc. Am. B* **1985**, *2*, 1538.
65. Novotny, L.; van Hulst, N. Antennas for light. *Nat. Photonics* **2011**, *5*, 83–90.
66. Jana, N.R.; Gearheart, L.; Murphy, C.J. Seed-Mediated Growth Approach for Shape-Controlled Synthesis of Spheroidal and Rod-like Gold Nanoparticles Using a Surfactant Template. *Adv. Mater.* **2001**, *13*, 1389–1393.
67. Link, S.; El-Sayed, M.A. Size and Temperature Dependence of the Plasmon Absorption of Colloidal Gold Nanoparticles. *J. Phys. Chem. B* **1999**, *103*, 4212–4217.
68. Potje-Kamloth, K. Semiconductor Junction Gas Sensors. *Chem. Rev.* **2008**, *108*, 367–399.
69. Subramanian, V.; Wolf, E.E.; Kamat, P.V. Green Emission to Probe Photoinduced Charging Events in ZnO–Au Nanoparticles. Charge Distribution and Fermi-Level Equilibration †. *J. Phys. Chem. B* **2003**, *107*, 7479–7485.
70. Ansari, S.A.; Khan, M.M.; Ansari, M.O.; Lee, J.; Cho, M.H. Biogenic Synthesis, Photocatalytic, and Photoelectrochemical Performance of Ag–ZnO Nanocomposite. *J. Phys. Chem. C* **2013**, *117*, 27023–27030.
71. Saravanan, R.; Karthikeyan, N.; Gupta, V.K.; Thirumal, E.; Thangadurai, P.; Narayanan, V.; Stephen, A. ZnO/Ag nanocomposite: An efficient catalyst for degradation studies of textile effluents under visible light. *Mater. Sci. Eng. C* **2013**, *33*, 2235–2244.
72. Sangpour, P.; Hashemi, F.; Moshfegh, A.Z. Photoenhanced Degradation of Methylene Blue on Cosputtered M:TiO<sub>2</sub> (M = Au, Ag, Cu) Nanocomposite Systems: A Comparative Study. *J. Phys. Chem. C* **2010**, *114*, 13955–13961.
73. Jing, L.; Zhou, W.; Tian, G.; Fu, H. Surface tuning for oxide-based nanomaterials as efficient photocatalysts. *Chem. Soc. Rev.* **2013**, *42*, 9509.
74. You, J.; Meng, L.; Song, T.-B.; Guo, T.-F.; Yang, Y.; Chang, W.-H.; Hong, Z.; Chen, H.; Zhou, H.; Chen, Q.; et al. Improved air stability of perovskite solar cells via solution-processed metal oxide transport layers. *Nat. Nanotechnol.* **2016**, *11*, 75–81.
75. Yip, H.-L.; Hau, S.K.; Baek, N.S.; Ma, H.; Jen, A.K.-Y. Polymer Solar Cells That Use Self-Assembled-Monolayer- Modified ZnO/Metals as Cathodes. *Adv. Mater.* **2008**, *20*, 2376–2382.
76. Khoa, N.T.; Kim, S.W.; Yoo, D.-H.; Kim, E.J.; Hahn, S.H. Size-dependent work function and catalytic performance of gold nanoparticles decorated graphene oxide sheets. *Appl. Catal. Gen.* **2014**, *469*, 159–164.
77. Wei, H.; Ratchford, D.; Li, X. (Elaine); Xu, H.; Shih, C.-K. Propagating Surface Plasmon Induced Photon Emission from Quantum Dots. *Nano Lett.* **2009**, *9*, 4168–4171.
78. Balamurugan, B.; Maruyama, T. Evidence of an enhanced interband absorption in Au nanoparticles: Size-dependent electronic structure and optical properties. *Appl. Phys. Lett.* **2005**, *87*, 143105.

79. Xie, X.N.; Zhong, Y.L.; Dhoni, M.S.; Xie, Y.; Loh, K.P.; Sow, C.H.; Ji, W.; Wee, A.T.S. UV-visible-near infrared photoabsorption and photodetection using close-packed metallic gold nanoparticle network. *J. Appl. Phys.* **2010**, *107*, 053510.
80. Jakob, M.; Levanon, H.; Kamat, P.V. Charge Distribution between UV-Irradiated TiO<sub>2</sub> and Gold Nanoparticles: Determination of Shift in the Fermi Level. *Nano Lett.* **2003**, *3*, 353–358.
81. Atwater, H.A.; Polman, A. Plasmonics for improved photovoltaic devices. *Nat. Mater.* **2010**, *9*, 205–213.
82. Lin, H.Y.; Cheng, C.L.; Chou, Y.Y.; Huang, L.L.; Chen, Y.F.; Tsen, K.T. Enhancement of band gap emission stimulated by defect loss. *Opt. Express* **2006**, *14*, 2372.
83. Cheng, C.W.; Sie, E.J.; Liu, B.; Huan, C.H.A.; Sum, T.C.; Sun, H.D.; Fan, H.J. Surface plasmon enhanced band edge luminescence of ZnO nanorods by capping Au nanoparticles. *Appl. Phys. Lett.* **2010**, *96*, 071107.
84. Jin, Z.; Gao, L.; Zhou, Q.; Wang, J. High-performance flexible ultraviolet photoconductors based on solution-processed ultrathin ZnO/Au nanoparticle composite films. *Sci. Rep.* **2015**, *4*.
85. Kahn, M.L.; Cardinal, T.; Bousquet, B.; Monge, M.; Jubera, V.; Chaudret, B. Optical Properties of Zinc Oxide Nanoparticles and Nanorods Synthesized Using an Organometallic Method. *ChemPhysChem* **2006**, *7*, 2392–2397.
86. Huang, X.; El-Sayed, M.A. Gold nanoparticles: Optical properties and implementations in cancer diagnosis and photothermal therapy. *J. Adv. Res.* **2010**, *1*, 13–28.
87. Nikoobakht, B.; El-Sayed, M.A. Preparation and Growth Mechanism of Gold Nanorods (NRs) Using Seed-Mediated Growth Method. *Chem. Mater.* **2003**, *15*, 1957–1962.
88. Khan, M.N.; Khan, T.A.; AL-Thabaiti, S.A.; Khan, Z. Spectrophotometric evidence to the formation of AuCl<sub>4</sub>–CTA complex and synthesis of gold nano-flowers with tailored surface textures. *Spectrochim. Acta. A. Mol. Biomol. Spectrosc.* **2015**, *149*, 889–897.
89. Perezjuste, J.; Pastorizasantos, I.; Lizmarzan, L.; Mulvaney, P. Gold nanorods: Synthesis, characterization and applications. *Coord. Chem. Rev.* **2005**, *249*, 1870–1901.
90. Torigoe, K.; Esumi, K. Preparation of colloidal gold by photoreduction of tetracyanoaurate(1-)-cationic surfactant complexes. *Langmuir* **1992**, *8*, 59–63.
91. Yu, H.; Chen, M.; Rice, P.M.; Wang, S.X.; White, R.L.; Sun, S. Dumbbell-like Bifunctional Au–Fe<sub>3</sub>O<sub>4</sub> Nanoparticles. *Nano Lett.* **2005**, *5*, 379–382.
92. Wang, C.; Daimon, H.; Sun, S. Dumbbell-like Pt–Fe<sub>3</sub>O<sub>4</sub> Nanoparticles and Their Enhanced Catalysis for Oxygen Reduction Reaction. *Nano Lett.* **2009**, *9*, 1493–1496.
93. Mahanti, M.; Basak, D. Highly enhanced UV emission due to surface plasmon resonance in Ag–ZnO nanorods. *Chem. Phys. Lett.* **2012**, *542*, 110–116.

94. Linic, S.; Christopher, P.; Ingram, D.B. Plasmonic-metal nanostructures for efficient conversion of solar to chemical energy. *Nat. Mater.* **2011**, *10*, 911–921.

## 4. Chapter 4 Conclusions and perspectives

### 4.1 Conclusions

This PhD thesis was devoted to investigate a simple chemical way for controlling the photoluminescence and the photocatalytic activity of plasmonic-semiconductor nanomaterials. A model system of Au-ZnO was investigated to this aim. This material was managed to adapt several applications especially for UV lasers and photovoltaic devices, as well as for photodegradation of organic molecules in aqueous suspensions needed for environmental appliances. This aim was achieved by the modification of the ZnO surfaces with plasmonic metal gold nanoparticles deposition. A wide overview of different semiconductors associated to metallic nanoparticles was introduced in the first chapter, and their characteristic properties were highlighted too.

Chapter 2 introduced a facile and reproducible low temperature-aqueous way to fabricate highly luminescent and photoactive ZnO NPs as the semiconductor part to be used in the hybrid systems in the next chapters. The produced ZnO were of rough and random morphology having amorphous structures. Consequently, a post thermal treatment at various temperatures ranging from 80 to 800°C was necessary to obtain photoluminescent crystalline nanostructures. The size, morphology, crystallinity, and the luminescent properties as well as the photocatalytic ones were controlled by the annealing process. The 250°C annealing temperature was an optimum temperature to crystallize well the obtained ZnO nanostructures and to have the strongest photoluminescence efficiency as well as high photocatalytic activity. The photocatalysis features of the obtained ZnO NPs were tested by photo-degradation of Methylene Blue (MB) dye. The samples annealed at 250°C also adapted the highest photodegradation activity (~98% in ~100 min). This property showed size dependency in addition to number and crystallinity of the nanostructures. Such facile synthesis method is very relevant for practical applications of low cost UV laser devices and catalysts based on the fabrication of highly luminescent and photoactive semiconducting materials.

Chapter 3 introduces a simple route to control both the photoluminescence and the photocatalytic characteristics of the ZnO nanostructures obtained in chapter 2 through their coupling with gold nanospheres. In the field of energy and environmental applications, ZnO is very suitable semiconductor serving for both fluorescent and photocatalytic efficiencies. However, its wide band gap induces the ZnO nanostructures to absorb only in the UV region

which limits the photocatalytic and photovoltaic processes. In addition, the fast recombination reduces the ZnO photoactivity by competing the charge transfer into the adsorbed species, which are aimed to be degraded. In this context, this chapter explored different strategies to solve these problems that limit the elaboration of ZnO in several applications. The surface modification of ZnO nanostructures with noble metal nanoparticles (GNPs) was investigated. To make it possible, ZnO NPs of different dimensions as obtained in chapter 2, were coupled to CTAB-capped GNPs. The highest PL enhancement was obtained using the ZnO NPs annealed at 250°C; which showed smallest 100% pure nanocrystalline structures. Accordingly, we selected these ZnO NPs for the next studies as a standard semiconductor to examine its exciton interaction with different gold nanoparticles. Different sizes and amounts of CTAB-capped GNPs were coupled to these ZnO NPs, and different PL behaviors were adapted by the ZnO nanostructures. PL enhancement and quenching phenomena were observed depending on the size and number of the attached GNPs. The best PL enhancement was achieved using the smallest size and amount of GNPs of initial acid gold precursor concentration  $5 \times 10^{-5}$  M. This gold concentration was then preferred to couple with the chosen ZnO (annealed at 250°C). The PL enhancement efficiency was then controlled by the way of the GNPs synthesis; *i.e.* by altering the order of addition of the capping agent (CTAB) and that of the reducing agent (NaBH<sub>4</sub>). It was also concluded that the CTAB was creating a beneficial distance between the ZnO nanostructures and the GNPs. This distance was excessively reported by theoretical studies, motivating the researchers to put molecular links in the heterojunction gap to promote the exciton enhancement. This chapter shows that the ZnO-GNPs inter-distance can be controlled chemically by the CTAB capping agent without the addition of further ligands, and thus, less chemical input is attained, leading into accessible pure hybrid NPs. The higher purity of NPs is useful for several applications especially in biomedicine and photocatalysis.

## 4.2 Future work and perspectives

Fluorescent nanomaterials are considered as the dynamos for analysis in various fields of current lab-on-chip (LOC) devices [1]. These systems enable new structural and functional biomolecule studies, enhance chip-based bioanalytical assays, in addition to many other applications [2]. On this basis, ZnO NPs were self-assembled inside PMMA holes on Si-substrates. Consequently, large area template of homogenous properties ZnO NPs was obtained. The resulted substrate could be promising as catalysts for growing ZnO nanowires,

hybrid materials, aiming afterwards to use this system as a fluorescent material in bio-labeling or catalysis operations.

These systems can be obtained by embedding the optimized ZnO NPs annealed at 250°C, into PMMA synthesized in MIBK solvent, following by spin-coating on silicon substrates at different evaporation rates ranging from 250 rpm to 10,000 rpm. The samples were then examined by photoluminescence measurements. The results are shown in the Appendix-A (in Figure 54 of section 5.1.6). The ZnO mass was also varied and spin-coated over Si wafer at speed 250 rpm after loaded into PMMA holes in order to examine the role of the ZnO mass. The PL results are shown in Appendix-A (in Figure 55 of section 5.1.7).

ZnO monolayers were grown on Si substrates using another approach. The second strategy was adapted from our previous studies [3–6], which is described in details in (section 5.1.9) of the Appendix-A. Finally, the obtained monolayer of ZnO NPs-loaded PMMA was evaluated by photoluminescence measurements as illustrated in Figure 47.

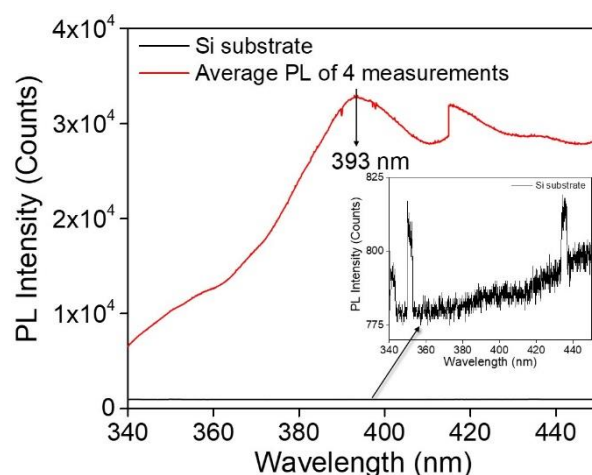


Figure 47 Room temperature average photoluminescence spectrum of ZnO NPs embedded PMMA nanolayer over Si substrate taken at four different positions. The inset corresponds to the PL measurements of the silicon (Si) substrate as a reference.

As observed in the PL spectrum, the obtained ZnO NPs have a UV emission at 393 nm, which corresponds to the exciton emission. The peak above 400 nm is due to noise interference and technical imperfections. The obtained ZnO-loaded PMMA system was consequently observed by optical microscopy and AFM; the corresponding images are depicted in Figure 48.

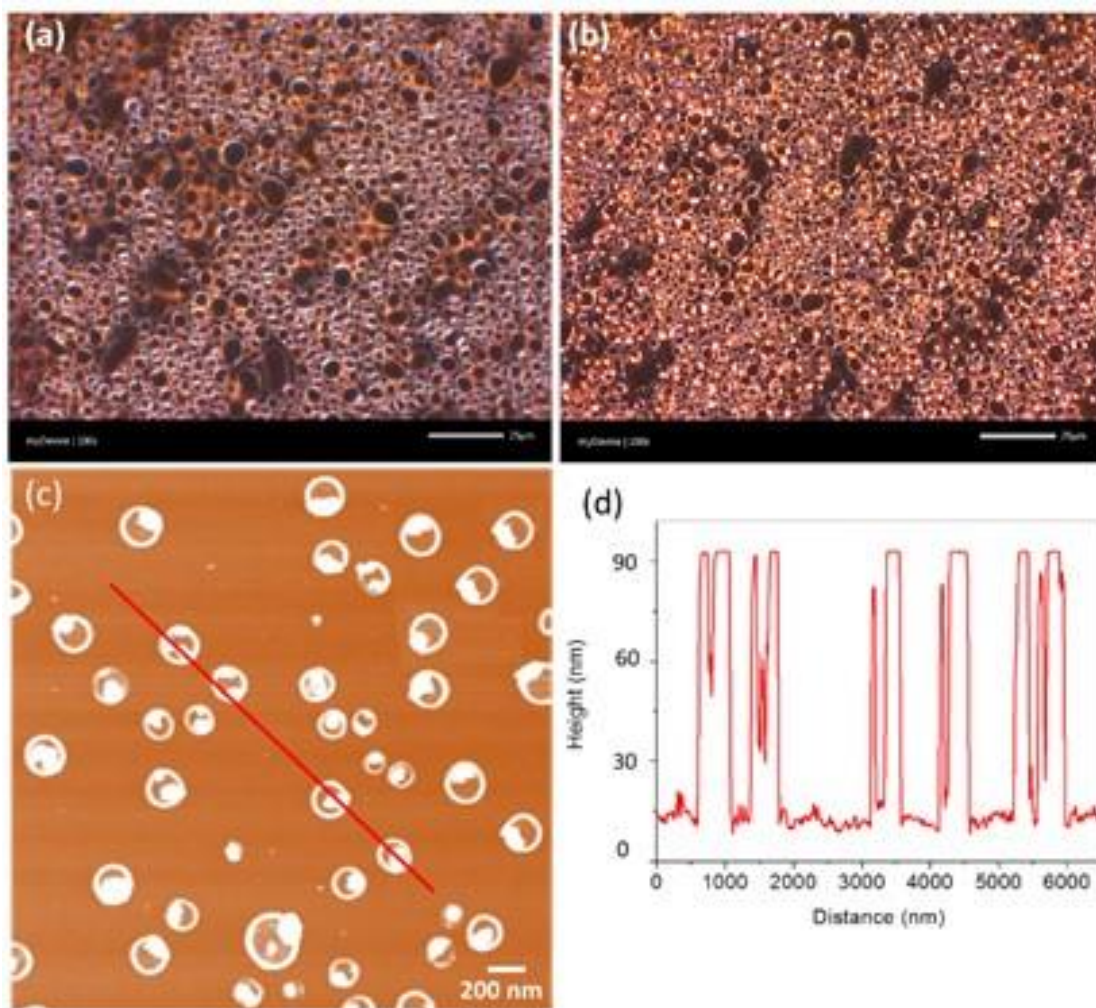


Figure 48 Optical Dark-field (a,b) and AFM (c) image of ZnO NPs-loaded PMMA nanolayer on Si substrate. (a) PMMA layer without ZnO and (b,c) PMMA nanoholes embedded with ZnO NPs, (d) AFM profile of (c).

One can see the presence of ZnO NPs as bright dots localized in the PMMA nanoholes in Figure 48(b) and Figure 48(c). In addition to the production of pure and size-tunable ZnO with a step synthesis process, this result reflects the major novelty because there are no approaches in the literature allowing the assembly of pure, stable and highly luminescent ZnO NPs on large area. It represents a stage forward in the current fabrication processes of nanomaterials that could be promising in biological, photocatalytic, optical, and electronic era. Further experimental studies including the control of the spin-coating parameters, type of substrate (Si, ITO or glass), and the polymer used (PVP, PEG, AG, etc.) are necessary to be investigated in the future, in order to attain a full insight over the growth control of the ZnO NPs into specific shapes and sizes. Besides, gold and/or silver precursors will be added into the zinc nitrate solution. Then, growing the hybrid ZnO-Au/Ag will be attained in the same manner. This creates an effective hybrid exciton-plasmon hybrids on the surface, beneficial for many applications especially in catalysis.

The fabricated layers could be also promising as SERS substrates. In the future, we aim to perform SERS measurements on the obtained chips after coupling with GNPs using the same self-assembly process.

### 4.3 References

1. Whitesides, G.M. The origins and the future of microfluidics. *Nature* **2006**, *442*, 368.
2. Improving fluorescence detection in lab on chip devices. *Lab. Chip* **2008**, *8*, 649–652.
3. Akil-Jradi, S.; Jradi, S.; Plain, J.; Adam, P.-M.; Bijeon, J.-L.; Royer, P.; Bachelot, R. Micro/nanoporous polymer chips as templates for highly sensitive SERS sensors. *RSC Adv.* **2012**, *2*, 7837–7842.
4. Khanafer, M.; Issa, A.; Akil, S.; Hamieh, T.; Adam, P.M.; Jradi, S. A general strategy to incorporate a wide range of metallic salts into ring-like organized nanostructures via polymer self-assembly. *RSC Adv.* **2016**, *6*, 102843–102852.
5. Khanafer, M.; Izquierdo-Lorenzo, I.; Akil, S.; Louarn, G.; Toufaily, J.; Hamieh, T.; Adam, P.-M.; Jradi, S. Silver Nanoparticle Rings of Controllable Size: Multi-Wavelength SERS Response and High Enhancement of Three Pyridine Derivatives. *ChemistrySelect* **2016**, *1*, 1201–1206.
6. Omar, R.; Naciri, A.E.; Jradi, S.; Battie, Y.; Toufaily, J.; Mortada, H.; Akil, S. One-step synthesis of a monolayer of monodisperse gold nanocubes for SERS substrates. *J. Mater. Chem. C* **2017**, *5*, 10813–10821.

## 5. Chapter 5 Supplementary information

### 5.1 Appendix-A

#### 5.1.1 Effect of dilution in PL measurements

The PL measurements highly depend on the number of particles detected. To clarify this behavior, one type of ZnO NPs dispersions (annealed at 250°C) were diluted by different volumes of D.I. water and characterized by PL. 5mg of the ZnO powders were dispersed in 2 ml water. The obtained solution was highly concentrated solution, which was turbid and white colored. Then, 0.5 ml of the obtained solution were diluted 50 times to obtain a clear solution. Then, this solution was diluted in three various dilutions factors (Df). 0.1 ml, 1 ml and 2 ml water were added respectively, to separate ZnO solutions in order to have the proportional dilutions Df1, Df2, Df3. (Df0) represents the clear dispersion solution before the addition of the water. Then, after stirring the solutions, PL measurements were performed, and the UV-PL intensity height ( $\Delta I$ ) for each sample was estimated by the following formula  $\Delta I = I_{\max} - I_0$ , where  $I_{\max}$  is the maximum intensity of the NBE emission, and  $I_0$  is the initial intensity. The difference represents the height of the UV emission at the maximum. The diluted samples were then ultrasonicated in an ultrasonic bath for 15 minutes to. The same dilutions were repeated, but these samples were normally stirred instead of ultrasonication. The results of the diluted samples are shown in Figure 49 that displays the variation of UV-PL intensity height ( $\Delta I$ ), as a function of increasing dilution factors Df1, Df2, Df3 corresponding to the addition of 0.1, 1 and 2 ml of D.I. water into the clear dispersion solution (Df0).

It is clearly observed that increased dilution factor of the solutions leads to a progressive decrease in the exciton emission height intensity. This confirms that the photoluminescence is a particle number-dependent measurement, where after dilution, the number of emitters aligning in the path of incident radiation is reduced, causing a decrease in the PL intensity.

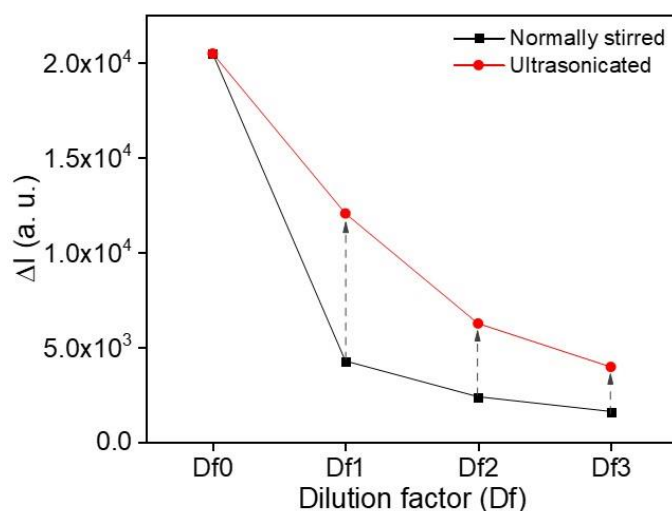


Figure 49 The variation of UV-PL intensity height ( $\Delta I$ ) as a function of increasing dilution factors Df1, Df2, Df3 corresponding to addition of 0.1, 1 and 2 ml of D.I. water to the clear dispersion solution representing Df0 as a reference. The black squared line represents the variation of  $\Delta I$  of the diluted solutions that were normally stirred,

In Figure 49, the black squared line represents the variation of  $\Delta I$  of the diluted solutions that were normally stirred, and the red-circled line represents the variation of  $\Delta I$  of the diluted solutions after ultrasonication in an ultrasonic bath for 15 minutes. After ultrasonication of the diluted samples, a pronounced exciton emission in comparison to the stirred ones was observed for all dilution factors. Hence, the ultrasonication affects the PL measurements of ZnO nanocrystals. Generally, ultrasonic radiations are powerful enough to dissociate the particles, and thus produce more fine particles having higher surface/volume ratio. Consequently, after the excitation by the PL laser, the incident radiation is then able to excite larger number of dissociated particles, which increases the exciton recombination process translated by an increase in the PL intensity.

In fact, the solution with Df1 is more concentrated than that with Df2 and consequently Df3. The exciton emission is strongly enhanced for the concentrated solutions, *i.e.* the efficiency of enhancement of the more concentrated solution was higher than the diluted ones, where the enhancement efficiency was found to be weaker with dilution. This is resulted from the fact that in the concentrated solution, the particle-particle distance is small, and thus, there is a probability for the particles to absorb the emitted light from the neighboring particles. As a result, excitation is doubled through this process, producing more photoexcited electrons, which increases the exciton emission, and the PL is then pronounced.

### 5.1.2 Reproducibility (Stability of dispersions)

In order to examine the stability of dispersion of the ZnO NC in the solution, six different samples of the same type of dispersion of ZnO NC that were annealed at 250°C (4 mg powders dispersed in 15 ml of water) were prepared. PL measurements were performed on 1 ml of each solution. The PL measurements showed that the samples have relatively the same spectrum with an inconsiderable difference in the PL intensities. This means that the solutions were well dispersed and homogeneous. The PL results are shown in Figure 50.

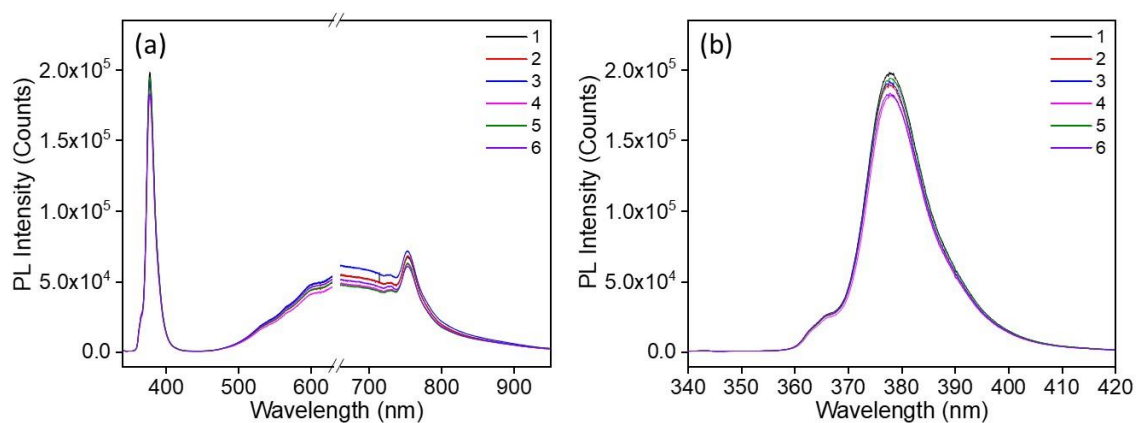


Figure 50 (a) Typical PL spectrum of the repeated samples of ZnO NC annealed at 250°C then dispersed in water, (b) zoom in the UV region of different repeated samples of ZnO NC solutions.

### 5.1.3 Raw materials ZnO coupled into different CTAB-capped GNPs

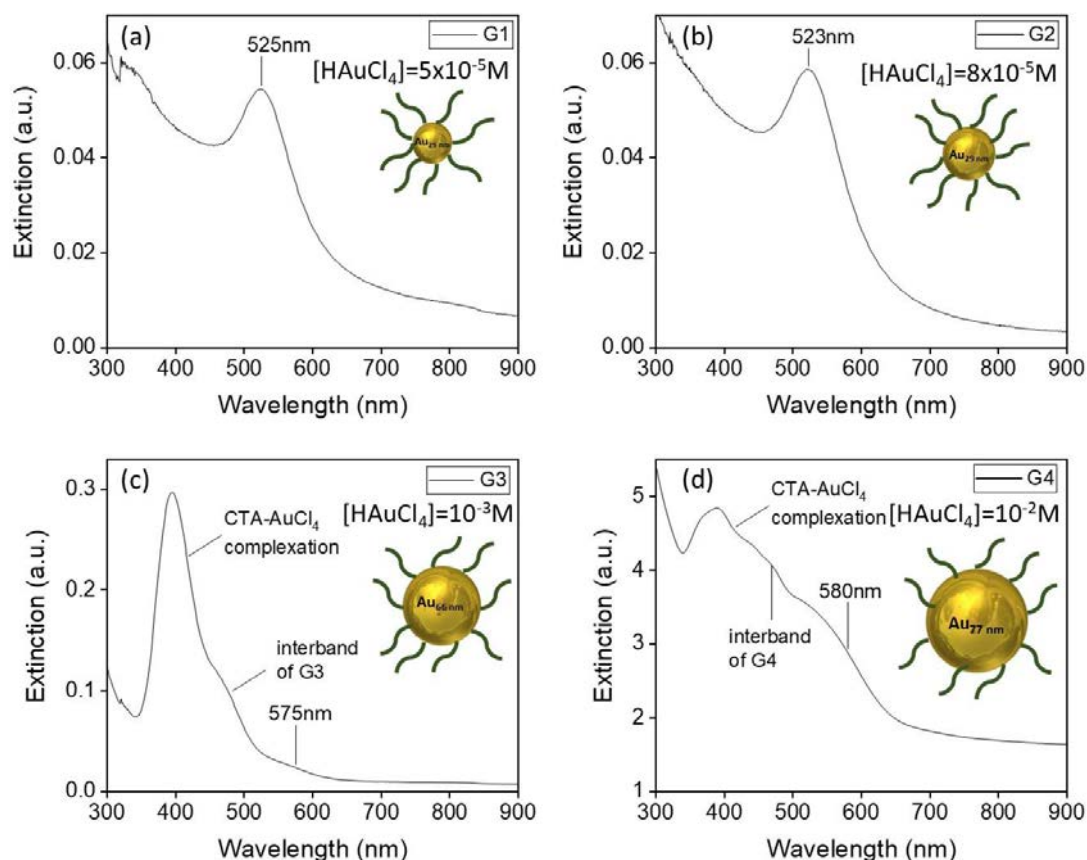


Figure 51 Full range (UV-Vis) extinction spectrum of CTAB-capped gold nanoparticles (a) G1 of  $[HAuCl_4]=5 \times 10^{-5}$  M, (b) G2 of  $[HAuCl_4]=8 \times 10^{-5}$  M, (c) G3 of  $[HAuCl_4]=10^{-3}$  M, (d) G4 of  $[HAuCl_4]=10^{-2}$  M. The inset in each spectrum illustrates the CTAB (green lines)-capped GNPs (golden spheres).

### 5.1.4 Raw materials ZnO coupled into different CTAB-capped GNPs

The coupling of the non-filtered raw materials ZnO nanostructures, after annealing at  $150^\circ\text{C}$ , into different sizes gold nanoparticles in different loading content, lead to the ZnO quenching luminescence in all conditions. The ZnO samples here contain microstructure complexes obtained through the ZnO synthesis. The quenching is attributed to the presence of the microstructures which created a huge distance bothering the synergic coupling between the ZnO NPs and the attached GNPs. Add to that, GNPs could trap the photoexcited holes in the ZnO NPs to decrease its radiative recombination, thus quenching its luminescence. It is clearly observed in Figure 52(a, b, c & d) that all the hybrids showed similar trends in the evolution of the UV-PL modification factor. As the GNPs/ZnO ratio increased from 0.1 to 0.5, the

quenching efficiency increased, which decreased after further addition of GNPs into higher ratios.

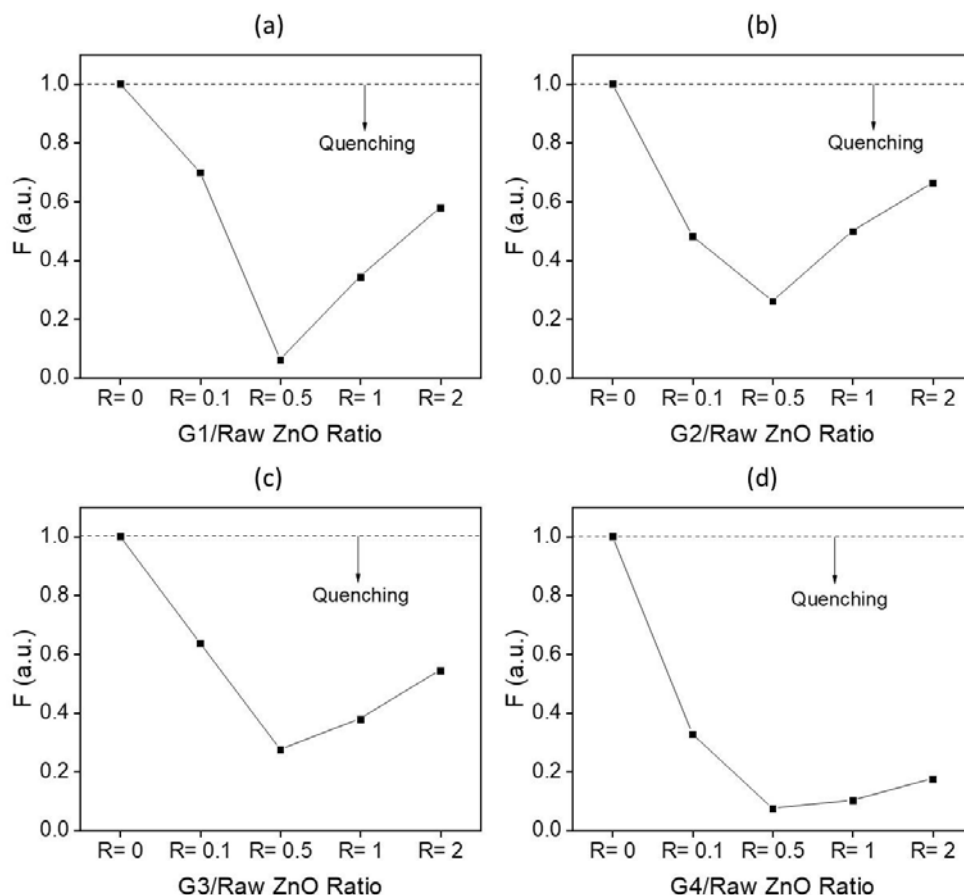


Figure 52 UV-PL modification factor of the raw material synthesis ZnO NPs annealed at 150°C upon coupling with different ratios  $R_{\text{GNPs/raw ZnO}} = 0.1, 0.5, 1$  and 2 into CTAB-capped gold nanoparticles ; (a) G1, (b) G2, (c) G3 and (d) G4.

The excessive addition of GNPs into the raw materials ZnO, the dispersion is then diluted by the GNPs solution. So, the microstructures may be separated from the ZnO NPs, and consequently, the ZnO-GNPs inter-distance decreases, leading to decreased quenching efficiency. The probability of the ZnO nanostructures to capture electrons from the solution released by the excited GNPs interband increases, which may also decrease the quenching efficiency.

### 5.1.5 CTAB-capped ZnO NPs (no GNPs)

As observed in Figure 53(a), after the addition of CTAB solutions in both concentrations, the ZnO NPs are not able anymore to absorb light. One can see that the peak at 375 nm relative

to ZnO absorption has disappeared after the addition of pure CTAB. Moreover, ZnO exciton emission also faded in the presence of the CTAB solution as shown in Figure 53(b).

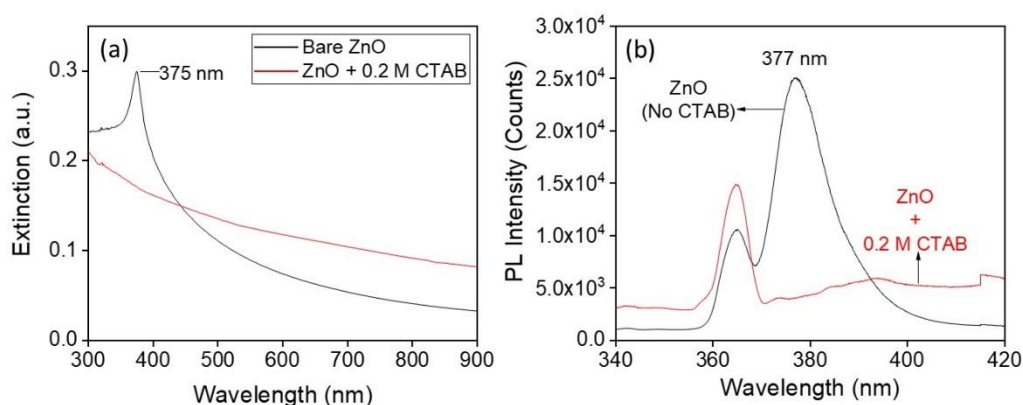


Figure 53 ZnO NPs before and after the addition of 0.2 M CTAB solution (a) extinction spectrum and (b) UV zone of the photoluminescence spectrum.

Therefore, the PL enhancement after coupling the CTAB-capped GNPs into ZnO NPs is resulted from the GNPs interference and not from the CTAB singly. Consequently, the proper inter-distance created by the CTAB between ZnO and GNPs resulted in the PL enhancement. This distance controls the charge-transfer between GNPs and ZnO NPs due to SP effect of the gold mediating the exciton emission of ZnO NPs. Therefore, CTAB may efficiently support this transfer between the ZnO and GNPs surfaces.

### 5.1.6 ZnO NPs embedded PMMA holes

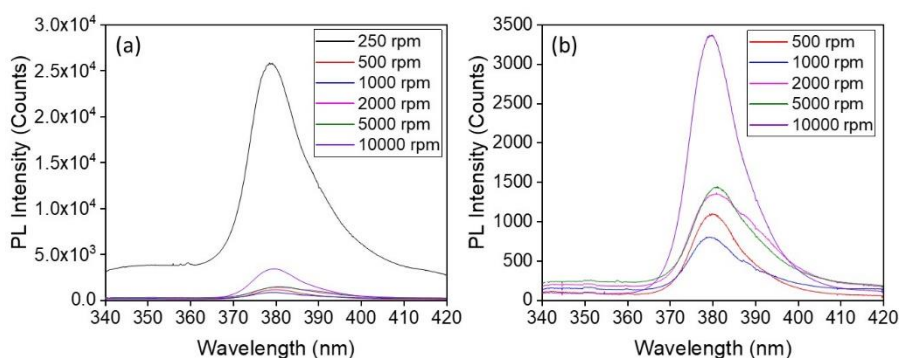


Figure 54 (a) Room temperature average PL spectra of ZnO dispersion embedded in PMMA holes with MIBK solvent. The average spectra for samples spin-coated over different speeds are taken over 5 different positions, except for the samples of 10000rpm speed that illustrates the average PL of 4 positions, (b) zoom in the PL spectra of the speeds higher than 250 rpm.

As the spin-coating speed increased, the average PL intensity decreased due to decreased thickness of the samples. The excessive increase in speed of spin-coating (10,000 rpm) lead to

re-augmenting the PL intensity with respect to others although the samples adapted ultra-thin surface thickness.

### 5.1.7 Role of ZnO mass embedded in PMMA holes

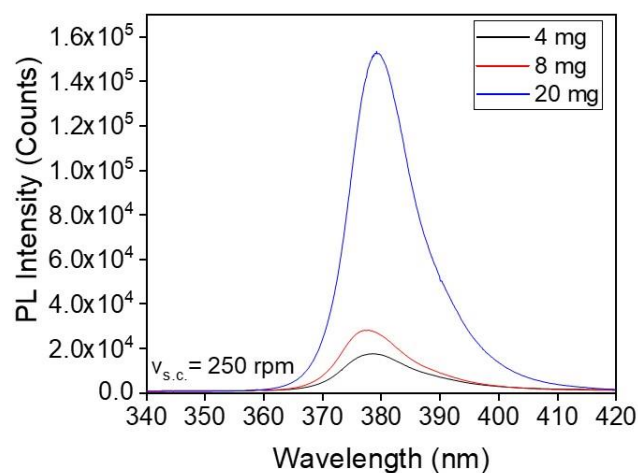


Figure 55 Room temperature PL spectrum of ZnO NPs embedded in PMMA dissolved in MIBK solvent, spin-coated over ITO substrate at a spin-coating speed 250 rpm.

The PL intensity of the spin-coated ZnO loaded PMMA is proportional to the mass of ZnO dispersed in the solution.

### 5.1.8 Different stabilizers mediated the heterojunction distance

Different precursors were examined by PL and UV-Vis (figure 54) absorbance in order to select the best agent for ZnO NPs, to stabilize them without affecting their absorption or emission of light. It is clear from the above results that tripotassium citrate ( $K_3$ citrate) is the best stabilizing agent that do not absorb or emit light in the same region as the ZnO. So it could be used as a stabilizer for the ZnO. The measurements were done over 1 ml of the solution initially containing 2 mg of the precursor dissolved in 2 ml water.

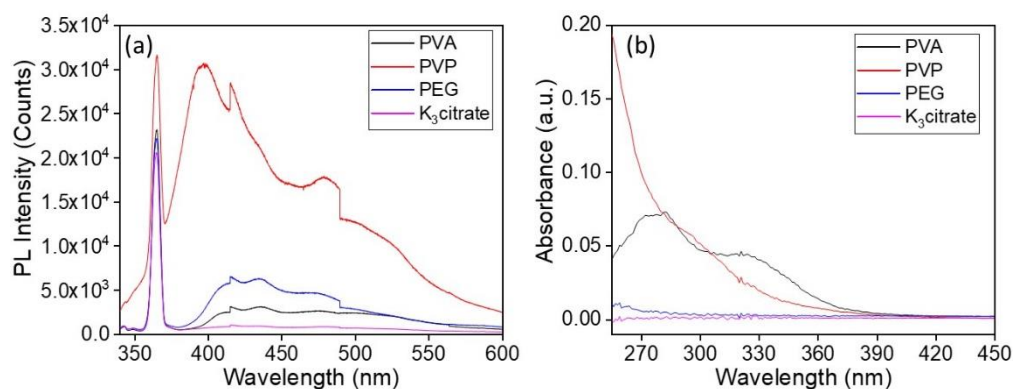


Figure 56 Different stabilizers as PVA, PVP, PEG,  $K_3$ citrate (2 mg) dissolved in 2 ml water (a) Room temperature PL spectra, (b) UV-Vis absorption spectra.

### 5.1.9 Large area monolayer of ZnO NPs

A polymer/zinc nitrate dispersion was formed by mixing solutions of  $Zn(NO_3)_2 \cdot 6H_2O$  and poly-methyl methacrylate (PMMA). The zinc nitrate solution was prepared by the dissolution of 20 mg of zinc precursor in 1ml of ethanol. Then, 1.5 ml of PMMA solution was added to the zinc nitrate and stirred for half an hour. Upon spin-coating of the obtained PMMA/zinc nitrate dispersion on a silicon (Si) substrate (speed=10,000 rpm, time = 30 sec and acceleration = 3000 rpm/sec),  $Zn^{2+}$ -loaded PMMA micelles are formed on the whole substrate. Then, a drop of 0.1M NaOH solution was deposited on the obtained substrate, and the Si-wafer was heated at 80°C for 20 min to obtain the ZnO nanostructures. Arsenic-doped silicon substrates (As-Si) that were used for coating the ZnO-loaded polymer dispersions, were purchased from Silicon materials society (100 orientation, ~525 ohm resistivity). These substrates were cleaned in an ultrasonic bath by soap, then by water followed by acetone during 5 minutes for each step, and finally rinsed with 2-propanol so that they are ready for spin-coating.

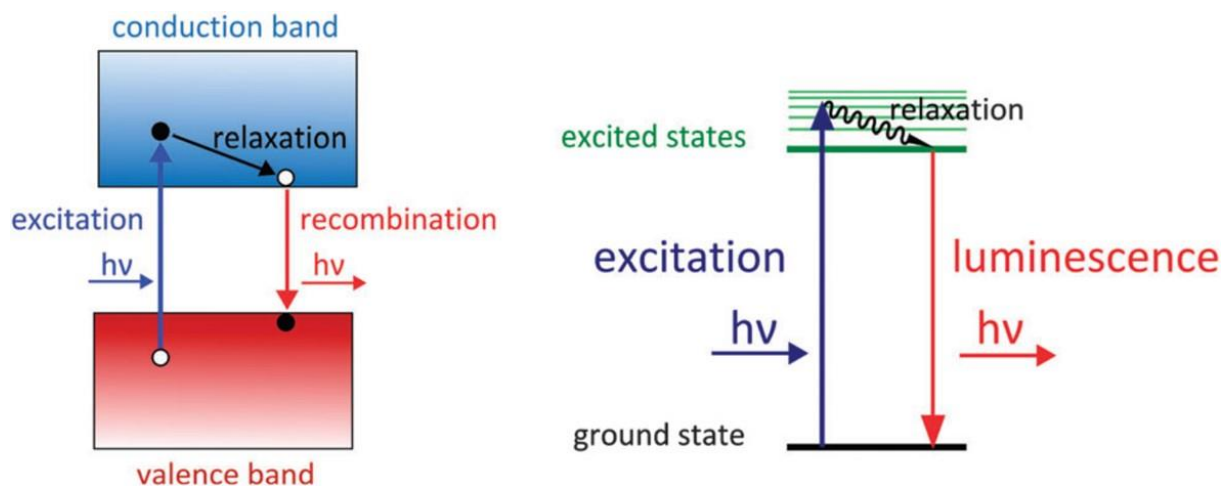
## 5.2 Appendix-B

### 5.2.1 Characterization techniques:

To characterize our product, several analytical methods were used to have an idea about its composition, morphology and structure.

### 5.2.1.1 Photoluminescence (PL)

PL, which is a contactless and non-destructive method, was carried out to investigate the photophysical and photochemical properties of semiconductor materials, in addition to estimate their electronic structure. In this process, light is focused on a sample to photoexcite the materials after the absorption of light and conferring the excess energy inside. This excess energy will be consumed through emission of light translated by photoluminescence. The typical photoluminescence process is illustrated in Scheme 15.



Scheme 15 Simplified mechanisms of semiconductor (electronic bands; left) and molecular based excitation/emission processes (discrete energy levels; right). Adapted from ref. [1].

The photoexcitation induces electrons in the material to move into excited states. When these electrons return to the equilibrium state, they release the excess energy gained through emission of radiative and non-radiative light. The photoluminescence energy corresponds to the difference between the ground and excited states. The energy difference between the conduction and the valence bands is the band gap energy and the PL intensity reflects the number of photo-generated charge recombination in the materials, illustrated by the radiative process that is related to the quantity of emitted light.

*Photoluminescence* measurements (*PL*) were carried out to estimate the optical characteristics of the ZnO exciton recombination using a He-Cd laser of wavelength 325 nm and photon energy 3.82 eV. The spectra were acquired in the range of 340-950 nm. The transmitted light was dispersed by grating and analyzed by a CCD camera. The measurements were performed at room temperature (RT), and the PL data were collected under the same conditions, *i.e.* light path, excitation power, acquisition parameters, exposure time, and split front entrance, to exclude any other effect on the PL measurements.

### 5.2.1.2 UV-visible absorption spectroscopy

*UV-Vis absorption* measurements were achieved to see the absorption of the NPs using a UV-Visible spectrophotometer Specor 205 from Analytic-Jena, where the transmitted light was dispersed and analyzed by a CCD camera with a resolution of 1 nm. These measurements allow us to characterize the optical properties of ZnO NPs giving information about the homogeneity and the size of the NC from their band gap width and the position of the peaks corresponding to the absorption of ZnO. In our experiments, the volume of the ZnO measured was 1ml in all experiments held in plastic PMMA cuvettes. The absorption data were investigated under the same parameters, *i.e.* wavelength range, speed and integration time.

### 5.2.1.3 X-Ray diffraction (XRD)

XRD is a non-destructive technique normally used to study the chemical composition, crystallographic structural and physical properties of solid materials. A constructive interference occurs when the electrons of arranged atoms interact with X-rays at specific angles. At certain incident angles called Bragg angles, parallel X-rays are diffracted by atomic planes that can be used to measure the inter-planar distance between rows of arranged atoms by the following Bragg's law:

$$2d \sin \theta = n \lambda \quad (23)$$

where  $d$  is the distance between atomic layers,  $\theta$  is the Bragg angle, and  $\lambda$  is the wavelength of the X-ray.

The diffraction of these X-rays at the Bragg angles manifests the crystal structure of the analyzed compound. Each material has particular diffraction patterns that identify it according to known database that varies according to different structures.

*X-Ray diffraction (XRD)* measurements were performed using a powder diffractometer (X'pert PRO PANalytique) in reflection mode to study the structure of ZnO samples. The measurements were made under a voltage of 45 KV and an intensity of 50 mA, in an angular range of 0 to 60° ( $0^\circ < 2\theta < 60^\circ$ ) using a copper source of  $\lambda = 1.54056 \text{ \AA}$ .

The measurements were done through collaboration with « Laboratoire de Cristallographie, Résonance Magnétique et Modélisation CRM2. UMR 7036, Institut Jean Barriol ».

#### **5.2.1.4 Transmission electron microscopy (TEM)**

TEM is a microscopic technique where a beam of electrons interacts with an ultra-thin specimen, to pass by it and transmit through, to form an image. The image is then magnified and adjusted onto an imaging device. Transmission electron microscopy could be managed through three different operating modes (imaging, diffraction and energy dispersive spectroscopy analysis (EDS)). This microscopy allows us to have a deep study over the inner structure of the fabricated nanostructures including the topology, morphology, composition, and crystallographic information of the studied material. High resolution transmission electron microscopy (HRTEM) is an imaging mode of the transmission electron microscope (TEM) that allows materials imaging at the atomic scale.

*Transmission electron microscopy (TEM)* investigations were carried out using a JEM - ARM 200F Cold FEG TEM/STEM operating at 200 KV and equipped with a spherical aberration (Cs) probe and image correctors (point resolution 0.12 nm in TEM mode and 0.078 nm in STEM mode). During the preparation of the samples a drop of each suspension was deposited on the TEM grid, in order to be ready for imaging. The measurements were done through collaboration with « Centre de Compétences en Microscopies, Microsondes et Métallographie (CC3M), Institut Jean-Lamour Campus ARTEM »

#### **5.2.1.5 Scanning electron microscopy (SEM)**

The scanning electron microscope (SEM) is a microscopy that produces images of a sample by scanning it with a focused beam of high-energy electrons. The incident electrons thermoelectrically emitted by an electron gun interact with the atoms in the sample, producing various signals, which in turn give several information about studied materials. These information include: surface topography, external morphology (texture), quantitative and qualitative chemical composition, homogeneity, crystallinity and orientation of materials [2]. This method provides a large global view of the particle's size examining their interactions and aggregations. The importance of SEM characterization emerges due to the versatility of its various modes of imaging, the excellent spatial resolution, the relatively straightforward interpretation of the acquired images, and its high level of automation besides its high throughput.

In this manuscript, *SEM images* were acquired using HITACHI SU8030 SEMFEG, with a typical accelerating voltage of 15KV having a large specimen stage with 110 mm traverse range in both of XY direction and a maximum 150 mm diameter sample exchange chamber as standard. The images were elaborated after depositing a drop of the suspension on a silicon substrate and drying at room temperatures. The measurements were done through collaboration with « Lumière, nanomatériaux, nanotechnologies (L2n), Institut Charles Delaunay (CNRS), Université de Technologie de Troyes (UTT) ».

### **5.2.1.6 Photocatalysis**

*The photocatalytic activity* was investigated using 1 ml of methylene blue (MB) dye solution ( $5 \times 10^{-4}$  M) and 1 ml of a  $\sim 0.267 \times 10^{-3}$  g/L ZnO catalyst solution in a 1.0 cm quartz cuvette under UV irradiation using high intensity mercury-xenon lamp with a mercury line filter of 365 nm light segment. The absorbance of the blank reference sample (MB blue irradiated in the absence of the catalyst) was determined using a specific volume of the dye. The quartz cuvettes were 0.4 centimeter apart from the light source in order to avoid the diverging of light through the filter. During irradiation, the solution of ZnO/MB was magnetically stirred and the absorbance of MB was measured by UV-visible spectrometry after the addition of the catalyst for studying the reaction kinetics. The amount of ZnO NCs and that of MB dye were kept constant through all the experiments. The measurements were done through collaboration with « Lumière, nanomatériaux, nanotechnologies (L2n), Institut Charles Delaunay (CNRS), Université de Technologie de Troyes (UTT) ».

### **5.2.1.7 Thermogravimetric analysis (TGA)**

*Thermogravimetric analysis (TGA)* is generally used to determine the evolution of the material's weight in relation to the change in temperature. The derivative weight loss can indicate the point at which the weight loss is mostly evident. This method gives basic information about the solvent residues, absorbed contents, and degradation temperatures. Thermal decomposition of the as-prepared samples was performed using a TA Instruments TGA 2050 Thermogravimetric Analyzer, coupling the heating rate with the mass loss. The thermal evolution of the natural materials was followed from room temperature up to 600°C under nitrogen atmosphere, with a ramp of 10°/min. The software used to extract the data is TA universal analysis.

### 5.2.1.8 X-ray photoelectron spectroscopy (XPS)

X-ray photoelectron spectroscopy, also called electron spectroscopy for chemical analysis (ESCA), is a quantitative spectroscopic technique used to quantify the chemical composition of surfaces by examining its elemental contents with their chemical and electronic states. The spectra are achieved after submitting X-ray beam under ultrahigh vacuum (UHV) to a specimen accompanied by extracting electrons from the valence layers leading to the transitions of electrons from the internal bands to occupy the generated vacancies. The spectra are achieved by measuring the number and kinetic energy of the electron transitions. The kinetic energy of the ejected photoelectrons is then analyzed and transformed into a binding energy for the specific atomic orbital of an electron by the following relation [3]:

$$E_B = h\nu - \varphi - E_K \quad (24)$$

where  $E_B$  is the electron binding energy (eV),  $h$  is the Planck's constant (eV.s),  $\nu$  is the frequency of the incident radiation ( $s^{-1}$ ),  $\varphi$  is the surface work function (eV), and  $E_K$  is the kinetic energy of emergent electron (eV).

XPS measurements for our samples were collected by using a VG Multi Lab 2000 instrument with Al K alpha ( $K\alpha=1486.6$  eV) X-ray source. The measurements were done in «Wuhan University of Technology, State Key Laboratory of Advanced Technology for Materials Synthesis and Processing» through the collaboration with Dr. Wen Luo and Prof. Liqiang Mai.

### 5.2.1.9 Atomic Force microscopy (AFM)

The AFM is one of the foremost tools for imaging, measuring, and manipulating matter at the nanoscale. The information is gathered by "feeling" the surface with a mechanical probe. The information is gathered by "feeling" the surface with a mechanical probe. Piezoelectric elements that facilitate tiny but accurate and precise movements on (electronic) command enable the very precise scanning. With an AFM, it is possible to image an object's surface topography with extremely high magnifications. Furthermore, the magnification of an AFM is made in three dimensions: the horizontal X-Y plane and the vertical Z dimension. An atomic force microscope (AFM) measures the topography of a surface by bringing a cantilever beam into contact with a sample and measuring the deflection of the cantilever as it is scanned across the surface. The cantilever is typically silicon or silicon nitride with a tip radius of curvature on the order of nanometers. When the tip is brought into proximity of a sample surface, forces between the tip and the sample lead to a deflection of the cantilever. As the tip scans a surface to be investigated, interatomic forces between the tip and the surface induce displacement of

the tip. A laser beam is transmitted to and reflected from the cantilever for measuring the cantilever orientation. In a preferred embodiment, the laser beam has an elliptical shape. The reflected laser beam is detected with a position-sensitive detector, preferably a bicell. The output of the bicell is connected to a computer to analyze the data and to obtain then a topographical image of the surface with an atomic resolution. AFM can be operated in a number of modes, depending on the application. In general, possible imaging modes are divided into static (also called contact) modes and a variety of dynamic (non-contact or "tapping") modes where the cantilever is vibrated.

A Nano-R2t AFM, operated in contact mode, performed the AFM measurements for our samples, and the obtained images were color-balanced using the imageJ software.

### 5.2.1.10 Optical microscopy

Optical microscope uses visible light and a system of lenses to magnify the images of small objects. The diffraction of light by the nanoparticles is detected by the light microscopy since the size of the nanoparticles to be detected is smaller than the wavelength of the visible light. The nanoparticles appear as bright and colorful. The light diffraction reveals the physical and spectral characteristics of the detected nanoparticles. The most common types of microscope are the bright and dark field microscopes, depending on the used specimens where the samples are deposited on. *i.e.*, transparent substrates are often observed under a bright field microscope, whereas, substrates that absorb or reflect light are observed under a dark field microscope. The change in the scattering color gives information about the size and homogeneity of the studied samples.

Our samples were deposited on Si-wafers. Dark-field images were obtained by using a straight BX51 Olympus optical microscope using a Halogen source.

## 5.3 References

1. Heine, J.; Müller-Buschbaum, K. Engineering metal-based luminescence in coordination polymers and metal–organic frameworks. *Chem. Soc. Rev.* **2013**, *42*, 9232.
2. Ahmad, R.; Bakar, M.A. Effect of a post-weld heat treatment on the mechanical and microstructure properties of AA6061 joints welded by the gas metal arc welding cold metal transfer method. *Mater. Des.* **2011**, *32*, 5120–5126.
3. Nordling, C.; Hagström, S.; Siegbahn, K. Application of electron spectroscopy to chemical analysis. *Z. Fuer Phys.* **1964**, *178*, 433–438.



Résumé de la thèse intitulée :  
**Synthèse par voie chimique de nanoparticules hybrides plasmoniques-  
semiconductrices à couplage fort pour la photocatalyse**

Par : **Issraa Shahine**

Les hétérojonctions hybrides composées de semi-conducteurs et de nanostructures métalliques ont été perçues comme une technologie durable en raison de leur efficacité parfaite pour améliorer, rénover et enrichir les propriétés des composants intégrés. Le couplage coopératif a pour résultat la variation des propriétés fonctionnelles du système, grâce auquel la résonance de plasmon de surface générée par un métal améliore la séparation de charge, l'absorption de la lumière et la luminescence du semi-conducteur. Ce phénomène permet de fortes interactions avec d'autres éléments photoniques tels que les émetteurs quantiques. Ces fonctionnalités à multiples facettes découlent de l'interaction synergique exciton-plasmon entre les unités liées. Ainsi, les systèmes hybrides conviennent à diverses applications, notamment: conversion de l'énergie solaire, dispositifs optoélectroniques, diodes électroluminescentes (LED), photocatalyse, détection biomédicale, etc.

Les nanostructures Au-ZnO suscitent un intérêt croissant dans ces applications, où le couplage entre des nanoparticules d'or (AuNPs) et ZnO NPs favorise la réponse du système à la région visible du spectre lumineux grâce à leur résonance plasmonique de surface (SPR). Basées sur une taille et une pureté spécifique de nanostructures de ZnO, ainsi que sur les AuNPs et une inter-distance précise entre les nanoparticules, les propriétés des nanostructures de ZnO varient, en particulier celles de photoémission et de photocatalyse.

Dans ce contexte, nous nous sommes concentrés sur la construction de nanocristaux de ZnO (ZnO NCs) de taille ajustable, puis incorporés dans les solutions AuNPs par un moyen chimique simple. Ce travail est donc divisé en deux parties: la première consiste à synthétiser des ZnO NCs purs présentant une excellente photoluminescence UV. Dans la deuxième étape, les ZnO NCs obtenus ont été ajoutés à des nanoparticules d'or de différentes tailles et fractions volumiques.

Dans la première partie, nous avons concentré nos efforts sur la fabrication de points quantiques luminescents et de catalyseurs extrêmement petits et efficaces dans des solutions aqueuses, par voie de synthèse simple et dans des conditions douces (la température, le temps, l'équipement utilisé et les matériaux). Ces paramètres affectent fortement la structure finale des

produits (taille, morphologie, structure de la surface, etc.) en adaptant les propriétés des matériaux. Ainsi, dans la présente étude, des nanoparticules de ZnO de petites tailles, uniformes et hautement stables sont fabriqués en utilisant de l'eau comme solvant non contaminant qui agit comme un agent auto-coiffant, stabilisant et dirigeant, permettant de contrôler la forme et la taille des nanocristaux. Cette méthode est un guide alternatif prometteur pour la préparation des ZnO NPs pur à une température relativement basse dans des conditions douces. Il s'agit d'une méthode simple, verte et à haut débit, ainsi que de la bonne stabilité et de la pureté des produits, où ces propriétés sont nécessaires à des fins photocatalytiques et biologiques.

Sélective, cette réaction se fait par simple mélange de volumes égaux de solutions aqueuses mères équimolaires de précurseur de zinc ( $\text{ZnNO}_3 \cdot 6\text{H}_2\text{O}$ ) dans un précurseur d'oxygène (NaOH), puis le mélange est chauffé 20 min sur une plaque chauffante normale à 80°C. La synthèse est suivie par filtration pour extraire les ZnO NPs obtenus de la solution.

L'analyse thermogravimétrique (TGA) des poudres de ZnO synthétisées a été réalisée pour examiner leur comportement thermique en sondant la décomposition thermique et la stabilité de notre produit avec la température. Le profil TGA indique que la température de 250°C peut être considérée comme une température optimale pour le recuit, ce qui contribuera à garantir la formation de nanostructures de ZnO stables. Par conséquent, les poudres obtenues ont été recuites à différentes températures inférieures (à 80, 100 et 150°C) et au-delà de 250°C (à 500 et 800°C) pour examiner l'effet de recuit sur l'évolution des nanostructures synthétisées. Le traitement post-thermique vise à cristalliser les particules obtenues. Les produits recuits sont ensuite suivis d'études structurelles et optiques (MEB, TEM, DRX, photoluminescence). Les activités photocatalytiques des ZnO NCs sont étudiées en adaptant leur capacité à dégrader le colorant bleu de méthylène (MB). De plus, la relation entre les structures du ZnO, la luminescence et les propriétés photocatalytiques sont explorées.

Les modèles de DRX correspondants ont montré que le produit de synthèse brut est principalement composé de structure cristalline de  $\text{Zn}_5(\text{NO}_3)_2(\text{OH})_8 \cdot 2\text{H}_2\text{O}$ , qui est incorporée dans seulement 9% de nanoparticules amorphes. Par la suite, le recuit thermique a permis la destruction de la phase  $\text{Zn}_5(\text{NO}_3)_2(\text{OH})_8 \cdot 2\text{H}_2\text{O}$  et une disparition complète au-dessus de 250°C donnant lieu à 100% de nanoparticules de ZnO. En augmentant les températures de recuit, le ZnO amorphe devient des structures cristallines. Ceci est également confirmé par les images MEB et TEM pour les échantillons recuits. Les profils d'extinction des échantillons montrent un pic d'absorption dans la région UV. Les résultats de photoluminescence montrent deux pics

d'émission: Une dans la région UV correspondant à l'émission d'exciton et une seconde dans la région visible attribuée à la luminescence du défaut. Les activités photocatalytiques des échantillons testées via la dégradation du colorant bleu de méthylène (MB) montrent également l'efficacité des nanostructures de ZnO en tant que photocatalyseur.

Sur la base de toutes ces études sur les ZnO NCs, 250°C est la température de recuit idéale pour laquelle on obtient la plus haute photoluminescence et principalement des catalyseurs ZnO purs à activité catalytique. Ainsi, ces échantillons ont été sélectionnés pour constituer des couples en AuNPs dans la suite de la thèse.

Dans la deuxième partie, le rôle effectif des AuNPs concernant leur taille, leur quantité et leur molécule coiffante sur la photoémission des nanostructures de ZnO est souligné par le transfert de charge et/ou d'énergie entre les constituants du système hybride. De la même manière, les activités photocatalytiques des systèmes sont examinées après couplage de ZnO aux AuNPs.

Pour ce faire, deux types d'AuNPs sont synthétisés.

1. Les premières AuNPs sans coiffage sont synthétisées par réduction directe (par  $\text{NaBH}_4$ ) du précurseur d'or sans addition de ligands, pour obtenir des AuNPs pures.
2. Deuxièmement, les AuNPs coiffées de CTAB de différentes tailles sont synthétisées par la méthode de réduction chimique en utilisant  $\text{NaBH}_4$  comme agent réducteur et le tensioactif CTAB.

Après avoir mélangé les différentes tailles de AuNPs (pure et coiffée CTAB) dans différentes fractions de volume en un volume constant des ZnO NPs, les activités photoluminescence et photocatalytique des échantillons hybrides ont été examinées, en plus de la caractérisation structurale par imagerie MEB. Le rôle de la partie semi-conductrice et celui de la partie plasmonique sont toutes les deux étudiées.

Les images MEB des échantillons hybrides montrent que les AuNPs purs sont en contact direct avec les surfaces des ZnO NPs et que la présence de AuNPs sans recouvrement est détruite des structures des ZnO NPs. De plus, des nanoparticules pures éteignent la photoluminescence des ZnO NPs sous irradiation UV par transfert de charge direct des surfaces de ZnO aux AuNPs. Ce transfert a été facilité par le contact direct des AuNPs sur les surfaces

de ZnO. D'autre part, l'agent de coiffage CTAB crée une distance entre les surfaces AuNPs et les NPs ZnO.

Les observations de PL montrent que le couplage de ZnO NPs avec des nanoparticules d'or coiffées de CTAB, dans tous les rapports et pour toutes les tailles d'AuNPs, augmente l'émission UV de ZnO par rapport à celle de ZnO pur, à l'exception de la taille plus grande des AuNPs ayant une réponse opposée. Les AuNPs de petites dimensions et présents en petites quantités dans les systèmes hybrides ZnO-Au donnent lieu à une amélioration des PL. À partir de là, on peut s'attendre à ce que le transfert de charge de petits AuNPs vers ZnO soit à l'origine de ce couplage réussi. Le transfert de charge des AuNPs vers les ZnO NPs est induit par le transfert d'énergie du ZnO NPs vers les AuNPs. En d'autres termes, les ZnO NPs ont une luminescence visible faisant référence aux émissions de défauts. Cette plage d'émission chevauche la plage d'absorption des AuNPs chargés. Par conséquent, la luminescence visible pourrait être absorbée par les AuNPs. L'absorption des AuNPs par la luminescence visible pourrait agir comme une excitation visible interne des AuNPs, conduisant à la génération d'électrons chauds à la surface des AuNPs. Ceux-ci pourraient être transférés dans la bande de conduction (CB) des ZnO NPs, augmentant ainsi la recombinaison radiative dans les ZnO NPs reflétée par l'amélioration de PL. Ce phénomène est connu par l'effet PIRET (Transfert d'énergie par résonance induite par Plasmon). Cet effet d'amélioration est validé par la distance entre les AuNPs et les ZnO NPs créés par l'agent coiffant CTAB, afin de permettre le transfert de charge indirect des AuNPs aux ZnO NPs sous irradiation UV, par le biais du transfert d'énergie. Les résultats de photocatalyse mesurés en vue de la dégradation du colorant bleu de méthylène (MB) montrent qu'un nombre optimal de chaque taille d'AuNPs devrait être ajouté dans les ZnO NPs afin d'augmenter l'activité du PC. De petits volumes d'AuNPs coiffée par du CTAB de petite taille peuvent augmenter l'activité de la PC sur les échantillons, alors que de plus grandes quantités de plus grands AuNPs coiffée par du CTAB sont nécessaires pour augmenter l'activité de la PC.

Ce travail montre que l'inter-distance ZnO-AuNPs peut être contrôlée chimiquement par l'agent coiffant CTAB sans l'addition de ligands supplémentaires, ce qui permet d'obtenir moins d'apport chimique, conduisant à des NPs hybrides purs et accessibles. La pureté supérieure des NPs est utile pour plusieurs applications, notamment en biomédecine et en photocatalyse.

D'autres études expérimentales sont nécessaires à l'avenir pour mieux contrôler le mécanisme de couplage. En perspective, l'effet de la morphologie des AuNPs pourrait être

étudié. Régler la distance des hétérojonctions par d'autres moyens, travailler sur d'autres matériaux plasmoniques pourrait être prometteur pour la présente étude.

De plus, les nanomatériaux fluorescents sont considérés comme des dynamos pour l'analyse dans divers domaines. Ces systèmes permettent de nouvelles études structurales et fonctionnelles de biomolécules, améliorent les analyses bioanalytiques, ainsi que de nombreuses autres applications. Sur cette base, les ZnO NPs sont auto-assemblés dans des trous de PMMA sur des substrats en Si. L'avancée de l'intégration des ZnO NPs dans les couches de polymère de PMMA est décrite afin d'obtenir un modèle à grande surface de propriétés de ZnO homogènes. Les nanoparticules de ZnO assemblées avec du PMMA pourraient constituer des substrats prometteurs en tant que catalyseurs pour la croissance de nanofils de ZnO, de nanoparticules métalliques et de nanomatériaux hybrides, visant ensuite à utiliser ce système comme matériau fluorescent dans des opérations de bio-marquage ou de catalyse.

Ces systèmes peuvent être obtenus en incorporant les ZnO NPs optimisés recuits à 250°C dans du PMMA synthétisé dans un solvant MIBK, puis par dépôt par centrifugation sur des substrats de silicium à différentes vitesses d'évaporation allant de 250 rpm/min à 10,000 rpm/min. Les échantillons sont ensuite examinés par des mesures de photoluminescence. La monocouche obtenue de PMMA chargé des ZnO NPs est évaluée par des mesures de photoluminescence. Le système de PMMA chargé en ZnO obtenu est par conséquent observé par microscopie optique et AFM. Outre la production de ZnO pur et réglable en taille avec un processus de synthèse par étapes, ce résultat reflète la grande nouveauté, car aucune approche dans la littérature ne permet l'assemblage des ZnO NPs purs, stables et hautement luminescents sur une grande surface. Il s'agit d'une étape dans les processus de fabrication actuels de nanomatériaux qui pourrait être prometteur à l'ère biologique, photocatalytique, optique et électronique.